DGK Deutsche Geodätische Kommission
der Bayerischen Akademie der Wissenschaften

Reihe C | Dissertationen | Heft Nr. 743

Gamage Sanka Nirodha Perera

Automated generation of 3D building models from dense point clouds & aerial photos

München 2015

Verlag der Bayerischen Akademie der Wissenschaften
in Kommission beim Verlag C. H. Beck

ISSN 0065-5325 ISBN 978-3-7696-5155-3

DGK Deutsche Geodätische Kommission
der Bayerischen Akademie der Wissenschaften

Reihe C Dissertationen Heft Nr. 743

Automated generation of 3D building models from dense point clouds & aerial photos

Von der Fakultät für Umweltwissenschaften
der Technischen Universität Dresden
vorgelegte Dissertation zur Erlangung
des akademischen Grades Doktor-Ingenieur (Dr.-Ing.)

von

M. Sc. Gamage Sanka Nirodha Perera

aus Puttalam – Sri Lanka

München 2015

Verlag der Bayerischen Akademie der Wissenschaften
in Kommission beim Verlag C. H. Beck

ISSN 0065-5325 ISBN 978-3-7696-5155-3

Adresse der Deutschen Geodätischen Kommission:

Deutsche Geodätische Kommission

Alfons-Goppel-Straße 11 ● D – 80 539 München

Telefon +49 – 89 – 23 031 1113 ● Telefax +49 – 89 – 23 031 - 1283 / - 1100

e-mail hornik@dgfi.badw.de ● http://www.dgk.badw.de http://www.dgk.badw.de

Explanation of the doctoral candidate:

This is to certify that this copy is fully congruent with the original copy of the thesis with the topic: "*Automated generation of 3D building models from dense point clouds and aerial photos*".

Dresden, 07.11.2014 Perera, Gamage Sanka Nirodha

Hauptgutachter: Prof. Dr. sc. techn. habil. Hans-Gerd Maas
Mitberichter: Prof. Dr. ir. M. G. George Vosselman
Prof. Dr.-Ing. Uwe Sörgel

Tag der mündlichen Prüfung: 07.11.2014

ISSN 0065-5325 ISBN 978-3-7696-5155-3

Dedicated to
my beloved father,
who passed away during my PhD journey

Abstract

Geometrically and topologically correct 3D building models are required to satisfy the increasing demand in, for instance 3D cadaster, virtual reality, emergency response, robot navigation, and urban planning. Airborne Laser Scanning (ALS) is still the preferred data acquisition system for automated building modeling. Although ALS point clouds are useful for a highly automated processing workflow with high vertical accuracy, their sparse point distribution reduces the planimetric accuracy of model boundaries significantly. In comparison to the ground sampling of digital aerial images to the centimeter level, the planimetric accuracy of building models derived from point clouds is severely limited. Since point clouds and images have rather complementary properties, the integration of these two data sources leads to building models of high vertical accuracy, as well as planimetrical accuracy. In order to preserve the topological relations in the reconstruction schemes, roof topology graphs (RTG) are widely used. Many methods rely on external primitive libraries, which is problematic because only few such data exist. At the same time, there is a lack of approaches that optimally exploit RTGs for the manipulation of roof primitive features, such as roof planes and boundaries.

In this research, a new framework for the automatic reconstruction of building models by integrating ALS point clouds and digital aerial image data is proposed. Topology preserving 3D roof models is first derived from point clouds. These models are subsequently refined to increase the planimentric accuracy with image data. In addition, some of the topological inaccuracies of the initial roof models are rectified. A novel approach employing a cycle graph analysis is introduced to generate the topology preserving roof models from point clouds. Inner roof corners can be recognized as the shortest cycle in a RTG and modeled by intersecting the corresponding feature lines. In this way, external targets (sub graphs) are no longer required. Orientation and placement regularities are applied on weakly defined edges using a piecewise regularization approach prior to the reconstruction, which assists in preserving symmetries of the building geometry. Outer roof corners are geometrically modeled using the outermost cycle derived from the RTG.

In the refinement process, the initially reconstructed roof models are projected onto the image space via collinearity equations. The projected line segments are then used to restrict the search space of candidate line segments that were extracted from the aerial images using the Burns extractor. Corresponding lines in the image are then matched. Afterwards, lines in the object space are constructed as the intersection of viewing planes. In order to minimize ambiguities that may arise in the matching process, scene constraints acquired from the initial roof models are introduced. In general, 3D roof models derived from point clouds represent unambiguous geometries of the scene, except for a few uncertain properties such as the positional uncertainty of roof outlines. As such, three main scene constraints, namely the gradient, the status of planimetric symmetry, and the perpendicular distance to the roof plane, are incorporated for optimizing the matching process. Defects and gaps of the retrieved boundary line segments are minimized based on well-defined evidences. Herein, the known structural arrangements of roof models and convergence priors are used. Weakly defined step-edges and roof outlines are refined by fusing line segments derived from images. Some of the topological defects of the initial roof models, such as defects caused by occlusion, are rectified by adding line segments derived from images. New topological relations that were hidden between roof planes are recovered as step-edges are inserted where necessary. This enhances the completeness and correctness of the refined building models.

Initial and refined roof models derived from the developed schemes are analyzed with the ISPRS benchmark test data. The results of the three test scenes show that both methods are acceptable, and can be used with more complex urban scenes. While proving the robustness of the cycle graph approach by the initial results, the refined models demonstrate that image integration improves the planimentric accuracy significantly, with almost 100% topological and geometrical correctness.

Zusammenfassung

Geometrisch und topologisch korrekte 3D-Gebäudemodelle werden gebraucht, um den steigenden Bedarf zum Beispiel in Rahmen von 3D-Katastern, Virtual Reality, Notfallschutz, Roboternavigation und Stadtplanung zu decken. Airborne Laserscanning (ALS) ist immer noch das bevorzugte Datenakquisitionssystem für die automatische Gebäudemodellierung. Obwohl ALS-Punktwolken für eine hochgradig automatisierte Prozessierung mit großer Höhengenauigkeit geeignet sind, reduziert die spärliche Punktverteilung die Lagegenauigkeit von Modellkonturen erheblich. Im Vergleich zur Bodenabtastung auf Zentimeterlevel von digitalen Luftbildern ist die Lagegenauigkeit von Gebäudemodellen, die von Punktwolken abgeleitet wurden, stark beschränkt. Da Punktwolken und Bilder weitestgehend komplementäre Eigenschaften besitzen, führt die Integration dieser beiden Datenquellen zu Gebäudemodellen von hoher Höhen- und Lagegenauigkeit. Um die topologischen Relationen während der Rekonstruktion zu erhalten, werden verbreitet Dachtopologiegraphen (RTG – roof topology graph) eingesetzt. Viele Methoden sind auf externe Bibliotheken von Objektprimitiven angewiesen, was problematisch ist, da solche Datensätze nur begrenzt zur Verfügung stehen. Gleichzeitig fehlen Ansätze, die die RTGs optimal für die Manipulation von Features von Dachprimitiven wie Dachebenen und Konturen nutzen.

In dieser Arbeit wird ein neues Framework für die automatische Rekonstruktion von Gebäudemodellen vorgestellt, welches ALS-Punktwolken und digitale Luftbilddaten integriert. Topologieerhaltende 3D-Dachmodelle werden zunächst von Punktwolken abgeleitet. Diese Modelle werden anschließend verfeinert um die Lagegenauigkeit durch Bilddaten zu erhöhen. Zusätzlich werden einige topologische Ungenauigkeiten des berechneten Dachmodells korrigiert. Um die topologieerhaltende Dachmodelle aus den Punktwolken zu generieren, wird ein neuartiger Ansatz, der eine Graphzyklenanalyse verwendet, eingeführt. Innere Dachecken können als die Zyklen minimaler Pfadlänge im RTG erkannt und anschließend als Schnittpunkt der korrespondierenden Featurelinien modelliert werden. Damit werden externe Targets (Teilgraphen) nicht länger benötigt werden. Unter Verwendung eines schrittweisen Regularisierungsansatzes um Symmetrien in der Gebäudegeometrie zu erhalten, werden vor der Rekonstruktion Regeln bzgl. der Orientierung und Anordnung auf schwach definierte Kanten angewendet. Äußere Dachecken werden auf Basis des äußersten Zyklus des RTG geometrisch modelliert.

Im Verfeinerungsprozess werden die anfangs rekonstruierten Dachmodelle mittels der Kollinearitätsgleichungen in den Bildraum projiziert. Die projizierten Linien werden dann genutzt, um den Suchraum der Kandidatenliniensegmente, welche von den Luftbildern mit dem Burns-Extraktor bestimmt wurden, einzuschränken. Korrespondierende Linien im Bild werden einander zugeordnet. Anschließend werden Linien im Objektraum durch die Verschneidung von Sichtebenen konstruiert. Um Mehrdeutigkeiten, die während des Matchings auftreten können, zu minimieren, werden *scene constraints* eingeführt, welche von den berechneten Dachmodellen bestimmt werden. Abgesehen von einigen unsicheren Eigenschaften wie die Positionsungenauigkeit der Dachkonturen, repräsentieren 3D-Dachmodelle, die von Punktwolken abgeleitet wurden, im Allgemeinen explizite, eindeutige Geometrien der Szene. Drei Szenenbedingungen werden integriert um den Matchingprozess zu optimieren: der *Gradient*, der Zustand der *planimetrischen Symmetrie* und die *orthogonale Distanz zur Dachebene*. Defekte und Lücken der berechneten Konturliniensegmente werden minimiert auf der Basis von wohldefinierten Beweisen. Hierbei werden die bekannte strukturelle Anordnung von Dachmodellen und c*onvergence priors* benutzt. Schwach definierte Stufenkanten und Dachkonturen werden verfeinert indem sie mit Liniensegmenten fusioniert werden, die von Bildern abgeleitet wurden. Einige der topologischen Defekte der Dachmodelle, wie Defekte, die durch Verdeckungen hervorgerufen wurden, werden durch das Hinzufügen von Liniensegmenten, die von Bildern abgeleitet wurden, korrigiert. Neue topologische Relationen, welche zwischen Dachebenen verdeckt waren, werden wiederhergestellt indem Stufen-Kanten an benötigten Stellen eingefügt werden. Dadurch wird die Vollständigkeit und Korrektheit des verfeinerten Gebäudemodells erhöht.

Ursprüngliche und verfeinerte Dachmodelle, welche mit den entwickelten Methoden generiert wurden, werden mit den ISPRS Benchmark-Testdaten analysiert. Die Resultate der drei Testszenen zeigen, dass beide Methoden akzeptabel sind und auf komplexere urbane Szenen angewendet werden können. Die ersten Ergebnisse zeigen die Robustheit der Graphzyklenanalyse. Die verfeinerten Modelle demonstrieren, dass die Integration von Bildern die Lagegenauigkeit wesentlich verbessert mit fast 100% topologischer und geometrischer Korrektur.

Acknowledgements

This period during my PhD is a unique experience filled with challenges, fruitfulness, joy as well as pain. This thesis would not have been possible without the support of many people, to whom I owe a great deal of gratitude for their guidance, support, and cooperation.

First and foremost, I wish to express my gratitude to my supervisor, Prof. Dr. Hans-Gerd Maas, who has been a true inspiration. You guided me and taught me how to think independently, and gain confidence in many, if not all, aspects of scientific matters. In addition, you opened my eyes to Photogrammetry and I respect the patience you had with me in my long silences. Furthermore, I owe you again for creating a fitting environment for me during the period of my bad health, and also for making arrangements for financial aids for the latter part of my work. It was an honour to work with you.

I extend my gratitude to Prof. Dr. George Vosselman who gave me a sound foundation on the processing of point cloud data during my Masters', and this was the main reason to choose this piece of work for my PhD. In addition, I am thankful to him for being a reviewer for my PhD work. Further, many thanks for his continuous support given to me in many aspects.

I am indebted to Prof. Dr. Uwe Sörgel for being a reviewer of my work. My special thanks to him for giving me an opportunity to meet him, and for giving me valuable guidance on my work.

I take this opportunity to thank Dr. Chris Hopkinson who gave me a chance to learn LiDAR for the first time in my life in Canada.

This thesis was financially supported by the German Academic Exchange Service (DAAD) and the TU Dresden through the GFF program. I extend my gratitude to them as well. I would like to thank the German Society for Photogrammetry, Remote Sensing and Geoinformation (DGPF) for making available the Vaihingen data set for research purposes. I also wish to thank the chair persons of ISPRS Commission III/4 for providing us with data and evaluating the test results.

I appreciate and would like to thank the time spent by Dr. Ranmalee Bandara for proof reading this thesis with many of her other work. My special appreciation goes to Dr. Anita Schilling, for translating the abstract (Zusammenfassung) into Deutsch.

Special thanks to Dr. Bernd Hetze who enhanced my programming skills, enabling me to manipulate long programming codes. I thank Dr. Danilo Schneider for his continuous support to me to have a better life in Germany. I am also indebted to all my colleagues at the Institute of Photogrammetry and Remote Sensing, including the Institutional Secretary Ms. Sigrid Pönitz.

Mr. Saman and Mrs. Gabriele Feyler, thank you for the encouragement that you offered to me, to take part in activities outside research work. To all my friends in Germany, as well as all over the world: you brought support, laughter, joy, care and love with you, and you have been with me in many touching ways.

I would like to express my heartiest gratitude to my parents who have been understanding, caring and passionate about my education. Unfortunately, I had to say 'Attain Nibbana..!' to my beloved father, who passed away during my PhD journey in Germany. Last but not least, I wish to thank Dr. Nalani, my beloved wife who always behind me and care me than her life. You certainly changed my life more than else during the last few years.

Table of Contents

List of figures

List of tables

1. Introduction

This thesis discusses uncertain topological and geometric reasoning of three dimensional (3D) building models by integrating Airborne Laser Scanning (ALS) point clouds and aerial photographs. It is motivated by different geometric and topological problems inherited in the building reconstruction process in recent developments, particularly, through building reconstruction from point cloud data. The current trend in increased applicability of 3D building models is also a motivation to introduce new concepts to this field. It is about the efficient manipulation of roof primitives for realistic roof reconstruction from point clouds only, by incorporating cycle graph concepts into Roof Topology Graphs (RTG). The work presents an outer boundary refinement in projective geometry by introducing a new version.

1.1 Motivation

More than 50% of the world population lives in urban areas. Statistics suggest that in 2050, this number will become over 70% (Un-Habitat, 2012). With the fragmentation of lands and reduction of living space per dweller, it is of great importance to manage living areas, particularly in urban cities. Many countries spend considerable amounts of money to collect remotely sensed data, *i.e.* space borne and airborne data, over urban cities for better planning strategies and continuous monitoring in relation to this urban growth. 3D city models are primarily used for this purpose. Among the elements of a city model, 3D building models are the most significant element as they are the most dominant manmade object in urban scenes. Thus, the reconstruction of 3D building models is of great importance for a diverse range of applications including urban planning, virtual reality, environmental studies, telecommunication, 3D cadaster, emergency response, robot navigation and so on. In addition, with the current trends in navigation systems and its accessible forms for general public, for instance, location-based services and augmented reality, the need for efficiently-generated building models become more urgent than ever (Brenner, 2005). In general, reconstruction of a complete 3D building model over a city is a time consuming and expensive task. Thus, the automation of the process is of great demand due to the massive amount of data to be processed, and the necessity of large manpower when doing the process manually.

So far, many research have focused on the automatic reconstruction of 3D building models in an efficient manner (e.g. Maas and Vosselman, 1999; Schwalbe et al., 2005; Khoshelham, 2005; Brenner, 2005; Oude Elberink, 2010). In terms of data used in the reconstruction process, algorithms can be classified into three groups. In the first group, the algorithms employ aerial imageries only. Although accurate roof boundaries are delivered by images, the major drawback of methods based on images is the low level of automation. Shadow effects, occlusion, and poor contrast are common to image data which often make barriers in efficient processing of image data (Brenner, 2005). Algorithms in the second group make use of Airborne Laser Scanning (ALS) point clouds exclusively in the reconstruction. With the advancement of sensor technologies, point clouds acquired by ALS are increasingly being used for building reconstruction schemes. Given the high automation and high vertical accuracy by present day point clouds, it has become the preferred data source for 3D building reconstruction. However, the success rate of the building reconstruction, including the level of detail (LoD) of the resulting models, depend mainly on the resolution of the point clouds. In comparison to the ground sampling of digital aerial images at the centimeter level, the resolution of ALS point clouds is still less considerable. This turns out that, similar to aerial images, it is hard to reach the same planimetric accuracy for the building roof models from the point clouds (Cheng et al., 2013). Due to this limitation of point clouds, integration of point clouds and different sensor data, preferably aerial

images, is recommended. Moreover, this compensates prevailing shortcomings of each data set, such as data gaps, resolution issues, and occlusion/shadow effects, and so on. It is noted that point clouds and images have complementary properties. In point clouds, vertical accuracy is far better than aerial images, whereas vice versa the planimetric accuracy of images is better (Lee et al., 2008). Recent *ISPRS benchmark test project on urban object classification and 3D building reconstruction* found that the vertical accuracy of building models reconstructed from point clouds is twice than that of the same buildings reconstructed from aerial images (Rottensteiner et al., 2012). Thus, algorithms in the third group fuse both point clouds and multiple aerial images, especially for achieving a high geometric accuracy for the 3D building models. The question of how to optimally use image data, together with ALS data, to increase the accuracy has still not been fully solved. Few approaches have been published (e.g. Ma, 2004; Kim et al., 2006; Ok et al., 2011) and further experiments are needed.

Of the existing approaches, two main processing strategies (a) *model-driven* and (b) *data-driven* are found (Vosselman and Maas, 2010). The model-driven categories opt for pre-defined model libraries (e.g. Maas and Vosselman, 1999; Haala et al., 1998) and perform well in the presence of data gaps. However, in some instances it could be of inferior quality, especially with complicated architectural designs. The data-driven categories perform well for complex roof shapes (e.g. Brenner, 2000; Vosselman and Dijkman, 2001; Sohn et al., 2008) by recognizing adjacent planar faces and their relations (e.g. status of being ridges and step-edges) to achieve topologically and geometrically correct 3D building models. Data fusion can easily be realized with data-driven methods which reduce the model errors caused by the incompleteness of data arising, for instance, from missed faces due to insufficient points, occlusion or vegetation clutter. It is said that having increased the point density of modern ALS, the data-driven approach allows to have a more accurate and robust result than that through the model-driven approach (Oude Elberink, 2008). A number of methods for doing the reconstruction, based on either model-driven or data-driven approaches using ALS data have been presented in the literature. When reviewing relevant literature, it is observed that the major problem is the efficient manipulation of the topology and roof primitives. From recent literature, it is seen that roof topology graphs (RTG) are widely used in both data-driven and model-driven approaches, especially for the efficient manipulation of topology and roof primitives (e.g. Verma et al., 2006; Milde et al., 2008; Oude Elberink and Vosselman, 2009), and in many cases, accurate results have been obtained. However, many unsolved problems need to be addressed within the processing chain of building reconstruction. This will be discussed in detail under Section 1.2.

Consequently, all these facts motivated to introduce new processing strategies by taking synergetic properties of both point clouds and aerial images. Herein, the focus is on data-driven approaches and point clouds are chosen as the primary data source in roof model reconstruction. Therefore, roof outlines can be refined afterwards as a consequence of image data integration. The performance of this approach is tested with the recent ISPRS benchmark test project on urban object classification and 3D building reconstruction organized by ISPRS commission III (Rottensteiner et al., 2014).

1.2 Problem statement

Much research have been conducted in automated reconstruction of 3D building models from ALS point clouds, but as explained in Section 1.1, there are still many unsolved problems, particularly in the enhancing of planimetric accuracy. One can say that working exclusively with image data enhances the planimetric accuracy. Although working with images may increase the planimetric accuracy, it can cause some other difficulties, such as low automation, incompleteness and so on. This means that model reconstruction from images itself is a difficult task. The conversion of image data into point clouds, maybe by dense matching, ensures a high automation but matching errors may lower the vertical accuracy than that of by ALS data. Therefore the integration of image data with point clouds is necessary. Data integration can be conducted in many ways, for instance by having ridge-lines derived from point clouds. This may be more efficient than working solely with images, but incompleteness of roof outlines may still exist because of shadow effects, matching ambiguities and so

on. Therefore, reconstruction of building models with a post-refinement would be sufficient. However, to design a highly automated algorithm yielding building models with high vertical accuracy which is more important in reconstruction, the reconstruction of roof models should primarily be accomplished from point clouds. Because of that, a higher percentage of contribution to the resulting building models should be given by point clouds. The best contribution rate may be 75% or more (or less) than that. It is still in the grey area and may be decided by future experiments or probably by future comparison tests (benchmark tests). The post refinement, thus, would contribute to the remaining percentage, may be 25% or less, through the integration of image data. Hence, some of the challenging issues relevant to each data source, as mentioned below, need to be addressed in the new development schemes.

State of the art of algorithms in 3D building reconstruction is still being developed. Currently many ALS based studies employ RTG for the correct manipulation of primitive features (e.g. planes for roof faces and lines for ridge-lines and step-edges); but in geometric reconstruction, these existing methods rely on external target graphs. For example as can be seen in Figure1.1, to reconstruct a hip roof, the sub graphs in the data should be matched with two triangular shaped target graphs having a common base in the database. The question is, if targets are unable to represent the real scenarios, the process will be wrong and the realistic model cannot be obtained. Therefore, model reconstruction is restricted to already available target graphs in the pre-defined libraries. On the other hand, it is difficult to handle more complicated roof structures although it is capable of working with data gaps or missing data. These problematic issues may be overcome if geometric reconstruction can be done without relying on existing target graphs. The geometrical fixing of roof corner P, for instance, could automatically be performed if the algorithm is able to recognize that the three ridge-lines (*i.e.* ridge-lines corresponding to sub graph 1-2-3) converge to one position without knowing the primitive shape of the roof and the type of ridge-lines, *i.e.* whether horizontal or oblique. Therefore, it might be important to extract the nature of convergence of roof planes from RTG or other data, without relying on the external targets in efficient building reconstruction which has not been considered yet by the research community.

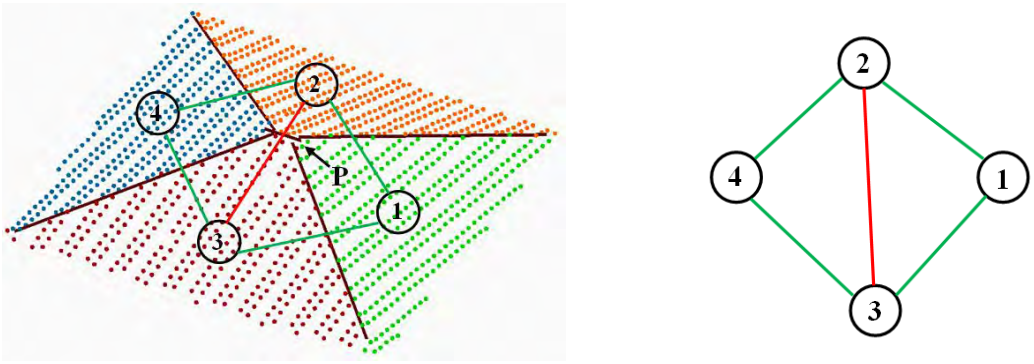

(a) (b)

Figure 1.1: Reconstruction of a hip roof: (a) RTG is embedded with the intersection lines (or roof ridge-lines) between roof planes; and (b) target graph (green – oblique ridge-lines, red – horizontal ridge-line).

Due to resolution issues and occlusion effects existing in ALS point clouds, defining a step-edge is questionable from point clouds. It is recognized that the reconstruction of step-edges, especially between flat roof faces, is still a challenge (Oude Elberink, 2010, Sampath and Shan, 2007). When the step-edge becomes a poly-line having more than one connected edge, as in Figure 1.2, then more effort is needed in defining the corner positions of the connected step-edge. It is said that even with the availability of 2D map lines, a strategy like subdivision of map lines into multiple directions based on cell decomposition (Kada and McKinley, 2009) is difficult, especially because map lines do not give a hint about inside edges (Oude Elberink, 2010). In addition to corner positions, the correct shape, orientation, and placement of the step-edge are also challenging. Since many flat-roof buildings have polygonal step-edges in most city areas, the solution for this issue is emerging.

Figure 1.2: Oblique image of a high-rise building with polygonal height jumps (Oude Elberink, 2010).

Regularization is an imperative necessity in data driven schemes. Zhou and Neumann (2012) introduced *global regularity* to planar faces in terms of orientation and placement constraints, which improves the quality of roof models and reduces scene complexity caused by intrinsic building structures and symmetries. However, one dominant building direction per building is questionable in some instances, particularly when connected buildings may contain more than one dominant direction (Figure 1.3). Furthermore, regularization based on one dominant direction might discard the gutter symmetry, thus how piece-wise regularization or other methods could apply should be experimented.

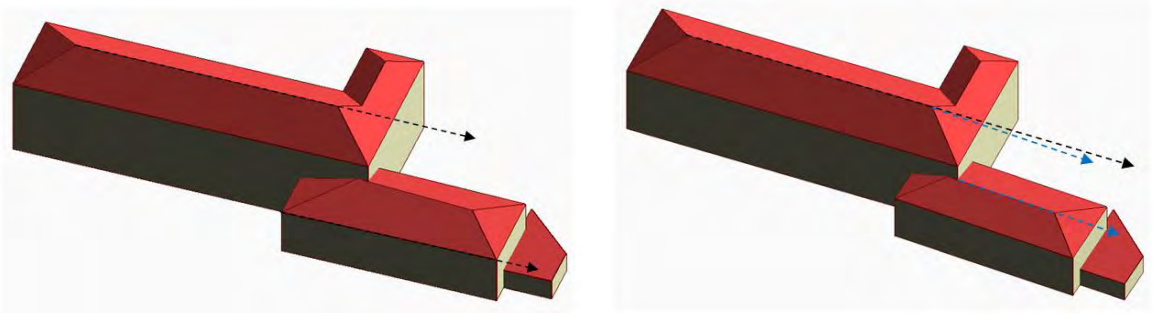

(a) (b)

Figure 1.3: Regularization of weakly defined roof boundaries: (a) the regularization based on one dominant direction; and (b) its actual situation (black dashed line – principal dominant direction, blue dashed line - second dominant direction).

Small building components often suffer from insufficient data, mainly due to a small number of laser points. This would be inadequate to fit a straight line segment to be able to represent the corresponding building edge (e.g. black arrow signed edges in Figure 1.4). Generally in data-driven procedures, these components may get neglected when reconstructing building models, thus the resulting models may differ from their realistic view or incomplete geometric models may result. However, if even one boundary edge of the component can be derived (edge shown by the red arrow in Figure 1.4), this indicates that the problematic building component maybe reconstructed. Then, by knowing the logical structure and well-defined meaning of the object arrangement *i.e. semantic information*, the issue could be addressed within the chosen data-driven approach. Rather than this simple example, there could be many complicated issues due to the complexity of the scene and errors/defects of data. Therefore, to cope with complicated scenarios, and also to suit future requirements, for example higher LoD, it is important to integrate semantic information, topological relationships, and so on, for the reconstruction scheme. This will definitely give a more robust result. Of course many efforts have been executed for example, integrating symmetry constraints (e.g. Vosselman, 1999; Zhou and

Neumann, 2012; Lin et al., 2013), building priors (e.g. Karantzalos and Paragios, 2010) and also grammar rules (e.g. Milde et al., 2008) to the building reconstruction schemes, but there is still room for more work.

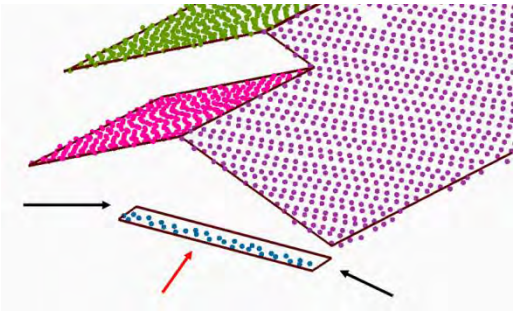

Figure 1.4: Small building components having inadequate data (black arrow – edges that are difficult to reconstruct due to inadequate points, red arrow – edge that can be easily reconstructed).

Most of recent building reconstruction approaches based on RTG describe the importance of using RTG for correct guiding of roof primitives in the reconstruction, since RTG represents topological relation between roof segments. They show that taking the topological relations instead of the geometrical relations helps to avoid problems with disconnected intersection lines (Oude Elberink, 2008). In some instances, RTGs also deliver erroneous relationships because of data gaps and errors that have occurred in pre-processing steps (e.g. segmentation). For example, in a connected building (Figure 1.5a), gaps caused by occlusion would lead to false negative graph edges and results would split separate building components (Figure 1.5b). This problem may be solved if the correct boundary edges can be extracted and (each) the corresponding two edges between two segments can be identified as step-edges (Figure 1.5c). These correct relationships may be realized with 3D information extracted from stereo aerial images. It would then be a boundary refinement in addition to correcting graph errors. Therefore, it may be important to integrate additional data sources into the process of building reconstruction based on the ALS points.

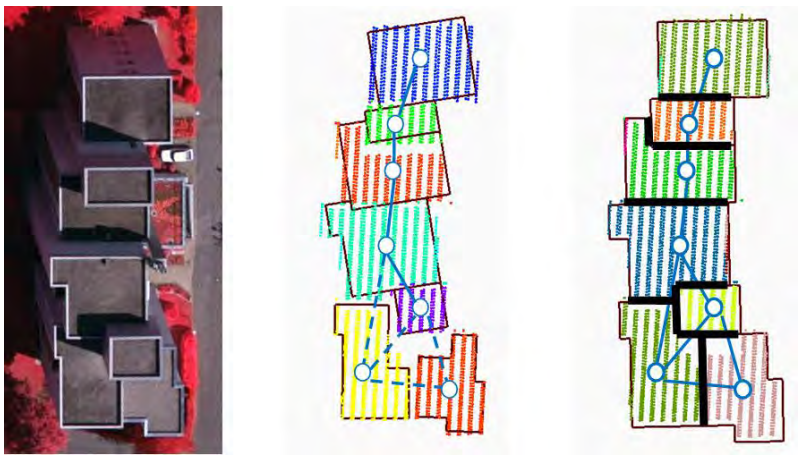

(a) (b) (c)

Figure 1.5: Split buildings caused by occlusion and correcting the respective graph errors: (a) pictorial view of a connected high rise building; (b) a split separate building components due to occlusion effect; and (c) extracted 3D boundary lines from external data sources (brown lines – building outlines, blue lines – graph edges, blue dashed lines – false negative graph edges, black solid lines – correctly identified roof outlines as step-edges).

On the other hand, it is a known fact that planimetric accuracy of point clouds relies mainly on the resolution of point clouds. In the case of refining building boundaries that have been reconstructed from point clouds, straight lines extracted from stereo images are necessary. The common issues arising in relation to correspondence matching (line matching) and gaps pertaining to extracted line segments from images are primarily important to focus on an efficient algorithmic design. In this case of post-refinement, scene constraints determined with initial roof models (*i.e.* already reconstructed models with ALS point clouds) may be considered to avoid ambiguities of the line feature matching. Further the structural arrangement of initial roof models and their convergence scenarios may also be used to deal with gaps and distortions (Figure 1.6) that would occur in the resulting refined models.

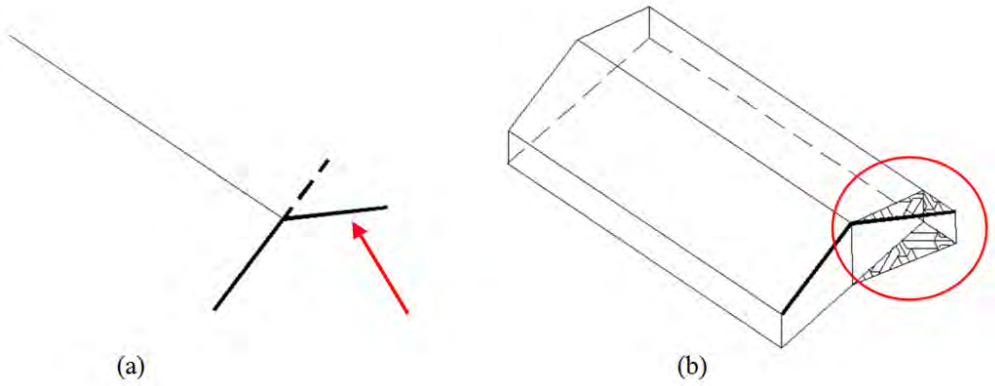

Figure 1.6: Strange building geometry associated with distorted boundary edges: (a) 2D view of the boundary edges derived from stereo images together with the defective edge (shown by red arrow) and (b) effect of distortion on to the real scene (red circle indicates the distortion).

Motivated by the importance of 3D building models for a broad range of applications, the work here is focused on devising a new processing scheme for automated reconstruction of geometrically accurate 3D building models.

1.3 Objectives

The main objective of the work presented in this thesis is to develop a new processing scheme for the automatic reconstruction of geometrically and topologically correct 3D building models over complex urban scenes from ALS point clouds and aerial images.

Specific objectives are:

1. To set up rules for the extraction of roof primitive features and the nature of convergence of topological relationships from graphs (RTGs) or data, without relying on external targets, and then to best use them for an efficient roof reconstruction.

2. To develop an efficient image-based and ALS-based feature (line segments) matching process for the reconstruction of object space (accurate) boundary line segments, and to perform topological and geometrical refinement of 3D building models while introducing solutions for defects and shortages associated with resulting building outlines derived from image data.

The first specific objective is achieved from the raw point clouds of ALS while the second is achieved by integrating images and point clouds.

1.4 Innovations in this work

1. The main innovative aspect of this study is the introduction of the novel cycle graph analysis approach for the automated building modeling schemes. It is possible to fix both the inner and outer roof vertices geometrically, based on the newly introduced method. The roof modeling is therefore done without prior knowledge of any primitive roof types, and as such, this is the specialty of the initial roof reconstruction approach that has been developed in this study.

2. Incorporation of scene constraints determined with the initial roof model has been done to avoid faulty correspondences in line matching via the viewing plane intersection process. According to our knowledge, this strategy is very new to building reconstruction schemes.

3. In addition to these, the third innovative aspect of the study is the demonstration of how (some of the) topological issues can be rectified by adding image information, while refining the planimetric accuracy of the building models. In these refinements, well-defined evidences have been taken from the known structural arrangements of initial roof models and specially defined roof corner convergence priors.

1.5 Scope and assumptions

The aim of the research is to reconstruct accurate 3D building models from ALS point clouds and aerial images. The scope of this PhD is limited to reconstructing initial (accurate) 3D roof models and then refining the planimetric accuracy of the building models. In the refinement, each weakly defined edge *i.e.* step-edge and roof outer-boundary, is only refined planimetrically while preserving ridge-lines at their original positions. This is because it is assumed that ridge-lines are accurate enough and refinement is not necessary. The rationale behind the assumption is that ridge-lines were derived by the intersection of adjacent roof planes that had been fitted from segmented point clouds. Also, due to the fact that the ALS point clouds have a higher accuracy of height than aerial images (ISPRS comm.3, 2011), the uncertainty of ridge-lines derived from point clouds should be very small. As such, refinement on ridge-lines is neglected in this study. Additionally, some irregularities which are less significant, as shown in Figure 1.7, are not considered during the refinement process.

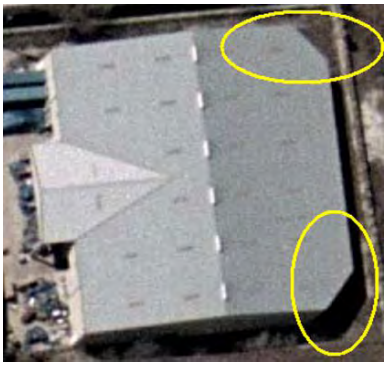

Figure 1.7: Insignificant irregular edges within the building outline (yellow color ellipse).

Beside this, in the reconstruction, it is assumed that buildings can best be described by defining several dominant directions rather than defining one single direction.

1.6 Outline of the thesis

To achieve the objectives, the thesis is organized into seven chapters, outlining and describing the proposed approach at each stage.

Chapter 2 presents additional details about the current approaches of building reconstruction from ALS point clouds. Both model-driven and data-driven reconstruction strategies are discussed in this chapter with more elaboration on the latter approach. At the end, some further research work involving model refinements with attention to how image data can be integrated with point cloud data is presented.

Chapter 3 gives an overview of the reconstruction strategy that this study introduces. The novel cycle graph analysis procedure and how 3D roof models can be reconstructed with this new method is explained. The process is described as a roof corner (inner and outer) fixing approach. Afterwards, refinement strategies are described briefly.

Chapter 4 outlines how the information described in Chapter 3 is used in the processing chain to reconstruct 3D roof models from ALS point clouds. Segmentation and classification of point clouds that this study followed is discussed briefly at the beginning of the chapter. It is followed by the set of rules enforced to extract potential roof planes from classified off-terrain segments. A shape-based recognition of irregular segments, which is introduced for excluding trees, is described afterwards. Extraction of roof topological relations and deriving of inner roof bounds is discussed next. How roof outlines can be extracted as rectilinear line segments to represent irregularities along the outer boundary are then presented. Afterwards, how weakly-defined edges, including step-edges and outer-boundaries, can be regularized in terms of orientation and placement is discussed. The geometric reconstruction of roof models using the closed cycle graph approach is explained next. In this part, how the cycle graph can be incorporated to fix inner and outer vertices is described. Later on, how complexities can be handled by the cycle graph approach is demonstrated.

Chapter 5 discusses the refinement strategies and how building models can be refined by adding image information. The chapter begins with an explanation of how corresponding line segments can be matched in projective geometry. It is followed by the method introduced to avoid ambiguities within the correspondence matching using scene constraints. Afterwards, how defects and gaps pertaining to the 3D boundary line segments derived from images can be avoided is described. An attempt that has been made to rectify topological errors is also briefly explained. Finally, to obtain complete 3D building models, the method of attaching wall segments to the 3D roof models is explained.

Chapter 6 presents the experimental results produced from each of the proceeding chapters applied to three sets of data. In addition, a result analysis is presented including the performance of the proposed approach. Accuracy is analyzed quantitatively, in terms of geometry and topology. Statistics specified by the ISPRS benchmark test project is also included. Finally, the accuracy enhancement is analyzed by comparing the results relevant to initial and refined roof models.

A summary (concluding remarks) of the presented work is given in Chapter 7. It highlights the achievements of the methods proposed, as well as the drawbacks, and some directions for further research.

2. State-of-art in 3D building reconstruction

2.1 Introduction

Many sophisticated approaches for the reconstruction of 3D building models have been presented in the past decades (e.g. Maas and Vosselman, 1999; Brenner et al., 2001; Suveg and Vosselman, 2004; Kim et al., 2006; Sampath and Shan, 2010; Lafarge et al., 2010; Haala and Kada, 2010; Huang et al., 2013; Lin et al., 2013). These reconstructions have mainly been realized from various data sources like aerial images, high resolution satellite images and point clouds acquired by ALS or derived by dense (image) matching. However, recalling the objective of this study: that is to find a new processing scheme for geometrically and topologically correct 3D building models from point clouds and images, and allowing the argument that over 75% contribution to the reconstruction scheme is given by the point clouds (see Section 1.2), the recent building reconstruction approaches relying on point clouds are mainly focused in this chapter. Also, the review is further restricted to the approaches reported in the automated building reconstruction based on the ALS point clouds.

In general, buildings in reality take many different architectural forms. The aim of building modeling is to represent these different forms as in the reality. So far, many studies have been done in reconstructing building models using point cloud data. These various approaches can be discussed based on different aspects, such as supporting object models, amount of user interaction, reconstruction process, and so on. Generally, of the studies using point clouds, two basic types of building models can be found: *generic* model and *parametric* model (Maas and Vosselman, 1999; Förstner, 1999). Parametric models are generally used for simple buildings and these buildings can be described using a few parameters. Generic models are based on generic knowledge of the buildings, for example a building can be described by sets of closed polygons. Such models are distinguished in two subclasses; *prismatic* and *polyhedral*. In prismatic models, it is assumed that the building can be described by a polygonal ground plan, vertical walls and a planar roof. Polyhedral models allow for the building to be modeled geometrically as an ensemble of planar surfaces (Förstner, 1999). Since the majority of buildings satisfy this polyhedral condition, complex buildings can be reconstructed by combining primitive models. Furthermore, such models describe building structures with their topological relations. Therefore, polyhedral models are considered as the most efficient way to represent different forms of building structures. Although the building models can be classified so, the classification is tightly bound with the methods (the processing strategy) used to reconstruct the building models. Based on literature, reconstruction methods can be categorized in to two main groups: *model-driven* and *data-driven*. Model-driven approaches often deal with the parametric building models while data-driven approaches deal with generic models. To discuss these two groups in detail, current building reconstruction approaches are reviewed separately, based on the model-driven and data-driven methods. Within the review, more emphasis is given to the data-driven approaches.

Automatic building reconstruction based on either model-driven or data-driven methods consists of several steps that are dependent on the applications, expected accuracy, LoD, data sources used, approaches used and so on. However, the process generally follows three main steps: (i) *detection*, (ii) *feature extraction,* and (iii) *geometric modeling*. The detection step recognizes the existence of desired buildings and then localizes them into regions. Feature extraction delineates primitive features, especially physical building boundaries, including ridge-lines and jump edges, preferably in 3D. The aim of the building reconstruction is to detect topological relations, internal architecture of primitive

features and then to fix features geometrically for representing reality. All these steps have an impact on the accuracy of the output data. Furthermore, based on the reconstruction approach, the method of feature extraction should also be chosen. Therefore, it is first necessary to know the method that will be adopted for the reconstruction (Ameri, 2000).

The remainder follows the developments of model-driven approaches, and a review of the prominent data-driven approaches that are based on point cloud segmentations. Additionally, each individual processing step, especially those relevant to data-driven methods, are discussed. The latter part of the review is an extensive discussion of the approaches that make use of roof topology graphs for the reconstruction schemes. After a general review of some aspects of both approaches, their benefits and drawbacks are discussed. Building model refinement using data integration is discussed afterwards.

2.2 Model-driven approaches

In the model-driven approaches, the relationship between model primitives is fixed but their geometry is unknown. The approach searches the most appropriate model amongst basic building models contained in pre-defined model libraries. This means a pre-defined model provides hypothesis to realize a model, and then the model should be verified from the features in the data. As such, from a pre-defined model library, the model which best fits the features in the data is chosen to determine the correct geometry of the model primitives and then to reconstruct the building (e.g. Maas, 1999; Haala et al., 1998; Kada and McKinley, 2009; Lafarge et al., 2010; Huang et al., 2013). The primitive building is described by a set of parameters. In the reconstruction process, the building roof details are described from the values of these parameters. Concerning the earlier publications, Maas (1999) demonstrates how parameters of gable buildings which best fit to point clouds can be obtained using invariant moments (Figure 2.1).

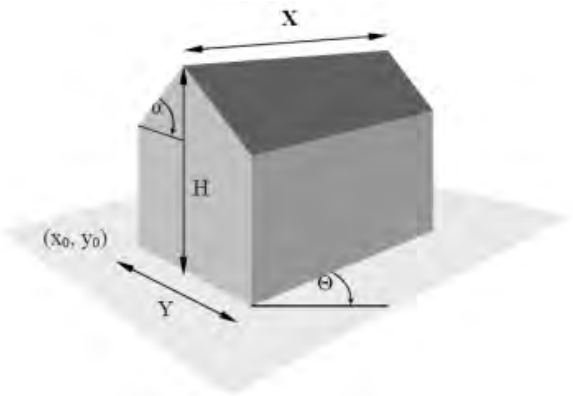

Figure 2.1: Parameter definitions of a building primitive (Maas, 1999).

It is said that the method performs well for individual buildings, thus object complexities should be handled by piecewise manner. Haala et al. (1998) use basic building primitives such as pent, flat, gable with 2D building footprints for the reconstruction. Since such basic building shapes are not enough for representing complex buildings, Taillandier (2005) reconstructs buildings by extruding building footprints to a given eave height. In this, symmetric roof shapes having global eave heights like gable roofs are mainly hypothetical, and so this method is incapable of coping with height discontinuations. Taking this idea, Kada and McKinley (2009), and Kada (2009), decompose the footprint into cells and reconstruct buildings by considering a cell as a primitive. Due to object complexities and accuracy issues in 2D map data, actual spatial partition is done separately in an enlarged block, which is then matched with the original building footprints. Points which come in to the matched cells are compared with a library of roof shapes and the one cell which most points fit with respect to the normal direction is chosen as the best model. In order to cope with more complex buildings, Suveg and Vosselman (2004) incorporate generic knowledge about building shapes to define most common building

primitives in their model libraries. In this approach, with the existing ground plans the reconstruction process is further enhanced by formulating the process as a multi-level hypothesis having a verification scheme.

Lafarge et al. (2008 and 2010) use Digital Surface Models (DEMs) that are derived from high resolution satellite imagery to extract building footprints. Both methods treat buildings as an accumulation of simple parametric blocks that have been defined in a library (like a LEGO set). 3D-blocks (library primitives) are assembled on extracted building footprints (2D-supports). The assembling of 3D-blocks into a complete model is optimized by finding the optimal configuration of 3D-blocks using *Markov Chain Monte Carlo* (*MCMC*) sampler and *simulated annealing* techniques. A spatial partitioning which consists of convex polygons that are perfectly connected and non-overlapping is obtained as the final result. Huang et al. (2013) present how generative statistics can be adapted for combining and merging of library primitives to one model. Within this process, the point cloud is first segmented into subzones containing a few buildings for speeding up the process. In contrast to previous methods, requisite of building footprints are excluded in this approach and predefined primitives are fitted to the point clouds. The primitives are assembled to the entire roof while accepting and merging of overlapping primitives with given rules. Selection of the primitives and their parameters are tuned using a variant of *MCMC* technique with a jump mechanism. Lin et al. (2013) show that in the decomposition of point clouds into symmetric and convex simple blocks, data gaps can be manipulated with symmetry constraints.

Although these methods work well for data gaps, they do not perform well for complex roof models - they lack a sufficient level of detail - as their input models generally consist of rectangular footprints. Further, buildings cannot get reconstructed by the described model-driven approaches when their height discontinuities are not available in the 2D footprints. Sometimes, the defined types of parametric roof shapes may not always fit the roof's ridge-lines exactly, for example the ridge-line of a saddleback roof. For the detection of such features, data-driven methods or incorporation of additional data, such as Digital Elevation Model (DEM) or planar segments, can be used (Haala and Kada, 2010).

2.3 Data-driven approaches

In data-driven approaches, the type or the number of primitives, their geometry and topological relations are unknown. They analyze the building point cloud as a unit, without relating it to a set of parameters. Since the method does not rely on a predefined structure, any building type can theoretically be modeled by this approach. Generally, they extract features directly, such as points or edges, from input data. Based on the derived 3D information, the objects or parts of objects can be described in the form of mesh models or volumetric models. The idea of this mesh based approach is reducing the number of faces in a mesh, and giving an abstraction level of the scene (Haala and Kada, 2010). However, these mesh based methods are not suitable to preserve the object shape of buildings, and therefore, these models are particularly appropriate only for visualization tasks. Thus, volumetric models like polyhedral models are needed to represent structure of building features (primitive) and their connectivity. However, the limited knowledge about geometry of buildings makes it harder for the reconstruction of polyhedral models directly from data. This leads for the necessity of robust automated primitive feature manipulation methods for these data-driven approaches. Most approaches in data-driven schemes usually follow three steps: (i) *building detection*, (ii) *primitive feature extraction*, and (iii) *geometric reconstruction*.

2.3.1 Building detection

Detection of building candidates from the sensor data is the first step in reconstruction schemes. It can be considered as a classification task which separates buildings, especially from the ground and also from other objects such as vegetation. Due to the fact that buildings are above-ground objects having a

considerable height difference from their surroundings, for example terrain, filtering techniques can first be applied to classify off-terrain laser points or segments. Point-based filtering methods (e.g. Kraus and Pfeifer, 1998; Vosselman, 2000) or morphological operations with DSM/nDSM analysis (e.g. Ma, 2005; Arefi and Hahn 2005; Meng et al., 2009) are mainly used for this purpose. However, having planar segments as a first step and then applying a segment-based filtering approach (e.g. Sithole and Vosselman, 2004; Tóvári and Pfeifer, 2005) is more useful in order to achieve accurate classification results. Sometimes, additional refining methods such as Eigenvalue analysis of local covariance matrices (Verma et al., 2006; Sampath and Shan, 2010) or height texture/roughness measures (Oude Elberink and Maas, 2000; Rottensteiner and Briese, 2002) are used to remove unwanted points, mostly on vegetation. Additionally, the availability of building ground plans may support the extraction of building planar regions (Vosselman and Suveg, 2001; Oude Elberink, 2010). The benefit of using 2D ground plans is to obtain an accurate result in building region extraction.

2.3.2 Feature extraction

The idea of the roof feature extraction is to extract roof primitive features including roof planes, ridge-lines, step-edges and roof outlines from detected building candidate points as explained in Section 2.3.1. From this primitive feature information, the building models are reconstructed. In general, planar faces are being used to describe the surface of building roofs. With the availability of high density point clouds, planar faces can be accurately defined from point clouds. Herein, planar segmentation is vital as it allows for a decomposition of point clouds (off-terrain points) into individual roof faces. Therefore, the common approach to feature extraction is to segment the point cloud into planar surfaces. Several segmentation techniques have been presented to detect planar surfaces from point clouds and to determine their parameters (see Section 2.3.2.1). With these planar segments, neighbor relations between roofs (roof adjacency) and roof primitive features could then be extracted. In order to extract primitive features, different steps can be followed. According to their processing hierarchy, these steps could be lined up as roof outline extraction and straight line fitting, determining roof adjacency, extraction of ridge-lines and step-edges, and determination of topology. Note that according to the processing workflow, the hierarchy could be interchangeable. These steps are discussed in Section 2.3.2.2. Once these features are available, then the 3D geometric models can be reconstructed.

2.3.2.1 Segmentation

Segmentation is a process of grouping points having similar properties based on a certain criterion. Mostly, it is the first step in information extraction from point clouds. A detailed overview can be found in Vosselman et al. (2004), Sampath and Shan (2010). Maas and Vosselman (1999) use clustering of TIN meshes to determine the planar faces as triangles that are part of the same roof represented by nearly equal one normal direction. Vosselman and Dijkman (2001) introduce 3D Hough space to the point clouds segmentation. From this, an improved segmentation is achieved by selecting planes which pass maximum number of seed points. Using seed surface generation by 3D Hough transform and subsequent plane growing by adding points into the seed surface according to their co-planarity and connectivity, further improvement is obtained by Vosselman et al. (2004). In this approach, several parameters require to be specified for growing the seed surface, such as the growing radius and the number of minimum points. Rottensteiner et al. (2003 and 2005) adapts a region growing approach for the planar segmentation based on the seed regions generated from image data. The seed regions are then integrated with DSMs generated from point clouds. Planar faces are finally obtained iteratively by growing the seeds on the DSM. Brenner (2000) and Tarsha-Kurdi et al. (2008) present how random sample consensus (RANSAC) is used for segmenting planar faces. The latter extends the RANSAC to be more efficient and to obtain best roof plane rather than the best mathematical plane. In contrast to the above approaches, Schwalbe et al. (2005) introduce the orthogonal projection method for segmenting roof faces in simple building models. The way to use hierarchical clustering is demonstrated by Dorninger and Pfeifer (2008). Combining fuzzy k-means clustering procedure to the point clusters, Sampath and Shan (2008) obtain smooth planes by

analyzing normal vectors of each point at a Voronoi neighborhood. Kim and Shan (2011) perform another segmentation approach by minimizing energy function as multiphase level set.

By introducing the point re-assignment concept to the surface growing, elegant planar segments are robustly obtained by Vosselman (2012). In this approach, Hough based seed surfaces are grown by adding neighboring points that are within a given distance to the plane. This process iterates until no more points are there to be added to the surface. To correct the overgrowing which would arise due to greedy surface growing, points that have been assigned to the surface may be re-assigned to an adjacent surface if this new surface better fits the point and its point neighborhood. Once planar segments representing individual roofs are generated, feature extraction can be performed more easily. More elaboration on the feature extraction, according to the different primitives, is given in the following sub section.

2.3.2.2 Roof primitive-feature extraction

Building roofs can generally be defined based on their primitives, for example, roof planes, ridge-lines and step-edges. In image based building modeling, these primitives can easily be obtained by extracting line segments. For this, image matching techniques are required to perform space intersection from stereo pair images (Baillard and Zisserman, 2000). In the detection of line segments from images, Canny (Canny, 1986) and Förstner (Förstner and Gülch, 1987) operators are mostly used. Further, 2D Hough transform (Hough, 1962) is generally used for extracting rectilinear line segments from the detected edges.

However, in the case of point clouds having planar segments for representing individual roof planes, the rough boundary of each roof face should first be obtained. This can be done by directly extracting edge points of roof segments. This, however, delivers a jagged boundary (see Figure 2.2). As such, rectilinear line fitting, or any other method of deriving straight lines, maybe even by generalizing of edge points to make straight line segments, is necessary. Prior to the line fitting, the extracted boundary points can be pulled to the roof planes in order to obtain a planar boundary, which further eases the line fitting. The advantage of extracting edge points is that it enables to determine adjacency of roof planes (roof adjacency) which are close to each other (Haala and Kada, 2010). In a roof adjacency, the topological relations between segmented roof planes are usually described. Determining the roof adjacency or the topological relations of the roof parts is also helpful in deriving roof ridge-lines where neighboring roofs are intersected and step-edges where height jumps reside in-between roof planes. From the roof segments, obtained boundaries and their neighbor relations, the roof primitives can then be determined. However, in order to reconstruct 3D models, properties of the topological representation should be determined during the roof primitive extraction process. Each of these steps is discussed in the following sub sections.

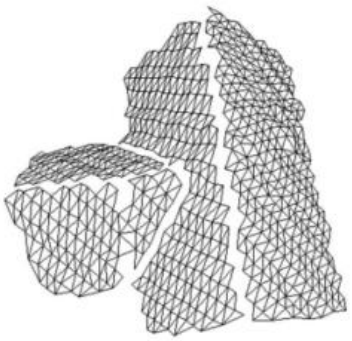

Figure 2.2: Rough boundary edges of the planar roof segments (points in each plane are connected by TIN) (Maas, 1999).

1. Roof outline extraction and straight line fitting

Maas and Vosselman (1999) extract the generalized boundary using Douglas–Peucker-like algorithm and it is further rectified using least square line fitting. Vosselman (1999) defines boundary points along the roof segments using contouring. The first two points of a contour defines the initial boundary line which is updated by adding succeeding points until the distance of a point to the line exceed some given threshold. The next line is extracted in such a way that it is orthogonal to the previous line. Verma et al. (2006) extract edge points using the ball-and-pivot algorithm, in which seed triangles are grown until they reach the outer edge points. By modifying the convex hull formation algorithm, Sampath and Shan (2007) trace building boundary points and connects them to form an approximate boundary, which is then refined by applying the hierarchical least square process. Dorninger and Pfeifer (2008) introduce 2D alpha-shapes in which the convex hull issue is overcome by determining proper alpha values. The jagged short edges given by the alpha-shapes are generalized by analyzing the angle between successive line segments along the alpha boundary. From the short edges whose deviations are within a given threshold, the mean angle is computed for deriving the generalized edge to be represented by rectilinear boundaries of the roof segments. To cope with building shapes having right angle boundary corners, such as L-, T- or U-shapes, Kwak (2013) find minimum boundary rectangles (MBRs) recursively, which decompose building boundary into sets of rectangles. Although boundary lines derived either by least square methods or by other boundary generalization method yield straight line segments, they may not represent the exact position and direction of building boundaries. Regularization, thus, is necessary.

2. Determining roof adjacency

The adjacency relations between roof segments can be determined in different ways. When two short edges corresponding to two successive points from the edge points, belonging to two segments respectively, are located close enough, Verma et al. (2006) consider these two segments as adjacent. Sampath and Shan (2010) follow a similar method and compute the distance between edge points belonging to two segments. If distances are less than a defined threshold, then segments are deemed to be adjacent. Milde et al. (2008) compute perpendicular distance between edge points and the intersection line given by the two segments. In this method, edge points are chosen from a narrow sharing zone along the intersection line. If sufficient number of points is located in both sides of the zone and they are close enough, the two segments are considered adjacent to each other. Oude Elberink (2010) uses a more convenient technique which measures the length of the intersection line to decide the roof adjacencies.

3. Ridge-lines and step-edges extraction

Roof ridge-lines and step-edge lines provide the interior limits of connected roof planes. The status of being a ridge-line or a step-edge is first recognized in order to reconstruct the reality. Planar segments, with known segment adjacencies, can be used to asses when an intersection line or a step-edge should be located at a common boundary between two segments. The decision relies on the way that the algorithm determines the spatial distribution of common boundary points against the point space of the data. Since these relations clearly demonstrate the behavior, and how roof planes are inter-related, deriving the intersection lines and the step-edge lines provide topological relation between corresponding roof planes (Oude Elberink, 2009). When two segments intersect, Rottensteiner and Briese, (2003) use *RMS* error with a defined threshold while Oude Elberink (2009) use local distance thresholds associated with the median point space to infer whether the intersection line corresponds to a ridge-line. For the step-edge, Rottensteiner et al. (2005) first determine edge candidates by analyzing profiles of the DSM which is orthogonal to the line passing through the rough boundary points. If a considerable height jump is found in between profile points which belong to two roof planes, it is considered a step-edge. Oude Elberink (2009) use 2D and 3D neighborhood analysis of edge points on a TIN structure. The cases where sufficient a number of edge points belonging to two segments are given, a 3D separation, rather than a defined threshold, are considered step-edges.

4. Determining topology and representation of topology

The purpose of topology construction is to identify the relationship between roof planes and how they should be installed to create 3D models. This can be done in different ways, and is bounded with the strategy that building reconstruction relies on. Schwalbe et al. (2005) project roof planes orthogonal to the main direction of each plane (*i.e.* side projections) to reconstruct ridge-lines and connectivity between roof planes. The topology construction by side projection is further extended by Rau and Lin (2011), in which detected 2D feature points are restored into 3D lines. By adopting line-constrained Delaunay Triangulation procedure, TIN corresponding to each 3D line is obtained. The topology between 3D lines is then constructed by an iterative merging of two resulting TINs whose shared edge does not corresponding to a 3D line. A reshaping process is however adopted by the authors in order to achieve geometrically correct roof types. The more convenient method to determine topology relations is extraction of ridge-lines and step-edge lines, as mentioned under ridge-lines and step-edge extraction.

Topology further assists for manipulation of extracted features more efficiently and robustly. Verma et al. (2006), Oude Elberink (2009), and Milde et al. (2008) store the topological relations in a graph called roof topology graph (RTG) while Sampath and Shan (2010) represent the relations with respect to an adjacency matrix. In Verma et al. (2006), the relationship between roof planes are given with respect to azimuth (the horizontal component of a plane normal) of each roof and azimuth's signed direction, *i.e.* either inwards or outwards as shown in Figure 2.3. Oude Elberink (2009) and Milde et al. (2008) use labels to indicate topological relations for instance horizontal, convex/concave, and so on. In the RTG, those relations are represented by the graph edges while corresponding roof planes are indicated by the respective graph nodes (see Figure 2.4).

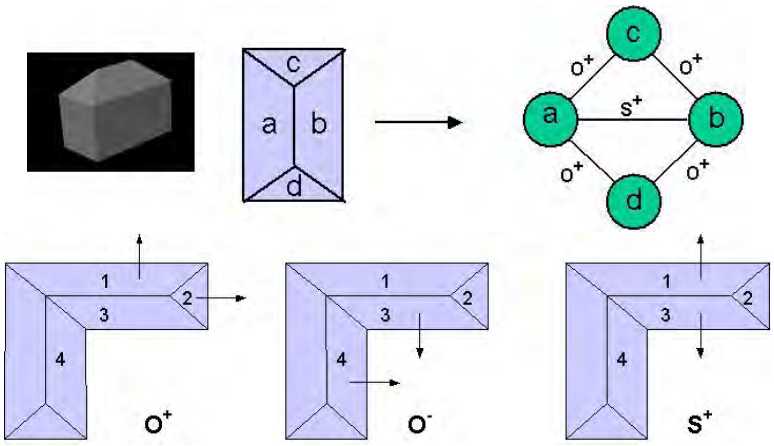

Figure 2.3: Representation of roof topology: (a) simple roof shapes and their corresponding RTG; and (b) relationship between adjacent planes in terms of azimuth angles (Verma et al., 2006).

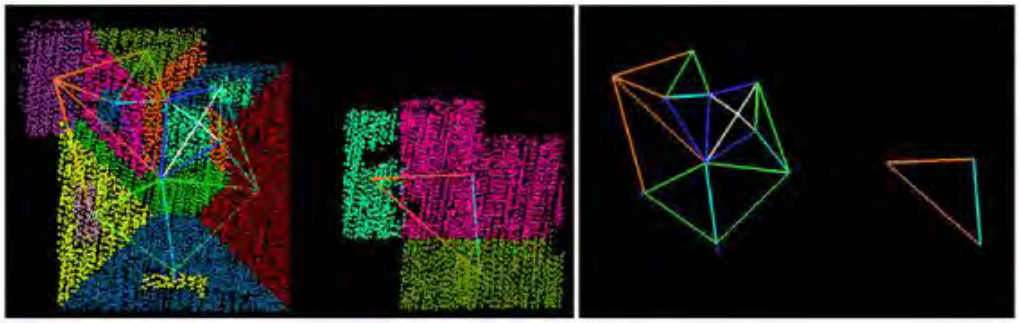

Figure 2.4: Labeled RTG with and without segmented laser data (Oude Elberink, 2009)

2.3.3 Geometric reconstruction

Having necessary primitive features such as roof planes, ridge-lines, step-edge lines, roof outlines, and also their topological relations, the 3D model reconstruction can be realized. When considering feature manipulation strategies, amongst the data-driven approaches, two groups of reconstruction tactics can be found: (i) direct primitive feature handling and (ii) primitive feature handing based on a graph or a matrix. With the availability of weakly defined step-edges and roof outlines, regularization is necessary for data driven reconstruction schemes. This is generally achieved by adding geometric constraints. In addition to obtaining a regular visual appearance, geometric constraints ease the reconstruction workflow and assists to improving geometric accuracy of the building models, especially when the sensor data have some weakness. For instance, due to the sparsely distributed nature of points, roof outlines derived from point clouds are not accurate, and thus regularizing them either parallel or orthogonal to a roof ridge direction may increase the geometric accuracy. In regularization, geometric constraints should only be considered when enough evidences are found (Rottensteiner, 2006).

Among the two mentioned groups, the first group of reconstruction is mainly followed by earlier works (e.g. Maas and Vosselman, 1999; Vosselman, 1999; Rottensteiner, 2003; Brenner, 2000; Dorninger and Pfeifer, 2008). Having extracted interior and exterior edges, by combining vertical walls through the outer edges, 3D building models are completed by Maas and Vosselman (1999). Vosselman (1999) extends the process to be compatible with connected buildings having step-edges (see Figure 2.5). When considering the weakly defined edges, in the given practices, the regularization is accomplished by assuming the building has one dominant direction and by rectifying the weakly defined edges either parallel or orthogonal to the main direction. The method presented by Schwalbe et al. (2005) is another example which follows the same assumption. Hofmann (2004) imposes a set of rules to intersect adjacent roof planes. Taking advantage of integrating building ground plans, Brenner (2000) restricts directions of building outlines to be compatible with ground plans. Rottensteiner and Briese (2003) describe problems related to the intersection line and step-edges construction, between two segments, and how geometric constraints can be added on such features mainly by statistical reasoning. Later, Rottensteiner et al. (2005) extend the work and obtain a more reliable result. Since these methods detect roof planes mostly as pair-wise, with no effort to detect adjacency of whole building i.e. global adjacency, primitive features are handled mainly per segment or pair-wise based on their relative geometry. The method presented by Dorninger and Pfeifer (2008) follows similar strategies. However, non-convergence of roof boundary lines leading to one vertex is a drawback of this approach. In recent studies, Zhou and Neumann (2012) introduce *global regularities* to planar faces in terms of orientation and placement constraints, which improve the quality of roof models and reduce scene complexity caused by intrinsic building structures and symmetries.

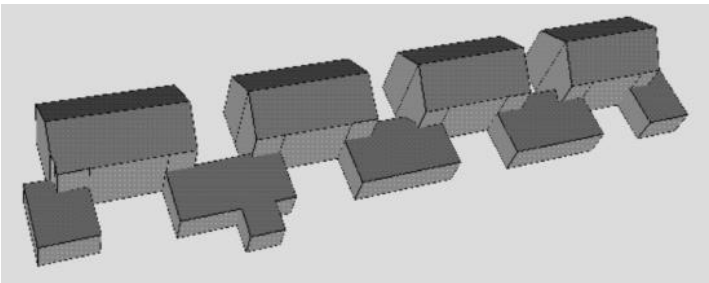

Figure 2.5: Resulting building models (connected) by the approach given by Vosselman (1999).

Primitive feature handing in the second group relies mainly on the roof topology graph or the adjacency matrix. This eases topology preservations of the resulting models and also enables for efficient data manipulation. Some approaches coming in this group incorporate primitive shapes. One could thus consider them as model-driven approaches. Although this is so, due to their level of contribution, in this study, the following methods are mainly considered under the broader approach of data-driven category.

Verma et al. (2006) reconstruct connected buildings using pre-defined primitives. Hip, L- and U-shaped primitives are defined with the help of RTG. The complex roof structures are then decomposed into these pre-defined primitive shapes by analyzing complex roofs' RTGs, and matching with the defined primitive graphs. In order to avoid matching ambiguities arising due to primitive graphs which share similar sub graphs, the matching process is carried out in the decreasing order of their complexity. Although the sub graph matching is a NP-complete problem, according to the authors, the *brute-force* search is adequate for their work as it is fast and sub graphs are rather simple. The complex roofs which are modeled by combining primitive shapes in this approach are given with a uniform ridge height and gutter height. For opposite roofs, which are adjacent to a horizontal ridge and having nearly equal slopes, a common slope is given. Roof outlines are aligned either parallel or orthogonal to the direction of the main building (Figure 2.6). However, the approach is restricted to a few primitive shapes.

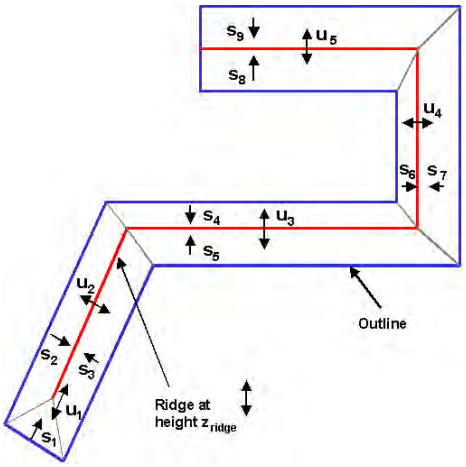

Figure 2.6: Preserving the roof geometry: equal ridge, gutter heights and equal slope are maintained (Verma et al., 2006).

Later, a formal grammar is applied on top of the primitive shapes which have been identified by the sub graph matching by Milde et al. (2008). In addition to the grammar rules, some additional corner connectors have also been used to get a valid roof model (Figure 2.7). The connection type depends on the type of the roof side which is to be connected. In case of a ridge wall (a wall touching a ridge), many possibilities arise when compared to an eave wall (a wall holding an eave edge). For instance, at a ridge wall, if the connecting roofs have identical roof slopes, they can be merged. Herein connector V1 (Figure 2.7a) is applicable and the resulting model would be the L-shaped building (Figure 2.7b). If the second roof is flat, a step-edge is defined between the roof primitives.

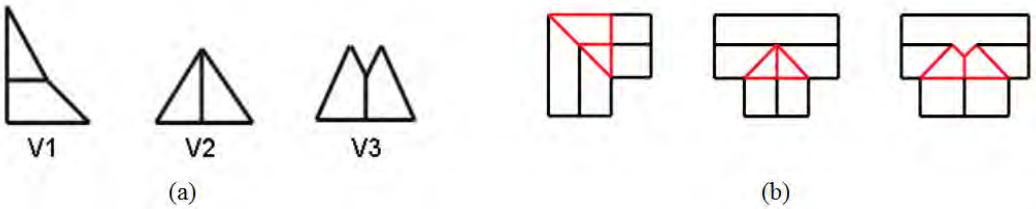

Figure 2.7: Grammar based roof reconstruction: (a) internal corner connectors and (b) connected roof shapes (Milde et al., 2008).

The most effective contribution (e.g. see Figure 2.8) for building reconstruction based on roof topology is given by Oude Elberink (2010) and he employs extended roof shape varieties for the sub-graph matching. The primitive roof shapes connected by graph edges are defined as targets. The knowledge of the intersection lines corresponding to neighboring faces is also incorporated to the targets in order to improve the matching process. Complete matching results with few incomplete

matches are obtained for some buildings having some missing planes. Subsequently, the incomplete result is attempted to be solved by suggesting a best matched option due to the fact that the incomplete result was a consequence of that missing data. In addition to roof topology construction, this method permits transferring of knowledge. As such, the optimal gutter height is decided with respect to data. Furthermore, the approach can be carried out either by a more model-driven or a data-driven manner. According to the authors, it is said that, interior edges of the roof models derived from model-driven concept don't coincidence with the ridge-lines obtained by intersecting neighboring roof planes. This issue can be considered as common to resulting models yielded by other model-driven approaches discussed in Section 2.2, as model-driven approaches generally align nearly equal roof slopes into one slope. In the approach developed by Oude Elberink (2009), the gutters are reconstructed by applying constraints to the direction of ridge-lines, and also to be horizontal through the lowest point of the roof segment. Additionally, the eaves are made orthogonal to the ridge-lines.

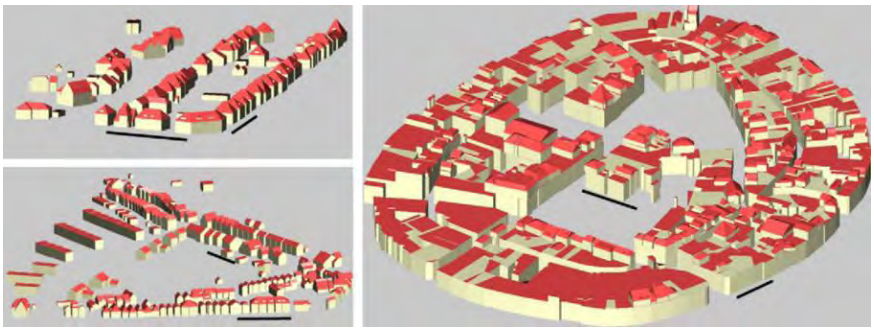

Figure 2.8: Resulting models by Oude Elberink (2009).

In the reconstruction scheme presented by Sampath and Shan (2010), the extracted roof ridge-lines and edges are used. Based on the assumption that the intersection of planes does not form a volume, inner vertices are directly obtained by intersecting corresponding planes (three or more) where vertices are associated with. Outer vertices are obtained by intersecting vertical planes defined parallel to the outer-boundaries, and passing through the end-points (outer) of the inner roof skeleton. In the case of flat roofs, the method proposed by Sampath and Shan (2007), using the modified convex hull is adopted. However, by identifying the longest line segment, the rough boundary line segments are regularized either parallel or orthogonal to the recognized direction, which is controlled by the constrained least square process.

2.4 Data-driven versus model-driven building reconstruction

The idea of the reconstruction is to model the reality, based on the measured data corresponding to a large set of points. To represent the reality, correct topology and regularizations should be maintained. Generally, combining building primitives, as described in model-driven schemes, may preserve this topological issue. Furthermore, model-driven approaches link the structural shape of buildings with primitive features and find best-fit models, thus model-driven approaches provide promising results and ensured plausibility of the reconstructed models. However, problems may arise when the pre-defined primitives are unable to represent a scene. Therefore, it is said that the model-driven approaches are popular among rough city modeling. Also, as mentioned at the end of the Section 2.2, they may fail at object complexities which further deviate selection of unambiguous best fit primitives. As such, these models are limited to the set of defined shapes in a model library and are unable to handle all shapes found in urban areas. Increasing the models in the library would result in an increased complexity, so that it reduces the robustness.

In contrast to model-driven approaches, with high density point clouds, data-driven approaches perform well in complex scenarios by recognizing adjacent planar faces and their relations (e.g. ridges and step-edges) to achieve topologically and geometrically correct 3D building models as explained in Section 2.3. The main drawback of data-driven approaches, however, is their sensitivity to the incompleteness of data arising from occlusion, data gaps or vegetation clutter. Similarly, intersection of best fitted planes, for instance four planes, may create more than one point which yields extra short edges leading to an erroneous topology. A thorough discussion on the problems relevant to building reconstruction scheme, including effects due to data and scene complexities, is given in Oude Elberink (2008). In the reconstruction, defining hypothesis about the building shape is the major difficulty as it has to be automated. Assumptions that could be defined based on data or general knowledge about the scene, of course, help in this regard. Sometimes, constraints may conflict with the actual scene, for instance in the regularization of roof outlines, along with the orthogonality and parallelism constraints, with respect to the fact that the main direction of the building may not always follow the actual direction. Taking into account topology representation, some approaches based on the topology graphs have been introduced (Sampath and Shan, 2010). They may be capable of handling more complicated scenes with a higher level of topology preservation. Some methods relying on RTG also use pre-defined primitive shapes and consequently, library graphs or target graphs (Verma et al., 2006). Although this would be a solution for data gaps, it would however be questionable when the targets are unable to represent a scene. Accordingly, the data-driven methods based on the segmented roof planes can be categorized into two groups: RTG-based and non RTG-based methods.

When considering everything, the data-driven strategy with primitive feature manipulation based on the roof topology graph, but without depending on external targets, seems to be a good solution in order to take advantage of the flexibility and the robustness of the data-driven approach which is chosen in this study.

2.5 Building model refinement

Although, ALS point clouds enable for a highly automated processing workflow, the major drawback of point clouds is its' sparsely distributed point nature, which still reduces the geometric accuracy, more specifically the planimetric accuracy, of model boundaries as explained in Chapter 1. In order to enhance the accuracy of building models, refinement processes have been applied in some reconstruction schemes. Due to the difficulty of enhancing accuracy of models by point clouds itself, most practices which deal with refinement have used external data sources. In this regard, image data is shown as the most prominent source because it has complementary properties than ALS point clouds. Integration of these two data sources enhances the quality of building models in many ways, for instance LoD, segmentation, planimetric accuracy. For successful data integration, data registration is important. For the refinement process, matching corresponding features is also important. Therefore, co-registration and matching steps are two major tasks in the image based refinement process. As such, these two steps are discussed separately in the following sub sections while continuing the discussion about approaches which use refinement procedures further.

Once data are properly integrated, image information can be used to increase the accuracy of roof point segmentation. Khoshelham (2005) use a single image for refining segmentation of point clouds. Rottensteiner (2010) illustrate that the segmentation can be further enhanced by integrating multiple images and it solves contrast issues of individual images.

In the approach proposed by Ameri and Fritsch (2000), image information is used to refine the building edges detected from the DSM that has been derived by point clouds. Similarly, in Mcintosh and Krupnik (2002), edges extracted from aerial images are matched and are used to refine DSM, derived from point clouds aiming to accomplish sharp discontinuation of urban buildings. In contrast, Ma (2004) proposes a post-refinement approach for the initial building models, which is derived by the clustering method from ALS point clouds. Stereo imagery is mainly used in this post-refinement

process. Chen et al. (2005) integrate building boundaries extracted from aerial images and roof planes derived from point clouds for reconstructing enhanced building edges with the help of split and merge strategy. Lee et al. (2008) extract initial building regions from the point clouds and merge them with the regions segmented from images to reach coarse roof edges. Precise roof boundaries are then extracted based on the coarse result through line segment matching and perceptual grouping. Cheng et al. (2011) derive the principal building orientation, and building roof edges are thus extracted robustly from aerial images. To determine 3D roof boundary segments, they integrate point clouds and 2D boundary segments extracted from multiple images. A strategy to recover boundaries which are lost is also included in their approach. Habib et al. (2010) propose a semi-automated way for enhancing the accuracy of roof patches generated from point clouds by integrating point clouds and stereo imagery. Herein, 3D image lines generated by stereo imagery are matched with the boundaries generated by point clouds, with line updating performed by manual mono plotting afterwards. However, insertion of erroneous and deletion of true boundaries occur due to contrast issues and relief displacement. Another interesting coarse-to-fine segmentation approach for deriving planar roof segments from the point clouds is proposed by Cheng et al. (2012). This includes initial normal estimation step and segment refinements by using aerial images, synthetically, based on the shrink-expand technique. This is followed by a point based feature integration mechanism to combine 2D line segments extracted from multi-view aerial images and 3D points determined from segmented point clouds, especially to refine 3D step-edges, by which geometrically improved 3D building models are achieved.

2.5.1 Co-registering

In ALS and image data integration, *co-registration* or *referencing* of one data set to another is first needed to fulfil as the data capturing is mainly done via different sensor systems. This is basically a problem of determining exterior orientation parameters of aerial imagery. The solution for this would be a block adjustment and can be realized using traditional ground control points, or lines and surface patches extracted from point clouds. Individual image orientation using single photo resection is also feasible (Schenk and Csatho, 2002). Currently, many data registering schemes have been developed and their applicability associates mainly with the processing workflow. Habib et al. (2001) perform single photo resection to estimate orientation parameters using a modified iterative Hough transformation. Schenk and Csatho (2002) illustrate that the images can be integrated with point clouds through the break lines and surface patches extracted from the point clouds. This then yields an information-rich surface description. In contrast, Habib et al. (2004) use straight lines as primitives for data registration. In the approach proposed by Ma (2009), stereo aerial imagery is adapted.

2.5.2 Linear feature matching

Section 2.5 illustrates that the geometric refinement of roof boundaries derived from point clouds can be achieved by integrating image information. For this, linear features need to be first extracted from the images as building roofs can be described by linear features. In the feature extraction, Gray scale images are usually used as it is computationally efficient. However, the approach presented by Ok et al. (2010b) shows that completeness of the detection can be optimized by using multispectral channels. They further show that principal component analysis technique can enhance the line extraction. In linear feature extraction, burns line extractor (Burns et al., 1986) and line growing – Förstner operator (Förstner, 1999) are widely being used (e.g. Nyaruhuma et al., 2012; Tian, 2011). These methods directly extract lines based on local gradient or intensity information. In contrast, extensively used edge operators to detect optical edges are canny edge detector (Canny, 1986) and Edison edge detector (Meer and Geogescu, 2001). Since these operators only detect boundary edges, to extract linear features from the detected edges, it is necessary to use an algorithm like Hough transformation (Hough, 1962).

From the extracted linear features, corresponding features can then be searched and matched. As the features extracted from image space are in 2D, matching of corresponding linear feature in stereo or multi-view images would lead to transform them in to 3D object space. Therefore, the remainder of

this section focuses particularly on discussing existing practices which relies on matching of image space linear feature. The main problems of linear feature matching are extraction of proper features, searching, and matching corresponding features. The line extraction has already been discussed in this section.

Current practices of line matching procedures can be divided into two main groups: (i) matching of individual line segment and (ii) matching of group (mostly pairs) of line segments (Schmid and Zisserman, 1997). In either way, during the matching process, the search space has to be restricted to reduce the complexity. In order to filter out irrelevant candidates, algorithms in the first group mainly apply basic geometric parameters of line segments such as orientation, length, and mid-point (e.g. Collins et. al., 1998; Noronha and Nevatia, 2001; Suveg and Vosselman, 2004; Kim and Nevatia, 2004; Jaw and Perny, 2008). In addition to geometrical information, some studies have also used radiometric information around the linear feature (e.g. Henricsson, 1998; Scholze et. al., 2000). Predominantly, epipolar geometry is useful in either way. On the other hand, to improve the matching correspondence, additional strategies, for example dynamic programming (Medioni and Nevatia, 1985; Ohta and Kanade, 1985), hierarchical matching strategy (Jaw and Perny, 2008; Zhongliang and Zhiqun, 2008), probability relaxation (Zhang and Baltsavias, 2000; Zhang, 2005), and weighted criterion (Henricsson, 1998) have also been used.

Group of line matching is also a quite popular approach (e.g. Park et. al., 2000; Kim and Nevatia, 2004; Ok et al., 2010a). Using relaxation labelling, Zhang and Baltsavias (2000) adapt a pair-wise searching strategy, while Kim and Nevatia (2004) illustrate how to use pair-wise approach for multi-view images based on the epipolar geometry. Similarly, Beder (2004) presents a graph based feature manipulation approach for multi oriented images. In the method presented by Ok et al. (2010a, 2010b), principle component analysis is first introduced to obtain accurate straight edges. With some new constraints (e.g. angle of intersection, proximity), line segments are matched pair-wise while reducing fault matches using probabilistic theories.

Another variant of multi-image linear feature matching is given by Elaksher (2008), in which simultaneous matching is carried out. In contrast, Heuel and Förstner (2001) illustrate that even without incorporating image intensities, adaptation of geometric information of linear features in multiple images with projective geometry is sufficient for recognizing correspondences, and also to construct 3D line segments.

3. Methodology and approach

This chapter deals with the new concepts that are introduced based on the literature to achieve the objectives explained in Chapter 1. These concepts are applied within the proposed building reconstruction approach explained in later chapters.

3.1 Outline

Motivated by the increasing demand of geometrically accurate 3D building models, and the usefulness of taking synergetic properties of both point clouds and aerial images for the reconstruction schemes as described in Chapter 1, the following facts are considered in the new algorithmic designing.

- Data driven-strategies
- High level of contribution by point clouds
- Efficient and highly automatable processing hierarchy with respect to ALS point clouds and aerial images

Based on the above facts, and the knowledge gained from the literature, the proposed building reconstruction scheme is designed to be executed in two stages: (i) 3D building model reconstruction from ALS point clouds, and (ii) model refinement by integrating point clouds and image data. Since the aim is to develop a highly automated algorithm for the reconstruction of building models having higher vertical accuracy, more attention in the automatic algorithmic design is put towards issues regarding roof model reconstruction from point clouds data. In order to achieve the first step, different concepts and strategies are introduced. Special attention was given on finding a new approach to automate the manipulation of roof primitive features based on roof topology and how RTG can be used more effectively for the building reconstruction process. This enables the method to reconstruct building models without an external graph. Besides, how regularization could accurately represent reality is considered for the sake of weakly defined boundary edges.

In the second step, *i.e.* in the refinement process, special emphasis was given on how to accomplish adequately accurate 3D boundary edges from the aerial images. Obtaining these 3D boundary edges from corresponding 2D line features that are extracted in image space is achieved by geometrically matching of candidate line segments in projective geometry. In order to cope with ambiguities arising in correspondence matching (line segments in image space) and gaps pertaining to 3D line segments constructed by adding image information, solutions are given from evidences that can be clearly defined from the known structural arrangement of initial roof models and the specially defined convergence priors. Once the accurate roof outlines are received, accumulation of wall polygons enables to obtain an entire 3D building model.

In this chapter, the key concepts used in the above two stages within the proposed reconstruction procedure, are highlighted in Section 3.3 and 3.4. Processing flow of the building model reconstruction from point clouds and images is shown in Section 3.5 with a short explanation to each step. As mentioned in Section 1.2, the RTG is essential for the efficient manipulation of roof primitive features such as roof outlines and roof plans. Therefore, the method starts with the initial retrieval of RTGs. Although RTG is extensively used for the building reconstruction (e.g. Verma et al., 2006; Oude Elberink and Vosselman, 2009), low level graph theories is incorporated in the processing chain.

In contrast to previous methods, the method presented in this study utilizes a high number of graph operations in order to obtain the possible flexibility in handling complex roof structures. Since the initial building modeling procedure is based on RTGs and uses different graph operations, some basic definitions and a few graph operations are briefly illustrated before presenting the new concept that this study will introduce. The reader can, thus, get a better understanding of graphs and consequently, the new concepts of the study.

3.2 Basics of graph

A graph G = (V, E) is a pair of sets of V and E such that $E \subseteq (v)^2$, which maps pairs of elements of V to elements of E: where V and E are vertices and edge sets.

G is planar (planar embedding or plane graph), if it can be drawn on the plane without crossing of edges (Figure 3.1). Having no intersection edges in a planar graph, the edges divide the planes into different regions. The regions enclosed by the graph edges are called *(interior) faces* of the graph.

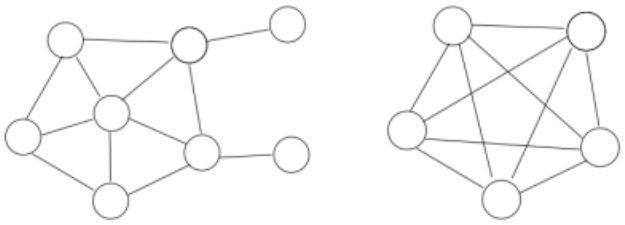

Figure 3.1: Planar and non-planar graphs: (a) planar graph (planar embedding) doesn't contain any cross edges and makes different faces or regions on the plane (b) non-planar graphs can contain cross-edges.

Graph *union*, *intersection* and symmetric *difference* are illustrated as follows:

The union of two graphs G1= (V1, E1) and G2= (V2, E2) is another graph G3= (V3, E3) denoted by G3=G1∪G2, where vertex set V3=V1∪V2 and the edge set E3=E1∪E2. The intersection of two graphs G1 and G2 indicated by G1∩G2 is a graph G4 consisting only of those vertices and edges that are in both G1 and G2. As such G1∩G2 = (V1∩V2, E1∩E2). The symmetric difference of G1 and G2, written as G1⊕G2, is the induced graph G5 on the edge set E1⊕E2= (E1\E2) ∪(E2\E1).

In order to gain a clear idea, the pictorial outcome of the above operations is illustrated in Figure 3.2.

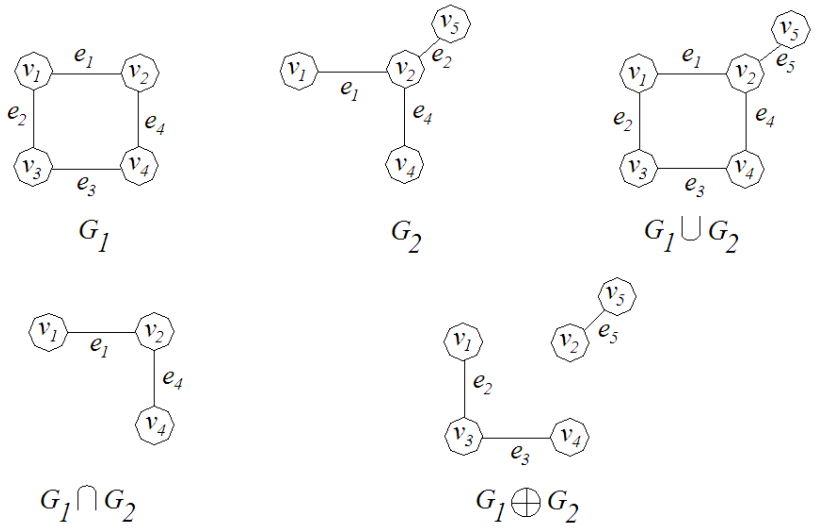

Figure 3.2: Union, intersection and symmetric difference of two graphs G_1 and G_2.

3.3 Reconstruction strategy

In this section, the strategy that this study introduces to the building reconstruction scheme based on the RTG is presented. The main idea of the work is to best use RTG and to reconstruct roof models using the data itself.

A man-made object can be detached into basic primitives composed of planes, lines and points. Of course the boundary of planes is given by lines, but in the sense of geometry, lines are produced by the intersection of relevant planes in which they are common for both corresponding planes. Points indicate the places where more than three planes or at least two lines meet (Figure 3.3). In reverse engineering, *i.e.* in reconstructing, objects can be reconstructed by assembling lines and fixing them at correct meeting points. This indicates that a similar approach can be applied for reconstructing 3D building roof models.

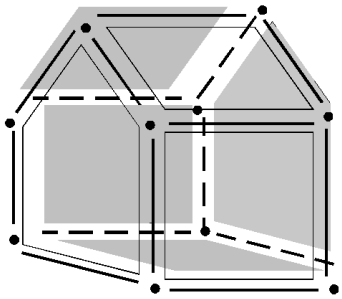

Figure 3.3: Representation of a 3D building using basic primitive features (planes, intersection lines and vertices are the basic primitives).

A 3D roof model can be reconstructed by determining the position of vertices at edge intersections. According to the designed architecture of buildings, different roof corners (vertices) forming different roof styles can be seen. For instance, in a hip or a pyramid shape building roof, the roof top vertex is formed by intersecting three or four ridge-lines (or roof edges) respectively. In hexagonal shape building roofs, six edges are intersected to produce the vertex. Figure 3.4 shows some examples for different roof styles with different roof vertices. In addition, those ridge-lines are standing with respect to a specific order or more specifically to a certain adjacency. This means that intersection may occur

at different complexity levels and in different manners. Therefore, in automated reconstruction, there should be a specific way to recognize these converging edges and to know how they meet.

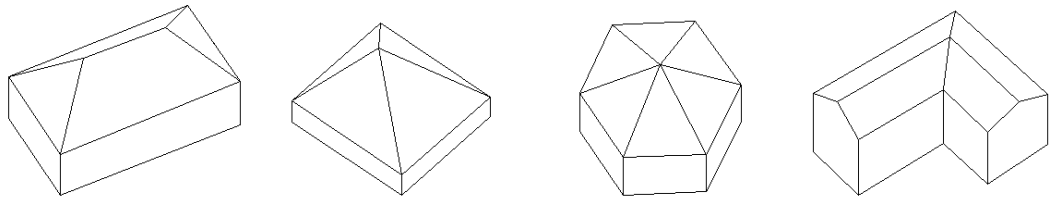

Figure 3.4: Complexity of roof top vertices (complexity of a vertex is proportional to the number of boundary edges going to converge).

Roof topology graph is an effective way to describe the roof structure of a building without considering its geometric positions. It can be observed that each RTG have many closed circles which relate different vertices in object space. In order to associate a vertex with a roof corner in 3D within this study, a strategy for recognizing the nature of convergence of roof planes through closed cycles available in an RTG is introduced. By this method, geometrical fixing of roof vertices or corners is executed at high precision based on the closed cycles. In 2D, an RTG can be considered a plane-embedded graph without crossing. In graph theory, a closed cycle is defined as the *face* of a plane graph on which the conceptual design of this research is based. But for the purpose of clarity, the term *cycle* is intentionally used instead of *face*.

Roof corners can be categorized in two ways: inner and outer corners. Inner roof corners can be geometrically modeled by intersecting ridge-lines and step-edges. Hereafter, please refer the term feature line to indicate ridge-lines and step-edges. In contrast to inner roof corners, outer-boundary line segments can be intersected with feature lines for outer roof corners. Relevant feature lines needed to fix such corners can be identified using different graph (cycle) analysis techniques such as graph decomposition, subdivision, union, intersection and difference (Section 3.2).

If feature lines are investigated in 2D space in conjunction with RTGs, a roof corner or convergence of feature lines usually refers to a closed cycle graph as shown in Figure 3.5. The closed cycles present the minimum *walk* to traverse over all segments relevant to a particular roof corner. The cycles can be defined as the *shortest closed cycles* (SCC) and could further be described as the shortest walk ($n>=3$) between two vertices in which the first and last vertices are the same, where n is the cycle length.

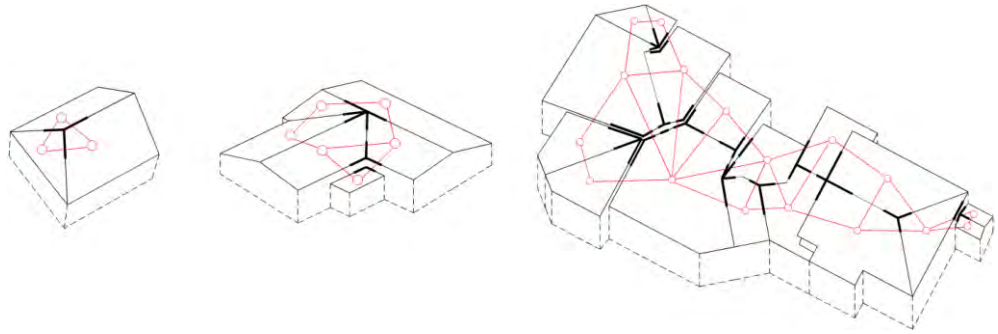

Figure 3.5: Convergence of feature lines referring to the shortest closed cycle in RTG (convergences indicated by dark lines).

3.3.1 Shortest closed cycles (SCCs)

The RTG is an embedded plane graph denoted by *G = (V, E)*. A vertex represents a roof face while an edge shows the adjacency relationship between roof faces (Figure 3.6). The traversing over G in-between given end-vertices provides different *paths*, for instance the graph shown in Figure 3.6(b) gives several different paths such as; P1{3,2}, P2{3,4,2}, P3{3,4,6,10,1,2} and so on, respective to end-vertices 3 and 2. If the starting node becomes the end node, then the path will be a *closed cycle*, having a certain *length*. The length is equal to the number of edges in the path. The closed cycles of path P1, P2 and P3 will become C1, C2 and C3 such that C1={3,2,3}, C2={3,4,2,3} and C3={3,4,6,10,1,2,3}, having lengths of 2, 3 and 6 respectively. Considering the shortest path problem, cycles having a higher degree of lengths can be disregarded and a unique ***shortest*** closed cycle whose length is equal to, or higher than, three (03) can be obtained for the given two end-vertices (C2 for the above example). The convergence corresponding to the SCCs refers to an inner roof corner.

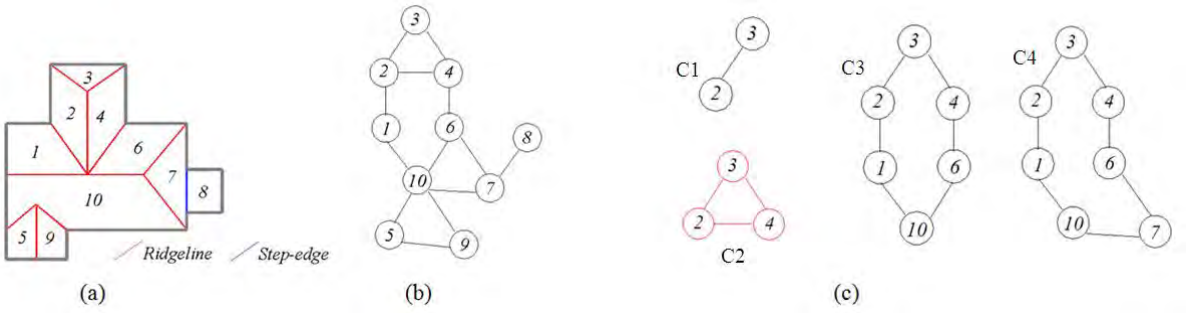

Figure 3.6: Layout of feature lines of a connected building and their topological relations: (a) top view of the building; (b) corresponding RTG; and (c) decomposed closed cycles for the given edge 3-2, (red cycle indicates the shortest cycle among the cycles - when cycle length ≠ 2).

3.3.2 Extracting shortest cycles

It is essential to find all shortest closed cycles contained in the RTG. The closed circles, as defined in Section 3.3.1, can be identified by the decomposition of an RTG into possible SCCs using a graph search algorithm such as Dijkstra's, depth-first or breadth-first (Diestel, 2010). However, to resolve ambiguities, the Dijkstra's algorithm is more convenient. In this study, the Dijkstra's concept is employed to search for each shortest closed cycle containing the edge of interest (given end-vertices). The SCC searching strategy based on Dijkstra's algorithm is explained briefly, as follows:

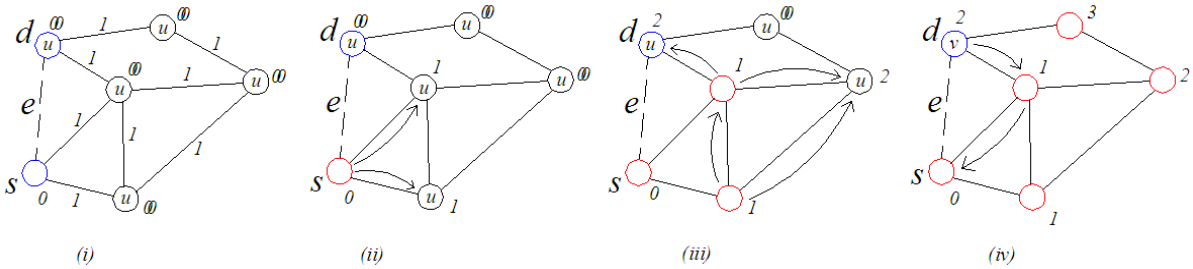

Figure 3.7: Dijkstra's concept for finding the shortest closed cycles between any desired end-vertices, (blue nodes – starting and ending vertices, red nodes – visited vertices, arrows – indicate paths).

For a given edge ***e*** with ***s*** and ***d*** vertices, if the shortest path from ***s*** to ***d*** that does not contain ***e*** can be obtained, then this enables the extraction of the shortest closed cycle, after inserting the starting vertex (Figure 3.7). Assuming the length of any graph edge is one, or all nodes are equally weighted by one, the smallest distance to the destination vertex ***d*** from the source vertex ***s*** can be computed through all

unvisited vertices ***u*** and their neighbor unvisited vertices ***v***. The search process of a SCC is developed in a way that selects the unvisited vertex with the lowest-distance among vertices ***u*** and finds the next vertex that is marked with the smallest distance from the unvisited neighbor vertices *v* of the selected vertex ***u***. It is repeated until the destination vertex is marked visited, while updating vertices as visited, once done with the neighbors. Once the smallest sum of distance is found from ***s*** to ***d***, by back tracking the path until the source vertex, the shortest closed cycle can easily be extracted using Dijkstra's Algorithm. In general, Dijkstra's algorithm require three inputs (*G,w,s*), where G contains vertices and edges, ***w*** is the weights or length (since both are equal), and ***s*** is the source vertex. Pseudo code of the search process is shown in Figure 3.8. With the idea of decomposing RTG into possible all SCCs, the source vertex is chosen automatically and the destination is set to its adjacent node in the candidate graph edge ***e***.

```
Dijkstra's Algorithm for extracting shortest closed cycles
Input Data: RTG, s, d
Output: Shortest closed circles SCC

dist[s] = 0                                   (distance to source vertex is equal to zero)
for all v ∈ V−{s}
    do dist[v] = ∞                            (Define distances to all other vertices to infinity)
    P = ∅                                     (P - the set of visited vertices, which is empty at the beginning)
    R = V                                     (R - a vector containing all vertices)
    while R≠∅
    do u = Extract(R, dist)                          (Find the vertex u from R with the minimum distance)
       P = P ∪ {u}                                   (Mark u as a visited one)
       for all v ∈ adjacent[u]
           do if dist [v] > dist[u] + w (u, v)
                 then dist [v] = dist[u] + w (u, v)
    End                                       (end while)
    While v ≠ u
        do Backtracking                       (backtracking the path until source node)
    Adding first node
    Push_back (SCC)
    Clear memories
End
```

Figure 3.8: Searching shortest closed circles – Dijkstra's algorithm.

Some examples for the extracted shortest closed circles which are obtained based on the Dijkstra's algorithm by decomposing the RTG in Figure 3.6 can be seen in Figure 3.9. It has four SCCs, having nodes: {2,3,4,2}, {2,4,6,10,1,2}, {6,7,10,6}, and {5,9,10,5}.

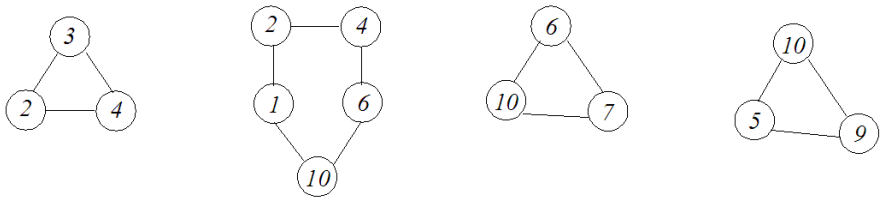

Figure 3.9: Decomposing of the RTG into shortest cycles.

This RTG decomposition into SCCs can be described with graph notations as follows:

> *Let G be a plane graph, and let G′ denote G after deletion of its bridges/cut-vertices. Let* $\Gamma = \Gamma(G')$ *denote the set of shortest cycles* $S_i \ldots S_k$ *of G′. If the union of the cycles* S_i *and* S_j

is defined as $S_i \cup S_j \coloneqq (V_i \cup V_j, E_i \cup E_j)$*, (where* V_i, E_i *and* V_j, E_j *are vertex set and edge set of the* i^{th} *and* j^{th} *cycles respectively), then for all* $i = 1 \dots k$*,*

$$\Gamma = \bigcup_{1<i<k} S_i$$

3.3.3 Splitting of shortest cycles

Although a convergence produces a single point in 2D, this is not always true in the 3D space. When step-edges are present at an SCC, there can be many convergence positions at different height levels in the same planimetric location as shown in Figure 3.10. In order to cope with such a situation, disjoint paths or *directed path graphs* can be employed at corresponding height levels. These paths can easily be obtained by splitting the cycle space into different sections, or theoretically using the operation called *subdivision* and then by *inserting* the new end-vertices. The number of split sections depends on the number of step-edges at a certain SCC. Inserted vertices give clues to the plane of a step-edge. For instance, by splitting the cycle space in Figure 3.10(b) into three sections (Figure 3.10c), relevant path graphs can be derived by configuring nodes in the order of $\{1_2, 1, 4, 4_3\}$, $\{3_4, 3, 3_2\}$ and $\{2_3, 2, 2_1\}$. The extraction of paths from a cycle can be written as follows:

Let $G = (V, E)$ *be a directed cycle, and let* $G' = (V', E')$ *denote* G *after splitting of its some edges. Let* $F \subseteq E$ *the subset of edges to be split.*

$$V' = V \dot{\cup} \{(U,V) \mid (U,V) \subseteq F\} \dot{\cup} \{(V,U) \mid (U,V) \subseteq F\}$$

$$E' = E \setminus F \dot{\cup} \{(U,(U,V)) \mid \exists (U,V) \subseteq F\} \dot{\cup} \{((V,U),V) \mid (U,V) \subseteq F\}$$

Two vertices v_i *and* v_j *are connected in* G'*, if there is no split edge* $f(v_r, v_{r+1})$ *in* F *with* $i \leq r \leq j-1$ *.*

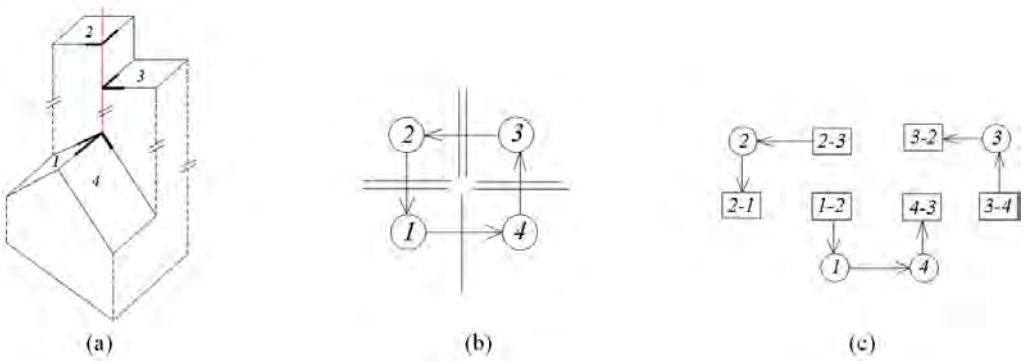

Figure 3.10: Convergence of step-edges (including ridge-lines) leading to a single planimetric location in 2D: (a) oblique view of 3D roof having multiple step-edges; (b) directed SCC given by Dijkstra's algorithm; and (c) disjoint paths.

3.3.4 Outermost closed cycles

Further continuance of the procedure in 2D would result in some of the successive outer-boundary line segments converging on feature lines, or inner roof skeletons, as shown in Figure 3.11. The respective skeleton edges that make roof outer corners can be simultaneously extracted by a cycle whose *path* goes along the outer envelope of the RTG. This closed cycle can be defined as the *outermost closed cycle* (OMCC): A closed path starts and ends on the same vertex and runs along the outermost edge of the original graph. In an embedded plane graph, this OMCC can be defined precisely with the *boundary of the exterior face*. However, the OMCC can be derived by taking the *union* of adjacent SCCs one after the other, including *bridges/cut-vertices*, while removing the edges present more than

once. This is done by taking the *difference* between *union* and *intersection*. However, during the edge removal, bridges/cut-vertices should not be avoided. For the RTG in Figure 3.6, the OMCC can be derived along vertices so that the end-vertices in {1,2,3,4,6,7,8,7,10,9,5,10,1} are equal to one (01). The OMCC construction is mathematically described as follows:

Let C_i is a shortest cycle and $i = 1 \dots k$. Let B_p denotes bridges/cut-vertices and $p = 1 \dots m$. Let G' denotes OMCC or outer face. If the union and intersection of the cycles C_i and C_j are defined as $C_i \cup C_j \coloneqq (V_i \cup V_j, E_i \cup E_j)$, $C_i \cap C_j \coloneqq (V_i \cap V_j, E_i \cap E_j)$ respectively, (where V_i, E_i and V_j, E_j are vertex set and edge set of the i^{th} and j^{th} cycles respectively), then

$$G' = (\cup_{1<i<k} C_i - \cap_{1<j<k} C_j) \cup_{1<p<m} B_p : for \quad i \neq j \neq p$$

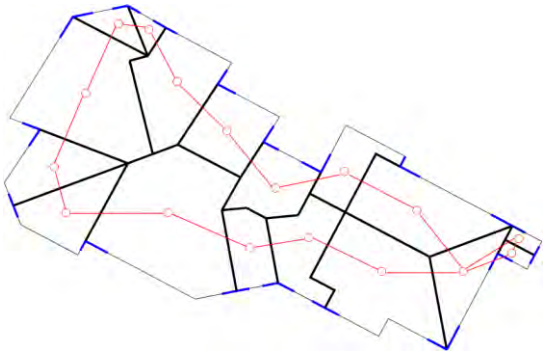

Figure 3.11: Convergence of outer-boundary line segments with inner roof skeleton (two outer-boundary line segments (blue) stay adjacent and both sides to a feature line (black) converge in 2D).

Once a closed cycle is known, relevant feature lines can be chosen directly, and the geometric reconstruction of roof corners becomes possible. Note that regularized edges should be utilized for the above processes.

3.4 Refinement strategy

Orientation and positional accuracy of roof primitive features, and their topological correctness, are important to be maintained in reconstructing accurate building models. In point cloud based roof model reconstruction; the process can be improved in several ways, and in various directions, in which an enhanced quality and more realistic view can be obtained for final models. However, the roof models derived from point clouds mainly need to improve planimetric position of the roof outlines and their topological correctness. These two aspects are only considered in the second step (model refinement) in order to get a higher accuracy in both vertical and horizontal directions.

If image data are used for enhancing the boundary lines of the reconstructed models from point clouds, it requires some kind of a correspondence matching process for the generation of 3D information from 2D line segments extracted from the image space (refer Section 2.5). The geometric relationships of line features at projective geometry can be considered in this regard. Although it can be achieved by the intersection of viewing ray planes as proposed by (Heuel, 2004; Ok et al., 2011), further enhancement to the process is needed. For enhancing the process, well-defined evidences that could be determined from the already derived 3D roof models can be introduced. Additionally, incompleteness is another major issue when working with image data. Sometimes the generated 3D boundary segments from image data may contain some errors, for instance due to the shadow effect or matching errors. These issues can also be minimized, if well-defined evidences can be found in relation to defective boundary edges.

In this study, *scene constraints*, *structural arrangement of roof models* and *boundary convergence priors* are introduced, as new notion, to solve these issues.

1. Scene constraints

Properties of a real scene, for instance the gradient of a roof outline (Figure 3.12), can be defined as a constraint which can be stably determined with the help of available roof models. For the first time, this study incorporates scene constraints to the projective geometry for enhancing matching correspondences in building reconstruction schemes. Three main scene constraints are introduced, namely; perpendicular distance, gradient and gutter symmetry. More details of these defined constrains are represented in later chapters.

Figure 3.12: Geometric properties of the scene are re-defined again as constraints, (for a certain roof edge, it has a specific gradient which is helpful to discriminate the desired line among many omni-directional line segments in 3D).

2. Structural arrangement of roof models

With the availability of RTG, roof adjacency and topological relations between roof planes can easily be determined. Further, properties of initial roof models such as self-similarity, symmetry, repetition pattern and regularity, can also be determined by analyzing feature attributes. All these information provide a definite idea about each roof model. By recalling stored attributes, the *structural arrangement* of roof models can be realized. This well-defined evidence is useful for determining the best reality for places where the refined boundary edges are missing (for e.g. see broken line in Figure 3.13). For instance, evidence of the symmetry can be hypothesized as:

> *If two gutters are members of a gable type roof pair (i.e. inclined adjacent roofs having opposite azimuths with a horizontal ridge) and they follow a rough symmetry, in terms of planimetry, then their gutter heights should be equal.*

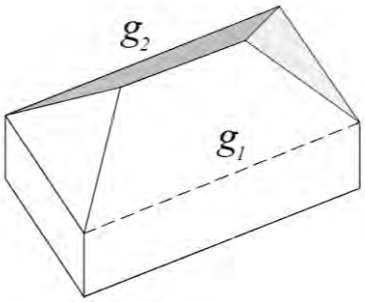

Figure 3.13: Structural arrangement of roof models lead to infer the missing edges (dark line – 3D edges derived from images, dashed line – missing edges).

3. Convergence priors

In addition to accurate boundary edges, defective edges would also be yielded in the course of boundary line generation from image data. This leads to deformed roof corners in some instances. Therefore, solutions are needed to avoid, or at least to minimize, such deformations by rectifying the defective edges. To cope with this, roof corner convergence priors can be used.

Basically, eaves and gutters converge mutually with feature lines, especially ridge-lines, where the transitions of roof planes occur. As explained in Section 3.3.4, these convergences produce external roof corners. Due to the regularity of manmade objects, common shapes can be seen from building roof corners. Figure 3.14 illustrates some basic roof corner scenarios, and most of them often correspond to a 90° or 180° angle difference with each other, though some variations exist. Although roof models derived from point clouds have some positional uncertainty, an acceptable shape can be derived maybe with less LoD. Since the refining of every irregularity, or more specifically increasing the LoD, is out of the scope of this study, this type of effects along the roof outlines is not considered. However, more concrete decisions can be taken by incorporating the structural arrangement of roof models, more specifically the status of the roof outer edges *i.e.* either eave or a gutter. The shape of the roof corners, as well as the type of the boundary lines, can be firmly determined with initial roof models. This information is defined as roof corner *convergence priors*.

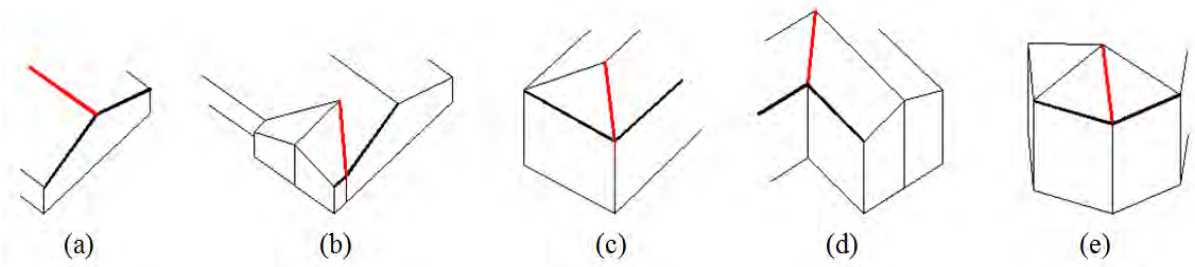

Figure 3.14: Basic roof corner convergence priors: (a) two adjacent eaves and a horizontal ridge-line; (b) oblique ridge-line with a gutter and eave; (c) and (d) convex and concave corners; and (e) irregular case which is deviated from general 90° or 180° angle regularities (red – ridge lines, black – eaves and gutter lines).

Convergence scenarios can be defined unambiguously as follows:

Definition 01

If two adjacent eaves and a horizontal ridge-line converge to each other, then the eaves should produce right angles with the ridge-line. Further, eaves should be collinear to each other (Figure 3.14a).

Definition 02

If one eave and a gutter converge with an inclined ridge-line, then the eave and the gutter could be collinear (Figure 3.14b).

Definition 03

If two gutters converge with an inclined ridge-line in a way one gutter is orthogonal to the other, then there should be a unique height for both gutters. This is applicable for both concave and convex roof corners (Figure 3.14c, d).

Definition 04

A variation of above definitions is also possible when the angles between eave/gutter are deviated from the 90° or 180° regularities (Figure 3.14e).

Since the priors are unambiguous, in the rectification process it is not necessary to know the shape/status of an entire building. Identification of a specific building part or a roof corner, concretely, is sufficient to continue the rectification procedure. Besides, if the recognized corner would follow a basic constraint, that will be enough for correcting the problematic defective arrangement. One important fact in this entire rectification process is that it's hierarchical means of access. First priority is given to the *gutter symmetry*, which is followed by the *arrangement of eaves*.

In order to describe a systematic procedure on refinement, each step of the refinement process is explained by giving reasons and significance of each step in Chapter 5. Descriptive information regarding the introduced new notions in the Section 3.4, and how can they be used in the refinement process, are given in the methodology chapter of model refinement.

3.5 Workflow

Figure 3.15 shows the workflow of the entire reconstruction scheme. It consists of three main stages. Each individual step in the processing chain is explained briefly in this section and more details of these steps are given in the following chapters.

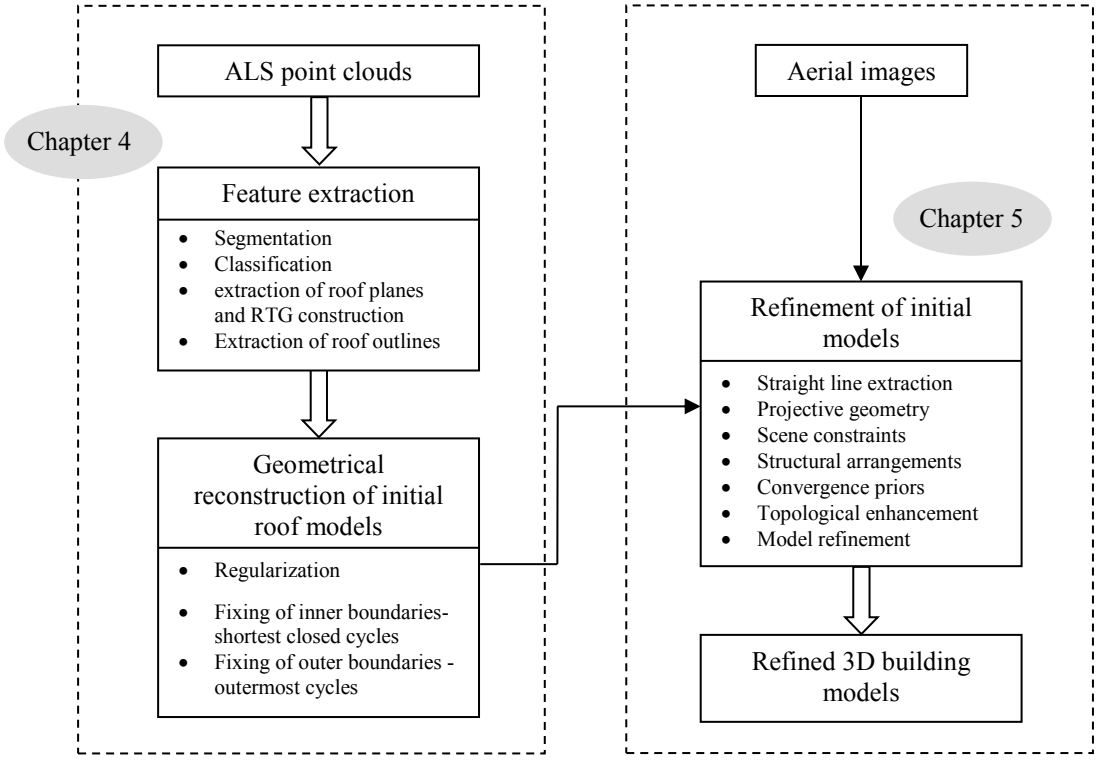

Figure 3.15: Workflow of the proposed methodology.

1. Feature extraction

Extraction of features is typically the initial step of data-driven approaches. Planar segmentation is carried out as the first step of the automated building modeling. This is followed by a segment based classification process in which terrain and off-terrain segments are classified. Based on the various rules that are defined to check the mutual relationship of real world roof scenarios from the laser segments, potential roof segments are extracted from the classified off-terrain segments. To cope with the errors caused by urban vegetation, a sufficient refinement step is included to the processing chain. Topology between potential roof planes is extracted and stored in each relationship in the RTG.

2. Geometrical reconstruction of initial 3D roof models

The geometric reconstruction of roof models is considered as a corner fixing dilemma. To tackle with that idea, reconstruction is achieved based on the novel closed cycle graph approach. Weakly-defined edges, including step-edges and outer-boundaries, are subjected to regularization in terms of orientation and placement. This regularization is carried out prior to the geometrical fixing of roof corners. While allowing flexible sweeping of unfixed outer edges, fixed boundaries (gutters) are snapped to the fixed inner-boundaries (feature lines) to construct a framework of closed polygons with their symmetries preserved. Closed status along the gutter or eave sides are achieved afterwards by the successive intersections of adjacent lines representing the corresponding roof outlines. In order to perform the fixing process of outer-boundaries more efficiently, relevant features are manipulated based on the outermost cycle of the RTG.

3. Refinement of initial models

Model refinement is achieved by integrating information acquired from images with the initial models. The well-known collinearity equation is used mainly for integrating model information onto image data. In the refinement process, boundary lines of each building are first extracted from images. An efficient technique, *i.e.* the intersection of viewing ray planes in projective geometry, is used for generating the necessary 3D boundary edges from the 2D line segments extracted from images. Different strategies such as scene constraints, convergence priors are taken to enhance the result.

3.6 Summary

This chapter introduced novel strategies that the proposed reconstruction scheme relies on. It is proposed to reconstruct 3D roof models geometrically by fixing of roof vertices. To fix the vertices, an efficient method is introduced based on the novel cycle graph analysis method which correlates the convergence of feature lines and outer-boundary line segments in different ways. Of the cycles, the shortest cycle can be used to fix inner corners geometrically while the outermost cycle can be used for outer corners. In the refinement of a roof model, existing models can be improved by adding external data. For guiding the external data, stable properties of existing models can also be used. Therefore, taking the advantage of a known structure of a roof model, the properties that could be defined well, such as gradient of an edge, plane parameters and symmetries, are incorporated to derive refined features from external data, in particular from images. To this end, while describing how image data can be integrated, the way to enhance the outcome is briefly explained. This introduces many new aspects, such as convergence priors, for the refinement process. The entire workflow is presented at the end.

4. Initial roof modeling

ALS point clouds are widely used for building reconstruction. The literature review in Chapter 2 showed the flexibility of data-driven approaches. This chapter deals with the reconstruction of initial 3D building models by point clouds acquired through ALS. Building reconstruction procedures can range from geometric concepts and sophisticated techniques used for the reconstruction process. Generally, the purpose of the reconstruction is to represent a building with points, lines and polygons. It can be done by assembling these primitives. However, in reality, a building has a certain structure or an arrangement, thus each element has a specific topological relation with others. Therefore, the correct topological formulation to achieve a successful building reconstruction is important. In the proposed approach, building reconstruction can be seen as a data driven process of roof shape fitting by extracting the nature of convergence of topological relationships from graphs. The cycle graph or cycle approach is emphasized in this chapter for efficient manipulation of roof topology and features acquired from data. This chapter introduces different aspects of the cycle approach used during the reconstruction for enabling to automatically manipulate feature lines, topological relations, and outer-boundary line segments.

Figure 4.1 illustrates the modeling pipeline proposed by this study for reconstruction of 3D roof models from ALS point clouds based on the concept developed in Chapter 3. Building model reconstruction frequently takes place in two stages. As it is well known, original point clouds do not provide sufficient hints about object characteristics like spectral signatures of object surfaces. This result in the necessity of a feature extraction step in any task of object reconstruction from point clouds, which lies at the center of Section 4.1. During the feature extraction, buildings, in particular roof planes, should be separated, especially from terrain and other objects such as vegetation, for automatically extracting individual features of buildings from point clouds. This can be accomplished by a segmentation and classification process. These processes are discussed in Section 4.1.1 and 4.1.2 respectively. While a shape-based recognition of irregular segments is introduced for excluding trees, different rules are enforced to extract potential roof planes from the classified off-terrain segments. Much of Section 4.1 discusses building feature lines approximating the RTG reconstruction. This incorporates extraction of feature lines *i.e.* ridge-lines and step-edges between roof planes, and presenting their mutual relations in the roof topology graph. In addition to inner-boundaries, roof outlines are essential input for the model reconstruction, which is discussed at the end of this section (Section 4.1.9).

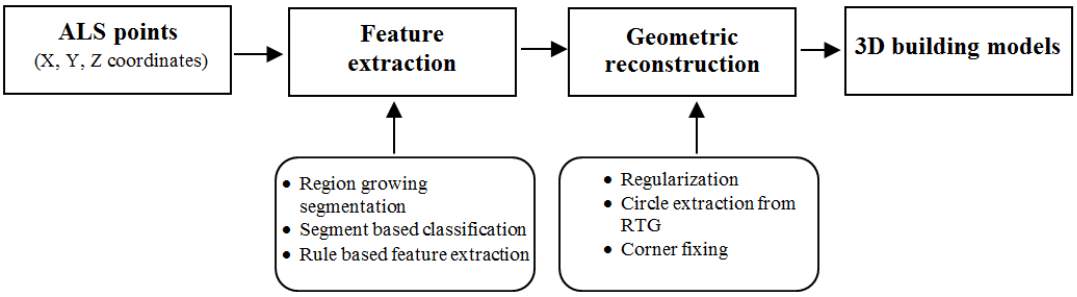

Figure 4.1: Schematic diagram of the geometric model reconstruction.

In the second stage, geometric model reconstruction is performed using the cycle approach, which is considered as a corner fixing dilemma. This geometric reconstruction and complexity handling are focused on in Section 4.2. To begin this process, weakly-defined edges, including step-edges and outer-boundaries, are first regularized in terms of orientation and placement. Based on the shortest

cycle graphs, inner skeleton or inner corners are first fixed at high precision. While allowing flexible sweeping of unfixed outer edges, fixed boundaries (gutters) are snapped to the fixed inner-boundaries (feature lines) to construct a framework of closed polygons with their symmetries preserved. Successive intersections of adjacent lines form a complete outer-boundary. The process runs efficiently with forward traversing along the outermost cycle. Dormer reconstruction is the subject of Section 4.2.5. A short summary is given at the end of this chapter.

4.1 Feature extraction

This section briefly outlines the procedure for extraction of basic roof primitives including roof planes, ridges and edges from 3D point clouds. An overview of the required steps in the feature extraction process is given in Figure 4.2 and detailed description of each step is given in the following sections.

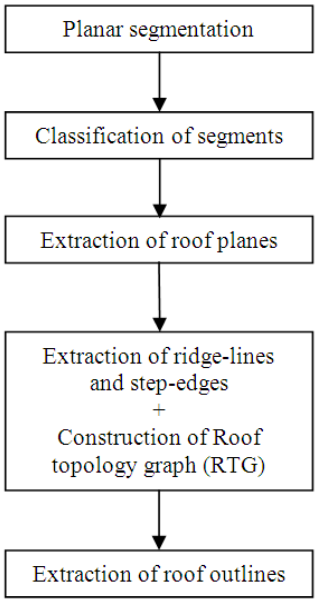

Figure 4.2: Workflow of feature extraction.

4.1.1 Segmentation

Generally, most roof planes are planar. Based on this assumption, the process of information extraction is started by segmenting planar surfaces from point clouds. It is said that the success rate of building reconstruction depends strongly on the result of the segmentation process, so that this is an important step in the processing chain of point clouds towards building reconstruction (Dorninger and Pfeifer, 2008). The surface growing method proposed by Vosselman (2012) is adopted as it performs well in the presence of noisy data. The process starts with the determination of seed surfaces by 3D Hough transformation. A seed surface is a group of nearest points that fit to a planar surface. It is followed by a surface growing by planar fitting. The growing is based on several segmentation parameters such as proximity, distance to plane and so on. It is hard to find parameters that can be fitted well with each and every object in a scene. As such, parameter tuning is invaluable. When a parameter doesn't fit the object complexity, mainly over- and under-segmentation might arise. Although, over- and under-segmentation is reduced as much as possible by tuning parameters within the process itself, such segmentation issues have to be accepted in some places as mentioned by many other experiments (e.g. Oude Elberink, 2009). Figure 4.3(b) shows the segmentation result of the original laser points shown in Figure 4.3(a).

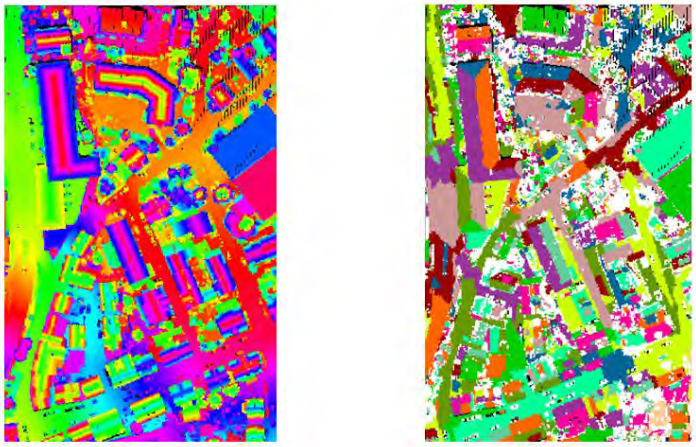

Figure 4.3: Results of planar segmentation: (a) original point clouds; and (b) segmented point clouds (right image - different colors indicate different planar faces, white patches indicate non-segmented points which are mostly vegetation and noise).

4.1.2 Classification of terrain and off-terrain segments

Assuming the resulting segments are correctly representing each planar object, classification of segments into terrain and off-terrain is done using an improved version of the segment based filtering method proposed by (Perera, 2007). In this process, an adjacency map is constructed to describe the connectivity among the extracted planar segments (terrain and off-terrain). For this, Delaunay triangulation of the segmented point clouds is created, and then the segment numbers falling into a desired Area of Interest (AOI) are selected. The radius of the AOI is set in a way that can be accommodated by at least one point from the two segments whose minimum distance separation stays within the distance which is preferred to be considered as an adjacent. In Figure 4.4, for instance, segment A, B and C are taken as adjacent and their mutual connection is obtained as (B, C), (A, C) and (A, B) respectively. Then, one or more neighboring segments to a given segment can be associated straightaway, which makes the subsequent processing steps efficient.

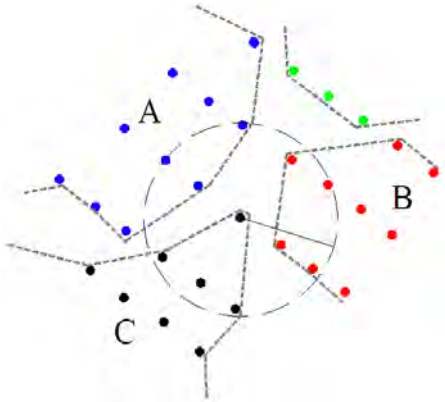

Figure 4.4: Mutual connection among proximity segments (different segments are indicated by a unique color, dashed line – segment margins, circle – AOI which connects all three segments).

Segments which represent parts of walls often reduce the success rate of roof plane (segment) extraction, if the discontinuity of segments is investigated by the processing algorithms. This is because wall segments link the roof faces and terrain or surrounding low vegetation. To reduce the influence caused by merging of terrain and roof segments, vertical segments are removed from the

process. Classification of an entire connected roofs as a single entity is rather simple than when it is done as individual roof planes. Hence, to reduce the object complexity, height variation of points at a given neighborhood (AOI) is tested, and smoothly connected segments are merged (e.g. Figure. 4.5). The resulting segment numbers (results of merging) are stored as an auxiliary attribute of a point, for instance, as the *second segment number*.

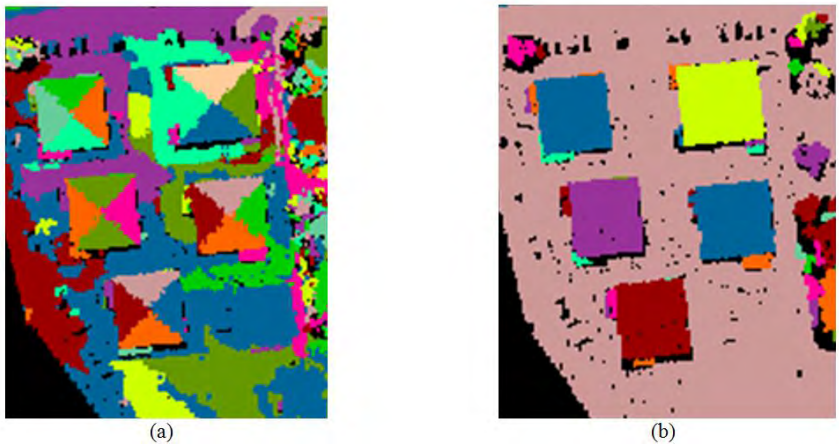

Figure 4.5: Merging of smoothly connected segments: (a) planar segments and (b) merged segments (different colors indicate different segments, black – no data).

Obviously, very large segments correspond to terrain patches (e.g. Figure 4.5b). To classify such a large segment ambiguously, a constraint on area is sufficient, but the constraint is able to discriminate large building surfaces as well. This issue is solved by applying prior knowledge about the scene. Therefore, a relevant area threshold is set for the classification of large terrain patches straightaway. Based on the terrain segments, the above ground objects are handled by computing discontinuities of segments along the segment borders. To measure the discontinuity, a height threshold (h1) is sufficient. This enables to classify off-terrain segments correctly. More explanation can be found in (Perera, 2007). To cope with complexities arising due to some cluster of proximity segments which are partly discontinuous to each other (e.g. Figure 4.6a), the adjacency of the existing segments is updated by merging segments those that are a continuation with respect to a given height threshold (h2). Having recognized continuous transitions in-between adjacent segments, segment merging is achieved in the adjacency space by discarding vanished segments while updating new segment adjacencies (see Figure 4.6b).

Within this discarding process, the role of each vanishing segment as a key for other adjacency elements (segments) is analyzed because neighbors of those vanished segments should first be inserted into their new key segments (the grown-up segments). According to the updates, second segment numbers of the questionable segments are updated. This enables to classify the entire list of segments either as terrain or off-terrain. The status of the classification is stored per laser point as a new attribute called label.

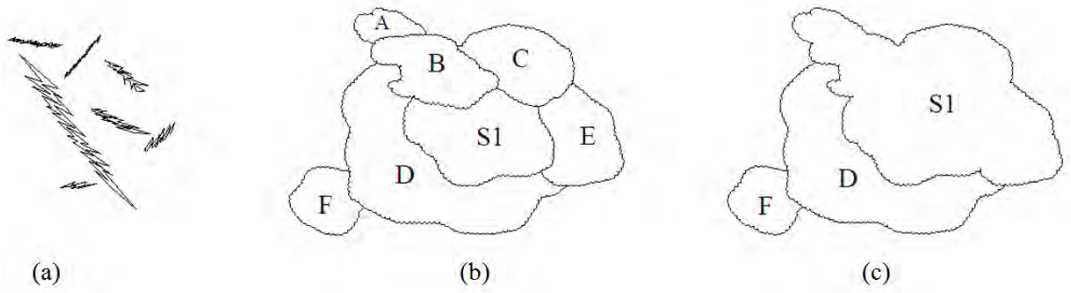

(a) (b) (c)

Original adjacency	Adjacency after updating
S1 – {B,C,D,E}	*S1 – {D}*
A – {B}	
B – {A,C,S1,D}	
C – {B,E,S1}	
E – {C,S1,D}	
D – {B,S1,E,F}	*D – {S1,F}*
F – {D}	*F – {D}*

(d)

Figure 4.6: Merging of partly discontinuous segments in adjacency space: (a) profile view of partly discontinuous segments; (b) aerial view of the segments; (c) merged segments; and (d) adjacency relations before and after merging process.

A subset of the classification result is shown in Figure 4.7. Since classified off-terrain segments may contain many other object classes in addition to building roofs, the extraction of roof plane is necessary prior to the reconstruction of building models. Point clouds captured by ALS deliver an aerial view of the scene. Thus, extraction of building is entirely a process of extraction of roof plane process.

Figure 4.7: Classification results of a sample data set (red – terrain, green – off terrain segments, black – no data).

4.1.3 Roof plane extraction

In the modern society, many complex roof styles can be seen, for instance multi-level gable roofs, flat roofs as shown in Figure 4.8. Although the roof styles are complicated, they are typically built by a combination of one or more primitive shapes such as gable, hip, gambrel, mansard, and so on. Therefore, if one can recognize such primitive shape from among the off-terrain segments, then extraction of roof planes can be realistic. To this end, the method developed in this study detects as many planar faces as possible, fulfilling one or more real shape primitive scenarios, and then considers those segments as potential roof segments for the subsequent reconstruction process.

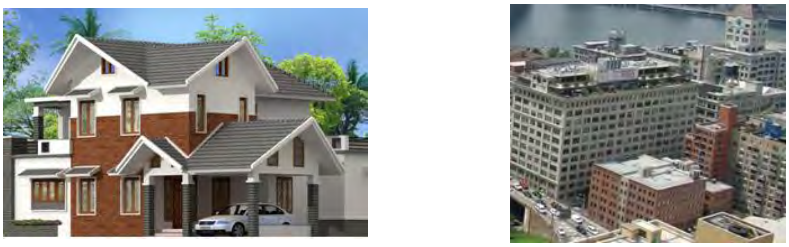

Figure 4.8: Complex building styles exist in the modern society.

The detection of planar segments which follow roof primitive scenarios is accomplished by defining various rules. Before explaining the rules, general characteristics of roof primitive shapes are discussed in the following paragraphs.

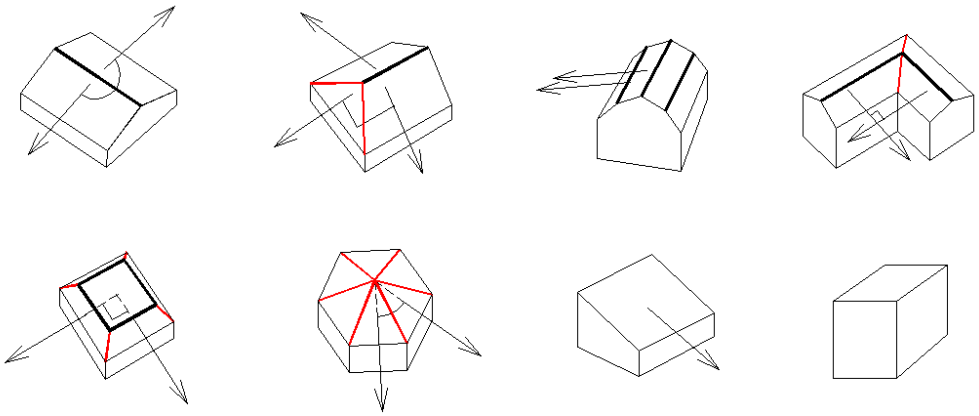

Figure 4.9: Building primitive shapes (dark black – horizontal ridges, red – oblique ridges, arrows indicate the azimuth of each plane).

4.1.3.1 Potential characteristics of roof primitive shapes

According to the building primitives shown in Figure 4.9, horizontal ridge-lines can be seen from many building primitives such as gable, part of hip-roof, mansard, and gambrel. Similarly, from a gable type dormer and at the place where a rectangular shape dormer meets its main roof, horizontal ridge-lines can be recovered. In general, oblique ridge-lines exist in buildings having primitive shapes like pyramid, hip, L-shape, gambrel.

In addition to ridge-lines, individual roof planes might have certain azimuth angle differences with respect to the azimuth of the adjacent roof plane. For instance, in a gable roof, one roof plane produces nearly 180° azimuth angle difference with the counter roof. In a hip roof, two angle scenarios can be found equal to 180° and 90° azimuth difference. The roof pair relevant to each case associates with a horizontal and an oblique ridge-line respectively. Thus, hip roof primitive can be further simplified into gable plus two convex shape roof pairs. In fact, many building primitives produce convex (e.g. pyramid) and concave (e.g. L-shape) angles through their adjacent roof pairs whose azimuth angle difference is equal to 90°. This indicates that horizontality of a ridge-line and an azimuth angle difference of adjacent roof pair are good measures to extract roof primitives. The validity of these measures can be further verified based on situations in mansard or rectangular shaped dormer roofs. In mansard roofs, 0° azimuth angle difference is generally produced by the roof pairs located on one oblique side. Similar azimuth scenario can be found when a rectangular roof is mounted on top of a base roof which is oblique. Apart from the above regular azimuth differences, some exceptional situations can be found, for example in hexagonal roofs. In such a case, estimation of the roof slope would be one criterion. The slope further assists for recognizing the shed and flat roofs as well.

Basically, gable roofs have a symmetrically slanted roof pair. But from some gable roofs, this symmetric situation cannot be expected. Therefore, slope symmetry is not always useful.

In addition to these primitive roof scenarios, the height above the ground is useful as it clearly discriminates low vegetation. Besides, this would be an additional criterion that can be incorporated to each of the above measures. Therefore, detection of ridge-lines, horizontality of ridge-lines, azimuth constraints on corresponding segment pairs and other general geometric characteristics are beneficial to define rules/constraints for extracting roof segments from the classified off-terrain segments.

4.1.3.2 Rule based roof plane extraction

In the roof extraction, there is no requirement to recognize whether a certain roof cluster is exactly a member of a certain primitive group such as hip or gambrel. As such, it is not necessary to identify the cluster at once. On the other hand, in the sense of algorithmic designing, the comparison of two roofs at a time would be more efficient. But, of course, some roof planes such as isolated shed and flat have to be extracted individually. Therefore, a pair-wise and/or individual segment analysis is carried out to extract potential roof segments based on an adjacency map constructed to describe the mutual connectivity of roof segments. In the adjacency map, the AOI radius is equal to the maximum distance between two roof segments which are supposed to be adjacent. During this pair-wise or individual segment analysis, various rules defined based on the characteristics of primitive roof types, as described in the previous section, are checked to find out potential roof segments.

Since wall segments are not necessarily required for the proposed reconstruction scheme, by giving less precision for segments that have $slope_{segment} \geq 80°$, they are straightaway labeled as wall. Generally most of the roof primitives are oblique, as shown in Figure 4.9. Thus from planar segments, whose $slope_{segment} > 5$ and $slope_{segment} < 80$, potential roof segments are extracted based on the identified measures. Among the measures, azimuth constraint is mainly tested for oblique roofs because azimuth angle can be firmly determined from an oblique plane. Therefore, if two adjacent segments satisfy one of the following conditions, they are identified and extracted as potential roof planes.

(i) a 180° azimuth difference together with a horizontal intersection line
(ii) a 0° azimuth difference together with a horizontal intersection line
(iii) a 90° azimuth difference together with an oblique intersection line

During the pair-wise comparison, roof's ridge-line is directly derived by intersecting corresponding plane pairs. (See Section 4.1.7 for more details about the extraction of intersection line.)

The slope constraint is further used to extract flat, $i.e. (slope_{segment} < 5)$, and other oblique roofs, for instance shed roof. Moreover, oblique roofs, which have not followed the defined azimuth constraints at their given adjacencies, but may have remained adjacent to the previously detected roof faces, are extracted by calling the slope constraint. A height threshold, well above the terrain, is always imposed to reduce the low vegetation being portrayed as roof planes. Isolated flat and shed roof extractions are a bit critical as they are extracted independently. Thus, vegetation patches that follow the slope constraints similar to roof planes and also well above the ground may mislead extraction in some instances. Therefore, a shape-based vegetation detection step is introduced to exclude erroneous detections.

Once a roof plane is extracted, it is assigned a label indicating that it is a roof. The status of flat or oblique roof and the rule used to extract the segment, *i.e.* either by slope constraint or by azimuth constraint, is also recorded per extraction (roof segment). Besides, after deriving an intersection line, its status, *i.e.* horizontality and quality of intersection, are recorded as additional attributes to those lines. This is mainly because having those attributes shorten the processing time of subsequent steps of

the reconstruction as the algorithm can access this information when needed from the databases. A sample result of roof extraction is shown in Figure 4.10.

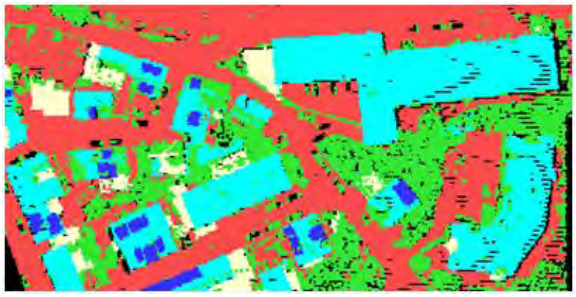

Figure 4.10: Sample result of the roof plane extraction process (cyan- detected roofs by azimuth constraints, white – detected flat roofs, green –vegetation patches, red – terrain segments, dark blue – identified dormers, and black – no data).

Available step-edges are not attempted to be extracted during the roof extraction process since detection is incomplete as yet. However, step-edges are reconstructed later on, after the completion of the extraction process. Missing intersection lines between some segments are also realized in this step. In general, parameters shown in Table 4.1 are used for the roof plane extraction.

Table 4.1: Parameters for rules on roof segment extraction.

Nature of the constraint	Statistics
Threshold for the azimuth difference between neighboring segment pair	±3° from the defined limit
Threshold for the horizontality test of ridge-line	< 3°
Slope constraint for the oblique roof extraction	> 5° and < 75°
Slope constraint for the flat roof extraction	< 5°
Height threshold	2.0 meter

4.1.4 Vegetation removal

Since the procedure continues with the planarity of segments, this research exploits geometric shapes to discriminate regular roof segments from irregular vegetation patches. In terms of the complexity of a segment boundary, the shape is described by the ratio between the ground area of a minimum bounding rectangle (MBR) and the enclosed contour (see Equation 4.1). Pu et al. (2011) and Nalani (2013) illustrate the applicability of segment shapes to discriminate vegetation and road signs from mobile laser scanner data.

$$Shape_{segment} = \frac{\text{area of the MBR}}{area\ enclosed\ by\ the\ contour} \tag{4.1}$$

Assuming that vegetation has a more irregular boundary than a typical man-made object, a segment characterized by a low ratio (< 60%) is considered for vegetation. As this process is exclusively designed to run over roof planes that are extracted by slope constraints (shed and flat roof, see arrow in Figure 4.11a), a triangular shaped hip roof part detected by azimuth constraints is not affected though its ratio (nearly 50%) is lower than this defined threshold (*i.e.* 60%). Additionally, small roof segments that are either isolated or close to each other, are taken and roof labels are discarded assuming that there should not be any isolated small buildings or connected roof parts in reality. In this case, a segment may have a single neighbor belonging to the classified terrain or many neighbors belonging to

falsely detected buildings and terrain (Figure 4.11c). The size of the candidate segment depends on the point density and the size of the minimum roof plane that the study is intended to be modeled upon. In experiments done in this study, 25-32 points (about 4-5m^2) are chosen as a threshold for excluding trees.

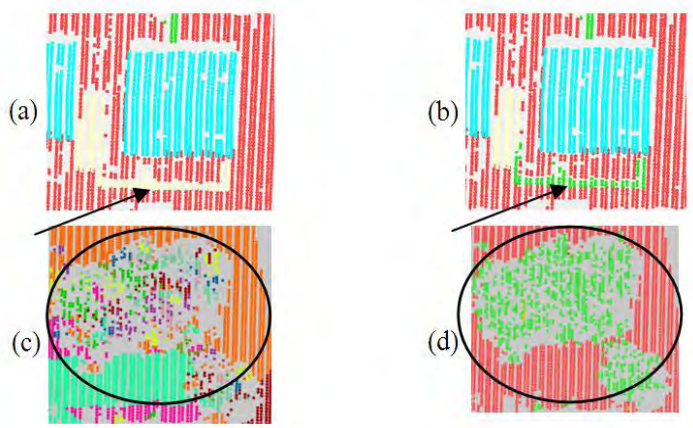

Figure 4.11: Strategies used to remove vegetation effect: (a, c) and (b, d) before and after excluding vegetation by shape ratio and connectivity test respectively; (arrow – erroneously recognized flower bed as flat roof, ellipse – small connected vegetation segments, green - vegetation).

4.1.5 Dormer detection

The recognition of roof planes having dormers is a requirement in the proposed approach. Dormers are usually characterized by the fact that they fall completely into other roof segments. However, a simple comparison of segment size (number of points belonging to a segment) and its adjacency cannot always be used to detect segments that are parts of other roof areas, as the main roof might be partly occluded by dormers (Figure 4.12). In this case, if a centroid of a segment falls inside the MBR of its adjacent segment, the two segments can be recognized as a dormer-plus-main-roof pair, whereby the segment with the smaller MBR area is labeled as the dormer. In addition, unnecessary search is restricted by defining a ceiling for segment size. Atriums may be detected using a similar approach.

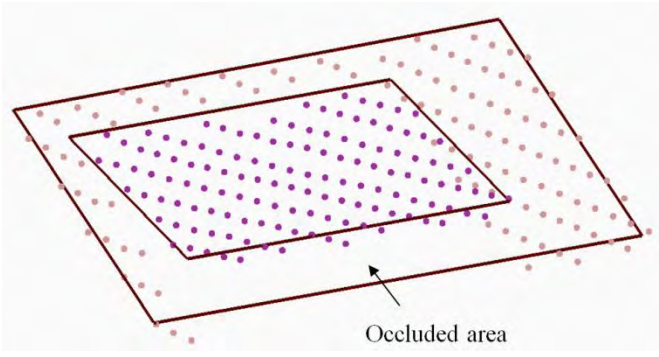

Figure 4.12: Detection of dormer segments (dark magenta – dormer points, light magenta – points on the main roof, outlines – MBRs of both segments).

4.1.6 Grouping of roof planes

Once the roof plane extraction is completed, segment adjacencies should be updated to be the roof adjacencies. This can be achieved by discarding non-roof segments from the segment adjacency map and the resulting map is called a roof adjacency map. Although roof adjacencies are known, member roofs belonging to each building are not known. By analyzing the elements (segments) in the adjacency space, all the connected roof segments to a certain roof in the roof adjacency map are grouped and assigned with a building number. This leads to obtaining a unique building number for each roof. Due to the unavailability of any additional data to demarcate building boundaries, this grouping is assumed to be correct at this stage. Therefore, each connected roof plane is represented by a single building having ridge-lines and step-edges in-between. Step-edges and some ridge-lines which are unable to be extracted as yet can now be extracted.

4.1.7 Deriving ridge-lines and step-edge lines

In general, inner-boundaries of a building (cluster of roof planes) are mainly given by the feature lines *i.e.* ridge-lines and (or) step-edge lines. These feature lines can generally be extracted by considering adjacency of roof segments. The extraction of such features between adjacent roof planes allows the producing of the required vector data of inside polygon edges in polyhedral building models. At the same time, feature lines can be used to identify correct topological relations among roof planes. Knowing the topological relations ease the reconstruction of the outer-boundaries as well. Oude Elberink (2009) and Verma et al. (2006) illustrate the way of representing topological information in an RTG (see Section 2.3.2.2). Section 4.1.8 carries a brief description of the procedure for creating the RTG.

As mentioned in Section 2.3.2.2, to extract feature lines correctly, it is necessary to analyze the spatial distribution of boundary points along the common boundary of adjacent segments. In this research, a distance threshold is used in a global form and the line of intersection is constructed by recognizing the boundary points that lie within a narrow sharing zone (buffer) along the common border as shown in Figure 4.13. Half of the zone width is equal to the distance which is slightly less than twice the point spacing. The boundary points of both segments that lie within the defined distance zone are projected into the line of intersection for determining the overlap between two segment boundaries. If it forms a considerable overlap *d* (Figure 4.13b), then the line is accepted under the ridge-line relation. From the projected points, the most distant two points are set as the end-points of the intersection line.

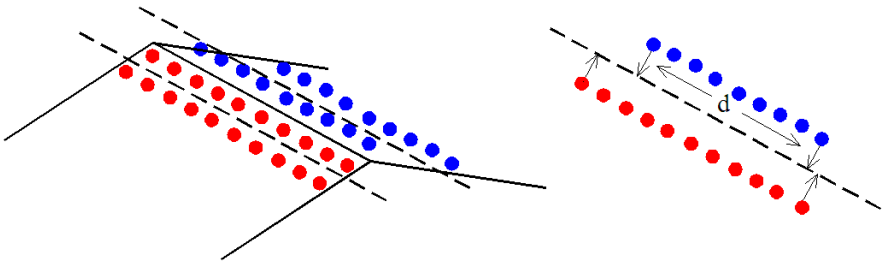

Figure 4.13: Extraction of intersection lines.

If two adjacent segments do not share an intersecting line, then they might form a step-edge. At a common segment border, if every or higher percentage of boundary points can be separated from their nearest counter border points by height jumps *h*, then there would be a step-edge (Figure 4.14a). In fact, in step-edges, the best fitted two boundary segments are needed to represent two edges: up and down. In general, it is hard to find horizontal step-edges at all times (see Figure 4.14b), and therefore edges where a higher percentage of points is still away from the height threshold is still accepted. Additionally, step-edge extraction is further enhanced by recognizing cases that require more than one

connected line segment for the edges to be fitted (Figure 4.14c). This is accomplished by identifying a feature line as a step-edge and finding the distances of the edge points to the fitted line. When a distance exceeds a threshold (1.0*m*), a poly-line preserving the major irregularities is fitted by identifying the correct order of the upper edge points. The fitting of the step-edge into a rectilinear line segment (or to a poly-line) is only performed at this stage. Later in the geometric reconstruction of step-edges, the regularization process is applied and this will be discussed in Section 4.2.1. The planimetric coordinates of upper edge terminals are then transferred to the down edge, assuming that the connecting wall is vertical and passing through the upper edge.

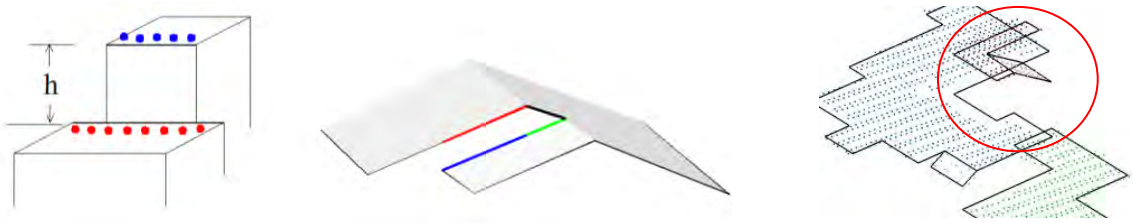

(a) (b) (c)

Figure 4.14: Extraction of step-edges: (a) step-edge detection strategy; (b) oblique step-edges; and (c) generation of polygonal step-edges.

4.1.8 Roof topology graph (RTG) construction

Based on the ridge-lines and step-edges, an RTG is constructed. According to the definition of RTG described in Chapter 3, each graph edge represents the topological relation between two segments. Basically ridge-lines and step-edges are the two possible relations that the graph edge allows, while each node in the graph represents a specific roof face (segment). With this definition, the identified roof segments and the status of extracted feature lines (ridge-lines and step-edge lines) are stored in the RTG representing individual buildings, by assigning segment numbers and a label to graph nodes and their connected edge, respectively. Figure 4.15 shows how constructed RTG indicates the topological relations between segments.

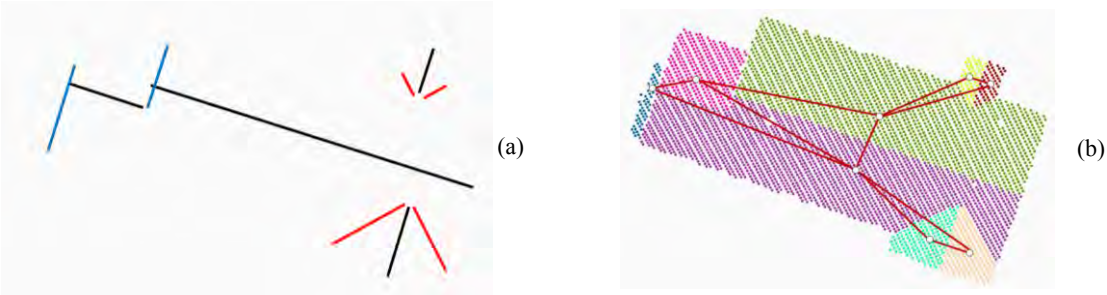

(a) (b)

Figure 4.15: Feature lines and their corresponding RTG: (a) intersection lines and step-edges; and (b) RTG overlaid on planar segments (black – horizontal ridge-lines, red – oblique ridge-lines, blue – step-edges, and brown – graph edges).

4.1.9 Rectilinear line fitting for roof outlines

Defining an accurate roof outline is necessary for effective building modeling. Boundaries of a complex building might be more irregular than a simple rectangular shape. Although point clouds are sparsely distributed, they are capable of representing major irregularities. Extraction of boundary points from the roof segments and fitting rectilinear line segments, maybe by using least squares theories, enable to represent those irregularities of the roof outlines. By obtaining a triangular irregular network (TIN) for a segment and performing a 3D contouring, edge points can be extracted. Point

extraction can be done either as per segment or per building (cluster of segments) at one time. The first case deals with both inner and outer edge points whereas the latter case deals only with the outer envelope of connected roof planes. Since most of the inner-boundary segments are already extracted in the course of previous sections, outer-boundary points of the connected roof segments are extracted using contouring (e.g. Figure 4.16). Special care is taken to recover concave outlines, as for a detailed representation of a building boundary it is vital to extract each boundary edge. This is achieved considerably by eliminating the long TIN edges as shown in Figure 4.16(b). Besides, obtaining the 3D contour along the outer envelope of the connected roof cluster, it further enables to collect boundary points of small elongated roof components which are located next to the main building (for e.g. see Figure 4.38). Since the study is also willing to reconstruct these components, the capturing of at least one edge from such buildings is important.

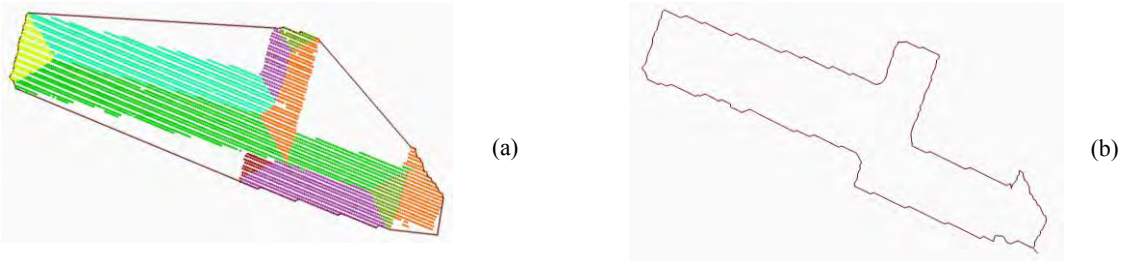

Figure 4.16: Contouring along the outer envelope of connected roof segments: (a) and (b) before and after removal of long TIN edges (planar segments are included in (a) for more clarity).

To work with individual segments, splitting of the contour into components corresponding to each roof plane is done based on the segment numbers of the contour points, which are then pulled onto the corresponding roof planes (Figure 4.17). This enables to establish 3D roof outer-boundary segments per roof plane.

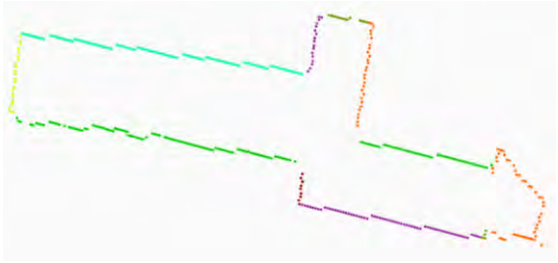

Figure 4.17: Contour segments corresponding to each roof segment (different colors indicate contour points belonging to each roof plane).

Starting from the first two points in a contour segment, a straight line is defined, which is then updated from the succeeding points of the contour until the *distance of a point to the line* exceeds a certain threshold. From the line, a line segment is later derived by identifying the first and last points that contributed to fit the line after projecting them onto the fitted line. The next line and its corresponding line segment are also generated following the same procedure in which freely oriented line segments are achieved (Figure 4.18). This enables to deliver major irregularities along the building outlines. Since two points are sufficient for defining a line and a line segment, short edges representing two points are recovered in this process.

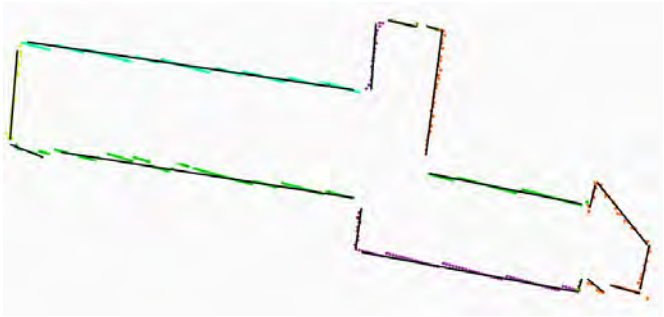

Figure 4.18: Rectilinear lines fitting for roof-outlines (black lines - fitted straight line segments without doing regularization).

Once necessary features are obtained, including straight line segments representing inner-boundaries, regularization of weakly defined edges is taken as the first task in the working flow. Because both strongly and weakly defined edges would be involved at the same time in the geometric reconstruction, more specifically for fixing boundaries or vertices. Thus, if a weakly defined edge suffers from positional and orientation errors, this yields a wrong reconstruction. For instances, if a weakly defined edge is associated with

(i) some other edges (may be ridge-lines) supposed to intersect at one point in reality – they may not intersect at a single point in the reconstruction.

(ii) an edge collinear to each other in reality – the merging of collinear edges may not be realized if the weakly defined edge undergoes some orientation and positional error.

This elaborates why regularization is important and when it should be performed. The process of regularization is explained as the first step of geometric model reconstruction (see Section 4.2.1). At this point, topological relationships between the roof segments are known and the required roof primitive features (e.g. outer-boundary line segments and feature lines) are accomplished. Thus, the new modeling approach based on the RTG is introduced without the identification of primitive roof types (e.g. hip, mansard).

4.2 Geometric reconstruction of 3D roof model

The main objective of this section is to implement the concept developed in Chapter 3, in which it elaborates how regularization and complexities can be handled by the cycle analysis concept in order to obtain geometric models of buildings. As ridge-lines contribute to most inner-boundaries of building roofs, and can be defined more precisely than other object edges, inner-boundaries are first fixed in the proposed approach. However, regularization is needed, as mentioned at the end of Section 4.1.9, prior to fixing of both inner- and outer-boundaries. In the on-the-roof object modeling, only sufficiently large objects (e.g. dormers) are considered. The entire geometric model reconstruction process is discussed by dividing the workflow into three main stages: (i) regularization of weakly defined boundary edges, (ii) geometric fixing of inner skeletons via SCC, and (iii) fixing the outer-boundary via OMCC (Figure 4.19). Further to that, handling scene complexities and dormer reconstruction steps are included to achieve more reliable outcomes. The following sections elaborate each of these steps in detail.

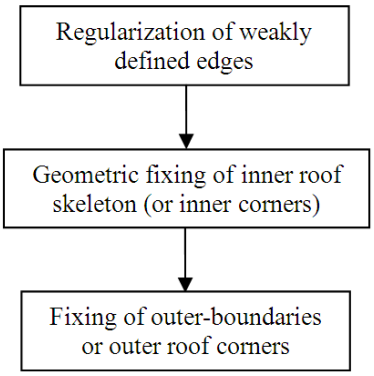

Figure 4.19: Geometric reconstructions of initial 3D roof models.

4.2.1 Regularization of boundary edges

Man-made structures usually show various symmetries and regularities. In automated reconstruction, such properties should be retained to improve the geometry of roof models. They may also be helpful by providing constraints. In this study, orientation and placement regularities are applied to weakly defined boundary features such as outer-boundaries and step-edges. The constraints can be global or piecewise, and depend on how dominant horizontal ridge-lines deviate (say by angle alpha) from each other by their relative orthogonality and parallelism, and how gutters are placed. A building may have several directions reflected by dominant ridge-lines with and without multiple gutter heights (Figure 4.20a). A similar situation can be found even in a multilayer flat roof (Figure 4.20b).

4.2.1.1 Angular regularization

1. If multiple gutter heights exist in a building roof, a uniquely oriented sub cluster of roofs with equally elevated (major) gutters can be identified by partitioning an RTG via edges denoted by step-edges as indicated by broken lines in Figure 4.20(a). When adjacent to a sub-cluster, a flat roof is assigned to the identified direction of the sub-cluster.

2. If there are no height jumps, but are having more than one directional horizontal ridge-lines in a building roof, for instance in Figure 4.20(c), then each horizontal ridge-line can be considered the dominant direction for its direct adjacent roof planes (or roof sub-cluster) and consequently for their associated gutters or eaves.

3. In the case of an isolated flat roof, the longest boundary can be taken as the dominant orientation (Figure 4.20b).

To rectify orientation errors for outer-boundaries and step-edges of each sub-cluster, orthogonality and parallelism constraints are then enforced with an angular threshold (say angle beta) for the identified directions.

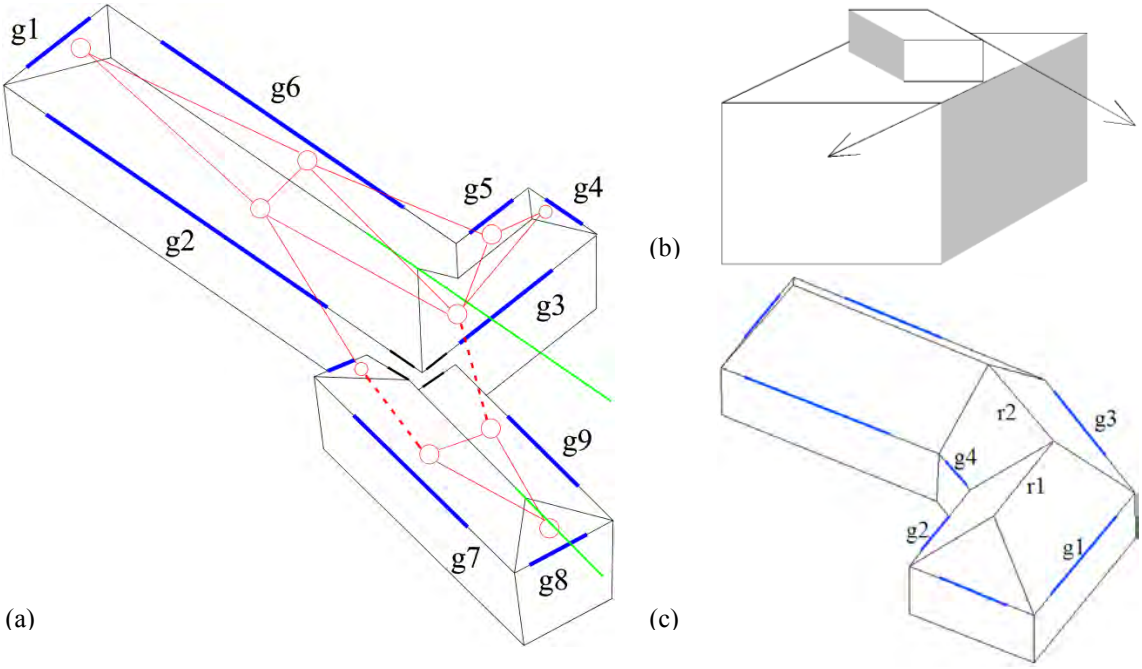

Figure 4.20: Multiply oriented buildings: (a) unique sub-cluster having equal gutter and orientation given by splitting RTG; (b) multi-level flat roof having multi oriented layers; and (c) multiply oriented connected roof model (green lines – building sub-cluster direction, red lines – RTG, dash lines - step-edges, blue lines – gutters).

In regularization of outer-boundaries, resulting line segments obtained in Section 4.1.9 are directly used. They are rectified by rotating their mid-points until orthogonality or parallelism is met with respect to the identified direction. Otherwise the original line segments are maintained. End-points of the rectified line segments are approximated by projecting original ends to the new lines. As a result of regularization, sometimes closely located parallel line segments would yield along some boundaries. The closely located consecutive parallel line segments are then merged by means of introducing a line simplification step that further reduces the underestimation of building boundaries.

In the simplification, line segments near the roof segment centroid are always replaced by parallel outer line segments. The objective of choosing the outer edge is to compensate underestimation caused by least square line fitting and uncertainty arising due to the sparsely distributed point nature. For instance, if three parallel lines A, B, and C represent a gutter for a roof plane with A and B within a defined threshold distance and C outside (Figure 4.21), A is replaced by extending B while C remains in its original position. Then a new perpendicular line is added to the end of the modified B to produce a complete outer-boundary by successive line intersections.

Figure 4.21: Outer-boundary simplification: (a) outer-boundary segments after regularization and (b) simplification. (Solid lines – outer- boundary segments, dash lines - the shortest distance between respective edge and segment centroid).

The same orientation rectification method is adapted for step-edges. The parallel line segments of a polygonal step-edge, however, are simplified using a pipeline-like concept. For instance, if A and B

are parallel and enclosed by a pipeline of width *d*, the two lines will be replaced by a line passing through the pipeline's center, and new terminals will be the perpendicular projection of the previous ends (Figure 4.22). The non-parallel consecutive line segments (lines B and C) should also be intersected to get exact corner points within the edge. The bottom edge will be reconstructed by the projection of upper edges. Consequently, multi-layer flat roofs appearing as polygonal step-edges can then be accurately reconstructed with fine detail (e.g. Figure 4.23). Since step-edges are common for two roof planes, to optimize the placement regularization of step-edges, the center line of the pipe-line is used in this study.

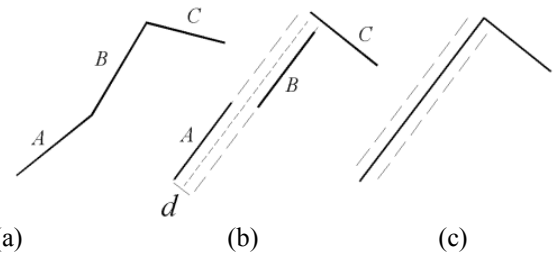

Figure 4.22: Pipeline-like concept for simplification of a polygonal step-edge: (a) a polygonal step-edge extracted by least square fitting; (b) orientation regularization; and (c) simplified polygonal step-edge with major irregularities preserved.

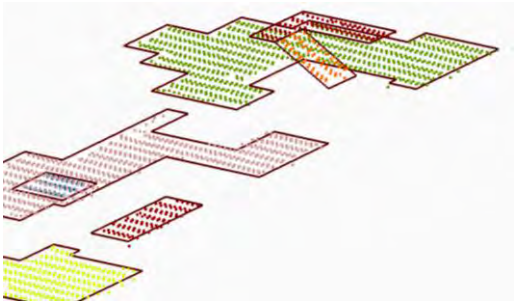

Figure 4.23: Multi-layer flat roofs appearing as polygonal step-edges are properly derived.

4.2.1.2 Placement regularization

Apart from the above rectification, positions of horizontal gutters should be maintained in placement regularization. This issue can also be addressed as maintaining the gutter symmetries. From a recognized roof sub cluster, only the longest horizontal gutter line of each side, whose height falls into a certain height range, is selected (g1, g2, ..., g6 in Figure 4.20(a) and g1, g2 , g3 in Figure 4.20c) for the placement rectification. In the gutter selection, care is taken to obtain sufficiently long edges in order to prevent erroneous gutters caused by noises. The lowest height of the selected gutters is taken as the base height, assuming that this boundary represents the reality. Other gutters are aligned to the base height and assigned a label *fixed*. This enables to preserve symmetries of gutters, but according to the actual slope of the corresponding roof pair, an equal planimetric distance between ridge-line and gutter is unable to be obtained at all the times. This, of course, is acceptable.

Although step-edges are regularized mainly by direction, their positions may still not be accurate (e.g. Figure 4.24). Once gutter lines are regularized, both direction and placement, open step-edges can be aligned with fixed gutter lines by a sweeping process. Due to scene complexities, some of these sweepings are, however, designed to realize later at the time of geometrical fixing of outer-boundaries (see Section 4.2.3).

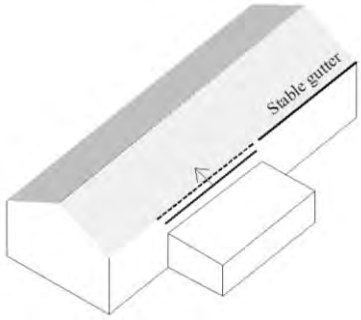

Figure 4.24: Adding placement regularity for open step-edges (dash line – correct position for step-edge, arrow indicates sweeping direction).

4.2.2 Geometric fixing of inner skeletons via shortest closed cycles

Since the reconstruction strategy of this study is to determine the position of vertices at edge intersections, the reconstruction is considered as the geometric fixing of building corners. Vertices of the inner skeleton, which consists of feature lines, represent internal 3D roof corners of the resulting building model. As described in Section 3.3, the convergence of feature lines produce these roof corners and is represented by the shortest closed cycle. Regarding the inner roof skeleton, two types of corners are found: (i) corners produced by converging ridge-lines and (ii) corners produced by converging mixed feature lines. To fix such corners, corresponding SCCs should be extracted first. This is done by decomposing the RTG into possible SCCs using Dijkstra's algorithm as shown in Figure 4.25. Graph edges in the SCC relate which feature line to be intersected and which not to be intersected. Based on the attributes of SCCs, relevant features lines are efficiently accessed from databases. The geometric reconstruction of type–*i* and –*ii* corners is done separately (see Section 4.2.2.1 and 4.2.2.2) as two different strategies are introduced for optimizing the process.

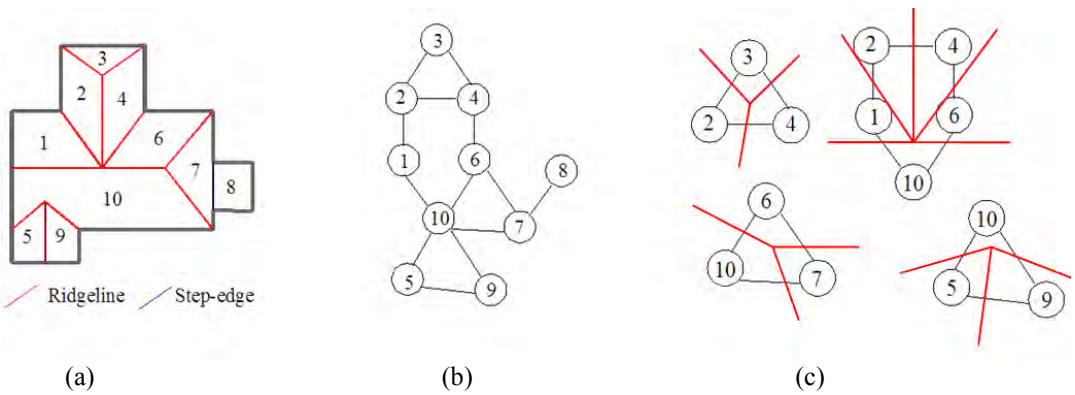

Figure 4.25: Subdivision of shortest closed cycles: (a) internal skeleton of the roof model; (b) relevant RTG; and (c) decomposed SCC and their associated inner roof corners (dark thick line –roof outline, red line – ridge lines, solid lines – graph edges).

4.2.2.1 Geometric fixing of corners associated with ridge-lines

The SCCs with edges labeled as *ridge-line* are chosen for fixing convergences solely by ridge-lines (Figure 4.26). Since the convergence produces a single intersecting point in 3D, the fixing can be considered as a weighted least square process. The intersection point produced by these converging ridge-lines is the point closest to all corresponding ridge-lines.

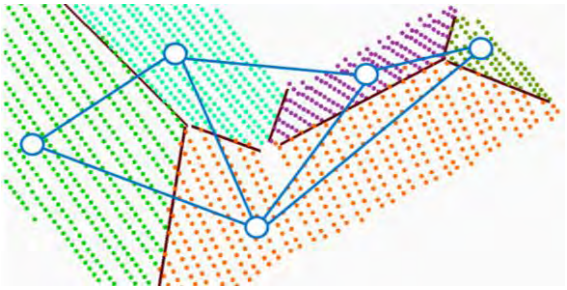

Figure 4.26: Convergence exclusively given by ridge-lines (blue lines – graph edges, brown lines – ridge-lines).

The question now is how to define the weights. Since the procedure copes with intersection lines, weight of the ridge-line should be proportional to the accuracy of the intersection line. Generally, more accurate intersection lines are given when the angle between planes are equal to 90°. Assuming the maximum weight is one (1) and weight is distributed between 1 and 0 (Figure 4.27), *sinus* of the angle between corresponding roof planes is directly taken as the *weight* of the ridge-line. The weight assignment is synchronized with the generation of intersection lines described in Section 4.1.7.

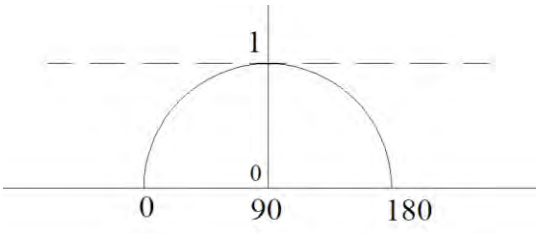

Figure 4.27: Behavior of weights against angle between roof planes. (X, Y axes represents angle between roof planes and degree of weight respectively. The maximum weight is set to 1).

The following section elaborates how an optimum intersection point c can be achieved, if m ridge-lines are assumed to converge as shown in Figure 4.28.

- **Determination of point closest to the many lines**

In order to determine a point c which is close to several (say m) lines, the sum of the square distances should be minimized.

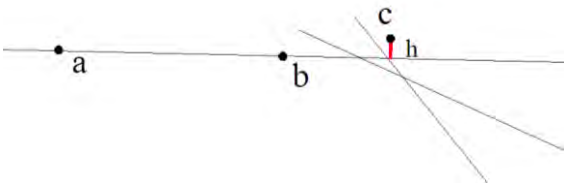

Figure 4.28: The position close to many ridge-lines that are supposing to intersect (c – intersection point, a, b – any two points on a line, h – minimum distance to a given line).

Let a, b are two points of a line and let vector $\vec{d} = b - a$, the distance h of a point c to the line is given by

$$h = \frac{\|(c-a) \times \vec{d}\|}{\|\vec{d}\|} \tag{4.2}$$

Using identity $(a \times b) \cdot (a \times b) = \|a\|^2\|b\|^2 - (a \cdot b)^2$, the Equation 4.2 can be modified as

$$h^2 = \|c - a\|^2 - \frac{\left\|(c - a) \cdot \vec{d}\right\|^2}{\left\|\vec{d}\right\|^2} \tag{4.3}$$

In order to determine the optimal c, the objective function should be minimized and by considering the i^{th} line (where $i = 0, \ldots, m$), the Equation 4.3 can be reformulated as;

$$\sum_{i=0}^{m} c - a^i - \vec{d}^i \frac{(c - a^i) \cdot \vec{d}^i}{\left\|\vec{d}^i\right\|^2} = 0 \tag{4.4}$$

With the incorporation of weights w, Equation 4.4 can be rewritten as

$$\sum_{i=0}^{m} \left\{ w^i \left[(c - a^i) - \vec{d}^i \frac{(c - a^i) \cdot \vec{d}^i}{\left\|\vec{d}^i\right\|^2} \right] \right\} = 0 \tag{4.5}$$

Let $\hat{d}^i = \vec{d}^i / \left\|\vec{d}^i\right\|$ and let $\times$ and $\cdot$ denote the cross and dot products respectively then

$$\hat{d}^i(\hat{d}^i \cdot \vec{c}) = (\hat{d}^i \times \hat{d}^i)\vec{c} \tag{4.6}$$

Let $P = \sum_{i=0}^{m} w^i (I - \hat{d}^i \times \hat{d}^i)$ and the vector $\vec{\alpha} = \sum_{i=0}^{m} \vec{a}^i$, where I is identity matrix
The Equation 4.5 can be abridged to

$$P(\vec{c} - \vec{\alpha}) = 0 \tag{4.7}$$

Which can be reformulated in matrix form as,

$$[w_i I \;\; w_2 I \ldots w_m I] \begin{bmatrix} P_1 \\ P_2 \\ \vdots \\ P_m \end{bmatrix} [c] = [w_i I \;\; w_2 I \ldots w_m I] \begin{bmatrix} P_1 & & & \\ & P_2 & & \\ & & & P_m \end{bmatrix} \begin{bmatrix} a_1 \\ a_2 \\ \vdots \\ a_m \end{bmatrix} \tag{4.8}$$

Solution of Equation 4.8 is given by the optimum c.

Therefore, ridge-line intersections which are associated with pyramid, hip, L-shape and so on, can be robustly adjusted without knowing their primitive shape types as shown in the Figure 4.29. However, the other ends of the ridge-lines which are closer to the eaves or the gutters are still necessary to be reconstructed and will be discussed in Section 4.2.3.

Figure 4.29: Geometrically fixed roof corners associated with ridge-lines.

4.2.2.2 Geometric fixing of corners associated with step-edges

In the RTG, the remaining SCCs (length > 3) refer to the corners associated with mixed-feature lines (e.g. Figure 4.30). These corners generally lie different height levels because of the availability of step-edges. The number of height levels is equal to the number of step-edges available in a given SCC. However, all those corners generally preserve one planimetric position. Since the convergence of each corner arises at different height level, as described in Section 3.3, the SCCs are split into disjointed paths and converted to *directed path graphs*. The feature lines relevant to each path are fixed separately (Figure 4.30b). Here, step-edges may produce more than one intersection point with ridge-lines or among each other (Figure 4.30c), so that an average intersection point is chosen. Further, less accurate step-edges are allowed to sweep while preserving their direction based on the influence of the ridge-lines, as highly accurate ridge-lines are fixed in the fixing process. For optimizing the fixing accuracy, the fixing process is started from the highest roof sector having at least one ridge-line. Based on this principle, the average intersection position of the highest sector corresponds to the convergence position for that cycle. The planimetric coordinates of that average position is then transferred to all the other intersection points corresponding to other path graphs, and the step-edges are shifted accordingly. By doing so, the remaining sections are fixed with respect to the already fixed section by moving the step-edges. If two or more ridge-lines exist within a section, then the intersection point given by the ridge-lines take the final average position (planimetric) for that particular cycle. Sample results in Figure 4.30(d, e) demonstrate that the procedure is more robust and leading to topologically and geometrically valid roof top vertices.

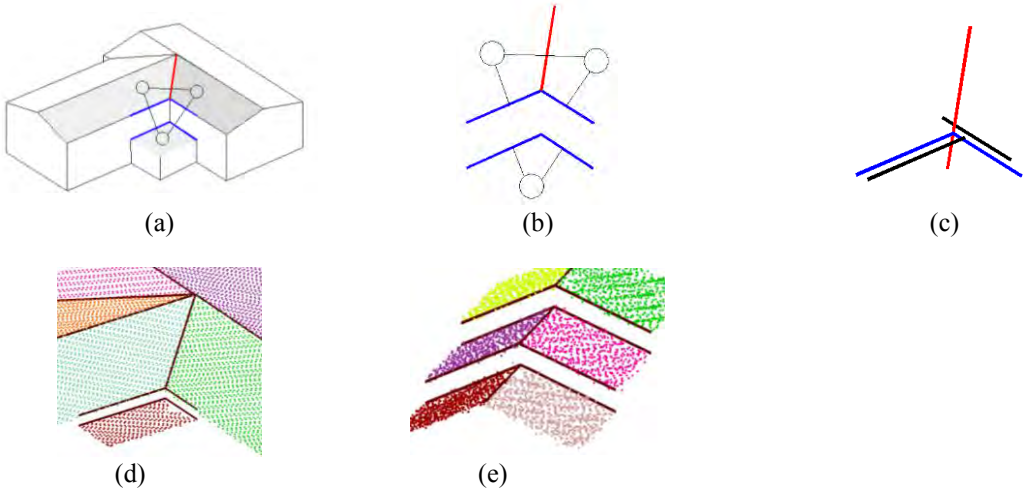

Figure 4.30: Convergence given by mixed feature lines: (a) inner roof corners associated with step-edges; (b) disjoint paths corresponding to each height level; (c) having many intersection positions leading to choose average position; (d) and (e) examples for geometrically modeled roof corners (red and blue lines are oblique-ridges and step-edges).

Unlike simple step-edges having one rectilinear line segment (with up and down edges), geometric fixing of polygonal step-edges is more complicated. For polygonal step-edges, however, proximity

relations have to be first analyzed to find the mutually closest terminal nodes and respective line segments to the ideal convergence position. The least complex feature line is initially chosen and one of its end-points is considered as the node closest to the convergence position. From that node, all possible end-distances to the other ends are computed. For instance, six end-distances are computed when three polygonal edges converge on a particular feature line as shown in Figure 4.31(a). The three nodes yielding the minimum total distance are thus taken as the mutually closest nodes to the end of that line. Similarly, the other end-point is also tested for making a decision. Among two minimum values, the node having the smallest minimum is taken. The identified pieces of the feature lines are then fixed using the same corner fixing approach as described above. Tightly fixed roof corners are obtained as shown in Figure 4.31(b).

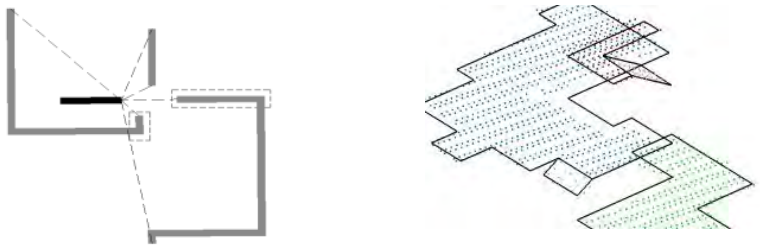

(a) (b)

Figure 4.31: Geometrical fixing of polygonal step-edges: (a) proximity relations for finding appropriate edge terminals to convergence position; (b) tightly fixed inner corners associated with polygonal step-edges.

In some complex buildings, inter-connected step-edges (edge 1-2 in Figure 4.32) can be seen within the inner skeleton. Fixing one corner (corner 2) may, therefore, affect an already fixed adjacent corner (corner 1) as the algorithm sweeps the step-edges while preserving their regularized direction. To solve this issue, each step-edge's end is labeled as *fixed* or *unfixed* once a fitting is completed. If a step-edge is found with a *fixed* label without finding the average intersection position and sweeping, *unfixed* step-edges are forced to sweep according to the fixed lines. Similarly, if many *fixed* step-edges are found at a certain corner, an average intersection is taken irrespective of the labels while restricting the sweeping.

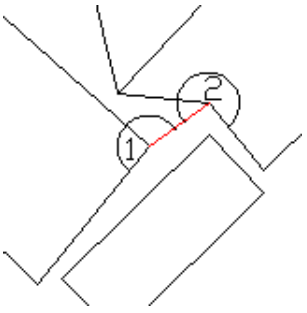

Figure 4.32: Fixing of connected skeleton edges (red line = an inter-connected step-edge).

4.2.3 Fixing of outer-boundaries via outermost cycle

Outer-boundaries of roof correspond to eaves and gutters. As illustrated in Section 3.3, some of the outer-boundaries (or gutters and eaves) meet outer ends of the inner roof skeleton. If one can recover the exact locations, where the inner roof skeleton meets the outer-boundaries, then the outer roof corners can be accomplished (Figure 4.33). However, location of gutters and eave lines should first be corrected in order to establish geometrically correct outer corners at their correct locations. Constraints on gutter symmetries, aligning of outer-boundaries by sweeping and so on can be applied to achieve

this. In the process of maintaining the roof geometries, the top hierarchy can be given to preserving the gutter symmetries because of its global look. As such, individual boundary alignments can be performed based on the preserved gutters.

Since the inner-boundaries are fixed and the gutter lines have also been regularized in terms of both orientation and placement, outer-boundaries can be fixed more stably, from which geometrically acceptable roof models can be achieved.

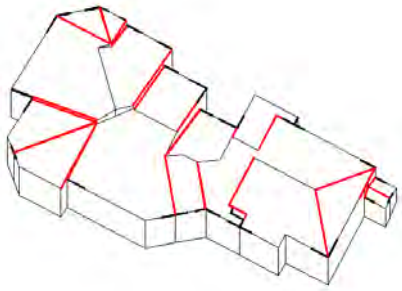

Figure 4.33: Convergence of outer edges with the inner roof skeleton (red – inner skeleton, black – outer edges that intersect inner skeleton).

If two regularized gutter lines converge, for instance on a ridge-line, as in case-II in Figure 4.35, then the corner position can be accomplished immediately by affixing the line segments, whereby the average intersection can be chosen if two convergences occur on the same ridge-line. Although the placement regularities are enforced to gutter lines, some outer-boundaries, mostly eave lines and short gutter lines, are still unfixed. Thus, it is necessary to stabilize the unstable edges by sweeping them, after which they can be affixed to inner-boundaries, with the aim of achieving a geometrically valid, symmetrically preserved closed polygon. Outer-boundary segments which are parallel and located close (< *sweeping threshold*) to the fixed gutters (e.g., g_1, g_2, g_f *and* g_3 in Figure 4.34) are chosen for the sweeping. Assuming that those edges may not represent edges at overhanging portions and belonging to a collinear edge, short edges are aligned with respect to a fixed one (e.g. g_f). Here, knowledge about the data is necessary to define a proper threshold and in this study $0.7m$ is chosen as the sweeping threshold.

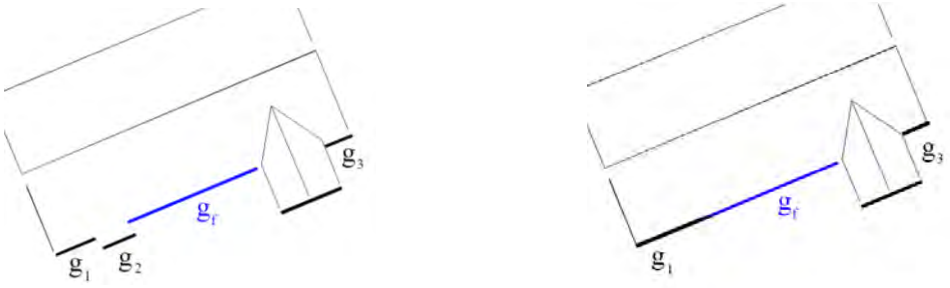

Figure 4.34: Sweeping of unstable edges to be aligned with stable edges (gutters).

Section 3.3 demonstrates that the respective skeleton edges that make the outer corners of the roof can be simultaneously extracted by the outermost closed cycle. Indeed, this enables to incorporate topological relations to the fixing of roof outer corners. Besides, OMCC permits for an efficient manipulation of outer-boundary edges at the places where the transition of roof planes arise. This is because the last and first outer-boundary edges belonging to any two consecutive roof faces always refer to this boundary transition. Therefore, with forward traversing over the OMCC, the roof outer corner fixing is effectively achieved while balancing errors. In this work, the following roof corner

scenarios are tested for validating the correct geometry. In short, two outer-boundary line segments (e.g., ***e1, e2***) adjacent to a feature line (e.g., ***f***) are required to fix the end-point of an ***f*** or a roof corner.

I. If ***e1*** and ***e2*** are labeled as *unfixed* and are positioned at a non-zero angle with respect to ***f***, the outermost intersection point is taken as the end-point of ***f***.

II. If ***e1*** and ***e2*** have *fixed* labels and are positioned at a non-zero angle with respect to ***f***, they are affixed to the intersection point.

III. If ***e1*** or ***e2*** is positioned a non-zero angle with respect to ***f***, a single intersection point is directly considered. If ***e1*** is unfixed, sweeping of ***e1*** through the intersection point is allowed.

IV. If ***e1*** and ***e2*** are labeled as *unfixed* and are parallel to ***f***, the context *beside* is tested to sweep or retain ***e1*** and/or ***e2***.

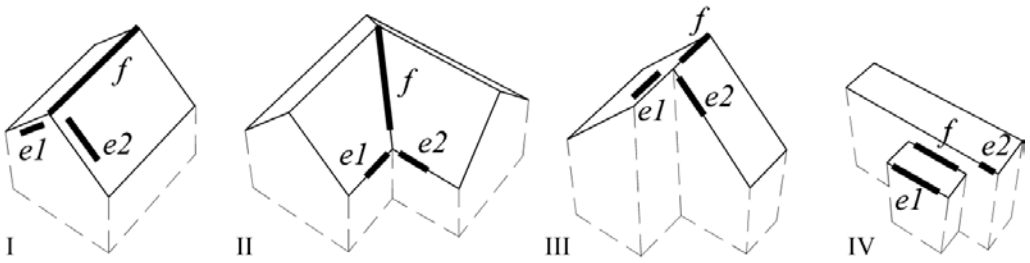

Figure 4.35: Convergence scenarios of feature line with adjacent outer-boundary line segments.

In the course of outer corner fixing, the above scenarios are first examined and fixed in 2D space because the algorithm deals with step-edges together with outer-boundary segments that belong to both up and down roofs. The z coordinate of the corresponding corner position is then computed with respect to the fixed feature lines associated to that corner in which the 3D vertex of the roof's outer corner is accurately accomplished. Besides, the algorithm is not intentionally restricted to search scenarios whose angle (between *e1-e2* or among others) is equal to 90° or 180°, so that unusual situations are allowed to be handled. However, due to regularization of the weakly defined edges, angle between *e1-e2* and *e1, e2* with *f* is often taken 90° or 180°.

After fixing the first and last roof outlines belonging to a certain roof (red lines in Figure 4.36a) remaining outer-boundaries are completed by a sequential intersection of other intermediate line segments between the fixed end lines of each laser segment as shown in Figure 4.36(b). Since the edges are now stable, this is accomplished easily. However, perpendicular short edges are inserted; in particular, when consecutive parallel edges which are not collinear are supposed to be intersected**.**

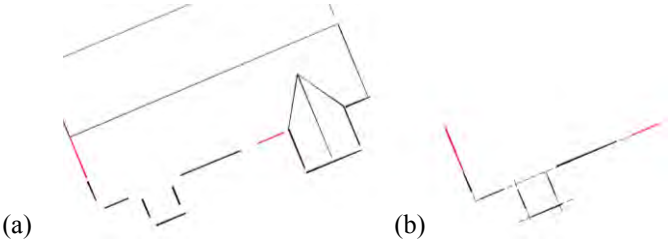

Figure 4.36: Intersection of intermediate edges leading to a completion of closed polygon.

4.2.4 Handling scene complexities

There could be situations where the above strategies are insufficient, owing to inconsistencies among parameters, assumptions and data or scene complexities. Therefore, an improvement in the above scheme is necessary and the complexities are discussed in terms of the closed cycle approach.

One of the drawbacks of point clouds is their nature of under-sampling. The extraction of outlines become much harder if there are very short boundary edges with few laser points; thereby giving rise to an inconsistency between the OMCC and the corresponding list of outer-boundary line segments. In Figure 4.37, for instance (arrow sign in Figure 4.37a), the traversing from vertex 2 to 1 in the OMCC should be referred to as outer borders belonging to segments 2 and 1 respectively. Due to the small edge from segment 1 being missing, fixing the outer-boundary lines might be invalid at this boundary transition. Similarly, traversing from vertex 1 to 3 is also invalid. Conversely, if one can traverse directly from vertex 2 to 3, the effect of missing edges can be avoided. Similarly, due to scene complexities, traversing from node 3 to node 4 is incapable of coping with adjacent outer-boundary lines referring to a particular corner. If the algorithm traverses directly from vertex 3 to 5 in lieu of vertex 3 to 4 and then 4 to 5, the relevant outer-boundary lines can be linked with two feature lines at once.

Though the issue caused by missing edge, in particular arrow sign instance, can be solved by inserting a short edge to be aligned with the dominant edge in the segment 1, the other issue cannot be solved. As such, the best solution for the above issues is to modify the OMCC by utilizing the concave cover along the outer border (for example, {1,2,1,3,4,5,4,6,1} into {1,2,3,5,4,6,1}). However, another problem may crop up owing to unrealistic graph edges (i.e. 2-3 and 3-5). This could be addressed by adopting a substitution by the existing graph edges and will be the shortest path (*i.e.* 2, 1, 3 and 3, 4, 5, respectively) to the desired end. As this path associates all feature lines relevant to the problematic corner, their convergence can fix the corner position correctly. For missing data to become a closed polygon (as in Figure 4.37c), a generalization notion allowing sweeping of unfixed edges through the intersection has to be accepted.

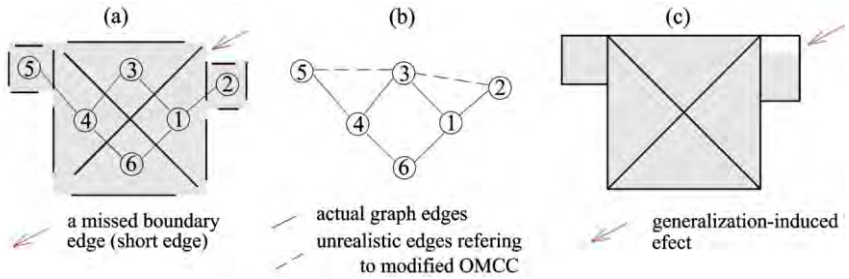

Figure 4.37: Handling data issues and scene complexities: (a) inputs for outer-boundary fixing; (b) OMCC and modified OMCC; and (c) 2d view of reconstructed model.

Additionally, other missing edges, indicated by black arrows in Figure 4.38, might occur due to a low number of boundary points. In this case, the remaining short boundary edge parallel to the gutter is recognized as an edge standing as *beside* from the gutter using contextual information (*i.e.* parallelism and overlap) and can be rectified by inserting orthogonal line segments passing through the ends of the edge.

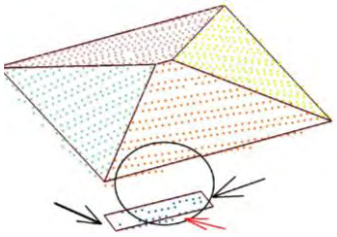

Figure 4.38: Gaps due to insufficient points residing on small roof planes.

Further, the study presents a single topological relationship via a graph edge even though both relationships exist between two adjacent planes (e.g. Figure 4.39). Although the result is an incomplete graph representation, the presented study has taken that option as single relationships often enhances computational efficiency in resolving ambiguities. To solve this issue, an additional model completion step, which links the nearest polygon nodes which are not connected by an edge, is included. This fills the gaps in each polygon caused by incomplete RTG representation. Besides, geometric constraints, such as vertical separation, parallelism and ownership of step-edges, are used to avoid confusion and predict the best reality in mixed convergences (e.g. Figure 4.40).

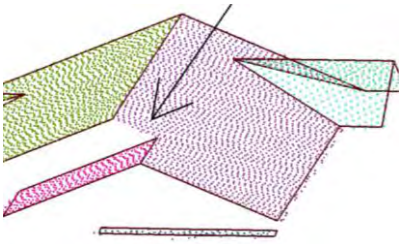

Figure 4.39: Availability of both ridge and step-edge between two roof planes.

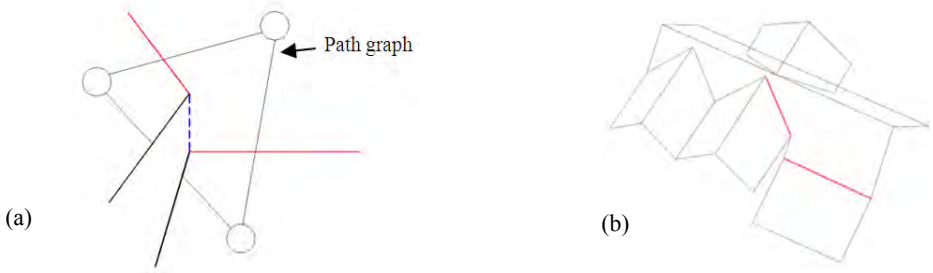

Figure 4.40: Elimination of confusion by introducing additional constraints: (a) disjoined path graphs and primitive edges; and (b) geometrically fixed corresponding roof model.

4.2.5 Dormer top reconstruction

In on-the-roof object modeling process, only moderately large objects such as dormers are considered. Small objects, such as chimneys, do not usually survive after the segmentation due to the inability to fulfill the minimum seed criterion (7 points) that has been imposed during the segmentation.

Dormers can generally be reconstructed by identifying shapes based on their primitive geometric properties. For example, rectangular shape dormers are defined by a single face with a horizontal ridge-line, while gable-shaped symmetric dormer tops are identified if three ridge-lines, including one horizontal ridge, converge on one position with two connected dormer faces. In terms of dormers having multiple faces, basic primitive shapes are investigated and primitives are sequentially reconstructed. Figure 4.41 illustrates basic primitive dormer types that this study considered. During

the reconstruction, dormer edges parallel to gutter lines are always kept inside or coincided with the gutter in case of exceeding the limit.

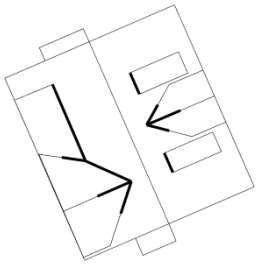

Figure 4.41: Basic dormer shapes (strong solid lines – ridge-lines associated with dormers).

4.3 Summary

As described in Chapter 3, geometric reconstruction is considered as a corner fixing problem. Feature lines and outer-boundaries produce these corners. As such, the task of this reconstruction process was to find an appropriate solution for identification and fixing of those corners correctly. The concept of cycle graph analysis was taken into account to find circles inherited from the roof topology graphs. Feature lines associated with each cycle have been used to produce such corners. Considering the inner corners of the roof, two situations were found: (i) corners produced by converging of ridge-lines and (ii) corners produced by mixed feature lines. Although the regularization step (Section 4.2.1) rectifies the weakly defined edges in terms of direction and position, they are less accurate than ridge-lines. Hence corner type–i is more accurate than type–ii. However, corner type–ii would be more accurate than corners corresponding to outer-boundaries. Therefore, one can say that errors are distributed from inner to outer.

In the reconstruction, fixing of outer-boundaries was considered as a fixing of boundary edges and roof outer corners. In order to execute an efficient feature manipulation process and to incorporate topological relations to the outer-boundary fixing, relevant roof edges and associated outer corners are proposed to be fixed in this study via the OMCC in the RTG. By fixing both inner and outer corners, the complete roof model was obtained. This cycle graph analysis method is more useful, especially when doing model reconstruction based only on point cloud data, because it is capable of correctly handling all corners associated with a building without relying on any external data source. Further, it is certainly beneficial to handle more realistic building shapes as it is not limited to given target graphs or model libraries. It has been shown in Section 4.2.4 that complex sceneries have been modeled successfully.

5. Refinement of 3D roof models

5.1 Introduction

This chapter deals with the refinement of 3D roof models reconstructed from point cloud data. In the previous chapter, a closed circle based roof reconstruction approach was presented. It is a known fact that height accuracy of ALS point clouds has already reached down to the centimeter margin ($\leq 15cm$). Figure 5.1(a) is some reconstructed building models based on the method explained in Chapter 4, and which are well fitted with benchmark reference data provided by ISPRS. The green color is because the majority of model planes correspond to low height residuals. This indicates that the vertical accuracy of the resulting roof models is adequate even for very high accuracy engineering applications. In contrast to the high vertical accuracy, a comparatively low planimetric accuracy can be seen from the resulting models. As shown in Figure 5.1(b), both false positive and negative errors may arise in roof outlines which can hardly be corrected by exploiting only the point cloud data. This issue is common to point clouds and is mainly caused due to the inherent sparsely distributed nature of the point clouds. This result shows the difficulty of obtaining accurate building models in both vertical and planimetry using only point cloud data. Contrastingly, information extracted from aerial photographs provides much better planimetric accuracy than point clouds. To this end, as mentioned in Section 1.1 and Section 2.5, the integration of images having centimeter level ground sampling resolution would lead to a high planimetric accuracy for building models derived from point clouds. On the other hand, image data integration compensates for some drawbacks of point data such as resolution issues, data gaps, and occlusion. Thus, data integration further enables to enhance the topological correctness of building models reconstructed from point clouds. Therefore, this chapter presents the integration of image data to increase the planimetric accuracy of the initial building models generated only from point clouds. In much of Chapter 5, some of the topological inaccuracies are rectified.

This chapter is organized as follows: first it gives an overview of the applied refinement method. Then it describes the extraction of linear features from images and how potential line segment candidates can be selected from the extracted line segments. This is followed by a brief quality assessment used to determine the quality of the co-registration. From the potential candidates, how corresponding image lines can be geometrically matched (correspondence matching) to construct object space line segments is explained afterwards. The strategy used to refine building models is then presented, and finally, a short summary is given.

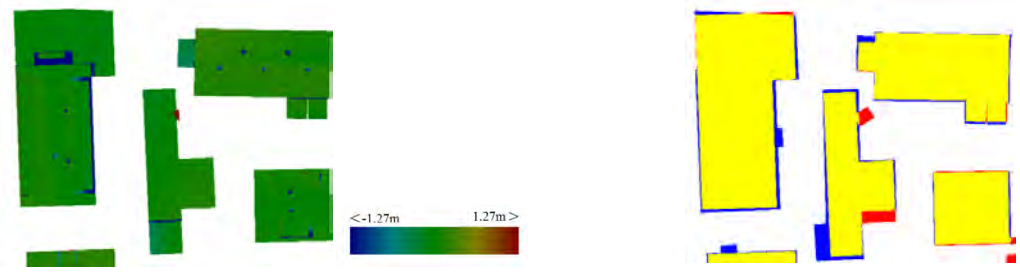

(a) (b)

Figure 5.1: Height and planimetric errors of resulting roof models derived from point clouds: (a) height error; and (b) planimetric error (blue - false negative, red – false positive, yellow – true positive).

5.2 Method overview

In roof models obtained from point clouds, the edges may have a certain displacement from their actual positions. Since edges are accurately delineated in images, in this research, image data are integrated with point clouds for the refinement of initial 3D roof models. Although data integration enhances the model quality in many ways, for instance geometry of building boundaries, segmentation of point clouds, and LoD of the resulting building models, the main objective of this chapter is to enhance the planimetric accuracy of roof outlines. In addition, rectification of defects (some) particularly relevant to topological issues in the existing models is focused as the second objective. To achieve the main objective, straight line segments are extracted from aerial images with known orientation parameters from which the initial model edges can be corrected, thus the process of co-registration is not focused in this study. However, testing of systematic errors (if any) in the given image orientation parameters are assessed prior to the boundary refinement to know whether the orientation parameters should be updated.

The working procedure can be summarized with some experimental results as shown in Figure 5.2. In detail, to find significant line segments from an image, straight lines are detected using the Burns line extraction algorithm (Burns et al., 1986). Model edges are then projected to the image space to match with the extracted image line segments. For the construction of boundary line segments in object space from the stereo (and multiple) images, this study follows the geometric relationships of line features at projective geometry as proposed by (Heuel, 2004; Ok et al., 2011). In order to minimize ambiguities which could arise in the matching process, scene constraints acquired from already derived roof models are applied.

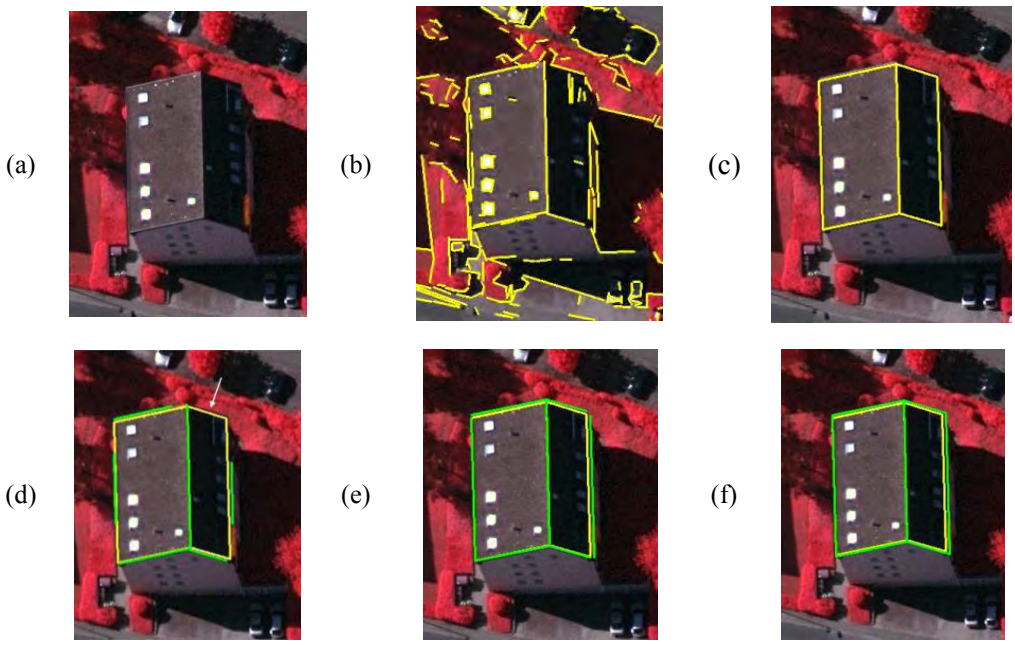

Figure 5.2: Model refinement procedure: (a) subset of original image; (b) extracted line segments from Burns line extractor; (c) projected model lines onto image space; (d) constructed 3D lines projected back on to the image space – gaps and defective lines are shown by arrows; (e) rectified boundary edges (overlaid lines on top of the image data is shown here); and (f) refined roof model – in image space (yellow – edges in initial model, green - edges in refined model).

Furthermore, defects and gaps pertaining to the boundary segments derived from the images are minimized by determining their correct behavior based on well-defined evidence. Herein, known structural arrangement of roof models and boundary line convergence priors which are specially defined to hypothesis how boundary lines behave in reality, are used. It also leads to adjust model

edges without any matching in image space, and to maintain a reasonable shape. Figure 5.3 illustrates the complete workflow proposed in the study. Note: as mentioned in Section 1.5, no refinement is made for ridge-lines.

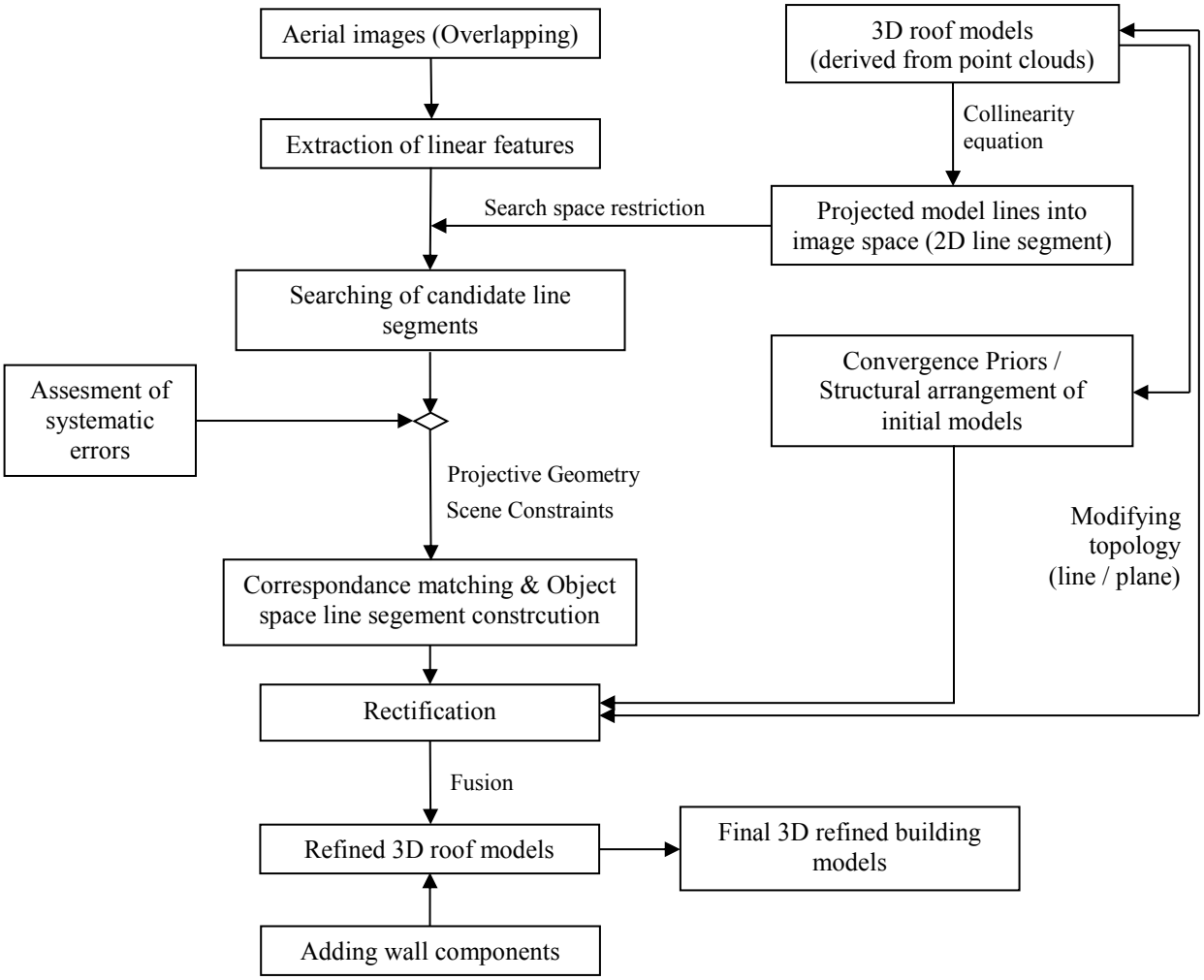

Figure 5.3: Workflow of 3D roof model refinement process.

5.3 Extraction of linear features from images

In general, sharp boundary information can be extracted from aerial photographs. To automatically extract straight line segments from aerial photographs, the Burns line extractor (Burns et al., 1986) is used in this research. Although line extraction is done at sub-pixel accuracy, the Burns line extractor - as in other line extraction methods - gave many irrelevant line segments related to unwanted objects such as vegetation patches, road features and border of shadow regions (Figure 5.4). In addition, due to the nature of images, some desired roof boundaries may not be extracted. For example, outlines in shadow areas can hardly be detected.

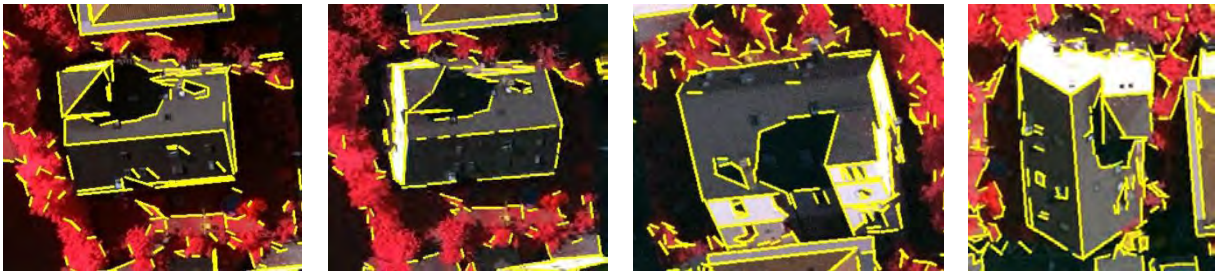

Figure 5.4: Extracted line segments using the Burns line extractor for a building taken from different images.

However, the line extraction method works in the context of weak evidence and does not consider relevant or correct line segments. Therefore, to minimize the influence of these problematic issues, instead of restricting the line extraction only for desired lines, all line segments are extracted, and then the most probable candidate lines for each boundary lines of initial models are selected during the correspondence searching (Section 5.4).

5.4 Searching of candidate lines

Although the roof models derived by point clouds are not accurate enough planimetrically, they are still good approximations for reality. This means that they can be treated as guides for finding corresponding roof boundary lines from the image. This can be achieved through the integration of data. Therefore, to find the image lines corresponding to the roof boundaries, both image lines and object lines should be compared either in the 2D image space or in the 3D object space. Since projecting an object from 3D to 2D is much easier compared with computing the 3D positions of an image pixel, corresponding searches can be done in image space. Thus, initial model boundaries are transformed to line segments in image space by projecting the 3D line segments onto the 2D image space through the collinearity conditions. This enables to integrate the model information to the image information. In the projection process, each rectilinear edge of an initial roof model is considered as a pair of end-points. For example, to project the gutter PQ in Figure 5.5 onto the image space, collinearity equations (Equation 5.1) are used, along with known exterior and interior orientation parameters. The object space point $P(X, Y, Z)$ is then transformed onto the camera coordinate system $p_c(x_c, y_c)$.

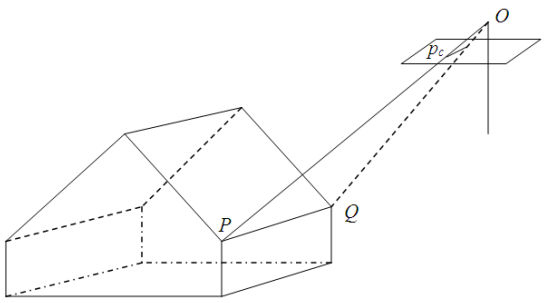

Figure 5.5: Projecting an object space point onto camera system.

$$x_c = \rho - f\frac{r_{11}(Z - Z_0) + r_{21}(Y - Y_0) + r_{31}(Z - Z_0)}{r_{13}(X - X_0) + r_{23}(Y - Y_0) + r_{33}(Z - Z_0)}$$

$$y_c = \sigma - f\frac{r_{12}(Z - Z_0) + r_{22}(Y - Y_0) + r_{32}(Z - Z_0)}{r_{13}(X - X_0) + r_{23}(Y - Y_0) + r_{33}(Z - Z_0)} \quad (5.1)$$

Where: f is the focal length of the camera, (ρ, σ) are the camera coordinates of the principal point, R=(r_{ij}) is the rotation matrix, and (X_0, Y_0, Z_0) are the object coordinates of the projection centre.

In the second step, internal camera model and the interior orientation parameters are used to transform the camera point p_c onto the image space pixel coordinate system (r, c) as given in Equation 5.2.

$$c = c_0 + \frac{x_c}{\Delta}$$
$$r = r_0 - \frac{y_c}{\Delta} \tag{5.2}$$

Where: Δ is the pixel size of the camera and (c_0, r_0) are centre coordinates of the projection in the pixel coordinate system.

The extracted line segments from images (let's introduce potential extractions as candidates) and the model edges projected onto the image space (let's introduce them as references) follow the same pixel coordinate system, which leads to the computation of their mutual geometric relationships.

For each model line segment projected into image space, all lines obtained from the image should generally be compared to find the corresponding image line segment. It is rather difficult due to the availability of irrelevant image lines. One way of reducing the noise lines is to limit the search space into a narrow corridor in which an efficient data manipulation can also be realized. In point matching processes, the basic strategy is to use epipolar geometry *i.e.* epipolar lines to restrict the search space and to get proper correspondences. But in the case of line matching, epipolar lines cannot be defined. However, epipolar beams demarcating the area bounded by two epipolar lines passing through the end-points of a particular line segment can be defined, when searching correspondence from the second (or another) image. Nevertheless, instead of having an ideal line segment and the possibility of reaching several fragmented line segments as an outcome of the line extraction, the procedure of the epipolar beam for space restriction would be impractical. Further, it may be computationally expensive. Thus, an alternative strategy would be more appropriate.

For defining the narrow buffer zones, guidance can be taken from reference line segments. Practically, defining a bounding rectangle along the reference line segment (red rectangle in Figure 5.6a) is time consuming due to the necessity of rotating the image space to be compatible with rectangle axes. As such, a capsule shape buffer is introduced with respect to each reference line segment (Figure 5.6b). The benefit of introducing a buffer having curved shape ends is that it enables the testing of an end-point, for example point $C1_s$, falling neither inside nor within the area of the capsule, using a simple geometric measure. This shortens the processing time significantly when compared to computing bounds of a rectangle. The geometric measure, *i.e.* distance to a point from a line segment, can easily be computed to accept a line segment extracted from an image, to be as a potential candidate. Herein, accepting a line segment based on the position of a single or both end-points would be an additional criterion, which basically depends on the type of the reference segment in which it corresponds to either the outer-bound line or a ridge-line.

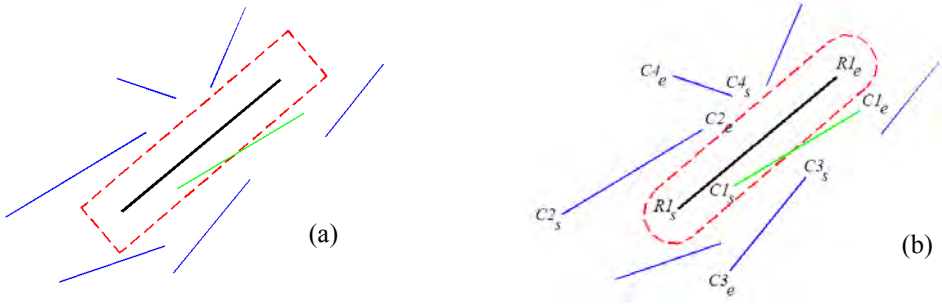

Figure 5.6: Searching of potential candidate line segments for a given reference line segment: (a) bounding rectangle along the direction of the reference line; and (b) distance measurement is enough to infer whether a line segment is falling into capsule area (dark black – reference line, green – candidate line, blue – irrelevant line segments extracted from the image).

Although the search space is restricted to a buffer zone, it includes dozens of desired or irrelevant edges. A limitation of this search process is that it can hardly find the correct corresponding image line when many similar line segments are within the search area. Due to the complexity of this scene, only the distance measure may not always be enough to accept all possible candidates. In order to optimize the candidate selection process, different geometrical measures can be used. All of the following geometrical measures have been focused in this selection process:

(i) Distance to a point from a line segment.

(ii) Angle between the reference line segment and a line segment extracted from an image.

(iii) Coverage given by the candidate on to the reference.

During the candidate searching, narrow and wider buffer widths (e.g. 5, 10 pixels) have been chosen for a reference corresponding to a ridge-line and an outer-bound (including step-edge) line segment respectively. Basically, reference ridge-lines are more accurate and should be coincided with the ideal image candidates. Based on this idea, in the selection of candidates related to ridge-lines, it is an obvious fact that the width of the buffer should be as narrow as possible. It should also be noted that ridge-lines derived by point clouds are not necessary to be refined. However, mainly for the purpose of assessing *co-registering* errors, it is necessary to collect most probable candidates for each reference ridge-line.

Obviously, there are some roof outlines that do not obey orthogonality or parallelism constraints (*i.e.* $\pm\delta$ angle deviation) with the dominant building directions (e.g. Figure 5.7). During the initial building reconstruction in Chapter 4, outlines are fixed by assuming that most of the buildings satisfied this constraint. As a result, candidates would not necessarily be always parallel to the reference. As such, the angle between the reference and candidate is tested for giving a provision for such edges, and also to filter out irrelevant candidates oriented significantly away from the reference direction but falls (at least one end) into the buffer area.

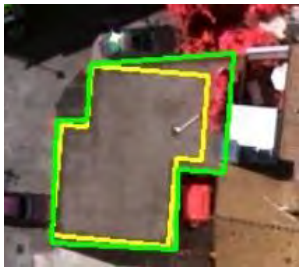

Figure 5.7: Ideal roof outlines which do not obey orthogonality or parallelism constraints (green – ideal edges extracted from image, yellow – reference line segments representing the edges of initial roof model).

Since the roof outlines derived from point clouds are good approximations for reality, they give clues about the correct shape or topology of roof outlines. Therefore, a reference and an exact candidate segment should be positioned having at least a common coverage. To cope with this, the coverage between the reference and candidate is also tested to accept best possible candidates from many line segments in the image space. The coverage is measured as a ratio between the common overlap and the length of the reference, as shown in Equation 5.3.

$$Coverage = \frac{length\ of overlap\ given\ by\ the\ candidate\ on\ to\ the\ reference}{length\ of\ the\ reference} \tag{5.3}$$

Selection of a candidate that follows all of the above criteria may mislead the ideal line matching, as two best candidates selected from a stereo pair image may not be ideally corresponding to the same object in the scene. It says that simply comparing the defined geometric measures of position, direction and coverage is not sufficient. This turns out that all potential candidates are needed to be collected, and allowed to select correspondences through some kind of a further matching process.

For optimizing the data manipulation and also the matching process, the selected candidates are treated in a different manner and stored accordingly. If a reference is corresponding to an outer boundary of a roof, the selected potential candidates are sorted with respect to (signed) the distance between the candidate and the reference, starting from the far most candidate line. Here, displacement of the candidate from the mid-point of the reference is taken and candidates that are falling into the projected roof polygon are taken with a negative sign, whereas the outsides are taken vice versa. For instance, the displacement $OM_2$of the candidate *C2* is computed as in Figure 5.8(b). Because one important phenomenon that this study recognized is that building outlines derived from ALS point clouds are often subjected to a little shrinkage, or an underestimation, than those in reality (e.g. Figure 5.8a). In general, this happens when rectilinear line fitting is done for edge points using the least square process (Vosselman, 1999). For that reason, it is beneficial to give higher weights to distant candidates, *i.e. descending sorting,* for instance, candidates {c1,c2,c3,c4} in Figure 5.8(b) could be sorted as {c3,c2,c4,c1}. This enables to achieve ideal roof boundaries (object space) more easily from candidates with higher weights in subsequent matching process.

Apart from that, when a reference is corresponding to a ridge-line, the candidate that is closest to the reference and gives the maximum coverage may probably be the ideal candidate. To this end, votes are assigned to the selected candidates in a way that they are inversely proportional to the distance (unsigned) and proportional to the coverage. When a reference is going to represent a step-edge, the edge which is corresponding to the upper step-edge is exclusively considered and is treated similar to an outer-boundary. This is because the step-edge is just the outer boundary of the roof for the upper roof. Therefore, the ideal selection may be the distant candidate, but consideration of the coverage may also be advantageous. Down step-edge can be obtained later, after the refinement of the upper step-edge's object space line segment.

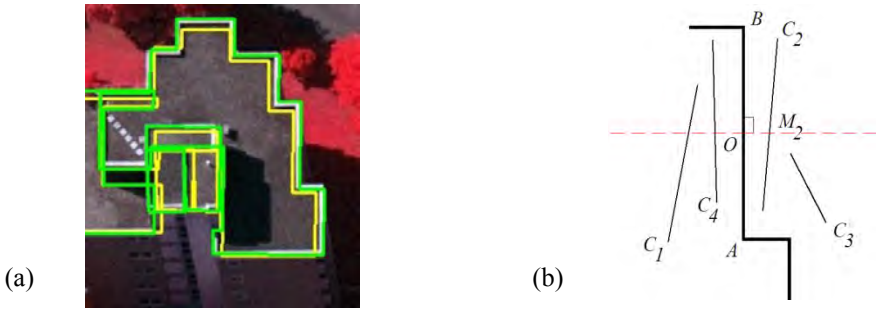

Figure 5.8: Underestimation of initial building models and measuring displacement on image space: (a) initial model edges and ideal roof outlines are overlaid on top of the image data; and (b) measuring displacements of candidates from a reference (yellow – projected model lines, green – selected best candidates, dark black –the reference, red - orthogonal line passing through the midpoint of the reference AB).

After collecting the potential candidates and their prioritizing using one of the above methods, the sorted candidates are stored as a list of line segment numbers, including estimated distances. This provides a neighborhood list similar to the one given by the r-tree (random tree) data structure for a particular reference line segment. This technique further assists for an efficient database handling, and also for designing robust algorithms. Having a sorted list of candidates for each image, for a particular reference, the next step is to match the correspondences. For each reference, all lines obtained from different images are compared.

Continuing the procedure, sometimes for a given reference, especially corresponding to an outer boundary, two nearly parallel candidates that have been chosen from two lists of candidates belonging to two different perspectives (stereo image pairs) may not correspond to the same roof edge in the scene or object space (e.g. Figure 5.9). This is because the image lines are not actually located on the same plane or elevation in the object space, even though they have similar orientations or lengths in the image space. As such, it will be more beneficial if the correspondences can be found on the object space rather than analyzing them in the image space. To find out correct lines in the object space, 2D candidate lines extracted in images based on a reference line are transformed to line segments in the object space (3D) by back-projecting the 2D line segment on to the object space. Detailed explanation of this process is given in Section 5.6. However, before doing this process, it is first necessary to analyze the accuracy of co-registration because if the two data sources are not properly registered, then the EO parameters should be updated.

Figure 5.9: Difficulties of selecting corresponding candidate line segments from different images: (a, b) results of line extraction of first two images and (c) ideal line segment representing the correct roof outline in the image space (white boxes indicate the desired edge and probable candidates which are nearly parallel to the line of interest, yellow – potential candidate with other unwanted line segments, green – ideal roof edge).

5.5 Quality assessment of co-registration

Prior to the continuation of the procedure, it is first necessary to know whether the image information is sufficiently registered with the point clouds. Otherwise, image orientation parameters should be updated. At this stage, one could select the most potential candidates relevant to ridge-lines from the image space. They would be given roughly by the first candidate in each sorted list, so that a qualitative assessment about the co-registration can be done in the 2D space.

If both data are properly registered, reference ridge-lines and their corresponding best candidates should be coincided, or at least closely located parallel to each other because of the lesser uncertainty of the ridge-lines. On the other hand, error vectors belonging to each line-end should be zero when there is no registration error. Although corresponding line pairs are exactly coincided (if there is no error), their lengths from each other are not equal. It is mainly because line extraction algorithms generally produce many fragmented lines based on the contrast conditions or due to occlusions and shadows.

Due to the length difference between the reference and its corresponding line, the estimation of dependencies of a line-end in the X, Y direction is done instead of estimating the error vectors of each line-end. For instance, if R_sR_e is chosen as a reference of the scene (Figure 5.10), then the deviation of each end-point of the selected candidate line segment (e.g. C_s and C_e) - with respect to its corresponding reference end-points (e.g. R_s and R_e) - is assessed in the X and Y direction. Finally their patterns are recognized as shown in Figure 5.11.

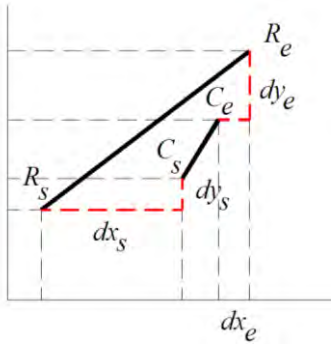

Figure 5.10: Dependencies of line ends in X and Y direction (dx_s, dy_s and dx_e, dy_e are deviations at respective end-points in X and Y direction).

The end-points of each selected candidate lines differ from end-points of their reference line with small deviations in both the X and Y direction as shown in Figure 5.11. According to the obtained error differences or error patterns, it can be assumed that no significant systematic errors exist. It illustrates that the updating of orientation parameters is not necessary. Therefore, the boundary refinement procedure can be continued. If large deviations are found, and then the EO parameters should be recalculated, for instance using the method proposed by (Wang and Tseng, 2002) and should reassess the new quality.

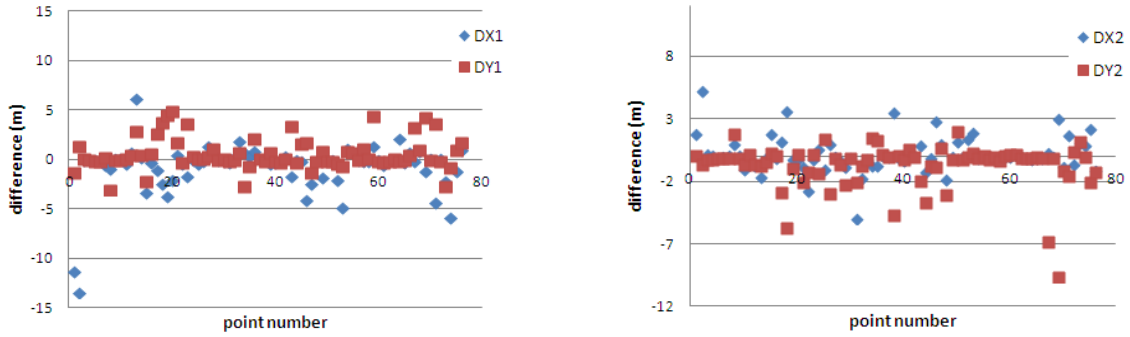

Figure 5.11: Dependency of each end-point in X, Y direction (DX_1, DY_1 - Differences of end-point_1 in X, Y direction).

5.6 Correspondence matching and constructing object space 3D line segments

In order to construct an object space line segment (3D) for a given reference, it is first necessary to find corresponding candidates from the stereo pair images. In the case of multiple images, one way to perform this is to match candidates, relevant to two successive images at a time, geometrically. Mathematically, matching 2D linear features and finding correspondences can be treated as a stereo (and then multiple - once redundant planes are avoided) plane intersection problem. To cope with it, the necessary planes in projective geometry could be derived from viewing rays passing through the end-points of corresponding line segments located on the image space (Figure 5.12). Intersection of two planes generated by such viewing rays produce a precise 3D line. It enables to obtain a required 3D line corresponding to the same object in the scene if the geometry of the 3D line can be ensured with the geometry of the scene.

Based on the projective geometry, how the plane intersection can be achieved in a homogeneous vector space is illustrated by (Heuel and Förstner, 2001) and (Heuel, 2004; Ok et al., 2010b). However, in this research, Euclidian coordinate space and the intersection of two or many planes are done to reconstruct object space line segments. Each step of the object space line reconstruction process is described in the following sub sections.

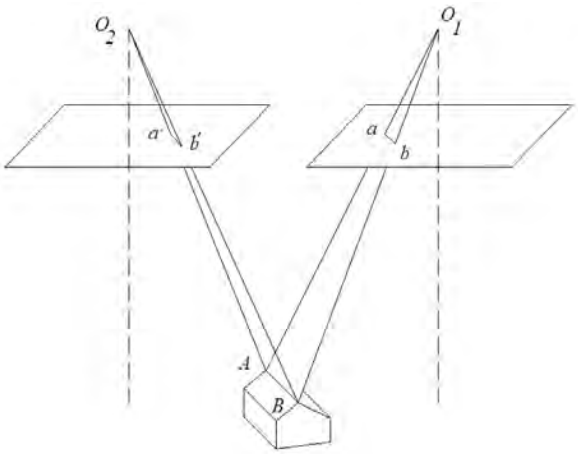

Figure 5.12: Back projecting the viewing rays (a, b and a′, b′ represent the object AB in image space).

5.6.1 Avoiding weak viewing geometries

Given that the intention is to construct viewing ray planes and intersect one with the candidate planes of the second image, different strategies could be followed to optimize the quality of matching correspondences.

Since the process relies on the projective geometry, the selection of an optimum geometric scenario could be given the ideal correspondence, or the one which is very close to reality. Accuracy of 3D lines constructed by the intersection of planes relies mainly on the accuracy of planes and the relative angle between each plane. A viewing plane is created based on the plane normal derived by taking the cross product of viewing ray vectors and coordinates of the projection center. As such, accuracy of planes may generally be equal to each other but their relative angles are different. To this end, in order to perform a precise plane intersection, images leading to weak (small mutual angles) geometries should be removed. For this, angles between each viewing plane and the roof plane are first estimated. Besides, images whose viewing planes produce a small angle with the adjacent images' viewing planes (or roof plane) are identified as images having weak geometries. By doing so, images (O_1 in the example case shown in Figure 5.13) leading to weak geometries, from the list of images contributing to the viewing plane intersection, are avoided. When computing angles with respect to the roof plane, there are various ways to determine incident angles relevant to each image holding non-empty candidates. The precise method is the computation of actual angles relevant to each viewing plane in each image. But the more efficient method is to compute angles relevant to vectors produced by each projection center and an end-point of the corresponding initial roof outline (e.g. O_3P). In this study, the second method is adapted to increase the computational efficiency.

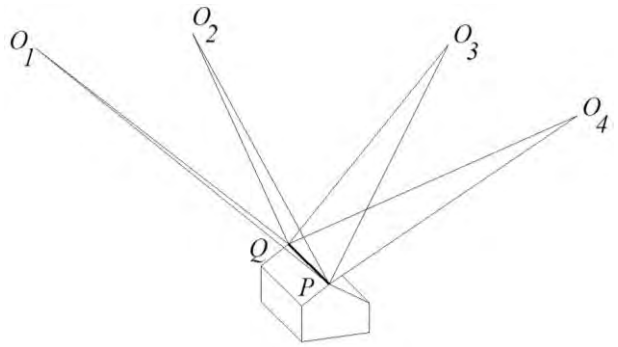

Figure 5.13: Determining weak geometries (O_1, ..,O_4 - projection centers, P – an end point of the ridge-line).

In relation to images holding strong geometries with non-empty candidates, three different viewing geometries could arise for a given reference.

(i) non-empty candidates only in a single image.

(ii) non-empty candidates only in two images.

(iii) non-empty candidates in multiple images.

In the first case, there exists only a single image but may have more candidate line segments. As such, viewing planes of each candidate in that image (Figure 5.14a) can be intersected with the relevant roof plane one after the other. The roof plane derived from point clouds is well suited for this purpose. For example, in Figure 5.14(b), ABCD and Oa`b` planes can be intersected. Dal Poz et al. (2009) followed a similar approach with *markov random field* to refine roof boundaries using a single image. The second geometry is basically an intersection of two viewing planes belonging to two stereo images (Figure 5.14c). The third scenario is more complicated and many planes belonging to more than two images have to be taken into account. A detailed explanation of matching process through the intersection of viewing planes is given in the next section.

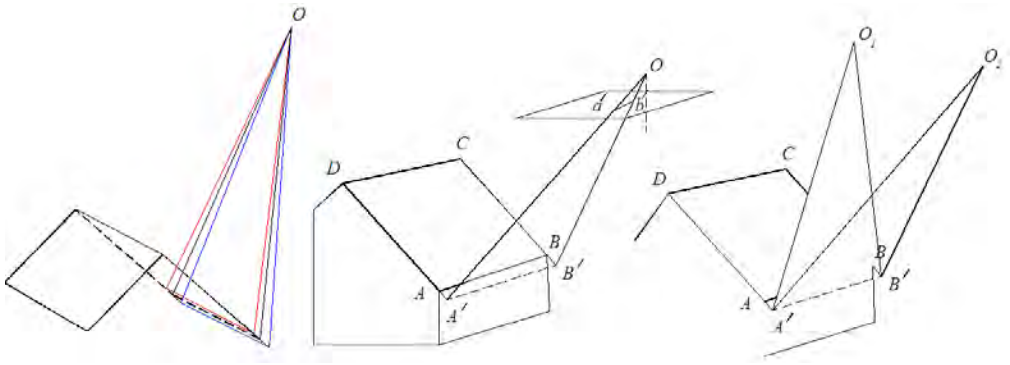

(a) (b) (c)

Figure 5.14: Different incidences of viewing plane intersection: (a) viewing planes relevant to selected candidates for a given reference; (b) intersection of viewing plane with the roof plane; and (c) intersection relevant to stereo image pair.

5.6.2 Intersection of viewing planes

The matching algorithm intersects pairs of viewing planes from a pair of images at a time, and compares the constructed 3D line with the given constraints (see Section 5.6.3 for some constraints). From all the possible candidate pairs, the best matched candidate pair or the best 3D line representing the known constraints are selected for a given image pair. Similarly, all possible image pairs are also compared one after the other through their list of candidates to find other corresponding pairs of candidates or 3D lines. In case of two images or one image with a roof plane, the constructed 3D line is taken straightaway as the goal is to construct the 3D line segment. But for multiple images, unique candidates are first chosen by removing redundancies in the selected pairs and multiple plane intersection is finally performed based on the least square theories. The process of finding the possible correspondence pairs as a nested approach is illustrated with some notations as follows.

Given n images $I_1 \ldots I_n$ of a scene and extracted candidates $C_1 = \{l^1_1 \ldots l^1_{r1}\}$, $C_2 = \{l^2_1 \ldots l^2_{r2}\}, \ldots, C_n = \{l^n_1 \ldots l^n_{rn}\}$ from these images, the problem is to find every possible pair of correspondence which satisfies the given constraints. Here, each matched pair (e.g. $l^1_i l^2_j$: in the case of matching i^{th} and j^{th} candidate in 1st and 2nd image), relevant to a given image pair (e.g. I_1, I_2: where 1st and 2nd image pair), should correspond to the same element of the scene. Though the number of all possible combinations is given by the ${}_nC_r$ relationship, where n – number of images and $r - 2$ (as the process matches pairs at a time), the algorithm doesn't always provide a similar number of combinations to ${}_nC_r$ as some image pairs are unable to match to given constraints.

5.6.2.1 Intersection of multiple viewing planes and forming a single 3D line segment

In order to determine a line in 3D, a point $p \in \mathrm{R}^3$ on that line and the vector $v \in \mathrm{R}^3$ which is parallel to the line is needed to be determined. Hence, to obtain the optimal intersection line relevant to intersected multiple planes, p and the v should be optimal, and which can be achieved in two steps.

Optimal *p*

Intuitively, optimal p could be chosen as the point that is closest to all the planes. Let $n_i \in R^3$ and $o_i \in R^3$ be the normal vector and the point on the i^{th} plane, respectively. The distance between the point p and the plane can be expressed as in Equation 5.4.

$$\left\| \left(\frac{n_i n_i^T}{n_i^T n_i} \right) (p - o_i) \right\| \tag{5.4}$$

In order to determine the optimal p, the objective function should be minimized and can be written as;

$$J_P = \sum_{i=1}^{n} \left\| \left(\frac{n_i n_i^T}{n_i^T n_i} \right) (p - o_i) \right\|^2 \tag{5.5}$$

Let P_i be denoted as $P_i = \frac{n_i n_i^T}{n_i^T n_i}$ then J_p can be rewritten as;

$$J_P = \sum_{i=1}^{n} (p - o_i)^T P_i (p - o_i) \tag{5.6}$$

Note: P_i is an orthogonal projection matrix satisfying $P_i = P_i^2$ and $P_i^2 = P_i$. Then it can be shown that

$$A^* = \left(\sum_{i=1}^{n} P_i \right)^{-1} \left(\sum_{i=1}^{n} P_i o_i \right) \tag{5.7}$$

Solution of the right side matrices in Equation 5.7 will lead to the required p.

Optimal *v*

To be the optimal v, intuitively the angle between vector v and a plane i should be as small as possible. In other words, v should be perpendicular to the normal vector n_i as much as possible. That means, the orthogonal projection of v on n_i should be as small as possible. As it is only required to determine the direction of v, it can be assumed that $v^T v = 1$. By minimizing the objective function as follows;

$$J_v = \sum_{i=1}^{n} \left\| \left(\frac{n_i n_i^T}{n_i^T n_i} \right) v \right\|^2 = v^T \left(\sum_{i=1}^{n} P_i \right) v \tag{5.8}$$

Let $A = \sum_{i=1}^{n} P_i$, which is a positive definite. By singular value decomposition (SVD), A can be written in the form of $A=UAU^T$. Hence,

$$J_v = v^T A v \geq \lambda_{min}(A) v^T v = \lambda_{min}(A) \tag{5.9}$$

Taking the Eigenvector given by the smallest Eigenvalue as the optimum direction parallel to the intersection line, the required direction v can be derived. From this, the optimum line can be achieved.

Based on these optimal v and p, a 3D line is generated. After obtaining a 3D line, to be a line segment, end-points for that 3D line segment in the object space is found by selecting the most distant two points produced by the two distant viewing rays. For instance, O_1B_1 and O_nE_n rays in Figure 5.15 give the required 3D line segment B_1E_n in the object space.

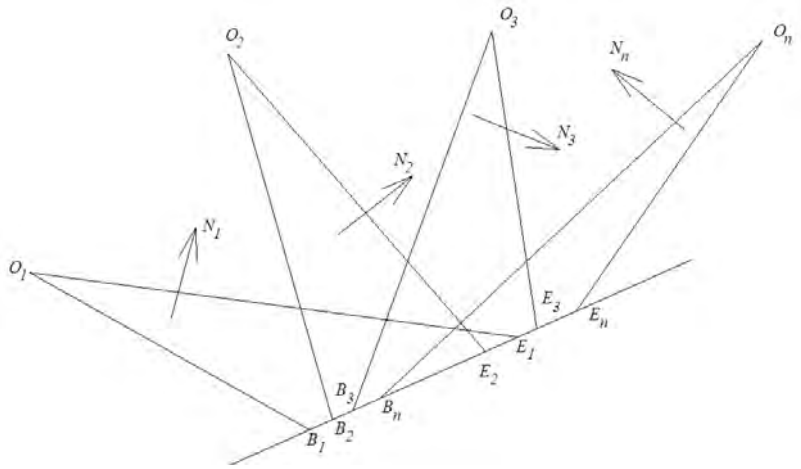

Figure 5.15: Forming a 3D line segment by the intersection of multiple viewing planes.

5.6.3 Constraints on correspondence matching

Since the strategy of corresponding candidate matching is to intersect successive pairs of viewing planes, one from each image, specific constraints *i.e.* scene constraints, are introduced for both rejecting fault matching and for obtaining optimal construction (*i.e.,* 3D line segments in object space as explained in previous section).

5.6.3.1 Scene constraints

In general, for a given reference, there exists more than one candidate for each image. From these candidates, several 3D line segments can be derived by intersecting their viewing planes as explained in Section 5.6.1 and 5.6.2. To find out a correct line segment from those derived lines, or to derive a 3D line segment from the image data, representing the ideal scene or one which is very close to reality, it is necessary to formulate well-defined constraints.

3D roof models derived from point clouds represent explicit unambiguous geometries about the scene, except for a few uncertain properties such as the planimetric positional uncertainty of roof outlines. However, the horizontality of a gutter and the degree of inclination of an eave (which is exactly equal to the slope of the roof plane) can be firmly and accurately determined with the roof models derived from point clouds. In general, the roof outlines that are horizontal could mostly be gutters, while inclined and having equal gradient to the roof plane could be eaves. Of course, from the labels, step-edges can easily be discriminated. Incorporation of these scene constraints may yield an unambiguous matching outcome. Therefore, in this work, three scene constraints are introduced to derive correct 3D lines for each reference line or roof boundary by minimizing the effect of detected wrong candidates. These constraints are defined considering the gradient, perpendicular distance and gutter symmetry.

I. Gradient

There are many incidences where un-parallel lines in the object space may appear as nearly parallel in the image space (e.g. arrow signed in Figure 5.16a and b). Also, these parallel edges in image space may not always exist on one plane in reality. Therefore, the intersection of such a pair of viewing planes produces a wrong line segment in 3D object space. Similarly, if the ideal candidate in one image may be intersected with a wrong candidate in the second image, it also causes an erroneous outcome. The erroneous constructions may be much deviated from reality (Figure 5.16c). Thus, the gradient of the desired roof edge determined from the initial model is useful to compare with the gradient of the derived line segment in order to accept or to reject the derived line (Figure 5.16d).

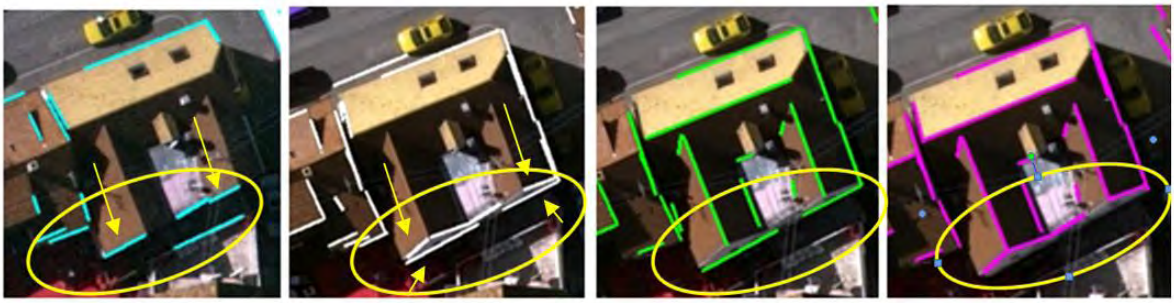

(a) (b) (c) (d)

Figure 5.16: Nearly parallel lines appeared in image space may not be parallel in object space: (a) and (b) subset of left and right images including potential candidates, (c) and (d) results of viewing plane intersection, without and with the gradient constraints, overlaid in image space respectively (yellow ellipses indicate desired edges and relevant image lines).

II. Perpendicular distance to the roof plane

Sometimes, from the closely located adjacent parallel candidates appearing in a pair of images (Figure 5.17a, b), the chosen candidate pair could be leading to a faulty result. Besides, the outcome could represent a building ground edge or another edge somewhere in a side wall, or even an arbitrary line in space, instead of the respective roof edge (Figure 5.17c). When the gradient fails to discriminate this ambiguity, the perpendicular distance to the roof plane from the midpoint of the constructed 3D line segment is used for accepting the outcome (Figure 5.17d).

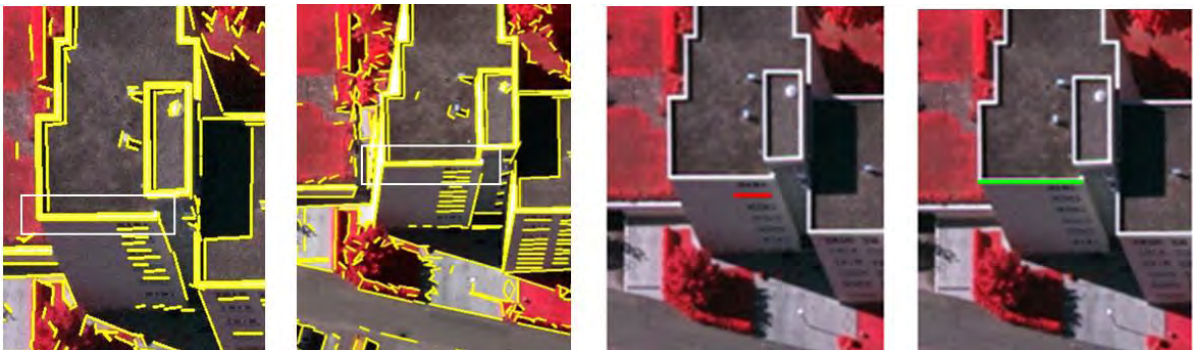

(b) (b) (c) (d)

Figure 5.17: Issues caused by selecting parallel lines: (a) and (b) selected candidates for a given reference (inside the white boxes); (c) and (d) constructed object space line segment *without* and *with* distance to plane constraints (yellow – extracted edges, red and green – constructed lines without and with the distance to plane constraint).

In addition to the above scene constraints, the stored distance (displacement of candidate from the reference) of each processing candidate is also compared with the counter candidate in the other image. Since in the ideal case, their relative displacement from the reference may not be too large, the displacement constraints are set less than half the width of the capsule buffer that is used to detect the candidate lines.

Given that there could be many constructions satisfying the above given constraints, a weight is assigned to each selection and the one which is given the smallest weight is taken as the best line. Here, the weight is directly proportional to the candidates' indices and the gradient difference. As candidates are already prioritized, one of the first few candidates from the list of candidates relevant to

each image should contribute to the ideal correspondence. Additionally, the least gradient difference should be given by the ideal construction. Therefore, the one which follows both criteria are chosen.

III. Gutter symmetries to the line feature matching

Man-made objects are often constructed with a regular shape having symmetric properties. In general, the scale of the adjacent overlapping photographs is almost equal and measurements in image space from multiple images can be acceptable. Based on that assumption, special care is given to buildings, or part of buildings, having horizontal ridge-lines and slanted roofs with opposite azimuths, *i.e.* gable type roofs. Besides, their status of planimetric symmetry is incorporated for optimizing the matching process. For such a building, the longest gutter pair that follows approximate symmetry is recognized based on the distances between reference ridge-line to corresponding (longest) reference gutters in the image space. The distance between the reference ridge-line and each candidate is obtained afterwards by adding the recorded distance (signed distance) as shown in Figure 5.18. Similarly, for other images, gutter constraints are added and the matching process is enhanced accordingly.

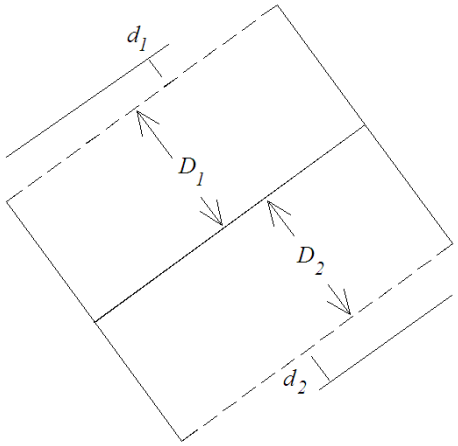

Figure 5.18: Incorporation of gutter symmetry for the matching process (D1 and D2 - gutter symmetry of initial model in relation to image space, d1 and d2 - displacement of candidates with respect to the corresponding references).

Based on those constraints and different intersection strategies, an increased effort is made to construct optimal object space boundary segments for each reference. However, factors such as poor contrast transition around the desired edge, occlusion, erroneous references, and misalignment of matching outcome with the constraints still result in many missing edges in the image space for some of the reference roof edges. Thus, it is not always possible to accomplish a line segment for each reference. Figure 5.19 shows that some results suffer from missing edges.

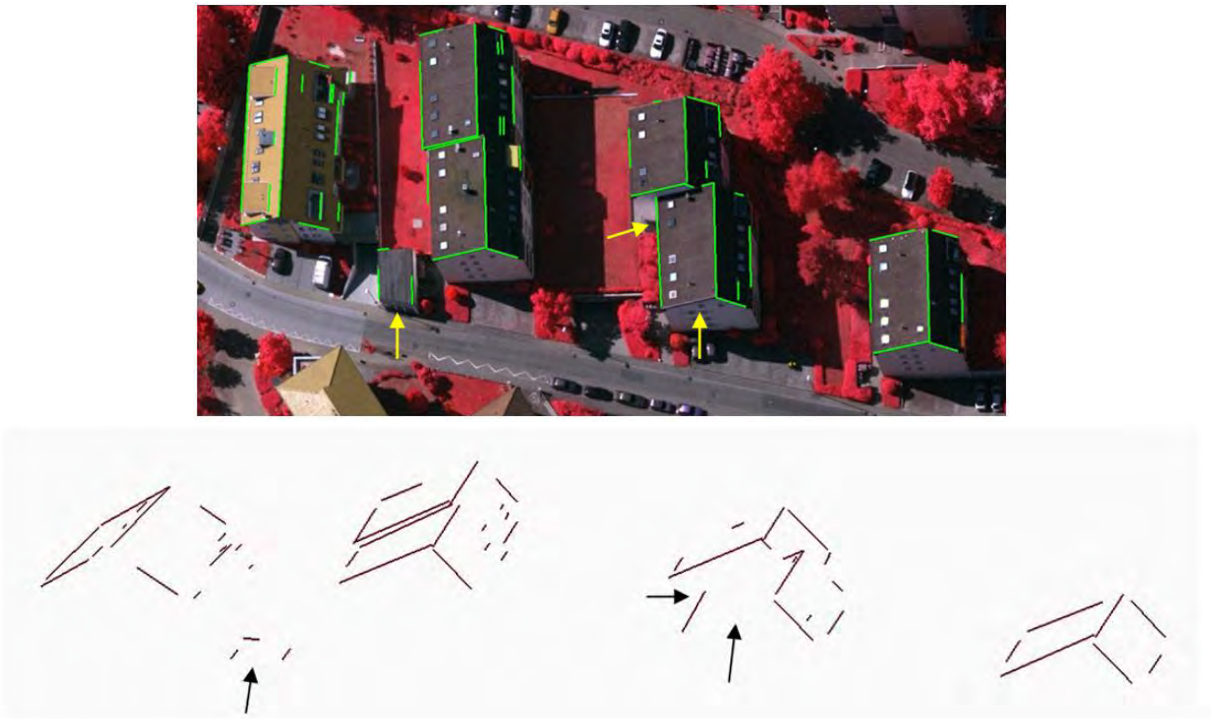

Figure 5.19: Derived boundary edges in object space: (top) derived edges overlaid onto image data; (down) derived edges as appear in 3D space (arrows indicate missed and defective edges).

5.6.4 Error assessment in 3D space

Since an object space line segment for any desired roof edge can be accomplished via image based method, further verification of *co-registering errors* can be done in 3D space. The perpendicular distance between each end-point of a line segment derived from ALS data, and its corresponding other edge derived from image data (e.g. r_1 and r_2), and vice versa (e.g. c_1 and c_2), are computed as shown in Figure 5.20. The average displacement per ridge-line is then plotted with respect to both point clouds and image data, as shown in Figure 5.21. In addition to acceptable displacements, few considerable deviations can be seen in Figure 5.21. Those higher deviations are mainly caused by exiting shadow effect along roof ridge-lines.

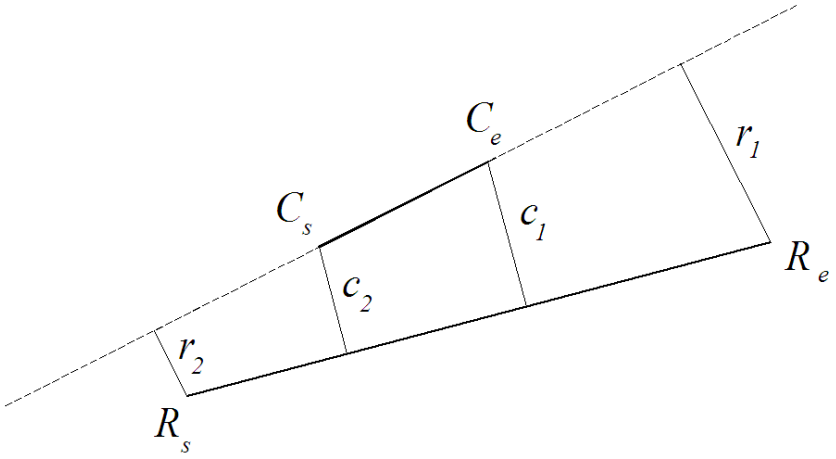

Figure 5.20: Computing perpendicular displacements from each end-point to counter edge (r_1, r_2 distances with respect to reference ends, and c_1, c_2 distances with respect to candidate ends).

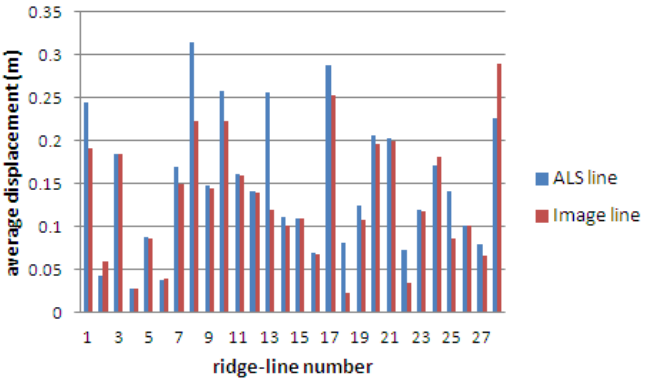

Figure 5.21: Average displacement per-line.

It is of interest to analyze how roof outlines derived from image based method behave within the orthogonality and parallelism constraints, and with existing ridge-lines of the initial roof model. Figure 5.22 illustrates that the majority of roof outlines deviate less than an angle of 3° with respect to the corresponding dominant or ortho-dominant direction. The very same phenomenon is obtained with the opposite gutter lines which are supposed to be parallel. Interactive investigation done with these outlines proved that these small deviations were mainly caused by shadow or poor contrast variation existing around the roof edges. Other higher deviations are mainly given by outlines which do not follow orthogonality or parallelism constraints. Therefore, outlines having larger deviations should be accepted while outlines having small deviations are regularized with respect to dominant directions.

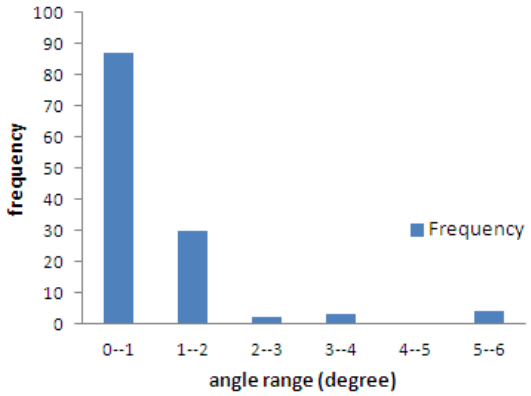

Figure 5.22: Deviation of outlines with respect to their counter parallel gutter lines (X and Y axes indicate angle intervals and number of occurrences).

5.7 The model refinement

Geometrical refinement of a roof model can be achieved by refining the planimetric accuracy of roof outlines and roof topology. With the help of matching processes, as described in Section 5.6, the best matched image line (or a 3D line segment) associated with roof outlines of initial models are derived. Those model edges can then be corrected by using their best matched image lines. However, some of the boundary segments constructed by the image based method may still contain some defects. One example is directional deviation of line segments due to the shadow effect. Missing line segments can also be seen relevant to some model edges defined by images. For a successful refinement of a building model, these issues should be overcome. With the aim of minimizing such defects and filling missing boundary edges, an additional step (Section 5.7.1) is introduced as an initial process of the model refinement to rectify the model edges derived from images.

5.7.1 Rectification of image line segments (3D)

The main objective of this step is to identify: (i) *missing* and (ii) *defective edges* in the result of 3D line segments constructed from image data, and then to rectify those issues enabling them to best represent reality. From labels assigned at the time of constructing image based 3D line segments, the reference lines relevant to missing edges can be recalled. The question, however, is how to construct accurate line segments for the edges without matched image lines. As such, well-defined evidences are necessary in making decisions. Otherwise, partly accurate edges and even strange shapes could arise. In this case, the known structural arrangements of roof models which are introduced in Chapter 3 are applied to those edges. In the case of defective edges, for instance eaves having directional errors, deformed *eave and ridge-line* convergences could result (Figure 5.23). In fact, in those example cases, though the constructed eave or roof outline may be placed on an acceptable plane, its orientation (azimuth) would not fully follow the basic shape or known regularities. This is mainly because of the shadow and poor contrast existing in more than one image, which causes straight lines to deviate a little bit from reality. Thus, such scenarios can be expected. Defective edges can be found by analyzing the shape of roof corners produced through the convergence of the corresponding edges. The convergence priors, which are introduced in Section 3.4, are used to identify and to rectify defective instances.

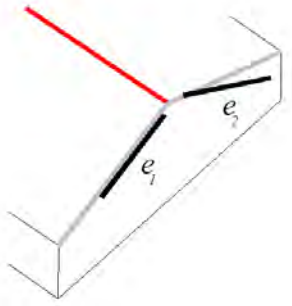

Figure 5.23: Defects of line segments derived from images (solid thick line – obtained edges from images, grey lines – building outlines, red – ridge line).

The advantage is that the priors are unambiguous, thus in the rectification process, it is not necessary to know the shape/status of an entire building. Concrete identification of a specific building part or a roof corner is sufficient to continue the rectification procedure. Besides, if the recognized corner would follow a basic constraint, that will be enough for correcting the problematic defective arrangement. One important fact in this entire rectification process is that its hierarchical means of access. First priority is given to the *gutter symmetry*, which is followed by the *arrangement of eaves*.

Continuing the explanation of the procedure in detail, when a reference which does not possess a 3D boundary segment derived from images is found; the rectification algorithm determines the edge's status based on the structural arrangement of the corresponding initial roof model and the convergence priors. Based on the status, a new boundary edge representing the best reality is inserted afterwards. Therefore, if the algorithm has found that the status of the problematic edge, for instance g1 in the Figure 5.24(a), as (i) is horizontal, (ii) has outer boundary label, and (iii) a member of the gable type roof pair following a rough symmetry, then the algorithm defines the reality for this reference in relation to the dominant gutter belonging to the opposite roof plane. If the corresponding counter gutter possesses a 3D line segment derived from image information, then a new horizontal line segment having an equal height to that known gutter (e.g. g_2 in Figure 5.24a) is installed. End-points of the new line segment are approximated by projecting the end-points of the gutter located in the initial roof model. By doing so, symmetry preservation is first accomplished for the missing edges.

Similarly, if the algorithm finds out that the problematic edge (i) is associated to a convex corner, for instance Figure 5.24(b) and (ii) is connected to two parallel gutter lines whose image based 3D edges

are available (e.g. g_1 and g_2), then a new horizontal line segment having equal height to one gutter and orthogonal to that gutter is installed to represent g_3. Since the establishment of this type of missing hip roof part is carried out after ensuring the gutter symmetries of each building, fault instances are avoided. Further to that, gaps existing in eave edges are also filled prior to rectifying the defects of edges given by the image based method. For instance, as shown in Figure 5.24(c), if reference e_1 or e_2 does not possess a 3D boundary line segment derived from images, then the missing eave is installed based on the available eave and the ridge-line.

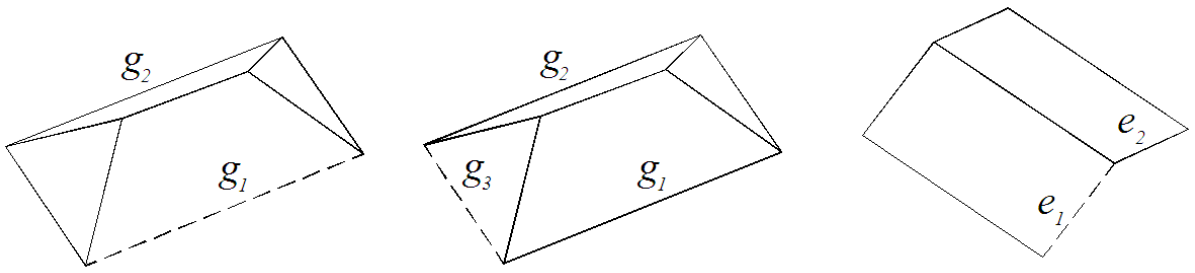

Figure 5.24: Establishing of missing edges: (a) lacking of gutter edge; (b) lacking of gutter associated to hip roof side (*i.e.* the edge which is orthogonal to ridge-line); and (c) missing eave (dashed lines – missing edges, solid lines – constructed 3D edges by adding image information).

When establishing a new 3D line segment for a missing edge, for instance the missing edge indicated by the red arrow in Figure 5.25(a), the following situations are also considered.

i. immediate neighbors to the problematic edge – edges shown by yellow arrows in Figure 5.25(a).

ii. other neighboring edges those that follow the same geometry as the problematic edge – edges that are pointed out by green arrows in Figure 5.25(a).

Condition (ii) has to be considered if at least one edge relevant to condition (i) doesn't possess a 3D edge constructed from images. Hence, gaps in this example are filled based on condition (ii).

Apart from the above cases, if a reference representing a step-edge is unable to be produced by the image data, the best reality is determined for that edge by substituting the position and direction of adjacent edges. Here, edges connected to both the upper and lower step-edges are searched based on the structural arrangement of the initial roof model. This is because edges adjacent to upper step-edge might not always be collinear with the upper step-edge (see Figure 5.25c as an example). After the upper step-edge is established and made stable, the lower step-edge is established simply by down projecting the upper step-edge. It is reminded that during the refinement of roof outlines, the corresponding upper step-edge is only extracted as the down edge would mostly be affected by shadow or occlusion.

(a) (b) (c)

Figure 5.25: Adjacencies of a desired edge: (a) filling gaps based on available line segments and other contextual information; (b) after filling gaps; and (c) up and down connectivity for a given step-edge (upper edge).

In addition to the above strategies, the direct linking of roof outlines' end positions is also considered. Generally, if the ideal edge or the edge which is very close to reality has been accomplished by the matching process, the successive ending and starting position belonging to two consecutive edges often hold the same coordinate with a little difference (arrow signed spot in Figure 5.26a). Based on this phenomenon, if the middle edge is missing among three consecutive edges derived from the image based method (white ellipse in Figure 5.26a for example case), the middle line is introduced by combining the closer end-points of the first and third edges (Figure 5.26b). This new line segment is only accepted if it deviates within a given angular threshold from its corresponding edge belonging to the initial roof model derived from point clouds. Based on the angular threshold, instances of fault linking occurrences are restricted.

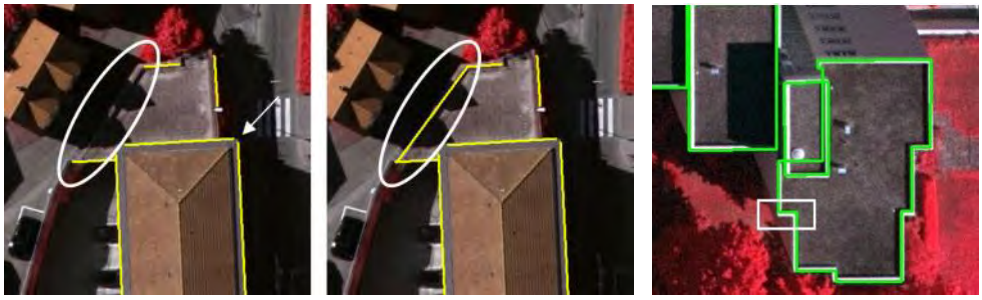

Figure 5.26: End positions of successive line segments and their interlinked line segment: (a) proximity of two consecutive line ends; (b) linking closer end positions of adjacent edges leads to establish the missing edges, (c) another example for the same case.

In contrast to introducing new boundary segments, defects within the accepted 3D line segments constructed from image information, for instance a slight deviation of an eave from its orthogonal status (Figure 5.23), are recognized based on convergence priors, and then those defects are rectified. Here, an eave giving a comparatively large deviation (but $< 3°$) with respect to the ridge-line's orthogonal direction is regularized by assuming that the position of the adjacent eave (e_1 in Figure 5.23) is correct. As such, both placement and directional regularizations are applied to the defective edge (e_2).

In order to optimize the entire rectification process, each roof corner (outer) is examined and necessary rectifications are performed. Once an edge is rectified or geometrically established using a new 3D line segment, it is assigned with a label. This indicates that the edge is strongly defined and is stable, so that subsequent rectifications may also rely on the newly introduced stable edges. It is noted that, as mentioned earlier, opposite gutters whose directions are not equal but $< 3°$ are subject to regularization within the rectification process. Further, to preserve right angle corners of boundary edges, especially in flat multi-layer high rise buildings (e.g. Figure 5.27), rectification is performed. The method explained in Section 4.2.1 is used for the boundary regularization process.

Figure 5.27: Regularization of boundary edges (on flat roof) extracted from images (black – before regularization, red – after regularization).

Since the rectification step minimizes gaps and reduces defects, further gaps which exist may be questionable. They could be assumed as gaps caused by incorrect guidance (or misalignment of references from the reality). In general, for an erroneous reference there would not be a candidate because in reality, there would not be an edge like that. Therefore it is reasonable to decide that the remaining gaps correspond to erroneous references.

5.7.2 Refinement of roof topology

Erroneous topology often causes geometric errors in building roofs. Errors can mainly be seen in line and area topology which are associated with the outer boundary of the roof and RTG respectively. Since the boundary of initial roof models were reconstructed based on the rectilinear line fitting for contour edge points, erroneous boundary could occur in some instances. In general, over- and under - segmentation, clutter by vegetation, and data gaps (for example see Figure 5.28) mislead the contouring, and the effect would be a roof outline having a distorted shape. On the other hand, missing roof planes, misalignment of parameters, and segmentation issues lead to erroneous RTG which may also yield isolated roof components, defected roof (inner) corners and so on. The issue will be discussed in detailed in Section 6.2.2. The objective of this step is to rectify some of those errors and to predict the best reality. As the prediction cannot be done by exclusively investigating the problematic edge, well-defined evidences are taken from the structural arrangement of roof models and convergence priors. By taking some example cases, how such an issue can be addressed is explained next.

As shown in Figure 5.28, many situations could come across gutters having some ragged edges. If such an excess 3D edge is unable to be derived from the image based method, then counter gutters belonging to the opposite roof plane is investigated. If the counter gutter doesn't contain such uneven overhangs, the problematic gutter can be assumed as straight. Thus, the line topology of the respective roof boundary is updated by discarding the ragged turnings. If this building follows the gutter symmetry, as the symmetry is already preserved, this modification doesn't discard symmetries.

(a) (b)

Figure 5.28: Defective contouring caused by under-segmentation: (a) erroneous overhangs due to merging of connected vegetation; and (b) after rectification the error.

In addition to that, there are some incidences where a certain gutter is located next to another roof plane(s) which is considerably elevated than the mentioned gutter (e.g. shown by an ellipse in Figure 5.29a). This means that, the gutter,

(i) does not possess a 3D edge derived from images, and

(ii) is planimetrically parallel to the edge of the elevated roof.

Then by assuming that the location of that gutter is wrong, and that there should be a step-edge in between them, the missing edge is established by down projecting the elevated edge. Thus a new graph edge is inserted to represent the new relationship, if there is no graph edge between the segments. With these updates, erroneous boundaries caused by a data gap are corrected while reducing the graph error to some extent. The next example further describes the correction of graph errors.

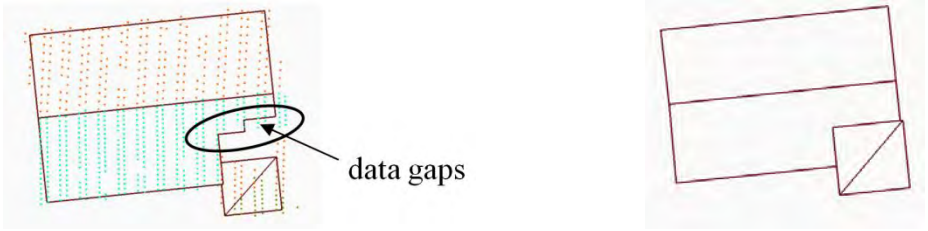

Figure 5.29: Defective roof outlines caused by data gaps: (a) erroneous roof outlines; and (b) rectification based on the guidance.

Of course, there are some instances where the derived topological relationships are wrong. For example, if it is difficult to derive a 3D line segment for representing a given step-edge from images, then there would not be a step-edge in the real scene. When such an instance is found (e.g. Figure 5.30), then the corresponding planes are investigated for recognizing whether they can be merged or can be intersected. If the plane intersection is acceptable, a new ridge-line is inserted along the intersection line instead of the problematic step-edge. Consequently, line topologies of the corresponding two planes (*i.e.* polygons) are updated while computing new end-points for the ridge-line. End-points are computed by intersecting stable eaves with the ridge-line (Figure 5.30).

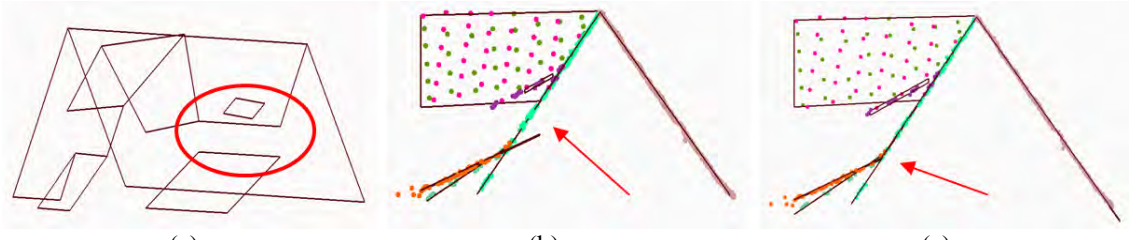

Figure 5.30: Updating of erroneous topological relations based on the image information: (a) initial roof model (red circle indicates that there is a step-edge in-between two planes); (b) initial model – profile view; and (c) rectified model.

When the algorithm recognizes a convex roof corner associated with a horizontal gutter, and which is part of the gable shape roof pair (Figure 5.31), then

(i) if there is a missing gutter associated to the hip side or gable side and it is filled as explained in Section 5.7.1 (refer Figure 5.24), and

(ii) if there is a missing edge which does not follow a hip side or a gable side as shown in Figure 5.31(b), assuming that it is incorrect,

the regular hip roof part is adopted to achieve the closed polygon. Hence, the intersection of the edges g_1 and g_2 produces the corner point relevant to the opposite convex corner. Linking of open nodes allows obtaining of the refined roof model at the end (Figure 5.31c). According to the accumulation of roof inner-bounds, updating of the graph edges can be performed.

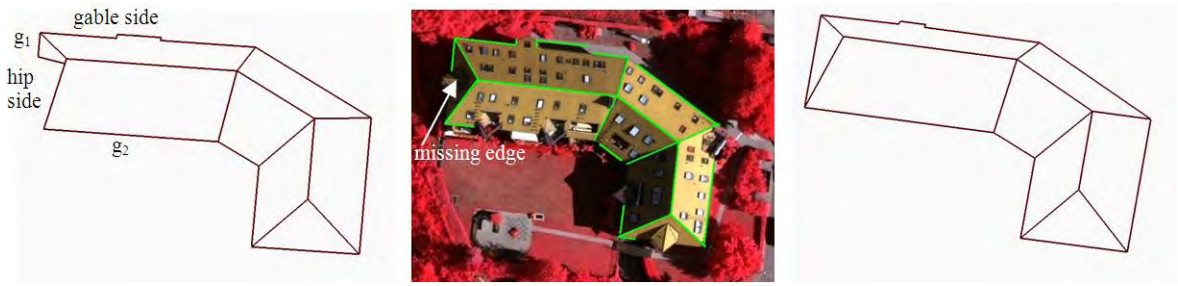

(a) (b) (c)

Figure 5.31: Correcting topological errors associated to data gaps: (a) initial model; (b) overlaid 3D edges derived from images; and (c) refined roof model.

Missing graph edges cause erroneous RTG. False negative edges break the connection between two roof planes and yield disconnected building components (Figure 5.32). Since the error is highly affected to the completeness of the resulting building models, an effort is made to rectify some issues with the help of image data. After gathering each and every boundary line segment from the image method, each boundary segment is analyzed based on the segment adjacency graph created while processing point clouds (see Chapter 4). Segment adjacency graph is not always equal to the RTG and provides excess relations indicating adjacency irrespective to the length constraint along the common boundary between two segments. Among the boundary edges derived from image information;

(i) If two parallel edges having different elevation with slight displacement or coincidence to each other (e.g. closely located green colored parallel line pairs in Figure 5.32c) are found, and

(ii) If these two edges (those that follow criterion - i) are belonging to two adjacent laser segments,

Then by assuming that there should be a step-edge in between the mentioned edges (or roof planes) a new graph edge is created while assigning a label *step-edge*. Vertical alignment of up and down step-edge is confirmed afterwards. Similarly, all other missing edges in the RTG are created, which in turn lead to a correctly connected roof model for the split separate building components (Figure 5.32d). The fixing of inner corners is explained in Section 5.7.3.

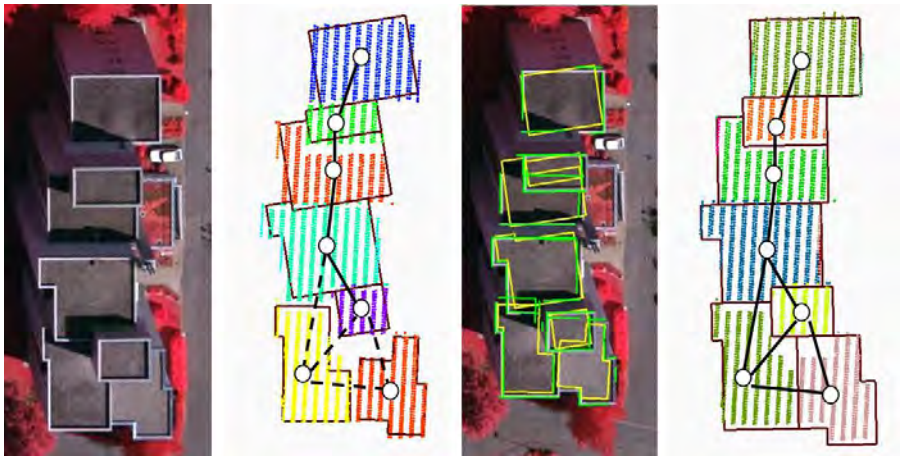

(a) (b) (c) (d)

Figure 5.32: Rectification of false negative topological relations: (a) subset image showing the reality; (b) split separate buildings and the defective RTG; (c) overlaid 3D edges derived from images and initial roof outlines; and (d) edges and RTG after rectification (dark brown – building outlines of reconstructed building, black lines – graph edges, black dashed lines – false negative graph edges, yellow lines – projected initial model lines, green – derived line segments (3D) projected back to image space).

5.7.3 Refinement of model vertices

With the strategies used in previous sections, accurate roof outlines and enhanced geometry for the initial roof models is achieved. Image-based edges can then be fused with the initial model edges. In the process of obtaining closed polygons, those stable refined boundary edges are intersected based on known line connectivity (or line topology) of each roof corner in the initial roof model and new vertices are obtained. Since the ridge-lines of initial roof models are adopted for the refined model, internal vertices associated to ridge-lines are not updated. However, when considering newly created step-edges, some internal corners are updated. During the calculation of the new 3D positions for each refined model vertices, two processing steps are used concerning the inner and outer vertices.

5.7.3.1 Fixing of inner corners

As a result of refinement, if a new graph edge is derived, then using Dijkstra's algorithm, new shortest cycles are checked. If new cycles are found and they are associated with the mixed feature lines, using a similar method as explained in Section 4.2.2.2, new vertices are computed. The only difference is that none of the edges is allowed to sweep as it is assumed that the edges are correct and represent stable boundary positions. Therefore, if convergences do not make a single intersection point, the obtained intersection points are maintained as they are. This enables to obtain the reality as shown in Figure 5.33. Before fixing the inner corners, if a down step-edge is not available, it is reconstructed by down projecting the refined upper step-edge.

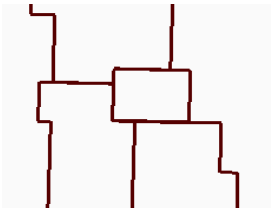

Figure 5.33: Geometrically fixed inner corners of a refined model.

5.7.3.2 Fixing of outer corners

With the refinement, line topology of some of the roof outlines has to be updated, especially for maintaining the placement of stable edges. Before fixing outer corners, outer lines should be cleaned, especially if two closely located parallel lines (image-based line segments) are found to lie on a plane as shown in Figure 5.34(a), one line which follows the global collinearity (if not the longest edge) is chosen, assuming such very short parallel outlines cannot be seen in reality. To find the correct roof outer corners respective to the refined boundaries, the following strategies are applied.

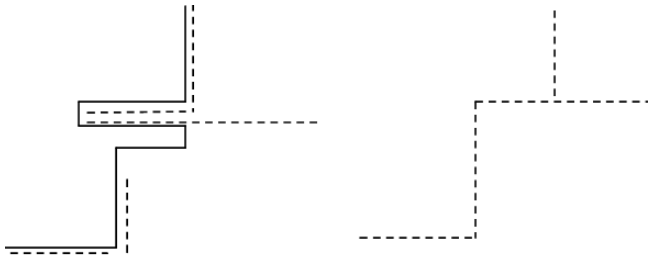

Figure 5.34: Fixing of outer corners: before (a) and after (b) merging of closely located line segments (solid line – outlines of the initial model, dashed line – derived new line segments).

(i) As seen in Figure 5.35, with the availability of refined edges, outer corners which have no changes to their line topology are updated directly by simply intersecting all corresponding edges.

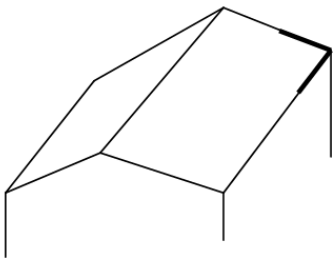

Figure 5.35: Intersection of refined boundary edges to obtain refined roof corner vertices.

(ii) In the case a roof corner is produced by the intersection of two orthogonal outer-boundary edges (or step-edges) and a ridge-line in the initial model as shown in Figure 5.36(a), if no single intersection is given by those two orthogonal edges with the ridge-line, then a new point (q in this example) is inserted to maintain the intersection of orthogonality of those edges while choosing one intersection point ($p1$) on the ridge-line as shown in Figure 5.36(b). Herein, from two intersection points that are given by the outer-edges with the ridge-line, the inner point is chosen to remain with the ridge-line because it always represents the inside polygon point even at a convex corner. In the point insertion, further precautions are taken to establish the new point on the corresponding roof plane.

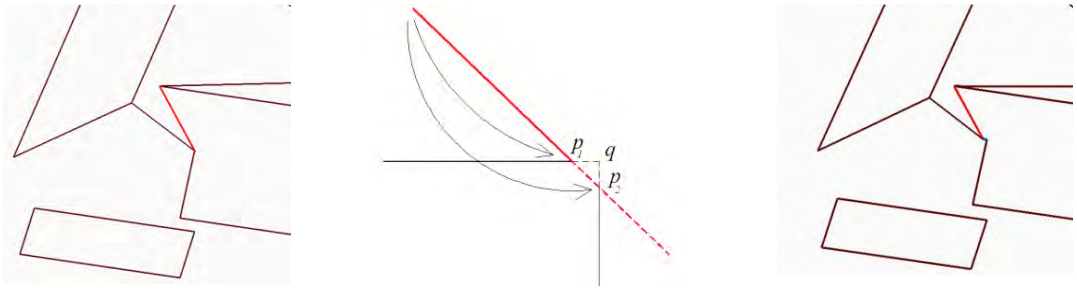

(a) (b) (c)

Figure 5.36: Maintaining the correct roof corner geometry when more than one intersection is occurred: (a) initial model boundaries; (b) intersection scenarios; and (c) refined roof model (red – ridge line, brown – roof boundaries).

(iii) When two horizontal gutter lines (dark yellow lines in Figure 5.37) having unequal heights are intersected with a ridge-line to produce a roof corner, for instance a concave corner in an L-shaped building as shown in Figure 5.37(b), the orthogonality of the corner is maintained while preserving their actual heights by inserting a new point as shown in Figure 5.37(c). Similar to the previous case, the inner intersection point (shown by an arrow) is chosen to remain with the ridge-line.

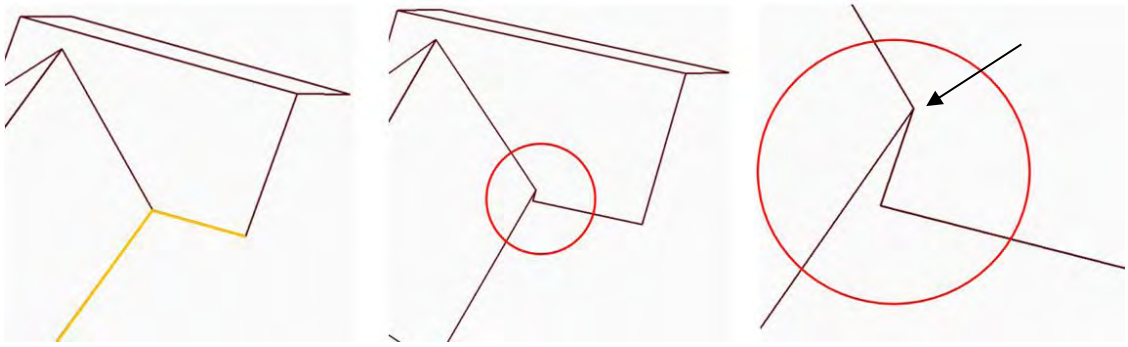

(a) (b) (c)

Figure 5.37: Geometrical updating of corner point related to unequal gutter heights: (a) roof corner in initial model; (b) new corner in refined roof model; and (c) magnified view of the corner position (yellow – horizontal gutter lines, red circle – area of interest, and brown – roof outlines).

(iv) In addition, misalignment between initial and refined outline can occur. This means that each vertex in the initial model doesn't match with the new situation of the refined model. Sometimes, additional short edges should be inserted in order to get closed polygons while maintaining the correct placement and direction of roof outlines as shown in Figure 5.38. The maintenance of the correct alignment (dark corners) is important as some of these edges may behave as step-edges with their neighboring roof planes.

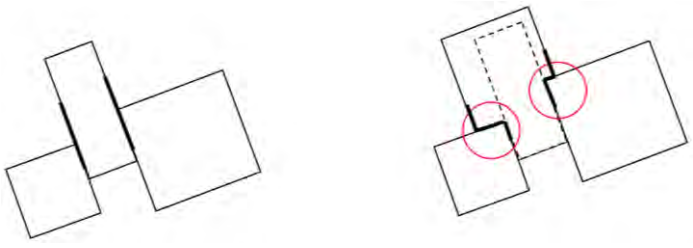

(a) (b)

Figure 5.38: Misalignment correction between initial and refined roof outlines: (a) initial model; and (b) refined model.

By applying the above strategies and fixing both the inner and outer corners, correct geometries are obtained. Figure 5.39 exhibits an example of the correctly refined model geometries. It is stated visually that the model reach close to reality through the proposed refinement method. The positional accuracy of the refined model is analyzed in Chapter 6.

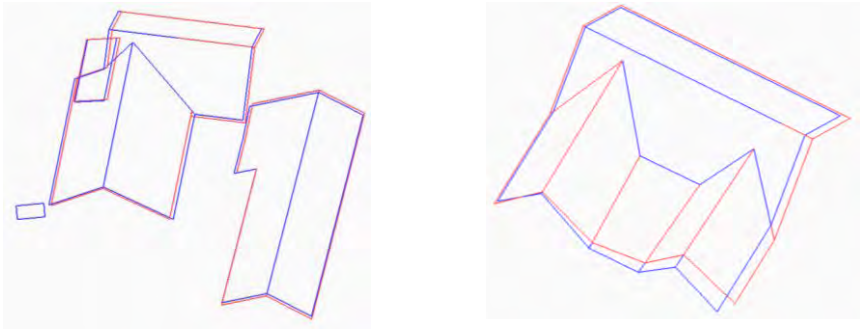

(a) (b)

Figure 5.39: Geometry of initial and refined roof models (blue – initial roof model and red – refined roof model).

Apart from the refining of main roof models, weakly defined dormer outlines are also refined to enhance their planimetric accuracy. According to the refined dormer outlines, new corner positions are obtained simply by intersecting the corresponding new line segments (Figure 5.40).

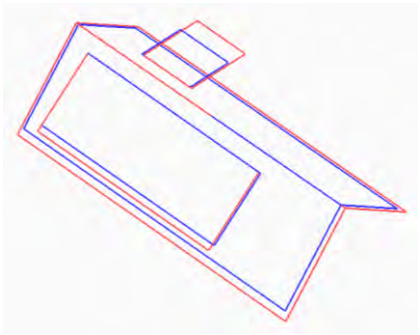

Figure 5.40: Refinement of dormer outlines (blue – initial roof and dormer outlines, red– refined outlines).

5.8 Reconstruction of wall segments

After the completion of the refinement process or correction of all roof edges, wall segments, *i.e.*, vertical planes are inserted for each building using the model vertices. The height beneath the roof model, along the roof outer boundary, is extracted from the laser segments. The lowest terrain height is taken as the basement of the corresponding building. Down projecting the roof outer boundary points (vertices) until the defined basement, each wall segment is reconstructed as shown in Figure 5.41. Small vertical wall segments associated with the dormer tops are also reconstructed by projecting boundaries of dormers on to the roof planes on which they are located (Figure 5.42).

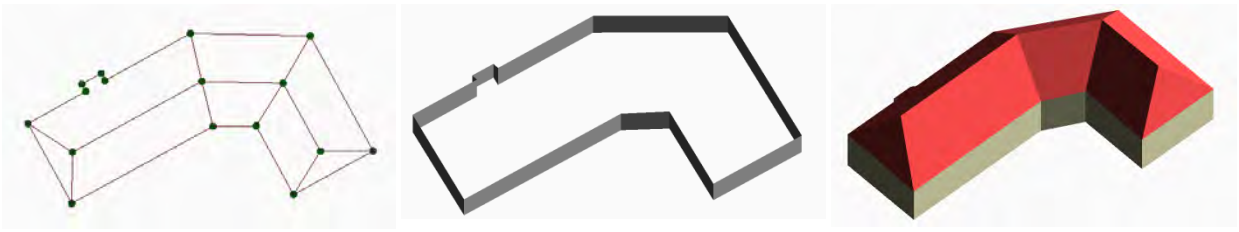

(a) (b) (c)

Figure 5.41: Reconstruction of building walls: (a) corrected model vertices based on image data; (b) reconstructed wall segments; and (c) complete building model.

(a) (b)

Figure 5.42: Reconstruction of dormer walls: (a) wireframe model showing the internal architecture of dormers; (b) colored wall surfaces in the 3D building.

5.9 Summary

In this chapter, a model refinement method which uses lines extracted from digital aerial photographs to improve the planimetric and topological accuracy of roof models reconstructed from point cloud data is presented. Object space line segment construction is done in the projective geometry after the extraction of line features from images using Burns line extractor. Ambiguities of this process are reduced by applying scene constraints. To obtain correct edges from images, scene constraints, structural arrangement of roof models and convergence priors are introduced for the first time to the building refinement process. With the refinement, several modeling errors such as planimetric deviation of outer boundaries, topological errors and some deformed shapes along the roof outlines are corrected with the help of image data. Therefore, building models having increased accuracy in both planinmetry and topology are achieved at the end of the refinement process.

Boundary extraction from images is very accurate, while laser points are more appropriate to obtain planar surfaces. Therefore, efficient integration of laser points and image naturally assists not only to improve the planimetric accuracy, but also to avoid many barriers for building reconstruction from using either data type. The attempt through the presented new refinement algorithm, especially using scene constraints, known structural arrangement and convergence priors, give a promising future to automated building model reconstruction by combining both laser and optical approaches.

6. Experiments and analysis

In previous chapters, the methodology of 3D building model reconstruction and model refinement from ALS point clouds and image data are described in detail. Some examples were also presented to illustrate how the proposed approach works. In order to examine the robustness of the entire working scheme, a separate analysis is carried out in this chapter, in which three test scenes having different shapes of buildings were employed. The chapter analyzes the results of the building model reconstruction with regard to the geometric accuracy in position and topological correction. The limitation of the approach is investigated and discussed.

In the experimental phase, initial roof models were first reconstructed from ALS point clouds (Chapter 4). This was followed by the post refinement process (Chapter 5) in which correcting of the roof outlines using image data was discussed. In addition, the refinement process focused on the correction of (some of) roof topologies. From combining these methods and results, complete 3D building models were reconstructed. The results will be interrogated to illustrate the working of the procedure, along with the benefits and eccentricities involved.

This chapter is organized as follows: Section 6.1 explains the design phase of the experiments, *i.e*. a description of the experiment configuration. The data used, and types of evaluation methods are also presented in this section. Section 6.2 analyzes the results and performance of the method with respect to the three experiments. A comparison of the results shown by previous (selected) peers, especially who took part in the ISPRS building test project, is given in Section 6.3. This enables the reader to get an idea about the capabilities of the method introduced in this study. A short discussion is given in the final section.

6.1 Experimental design

Both 3D building models reconstructed solely by point clouds, and their refined models by integrating image data, were assessed with respect to the reference data.

6.1.1 Test data sets

A well-documented study area provided by ISPRS comm.3 (2011) is chosen to test the proposed approach for automated building reconstruction. The data set was captured in Vaihingen, Germany, and consists of three test areas covering both ALS point clouds and digital images. This is actually a subset of data originally used for the test of digital aerial cameras by the German Association of Photogrammetry and Remote Sensing (DGPF) (Cramer, 2010). The test area 1, called *scene1*, is a subset of an inner city consisting of 37 historic buildings with rather complex shapes and surrounding trees, while *scene2* is characterized by 14 buildings including 4 connected high-rise residential buildings with dense trees. In contrast, *scene3* is purely a residential area having 56 small detached houses.

ALS point clouds

ALS point clouds over the test area were captured by 10 strips using the Leica ALS50 system, with a 45 degree field of view and 500*m* mean flying height above ground. The average point density of an individual strip is approximately 4$points/m^2$ (ISPRS comm.3, 2011). Multiple echoes and intensity

data were also recorded, but for the purpose of this study, only the last return data was used. Figure 6.1 shows the area of the data sets used in this study.

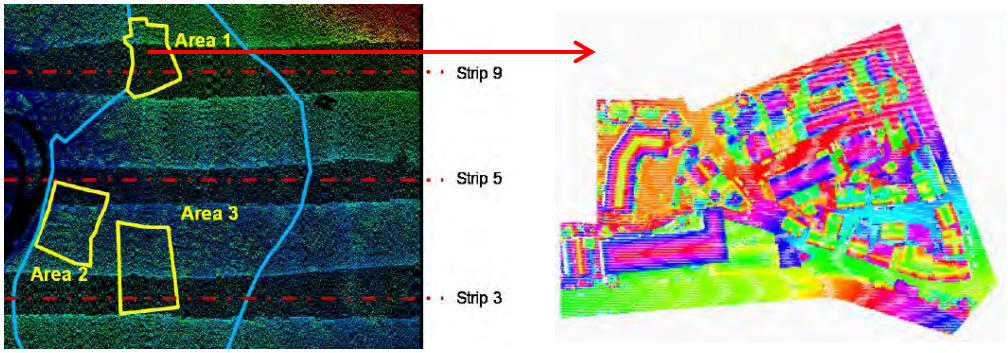

Figure 6.1: Experimental data – point clouds: (a) ALS point clouds of three test areas and (b) magnified views of ALS points over the area 1 (ISPRS Comm.3, 2011).

Digital images

The Intergraph/ZI DMC camera, having a focal length of 120*mm*, was used for the image data acquisition. The flying height is around 500*m*. This contains twenty pan-sharpened color infra-red images with an 8*cm* ground sampling distance. Images have a 65% forward overlap and a 60% lateral overlap. Figure 6.2 shows the digital aerial images of each test scene over the same areas used in ALS point collection, as displayed in Figure 6.1.

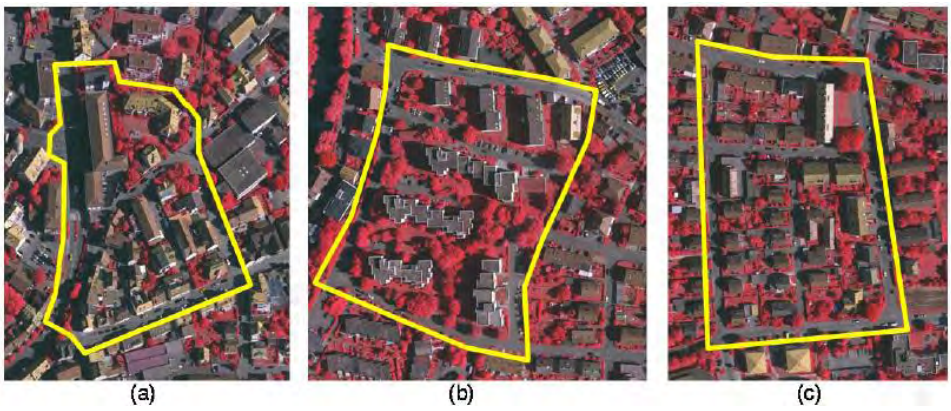

Figure 6.2: Experimental data – digital aerial images: (a); (b); and (c) aerial images of three scenes respectively (ISPRS Comm.3, 2011).

6.1.2 Reference data

Reference data over three test scenes were generated by RAG Steinkohle AG and SIRADEL (http://www.siradel.com) mainly by manual stereo plotting. The reference 3D building models were reconstructed having LoD2 according to the CityGML standard (Gröger et al., 2008). Hence, these models consist of roof information without containing roof overhangs and façade information. Figure 6.3 shows a created reference data set for the test *scene1*, which is used to analyze the constructed models using the proposed method. In addition to this, interactively created data were used for the assessment of some intermediate steps.

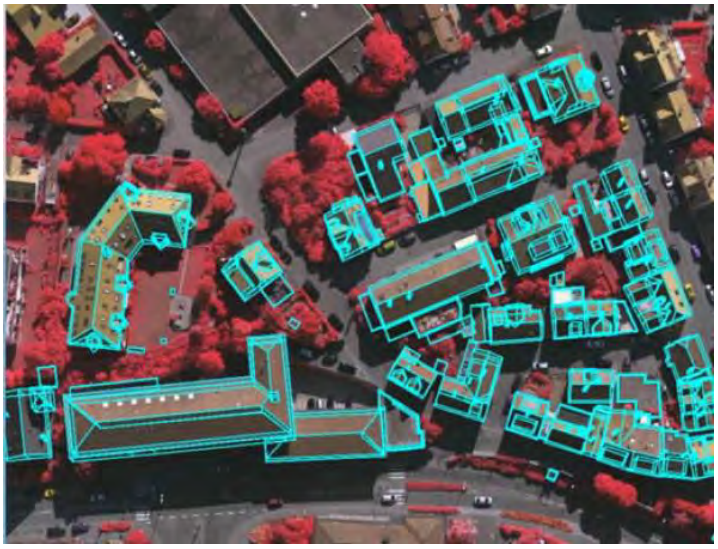

Figure 6.3: Benchmark reference data used in the ISPRS building test project: (ISPRS Comm.3, 2011).

6.1.3 Evaluation methods

After applying the proposed algorithms, the end results contain 3D geometrical models of each building. In order to analyze the performance and limitation of the proposed reconstruction scheme, the results are analyzed both quantitatively and qualitatively, with respect to reference data.

The evaluation methods for building reconstruction introduced by the *ISPRS benchmark test on object detection and 3D building reconstruction* (Rottensteiner et al., 2012; 2014), based on the evaluation procedure described in (Rutzinger et al., 2009), are followed. The assessment focuses on the evaluation of topological and geometric accuracy. Since the study attempted to preserve the roof topology, assessment of topological accuracy is carried out. In addition, the geometry of the resulting models is evaluated with respect to reference data. Further to these evaluations, two other quantitative assessments were carried out to evaluate the overall results: per-object level and per-pixel level evaluation. Per-object level evaluation is carried out based on the entity, in which the analysis focuses to evaluate the results. It should be noted that an entity is defined as a_pixel, a polygon, and a graph edge. Within the course of the evaluation, three different measures, namely the *completeness*, *correctness* and *quality* were mainly used (see below for the definitions). Before describing each assessment procedure in detail, some terms and definitions need to be clarified. The following terms that the study used is introduced in order to obtain a clear idea about the evaluation methods:

True Positive (TP): an entity is classified into the same class (e.g. building) as the corresponding entity in the reference.

False Negative (FN): an object entity in the reference but not in the resultant data.

False Positive (FP): an object entity in the results but not in the reference data.

Then the quality measures *i.e.* completeness, correctness and quality are defined as follows:

$$Completeness = \frac{\#\,TP}{\#\,TP + \#\,FN} \times 100\% \tag{6.1}$$

$$Correctness = \frac{\#\,TP}{\#\,TP + \#\,FP} \times 100\% \tag{6.2}$$

$$Quality = \frac{1}{\frac{1}{Completeness} + \frac{1}{Correctness} - 1} \tag{6.3}$$

Where: *#TP, #FP* and *#FN* are numbers corresponding to each measure.

1. **Per-object evaluation**

The numbers of TP, FN, and FP are mainly computed by converting the resulting and reference roof polygons into label images. When generating the label images, each pixel is assigned to the highest roof plane available at the respective X, Y position. The comparison between the reference label image and the image corresponding to the resulting model is done by overlaying each other. If the overlap between two roof planes is larger than 50%, then they are assumed to be corresponding to each other. According to the accuracy of resulting models as well as the overlap ratio, 1:1 correspondences cannot be expected at all times. Therefore 1: M, N: 1 and N: M relations are expected, and these numbers are related to the differences in the topologies of the resulting and reference roof planes. 1: M relations indicate that a plane in the reference is associated with M number of planes in the results, representing the degree of over-segmentation. Similarly N: 1 relation is an indicator of under-segmentation. Additionally, both over- and under-segmented results are indicated by N: M relations. This overlap analysis is used to find out the degree of TP, FP and FN, and accordingly, per-object level completeness, correctness and quality indices are computed.

2. **Per-pixel evaluation**

In the pixel-based evaluation, the raster representation of the reconstructed results and the reference are compared. The comparison is presented as a raster image showing the spatial distribution of the TP, FN, and FP in different colors.

3. **Evaluation of topological accuracy**

The topological accuracy can be assessed in two ways: (i) using overlap analysis of label images, and (ii) based on the RTGs.

In general, 1:M, N:1 and N:M relations arise owing to differences between roof topologies of reference and reconstructed entities (roof polygons). This indicates that those relations are also a kind of measure to assess topological inaccuracies.

In order to represent the correct topological relationships, a second assessment is carried out based on the RTGs. The automatically constructed RTG is compared with the manually created RTG representing the ideal situation of the corresponding roof model. This comparison is used to find the correct, missing and excess (erroneous) graph edges as shown in the Figure 6.4. These relations are represented using the same terms TP, FN and FP, and the completeness and correctness is evaluated afterwards by analyzing the results.

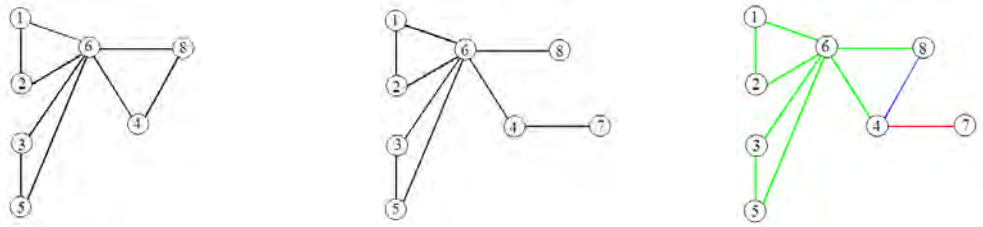

(a) (b) (c)

Figure 6.4: Evaluation of topological accuracy: (a) reference RTG; (b) automatically constructed RTG; and (c) the comparison graph showing errors (black – graph edges, green – TP graph edges, red – FP graph edges, blue – FN graph edges).

4. Evaluation of geometric accuracy

The geometric quality of 3D roof polygons, in particular the accuracy of vector outlines, is also evaluated. The planimetric deviation of boundary polygons is assessed by matching a vertex from the resulting boundaries to its nearest counterpart in the reference. Deviations are computed with respect to both directions. For each vertex of a reconstructed polygon, the nearest point on the boundary of the corresponding polygon in the reference polygon is searched (Figure 6.5). However, that point does not necessarily correspond to a vertex of the same polygon in the counterpart. The 2D Euclidean distance (*d)* between corresponding points is computed. If the *d* is larger than a threshold (3*m*), it is discarded assuming that the polygon does not belong to the same building. Finally, the root mean square error of distance RMS_d is computed as per polygon (Equation 6.4).

$$RMS_d = \sqrt{\frac{\sum_{i=0}^{n} d_i^2}{N}} \tag{6.4}$$

where d_i is the 2D Euclidean distance and *N* is the number of vertices used for the analysis in a polygon.

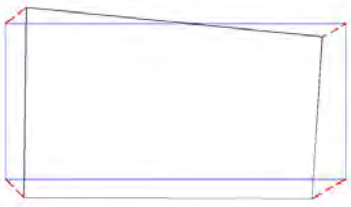

Figure 6.5: Difference of distance between vertices of reference and reconstructed polygon (blue – reference polygon, black – reconstructed polygon, red - displacement).

- The height accuracy is determined by comparing the *RMS* errors of height differences (RMS_Z) of two synthetic DSMs generated from 3D building models. This RMS_Z is based on the height differences between the reference plane and the corresponding reconstructed model planes. In addition to evaluating the height errors with respect to reference data, the plane fitting accuracy is also assessed with respect to segmented point clouds. The *RMS* error per segment is computed in order to get a further idea about the accuracy of model planes.

- The Horizontal gutter symmetry is assessed by computing the 2D distance between the ridge-line and the corresponding gutter lines, in order to evaluate the degree of symmetry preservation in the reconstructed models.

Further to the above evaluation methods, additional evaluation steps are included. Within the building reconstruction workflow, different processing strategies were followed. It is of interest to analyze core strategies that the processing chain relies on. Due to the difficulty of generating reference data for every individual step, the more convenient interactive analysis is followed. As such, interactive assessment is also conducted.

5. Interactive evaluations and performance analysis of intermediate steps

Interactive analysis methods are especially followed for estimating the number of correct, erroneous and total entities of desired object or object-class, such as roof segments, roof vertices (internal and external) and graph edges. External data, such as aerial images of the same scene, are also used for estimating the correct entity numbers. In fact, the vector data of the resulting roof models is overlapped on to the image data for enhancing the reliability of interactive measurements. This is an added advantage of the data integration done in Chapter 5. Different measures, such as *Extraction performance* and *Modeling performance*, are defined to represent a meaningful evaluation.

$$Extraction\ or\ modeling\ performance\ = \frac{\left(\begin{matrix}number\ of\ correctly\ extracted\ or\\ modeled\ entities\end{matrix}\right)}{total\ entities} \times 100\% \qquad (6.5)$$

Note: Some of the statistics provided by Rottensteiner et al. (2012) with respect to their benchmark reference data is included in this chapter to analyze the accuracy of 3D roof models.

6.2 Results and evaluation

Following the proposed evaluation methods, performance of some intermediate steps and results of final roof models before and after model refinement by integrating image data are evaluated. The evaluation on the refined roof models are presented in the form of a comparison with the previous results (results of initial roof models).

6.2.1 Feature extraction

As explained in Section 4.1, feature extraction deals with the extraction of roof primitive features such as roof planes, feature lines and roof outlines.

Although the main objective of this step is to extract roof primitive features such as feature lines and roof outlines based on the roof planes, the analysis is restricted to evaluating the performance of roof plane extraction. However, some intermediate results, in some test sites, are presented to give an idea about the procedure to the reader.

6.2.1.1 Results

Figure 6.6(a) illustrates the results of planar segmentation. It shows that though few (2 incidences) under-segmentation issues are found, the results are acceptable. For the purpose of reducing object complexity, segment merging was introduced. Results of the segment merging (Figure 6.6b) demonstrate that some uncontrolled merging has taken place, especially where vegetation is interlinked with roof planes (white ellipse in Figure 6.6b). In fact, vegetation with many branches often obscure or gets connected to roof surfaces. The false connections due to vegetation are the main cause of erroneous merging. Since the classification process relies on the results of the merging, this error was carried further. Therefore, some roof planes corresponding to merged segments appeared as terrain (white ellipses Figure 6.6c). Since this error was not given by the classification step, one could

say that the classification step performed well, and correctly separated terrain segments from the off-terrain segments.

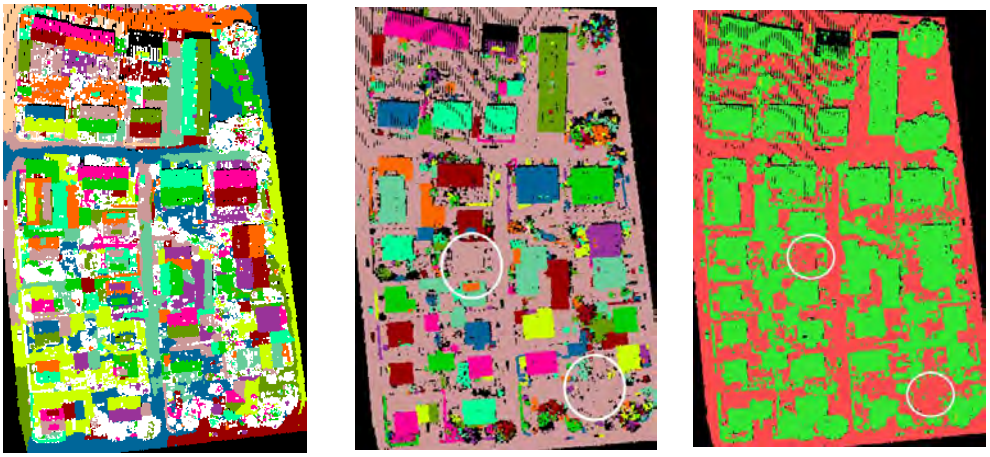

(a) (b) (c)

Figure 6.6: Intermediate results of initial processing steps: (a) planar segmentation; (b) segment merging; and (c) segment classification (different colors indicate different segments, red and green colors in (c) correspond to terrain and off-terrain segments respectively).

Based on the classification of results, potential roof planes were extracted as described in Section 4.1.3.2. Since different rules were applied to extract different roof planes, different colors can be seen from the extracted roof planes (Figure 6.7). It should be mentioned that the different roof planes were extracted at different accuracies. The highest extraction accuracy was given by the gable roof pairs. This was not because they were simple to extract but had to satisfy three constraints, namely azimuth angle, horizontality of intersection line and height above the ground. Flat and shed roofs which follow only two constraints (slope of the roof plane and height above the ground) were given the lowest extraction accuracy. This is the main reason for misleadingly classifying some vegetation segments as shed and flat roof planes.

6.2.1.2 Evaluation of roof plane extraction

The accuracy of roof plane extraction is evaluated by estimating reference roof planes interactively using image data. The interactive inspection revealed 209, 67, and 155 roof planes (reference) are available in each test scene respectively. It should be mentioned that small objects are left out from the statistics of this regard.

Table 6.1 shows that about 74% of the roof planes can be extracted by the proposed initial processing steps while the degree of incorrect extraction is relatively low (< 3%: 11 out of 431). As shown in Figure 6.7, two large connected buildings, one flat building part and three individual buildings (marked in circles) are classified as terrain objects. Obviously, as mentioned earlier, the planar segmentation and the merging step adopted prior to classification caused this defect.

Table 6.1: Summary of the roof plane extraction.

Nature	*Scene1*	*Scene2*	*Scene3*	Total
#existing roof segments	209	67	155	431
# extracted roof segments (ER)	149	64	117	330
# correct extractions (CE)	147	63	109	319
#incorrect extractions	2	1	8	11
Extraction performance (EP)	70%	94%	70%	74%

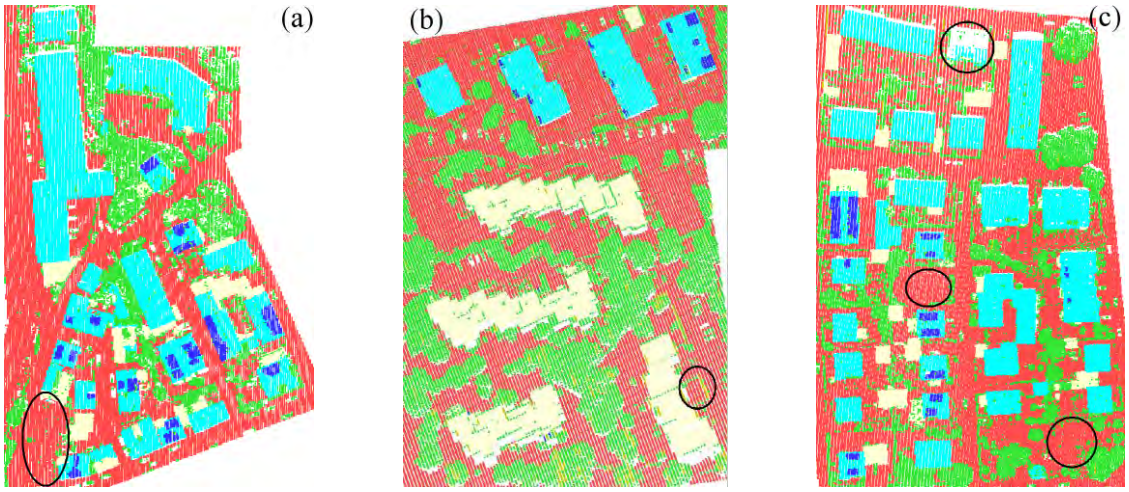

Figure 6.7: Final extraction results: (a) *scene1*; (b) *scene2*; and (c) *scene3* (cyan – roof planes extracted by azimuth analysis, beige – flat and some oblique roofs, blue – dormers; green – other objects (vegetation), red – terrain, circles indicate places where buildings were missed in the results.

Concerning erroneous roof extractions, vegetation removal strategies significantly reduce urban vegetation portrayed as roof planes. Most vegetation, including flower beds connected to the buildings, is discriminated by the area ratio criterion, though a few regular vegetation segments (three incidences in *scene3*) next to the buildings remain in some places (Figure 6.8). In such cases, constraints, for instance building orientation, can be used to reduce ambiguities between vegetation and buildings. Nevertheless, it is advisable to classify vegetation points prior to planar segmentation, which can enhance segmentation, classification and feature extraction. In *scene2*, the irregularity test is switched off as the proximity segment analysis is sufficient to minimize vegetation issues.

Figure 6.8: Erroneously extracted vegetation patches as roof planes and under-segmentation effect (Initial model results are overlaid on image data - white circle indicates the mentioned erroneous cases).

6.2.2 Model reconstruction using ALS point clouds

Performance of the proposed scheme, described in Chapter 4, is evaluated using ALS point clouds. The evaluation is mainly based on the three test scenes mentioned above (see Section 6.1.1), and their reference data. First the experimented results are presented. Performance of the corner fixing procedure is then evaluated. The obtained results are then analyzed separately to evaluate their topological and geometrical accuracy. Afterwards, per-object and per-pixel level assessment is given in order to get a further idea about the performance. At the end, behavior of parameters is shortly described.

6.2.2.1 Results

Resulting roof models relevant to each test scene is presented in this section. The results indicate that the proposed approach is capable of reconstructing various roof models with the correct geometry, while preserving their topology. Figure 6.9 – 6.11 show the resulting roof models of the *scene1, 2* and *3*, validating the capability of the reconstruction scheme.

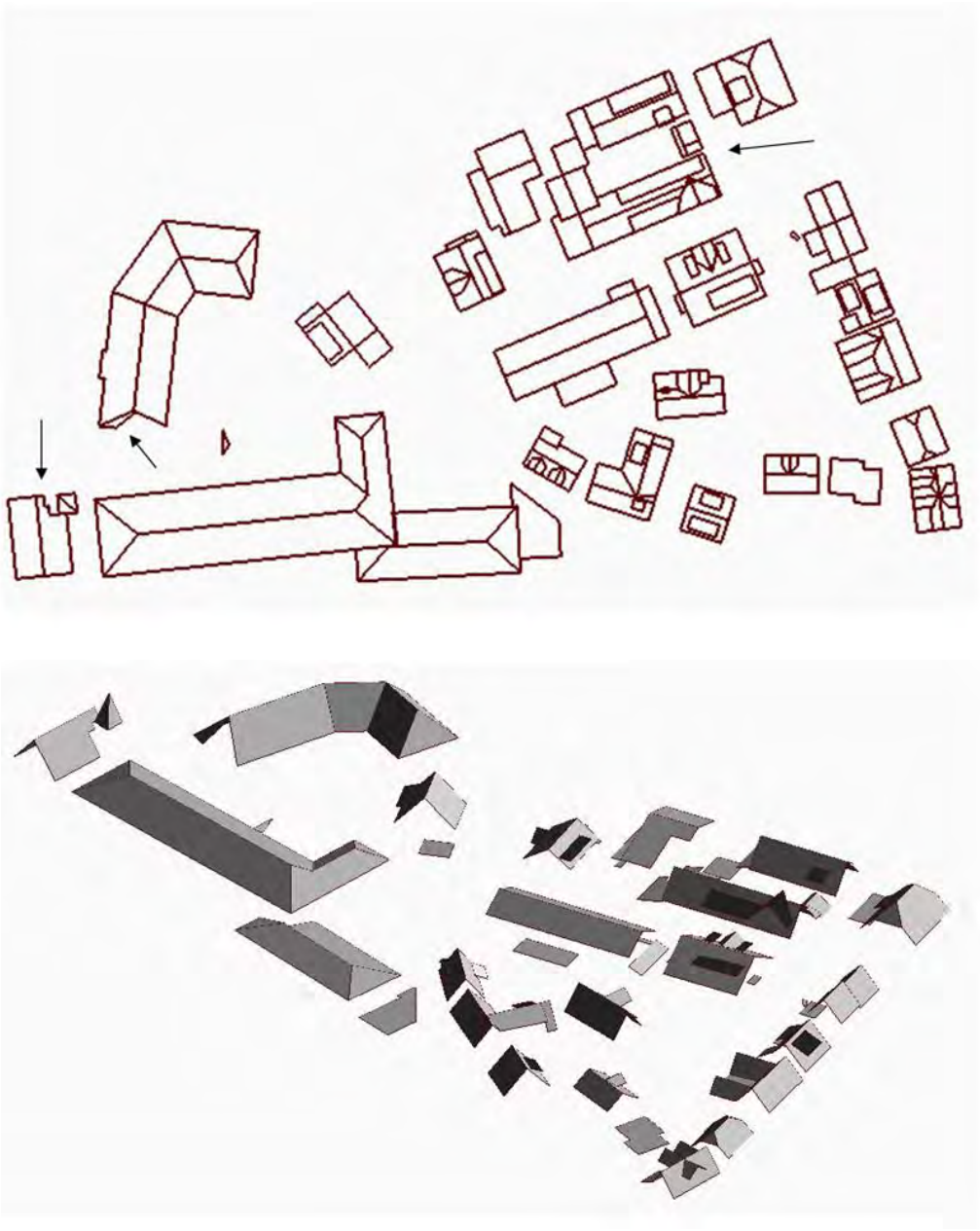

Figure 6.9: Final results of initial roof models in 2D and 3D - *scene1* (upper – aerial view of roof wireframe models, bottom – side view of 3D roof models, and arrows – erroneous reconstructions).

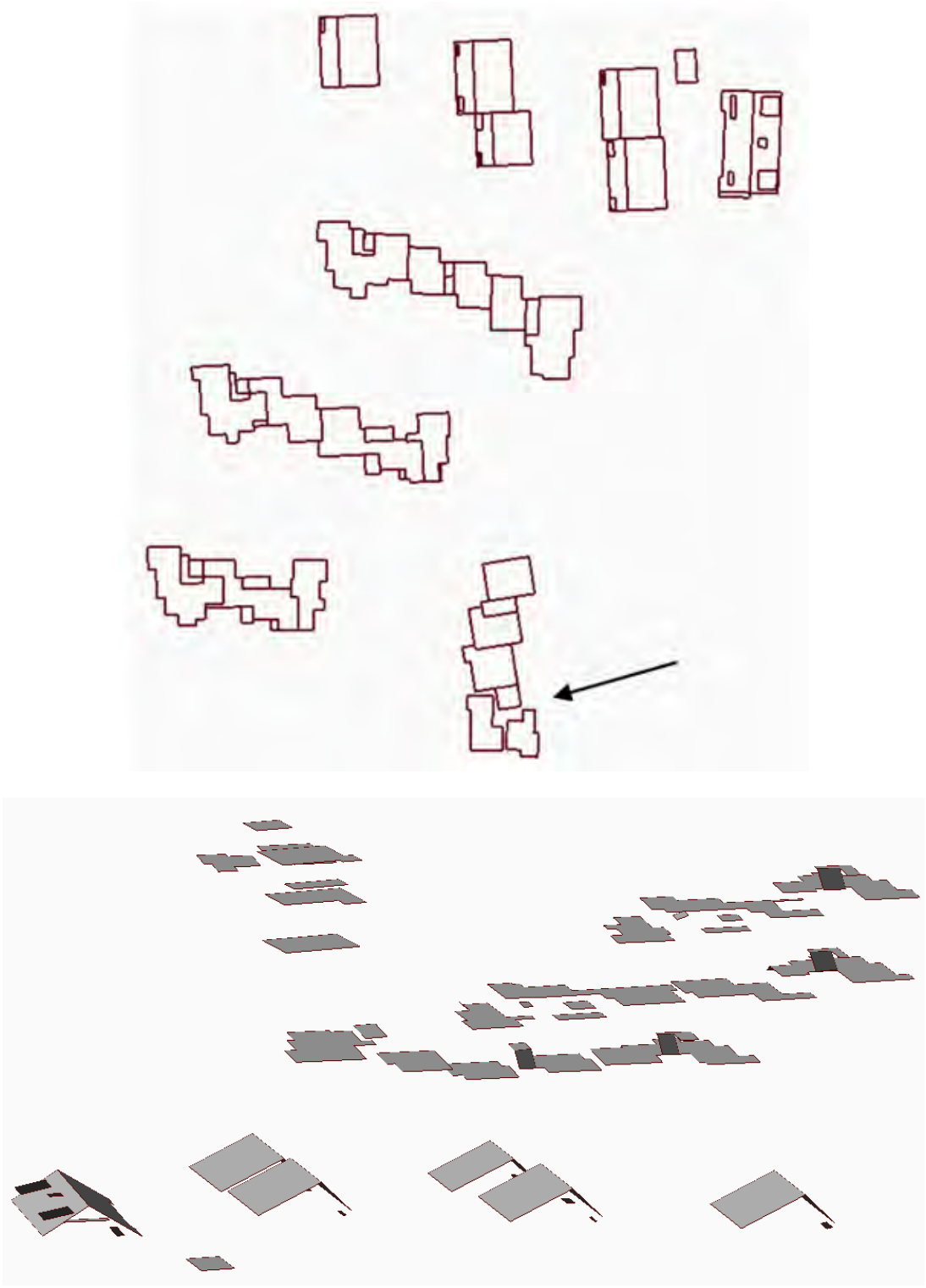

Figure 6.10: Final results of initial roof models in 2D and 3D – *scene2* (upper – aerial view of roof wireframe models, bottom – side view of 3D roof models, arrows – erroneous reconstructions).

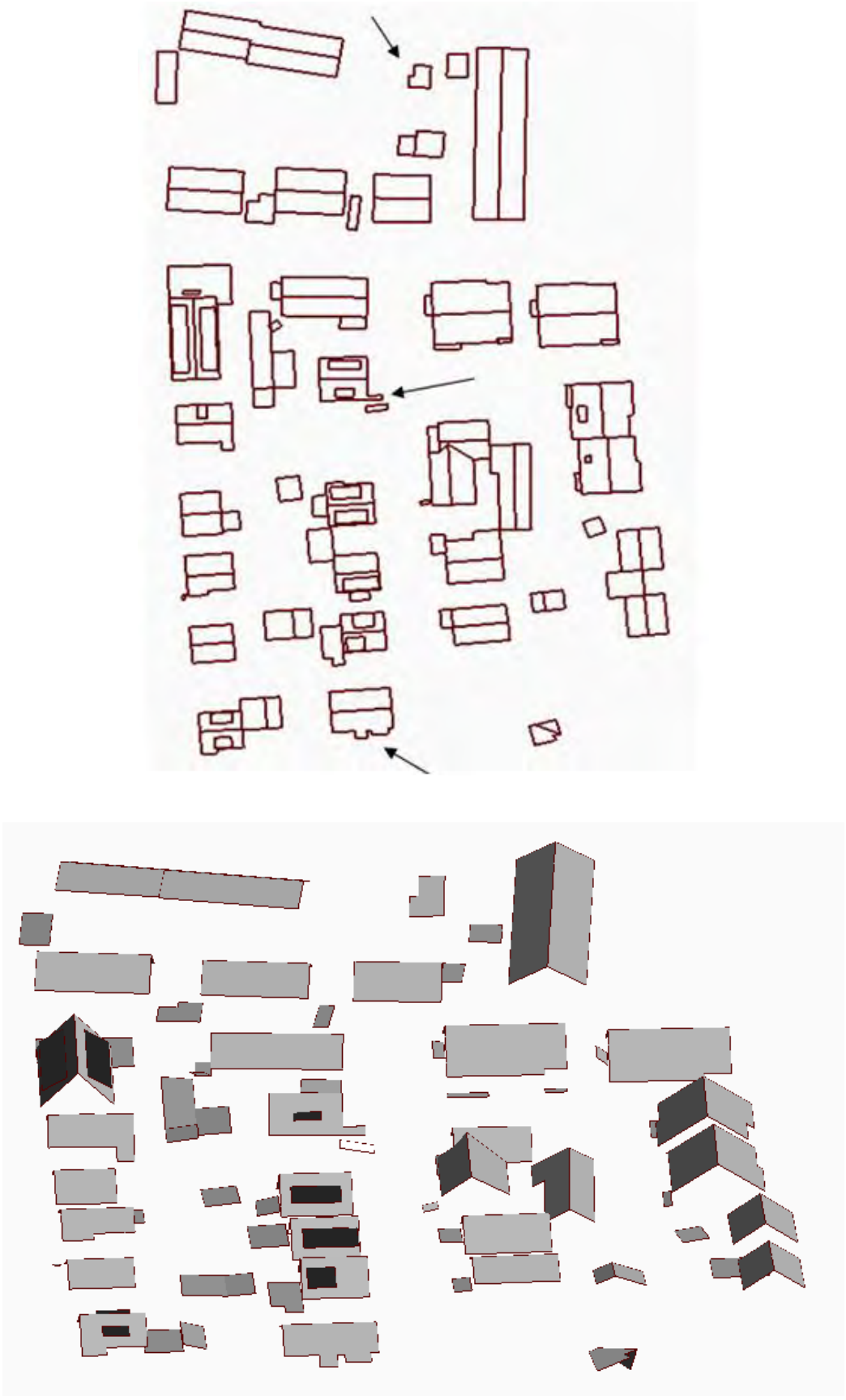

Figure 6.11: Final results of initial roof models in 2D and 3D – *scene3* (upper – aerial view of roof wireframe models, bottom – side view of 3D roof models, arrows – erroneous reconstructions).

Further investigation of the results demonstrated that the method correctly reconstructed multi-layer flat roofs, multi oriented roofs, gable roofs with and without gutter symmetries, and irregularities along the gutters (e.g. Figure 6.12). Based on the results, one could say that the major challenges: (i) maintaining the regularity along the roof outlines, and (ii) reconstruction of the multi-layer flat roofs, were sufficiently achieved.

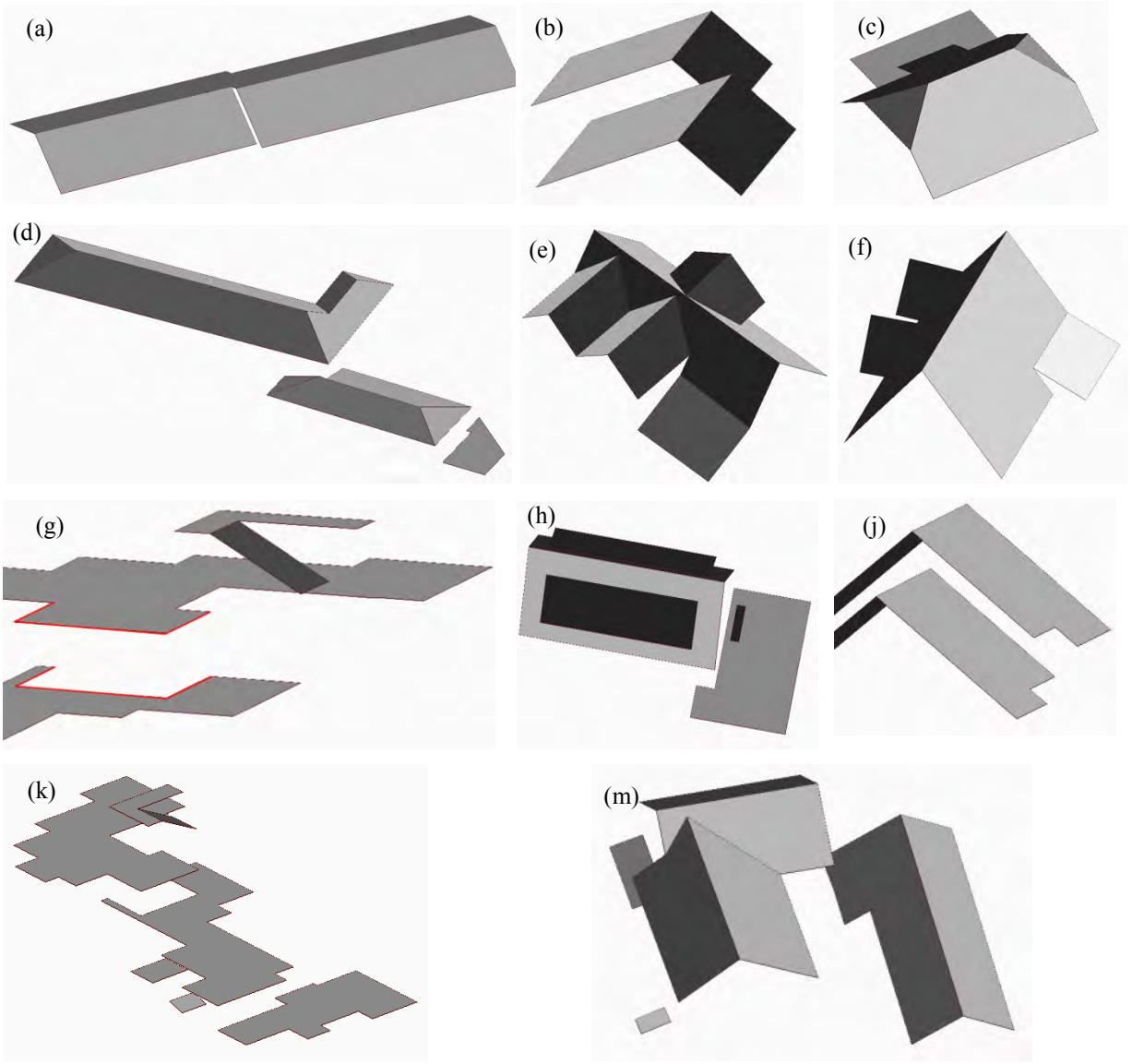

Figure 6.12: Correctly reconstructed different roof models: (a) maintaining regularity at step-edges; (b) preserving step-edges at multi-level gable roofs; (c) maintaining gutter symmetry and symmetry of triangular shaped roof planes; (d) preserving gutter symmetry at multi-level roof models having differently orientated components; (e, f) preserving internal roof corner geometry in complex roof models; (g, k) reconstructing of multi-level flat roofs having polygonal step-edges – '*g*' is magnified view of building '*k*'; (h) examples of reconstructing another polygonal step-edges; (j) maintaining correct alignment of gutter lines at step-edges; and (m) example of connected building having differently oriented roof sub-clusters.

However, there were few incidences, shown by black arrows in Figures 6.9 – 6.11, where fault geometries occurred. The main reasons to cause fault geometries are data gaps and segmentation errors. Defective constructions caused by data gaps and under-segmentation are shown in Figure 6.13.

Besides, with respect to wrong extractions mentioned in Section 6.2.1.1, very few FP polygons exist though it is not an error in the reconstruction itself.

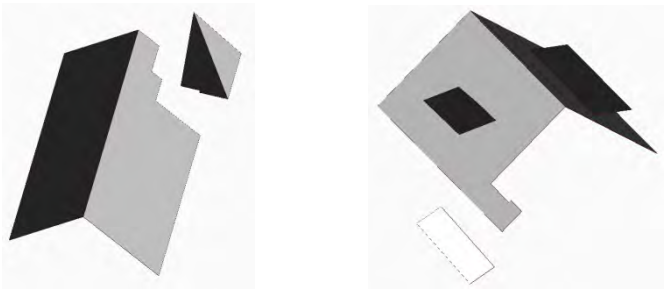

Figure 6.13: Some of defects caused by data gaps and under-segmentation.

6.2.2.2 Performance of SCC

Because of the novelty of the proposed cycle analysis approach, it is of interest to assess performance of the corner fixing procedure to ensure its suitability and stability for the complex scenarios. To cope with this, a quantitative assessment for cycle analysis has been conducted interactively by comparing statistics estimated from the resulting models with corresponding aerial imageries, as explained in Section 6.1.3.

Table 6.2: Summary of cycle analysis.

Nature	Overall (based on existing roofs)				Absolute (based on CE)			
	Scene1	*Scene2*	*Scene3*	*Total*	*Scene1*	*Scene2*	*Scene3*	*Total*
# extractable inner cycles	73	14	16	103	57	12	9	78
# correctly fixed inner cycles	50	10	9	69	50	10	9	69
# wrongly fixed inner cycles	3	0	0	3	3	0	0	3
# missed inner cycles	20	4	7	31	4	2	0	6
# geometrically acceptable closed polygon (CP)	131	58	103	292	131	58	103	292
# partially correct closed polygon	7	5	6	18	7	5	6	18
# available total polygon (TOT)	209	67	155	431	149	63	109	321
Modeling performance – polygon (MP)	63%	87%	66%	68%	88%	92%	94%	91%

Table 6.2 summarizes the evaluation of both the inner- and outer-boundaries fixed by the cycle analysis. It shows that, on average, 67% (69 out of 103) of the inner roof corners are correctly fixed by the approach, whereas the achieved modeling performance (MP) is 68% (292 out of 431). The MP is calculated based on Equation 6.5 (Section 6.1.3). The main reason for the low performance rate is misclassification of some roof segments as described in Section 6.2.1.1. The large number of missed cycles in scene1 is attributed to missing segments, more specifically entire buildings. The absolute figures of MP, on the contrary, illustrates a high performance rate (91% = 292 out of 321). Indeed, the objective of computing the absolute figures is to exclusively estimate the negative contribution of the cycle analysis approach. Higher absolute figures further reveal the robustness of the closed cycle analysis for fixing inner-boundaries having different complexities (e.g. Figure 6.12c, d, e, k), and it is safe to assume that almost all the height jumps on top of the multilayer flat roofs can be tightly fixed by the proposed method (e.g. Figure 6.12g, k). Fixing these boundaries, especially in flat roofs, remains a challenging task (Sampath and Shan, 2007; Oude Elberink and Vosselman, 2009). Considering this, the proposed method is a good solution.

In contrast to correct fixings, there are a few incorrect and missing fixings, mainly because of the absence of small roof segments, mismatch of parameters or over/under-segmentation. In fact, the absence of segments can lead to a lack of graph edges, and the resultant distorted cycles can cause

fault geometry. For example, in Figure 6.14(a) the corner *P* (arrow in Figure 6.14b) was incorrectly fixed to the corner *Q* due to the missing plane 8. When data gaps occur, defined parameters may hamper the detection of step-edges leading to a loss of connectivity with the surroundings (Figure 6.14c). The result may split separate buildings, each with its own orientation. In the case of over/under-segmentation, incorrect topological relations may occur. For example, the merging of two roof planes (4 and 7 segments in Figure 6.14a) caused the disappearance of relations (e.g. 7-3, 7-5) relevant to the vanished segment, and consequently created an incorrect relation (e.g. 3-4) with unrealistic adjacencies. These relations may create cross edges (borders) with another cycle on some occasions.

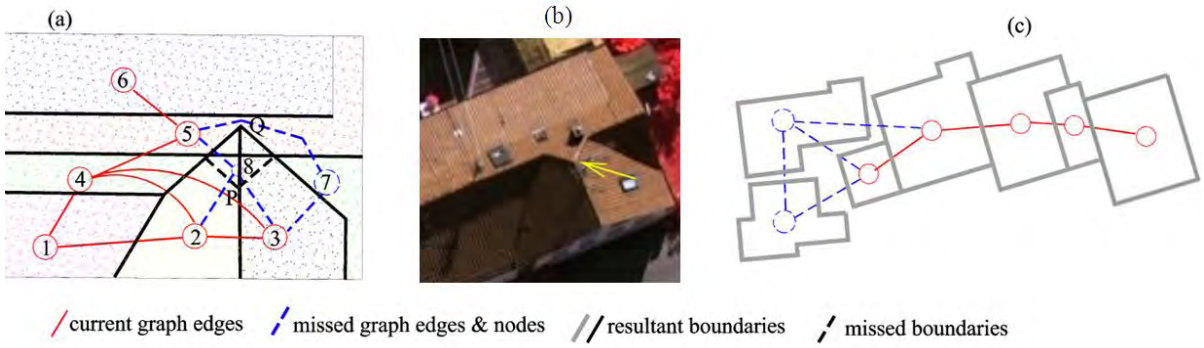

Figure 6.14: Topological defects: (a) wrong fixing due to missing roof faces plus under-segmentation; (b) corresponding image subset; and (c) loss of connectivity (missed cycles) with neighbor faces.

A widened search zone can be a solution to defects caused by insufficient parameters, but widening can cause fault topology in other places and should be restricted to adjacencies where topology is not known. Also, additional data sources (aerial images) may be very helpful in reducing defects caused by missing roof faces. By observing cross borders in RTGs, the over/under-segmentation-induced erroneous places can be identified as a plane graph should not consist of any cross borders. In such a case, an iterative segmentation approach would be sufficient to solve issues caused by over/under-segmentation.

6.2.2.3 Topological evaluation

The assessment of topological relations is carried out using overlap analysis of labeled images relevant to the reconstructed and reference models, as stated in Section 6.1.3. According to the analysis, Table 6.3 illustrates the degree of receiving 1:1 ideal instances, 69% on average, (193 out of 280) are higher than the partly related instances. Moreover, Figure 6.15 delivers a pictorial view of these values or how topologies of reference models differ with respect to reconstructed models. Since the label images are generally associated with the topmost polygon, no clear reflection about each individual plane-to-plane topological relations is given by this figure or values. As such, it is more reasonable to conclude this situation as merging of roofs rather than splitting. Indeed, in addition to (few) real merging of plane adjacencies (e.g. arrow signs in Figure 6.16b), 1:N relations are mostly caused by missing roof top chimneys, which is interpreted as merging in Figure 6.15. Thus, the RTG-based topology analysis (see Table 6.4) is more precise as it reflects each plane-to-plane relationship.

Table 6.3: Overlap analysis of label images relevant to reference and reconstructed results.

Site	Topological deviations			
	1:1	1:N	M:1	M:N
Scene1	95	1	33	2
Scene2	35	5	3	0
Scene3	63	0	42	1

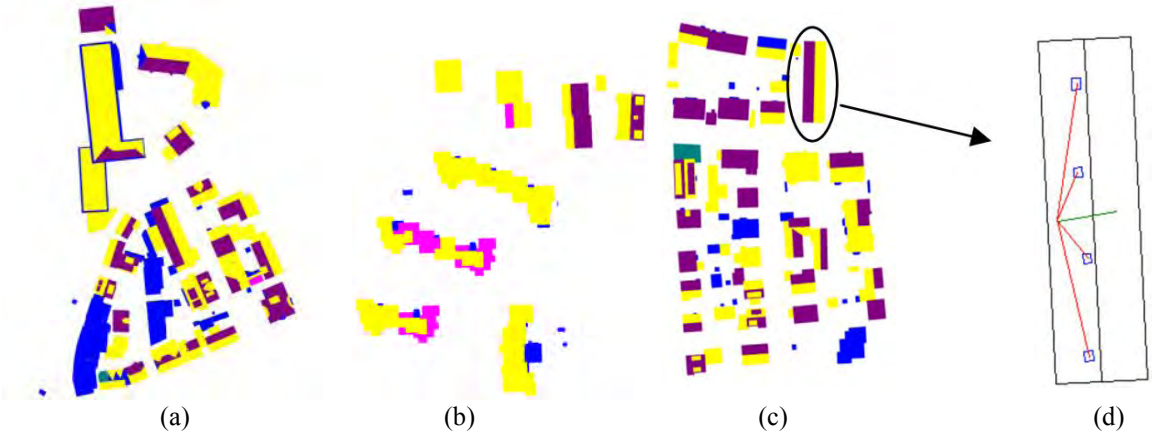

Figure 6.15: Topological differences in reference with respect to reconstruction: (a) *scene1*; (b) *scene2*; (c) *scene3* and (d) a gable roof with roof top chimneys (yellow – 1:1, magenta – 1:N, pink – M:1, dark cyan – M:N relations, and blue – missed buildings).

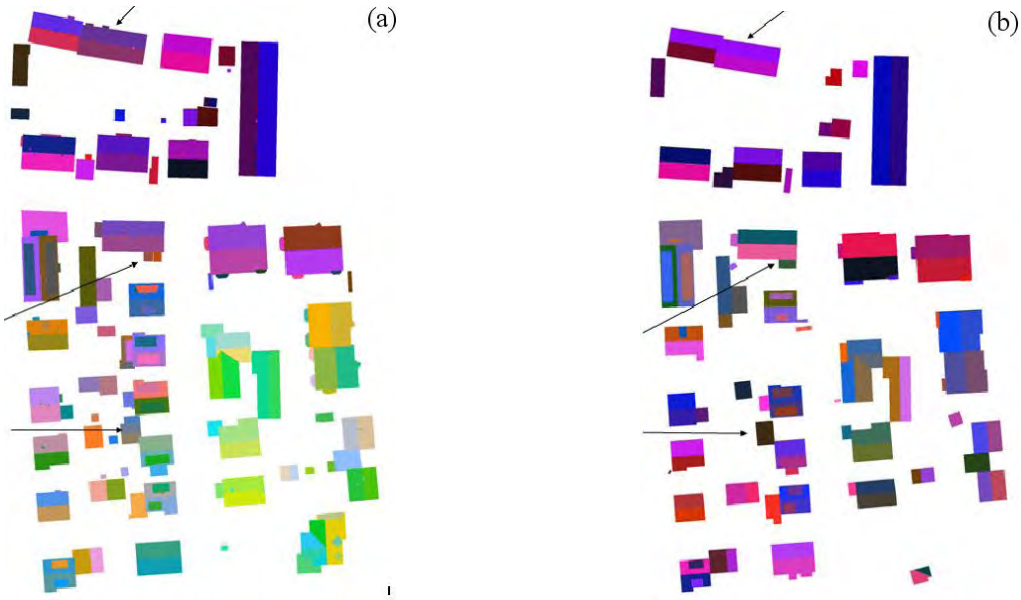

Figure 6.16: Roof planes (segments) of scene3 as label images: (a) reference segments; (b) reconstructed segments (comparison of corresponding segments reveals issues of segmentation, different colors indicate different segments).

Table 6.4 elaborates the accuracy of topology and illustrates the assessment of missing (FN) and excess (FP) graph edges in automatic reconstruction, with respect to manually constructed RTGs. In general, FP edges emerge due to FP roof segments while FN is the result of missing segments and data gaps. An example is given using a sample building marked by a circle in Figure 6.15(d), indicating where and how positive and negative alarms occur. The green line denotes correct topology, while the red lines denote wrong topology or FN graph edges caused by missing segments. Over/under-segmentation contributes to both FP and FN as it produces unrealistic adjacencies. The influence of missing segments, data gaps and over/under-segmentation to the reconstruction process is discussed in Section 6.2.2.2. As shown in Table 6.4, the absolute completeness of roof topology reaches 82%, while the overall figure falls to 70%. Encouragingly, the higher correctness (> 93%) reveals that the processing chain performs well by yielding an acceptable topological correctness of roof models.

Table 6.4: Assessment of roof topology.

Site	Overall (based on existing roofs)						Absolute (based on CE)					
	Reference	reconstructed			Completeness	Correctness	Reference	reconstructed			Completeness	Correctness
		TP	FN	FP				TP	FN	FP		
scene1	240	130	105	5	55%	96%	187	130	52	5	71%	96%
scene2	48	40	5	3	88%	93%	48	40	5	3	89%	93%
scene3	108	71	35	2	67%	97%	85	71	12	2	86%	97%

6.2.2.4 Geometrical evaluation

As explained in Section 6.1.3, the geometric quality of resulting roof models is evaluated by analyzing the deviation of polygon vertices with respect to reference models. Due to the shape changes of respective polygon candidates, very similar errors may not be expected from both directions, as such RMS_d may not be symmetrical even for the same polygon. This is evident from Figure 6.17 as it shows a similar trend in RMS_d, further illustrating that the smaller errors may often arise in many polygons, and is a common scenario especially for *scenes1* and *3*. In contrast to this, *scene2* has considerably large planimetric errors from many vertices. This is justifiable as determining a dominant direction for a flat roof gives a higher uncertainty than that related to a ridge-line. Therefore, in addition to the uncertainty which is common when determining straight line segments from point clouds, additional errors may be expected as in Figure 6.17(b).

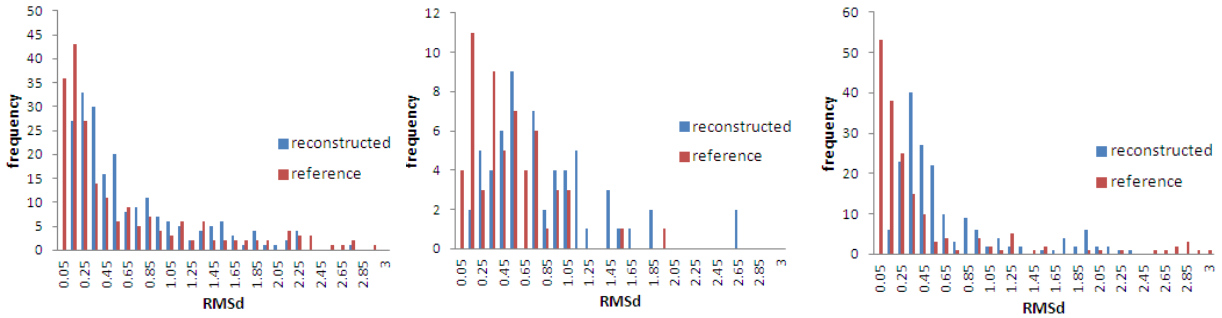

Figure 6.17: Planimetric errors of resulting roof models against the reference models: (a) *scene1*; (b) *scene2*; and (c) *scene3* (unit of X axis is in meters).

Table 6.5 shows that the mean RMS_d is in the range of 0.6m-0.8m, which is less than twice the point spacing of laser data. Table 6.5 and Figure 6.18 describe the assessment of vertical accuracy and demonstrate good height accuracy with a few large errors where small objects or height jumps exist. Errors close to step-edge locations show the uncertainty of edges (and are thus in fact planimetric errors). This error is not a failure of the cycle approach as it is common for sparsely distributed ALS data. Additionally, weakly fitted roof segments can be recognized by dark brown regions, mainly because under-segmentation of planar faces produces small discontinuations like small slope changes with neighboring planes.

Table 6.5: Geometrical assessment of roof reconstruction

Site	RMS_d (*m*) planimetry	RMS_Z (*m*) height
Scene1	0.8	0.2
Scene2	0.6	0.3
Scene3	0.7	0.1

Figure 6.18: Height errors in each scene: (a) *scene1*; (b) *scene3*; (c) *scene2*; and (d) closed up view of a building selected from *scene3* (rectangular box) with corresponding image subset.

During the quality analysis, the orthogonal distance between model planes and laser points can be used as a quality measure. Dorninger and Pfeifer (2008), and Oude Elberink and Vosselman (2011) also used it as a segmentation quality measure in the absence of reference data. This study also computes the *RMS error* between model planes and laser points by means of the orthogonal distance. The objective is to measure how final roof models fit laser points as some of the original roof planes are slightly adjusted over the course of ridge-line intersection. Figure 6.19 shows that model planes fit laser points well as the majority of planes exhibit an *RMS* error less than 0.2*m*. Higher errors occur mainly in small roof models such as dormers or garages.

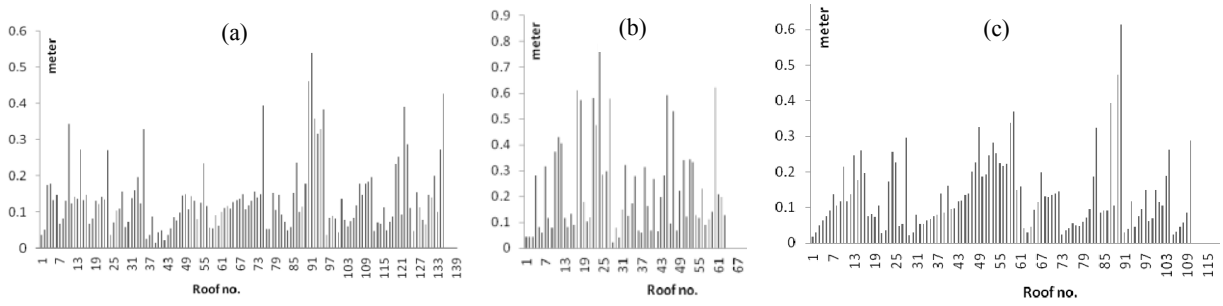

Figure 6.19: RMS error between model planes and laser points: (a) *Scene1*; (b) *Scene2*; and (c) *Scene3*.

Enforcing piecewise regularities is a key factor in maintaining the outer geometry of complex roof models. The gutter height alignment maintains the correct position of outer-boundaries, and consequently the symmetries of roof shapes. In Figure 6.20, the process maintains the symmetries of most of the gable-shaped roof pairs within ±0.1*m* tolerance, although a few buildings in *scene1* and *scene3* show a significant deviation. The deviations are caused by unequal roof inclination or non-

symmetry. In order to maintain the quality of roof fitting, constraints on inclination are not enforced, and thus deviations can be expected. Similarly, a correct alignment of gutter positions can easily be achieved even when gutters reside at different height levels (Figure 6.21a).

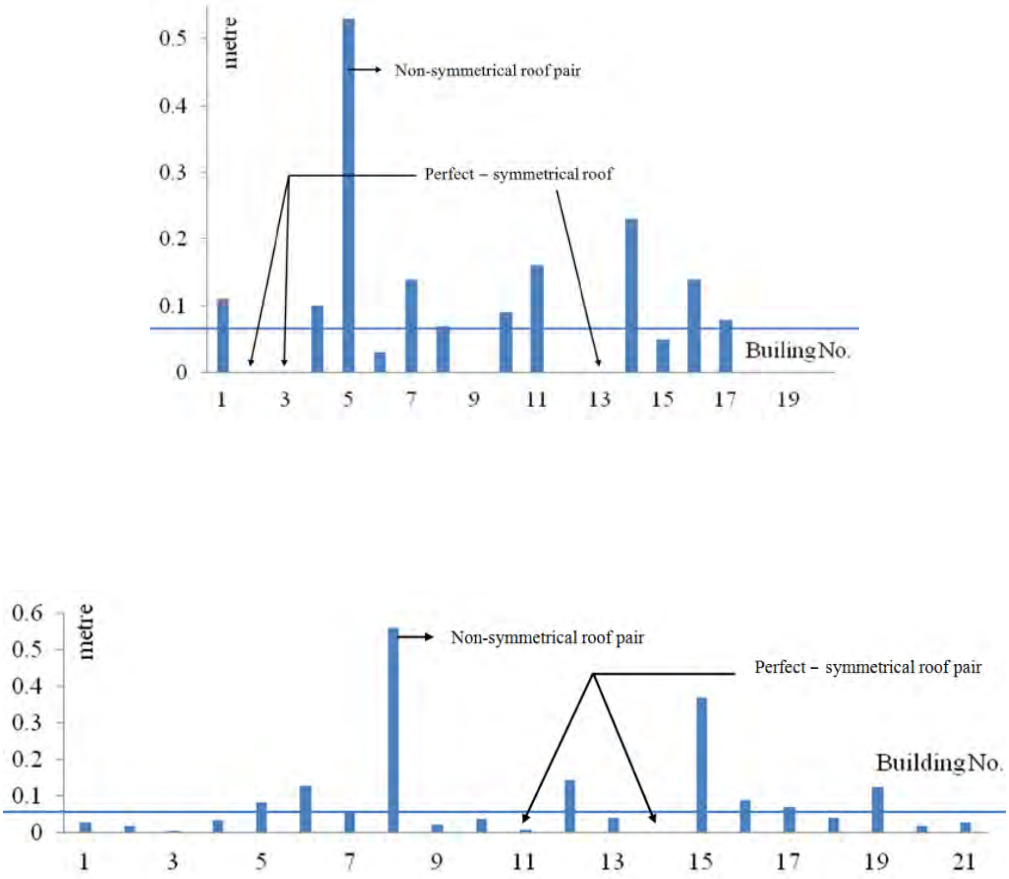

Figure 6.20: Gutter symmetry of reconstructed roof models (*scene1* and *scene3*).

The proposed orientation regularization maintains the correct geometry of multi oriented buildings. Figure 6.21(b) demonstrates that the bi-directional orientation regularization is more capable of preserving the correct geometry than the single directional orientation regularization (Figure 6.21c).

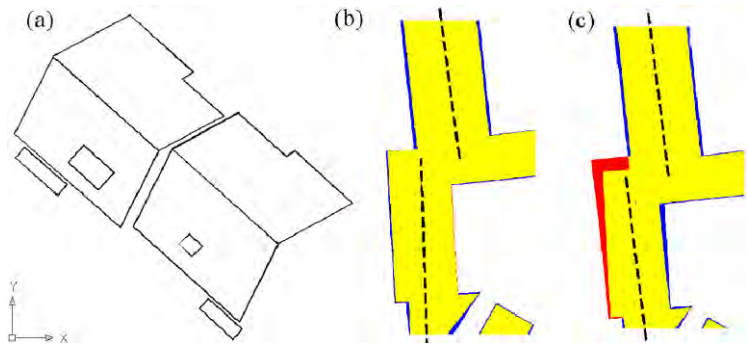

Figure 6.21: Correctness of geometry: (a) valid gutter alignment at multiple height levels; (b) orientation rectification by piecewise regularization; and (c) by single direction regularization (yellow - TP, red - FP and blue - FN effects, and dash lines - used dominant directions).

6.2.2.5 Per-object evaluation

Overall, per-object level performance of the roof reconstruction process is reported via completeness, correctness and quality, as defined in Section 6.1.3. Statistics of the measures are shown in Table 6.6.

Table 6.6: Overall assessment of building reconstruction - per object-level.

Site	Completeness	Correctness	Quality
Scene1	69.4	97.1	68.0
Scene2	68.1	98.1	67.3
Scene3	74.0	93.8	70.6

In general, end products of the initial roof reconstruction exhibit 93-98% correctness per roof plane. However, the completeness is fairly low, as almost 30% of the roof planes are missing in the final closed polygons. According to the fluctuations of the first two measures, the quality remains within the range of 67-71%. Possible error sources for low completeness are over/under-segmentation, misclassification of building segments, incorrect roof plane extraction, and the inability to make closed polygons due to some missing feature lines. It can be concluded that the negative contribution of the adopted merging step is greater than that of other defects. Although the merging step causes an incorrect growth of terrain points over building points, it does not affect the quality of building segments because subsequent steps relies on the original attribute of planar segmentation. Figure 6.22 exhibits how correctness, completeness, and quality behave in a roof plane area. The graph shows that the method performs well in terms of large roof planes with all performance measures reaching their peak. In contrast, low completeness is found in small objects with an insufficient number of points.

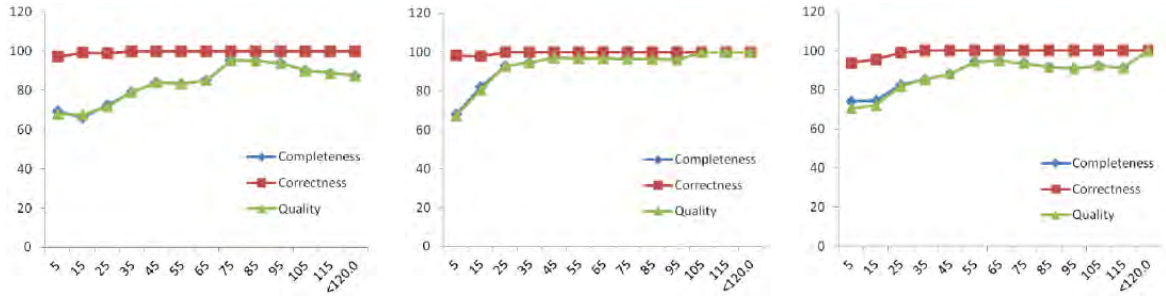

Figure 6.22: Overall quality of roof plane (cumulative) in scenes 1, 2 and 3 respectively – X and Y axes indicating areas and percentages.

6.2.2.6 Per-pixel evaluation

Spatial difference between the reconstructed and reference models, at pixel level, is shown in Figure 6.23. Large blue regions indicate missing buildings caused due to feature extraction. Hence, when errors caused by reconstruction are concerned, effect due to large blue regions can be left out from the analysis. Neglecting the large FN errors, it can be concluded that no large errors occurred by the processing scheme itself. However, erroneously detected vegetation having regular shapes was a main contributor for the FP errors. Additionally, under estimation of building size caused by line fitting for boundary points is the main source of FN errors.

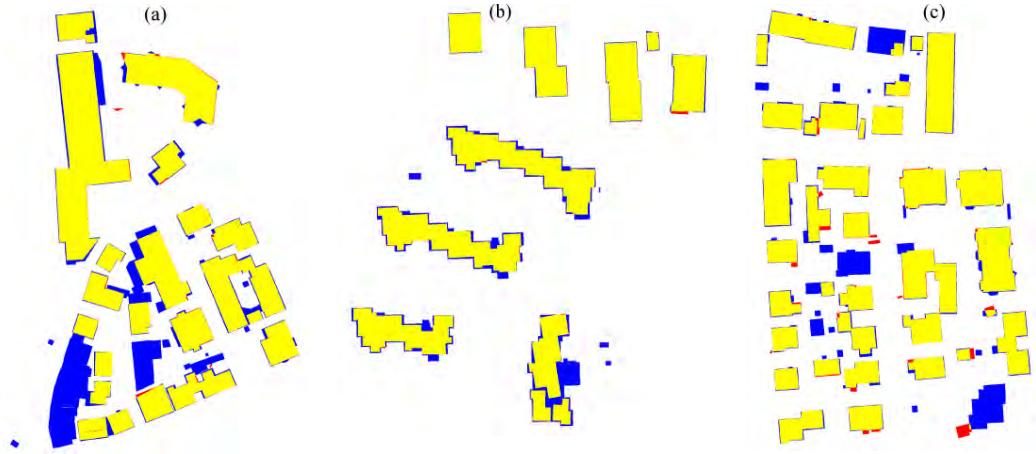

Figure 6.23: Pixel-based analysis of roof reconstruction in each scene: (a) *scene1*; (b) *scene2*; and (c) *scene3* (yellow-TP, blue-FN and red-FP).

6.2.2.7 Steering parameters

Table 6.7 summarizes the fundamental parameters used in the reconstruction approach. The parameters are set by the user, based on his knowledge about the data and landscape. In terms of scene complexity, for example having closely located feature lines, *scene1* and *3* are a bit complicated than *scene2*. This is illustrated by the narrow *half-width* equaling to 0.7*m* in Table 6.7. On the other hand, *scene1* consists of shorter edges than the other two scenes, which leads to the acceptance of short ridge-lines and step-edges roughly equaling to 0.5*m*. As for the remaining parameters, they behave in a similar manner, and thus, are set equally for every scene.

Table 6.7: Explicitly defined parameters

Parameter	Values (*m*)		
	Scene1	*Scene2*	*Scene3*
Min. Distance to accepting a topological relationship	0.5	1	1
Half-width of common boundary zone	0.7	1	0.7
Min. Height-range to be a step-edge	0.3	0.5	0.5
Distance threshold for reducing convex hull effect	2	2	2
Distance of a point to line threshold for least square line fitting	1	0.8	1
Angular threshold for rectification of orientation	20	20	20
Simplification threshold, including for pipeline-like	0.8	0.8	0.8
Height range for gutter height alignment	0.35	0.35	0.35

6.2.3 Model refinement by integrating image data

Model refinement makes use of the results of the roof models reconstructed from ALS point clouds. Therefore, the same test scenes are used for evaluating the performance of the refinement methods developed in Chapter 5. The same evaluation methods described in Section 6.1.3 are further used, since the outcome of the refinement is also a 3D roof model with some modified positions for edges or building corners. Similar to the previous section, the first experimental results are presented in this section. As the main objective of the model refinement (Chapter 5) is the enhancement of the planimetric accuracy of roof outlines, in particular weakly defined edges, the geometric accuracy of the roof models is evaluated. This is followed by the analysis of topological accuracy, per-object and per-pixel based analyses. Since it is necessary to compare the refined results with respect to initial results, the results of the refined models are analyzed in the form of a comparison under the afore mentioned themes.

6.2.3.1 Results

This section presents the results of the proposed building reconstruction scheme, including the refinement process. Complete building models of each test scene is visualized and discussed to demonstrate the results from each step of the reconstruction procedure. Figures 6.24-26 exhibit the refinement results as wireframe models, models projected on to image space, and complete 3D building models after adding wall components for three test scenes. According to the visual comparison with respective photographs, it is shown that all buildings in each test scene were reconstructed correctly.

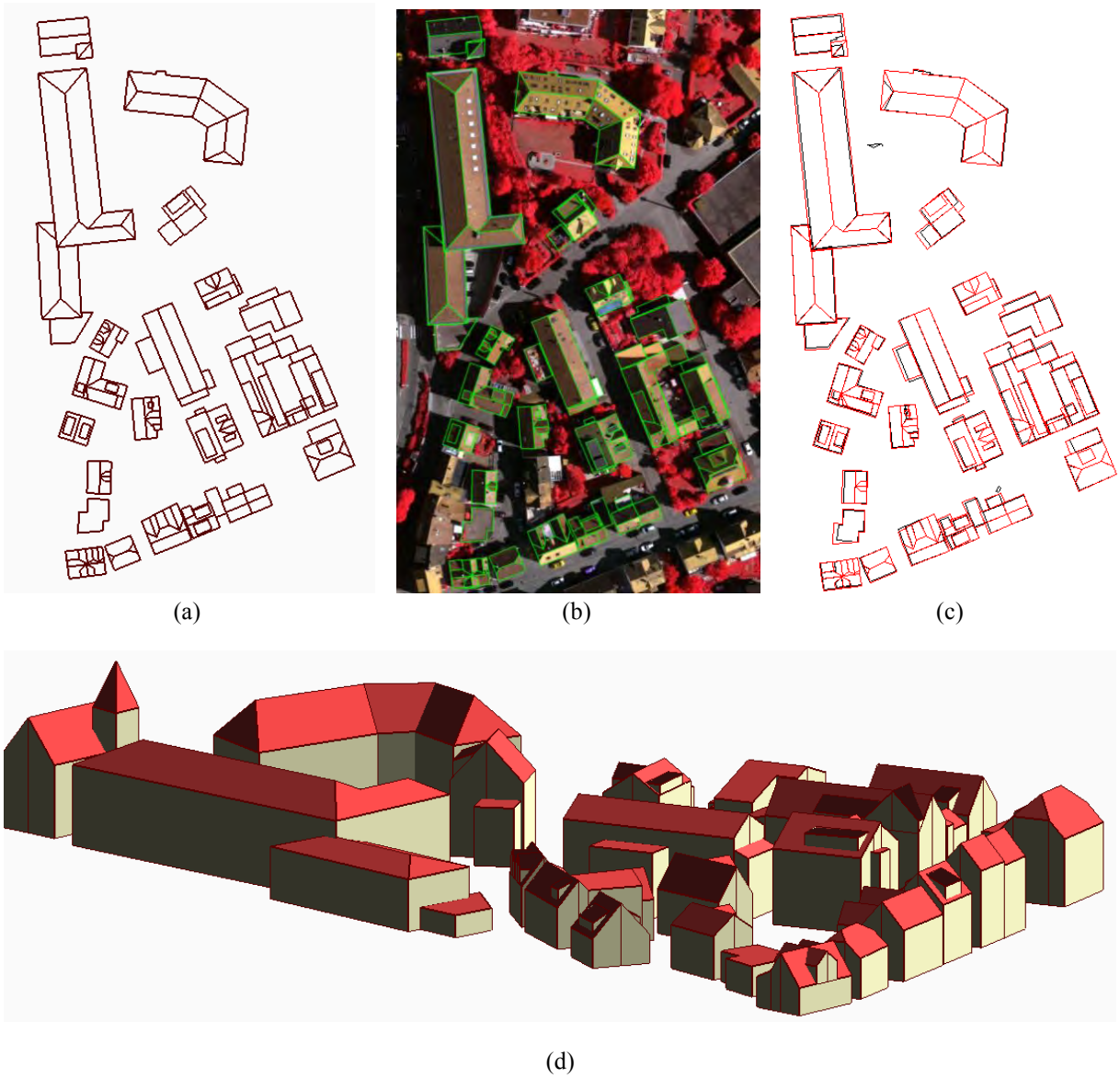

(a) (b) (c)

(d)

Figure 6.24: Refined building models in *scene1*: (a) top view of the refined models; (b) refined models are overlaid on top of the respective image; (c) superimposing of initial and refined roof models; and (c) complete 3D building models with wall segments (brown – roof outlines, green – projected refined models, black – initial model lines, red – refined model lines).

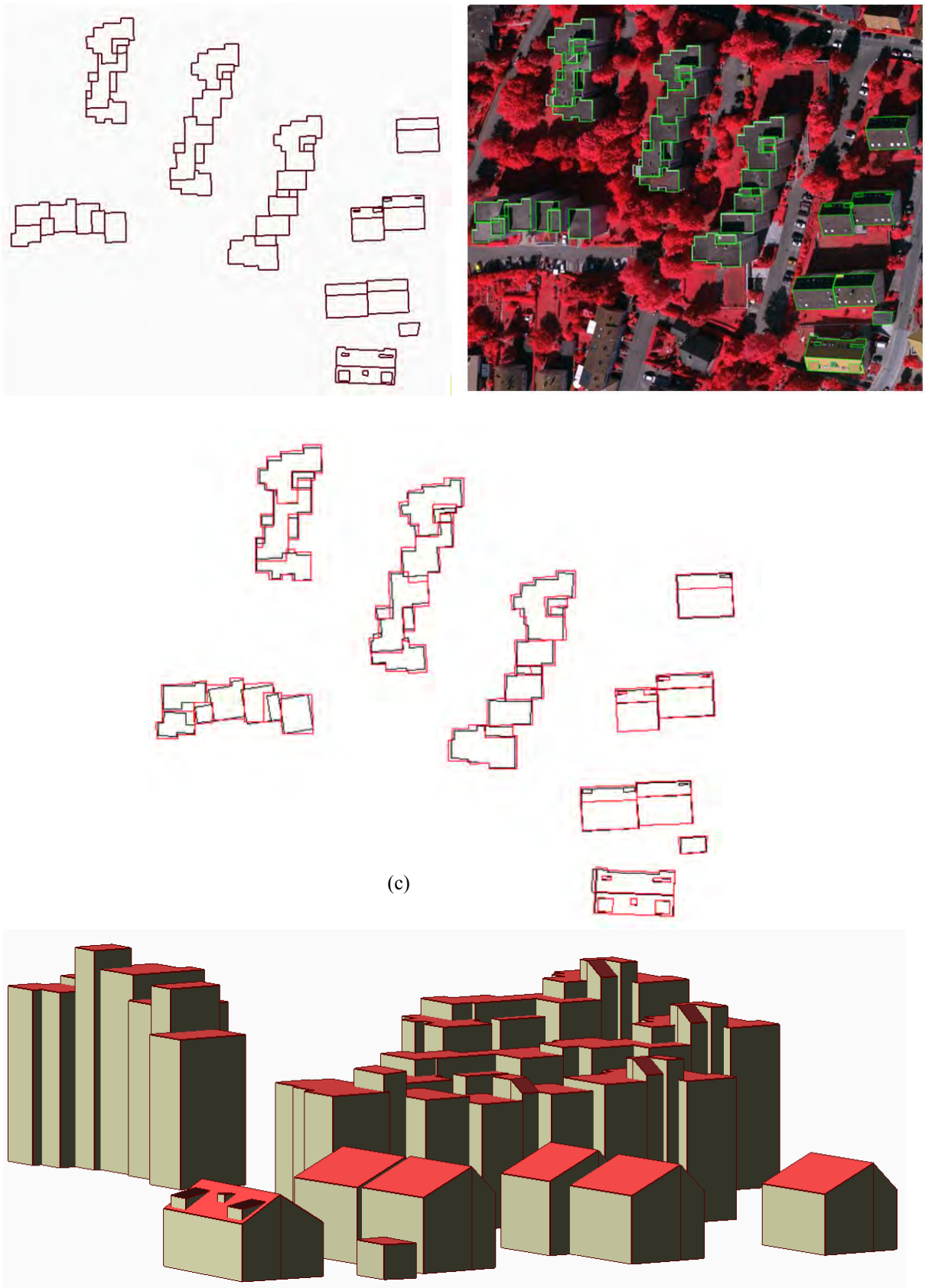

(c)

(d)

Figure 6.25: Refined building models in *scene2*: (a) top view of the refined models; (b) refined models are overlaid on top of the respective image; (c) superimposing of initial and refined roof models; and (c) complete 3D building models with wall segments (brown – roof outlines, green – projected refined models, black – initial model lines, red – refined model lines).

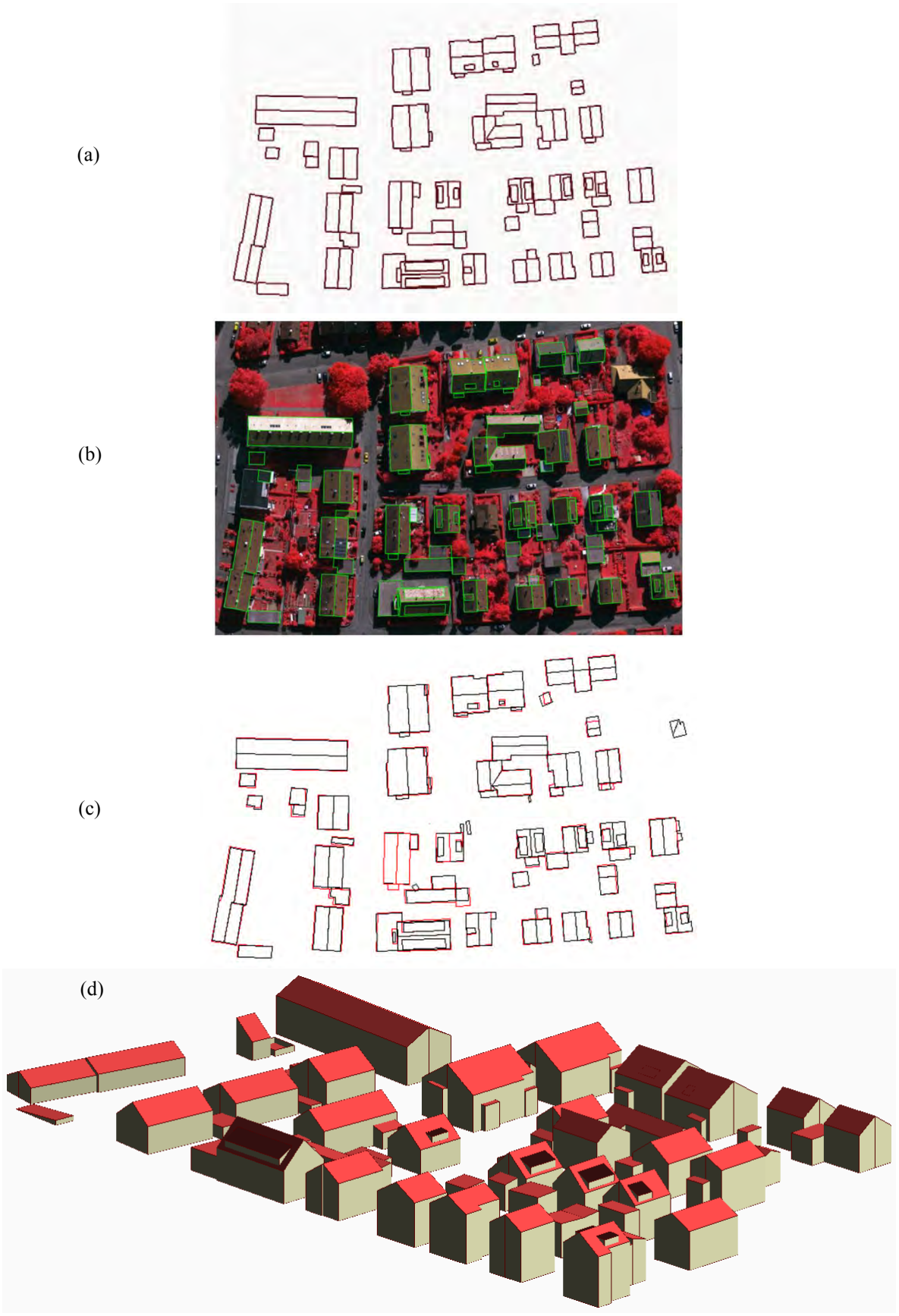

Figure 6.26: Refined building models in *scene3*: (a) top view of the refined models; (b) refined models are overlaid on top of the respective image; (c) superimposing of initial and refined roof models; and (c) complete 3D building models with wall segments (brown – roof outlines, green – projected refined models, black – initial model lines, red – refined model lines).

A closer view of some selected building models is shown in Figure 6.27, and it indicates that the shape deformations do not appear any longer. Moreover, split separate buildings and some other data gaps that were in the initial models have now been overcome.

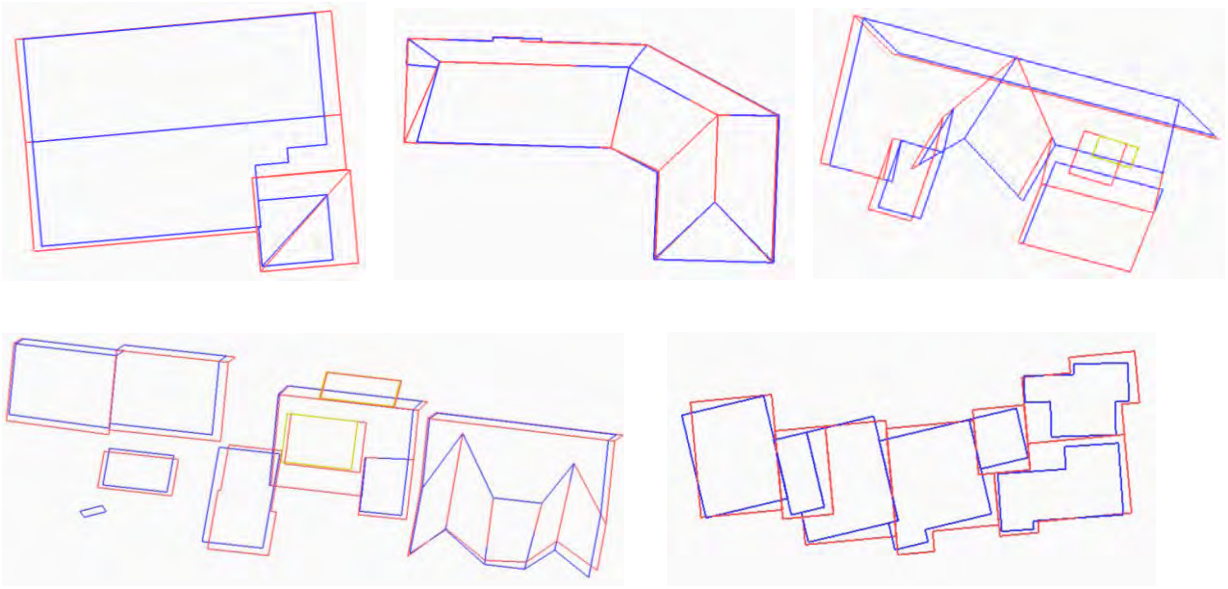

Figure 6.27: Superimposing of refined roof models on top of the initial roof models – closer view (blue – initial model, red – refined model, beige – dormers in initial models).

In principle, the missed buildings cannot be considered in the refinement process because image lines are searched based on the guidance of initial roof models. However, when a mismatch arises between model edges derived from ALS, and 3D line segments derived from image data, the defect is corrected with respect to image information assuming that it is a result of some defective reconstruction of the initial model. Therefore, new buildings or building components cannot be expected from the refined roof models, only significant improvements of the geometry and topology of the initial roof models can be observed, as shown in Figures 6.24 - 6.27. However, defects relevant to Figure 6.14(a) still remain as the process didn't attempt to rectify segmentation errors. In order to get a clear idea of the strengths and weaknesses of the refinement process, a quantitative analysis is given in the following sections.

6.2.3.2 Comparative evaluation on roof geometry

As shown in Figure 6.28, a similar error pattern can be seen from the planimentric positional errors in refined roof models when compared to planimetric errors in initial models. However, incidences of having higher positional errors like in the initial models are significantly decreased, especially in *scene2*, so that no large positional deviations appear as observed in the Figure 6.17. This statement is further confirmed by Figure 6.29, showing error patterns relevant to before and after the refinement process. It can be concluded that roof outlines in the refined models are closer to reality because a higher percentage of positional errors falls within less than $0.15m$, which is roughly equal to twice the ground sample distance of the image data. Thus, a significant improvement can be seen from the geometry of refined roof models.

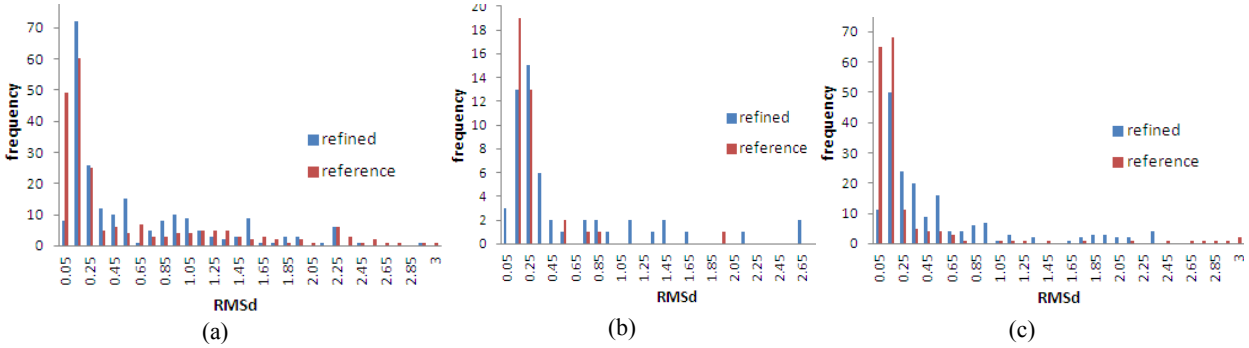

Figure 6.28: Planimetric errors of refined roof models with respect to reference models: (a) *scene1*; (b) *scene2*; and (c) *scene3* (unit of X axis is in meters).

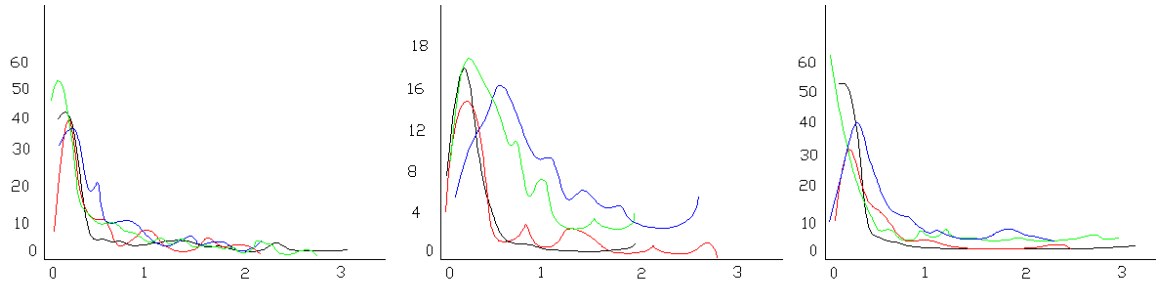

Figure 6.29: Error patterns of the planimetric deviation of results in *scene1*, *scene2* and *scene3* respectively: (red – errors in refined model with respect to reference; black – errors in reference with respect to refined; blue – errors in initial model with respect to reference; and green - errors in reference with respect to initial model): X, Y axes denotes planimetric deviations in meters and degree of frequency respectively.

In addition to the above graphs, Table 6.8 shows that the mean RMS_d is going down, on average, to $0.55m$. Concerning the vertical accuracy of refined models, it is almost equal to the resulting models relevant to point clouds. It is an obvious fact because plane parameters derived from the initial roof models were not updated in the course of the refinement process.

Table 6.8: Overall positional accuracy of refined roof models.

Site	RMS_d (m) planimetry	RMS_Z (m) height
Scene1	0.78	0.2
Scene2	0.34	0.3
Scene3	0.53	0.1

Label images of the difference of DSMs (see Figure 6.30) elaborate that the height errors close to the step-edge locations are restricted to a very narrow area. This is because the planimetric uncertainty of step-edges has decreased. In contrast to this characteristic, weakly fitted roof segments still appear in a similar way to the previous model results (Figure 6.18). Although inner bounds of some roof planes are updated via step-edge locations (e.g. in Chapter 5, Figure 5.30 and 5.32), some segmentation issues still remain. Considering the segmentation issues, additional image processing techniques are needed, for example extraction of homogeneous regions from image space for representing roof planes. However, it is not considered during the reconstruction process as it is out of the scope of this thesis.

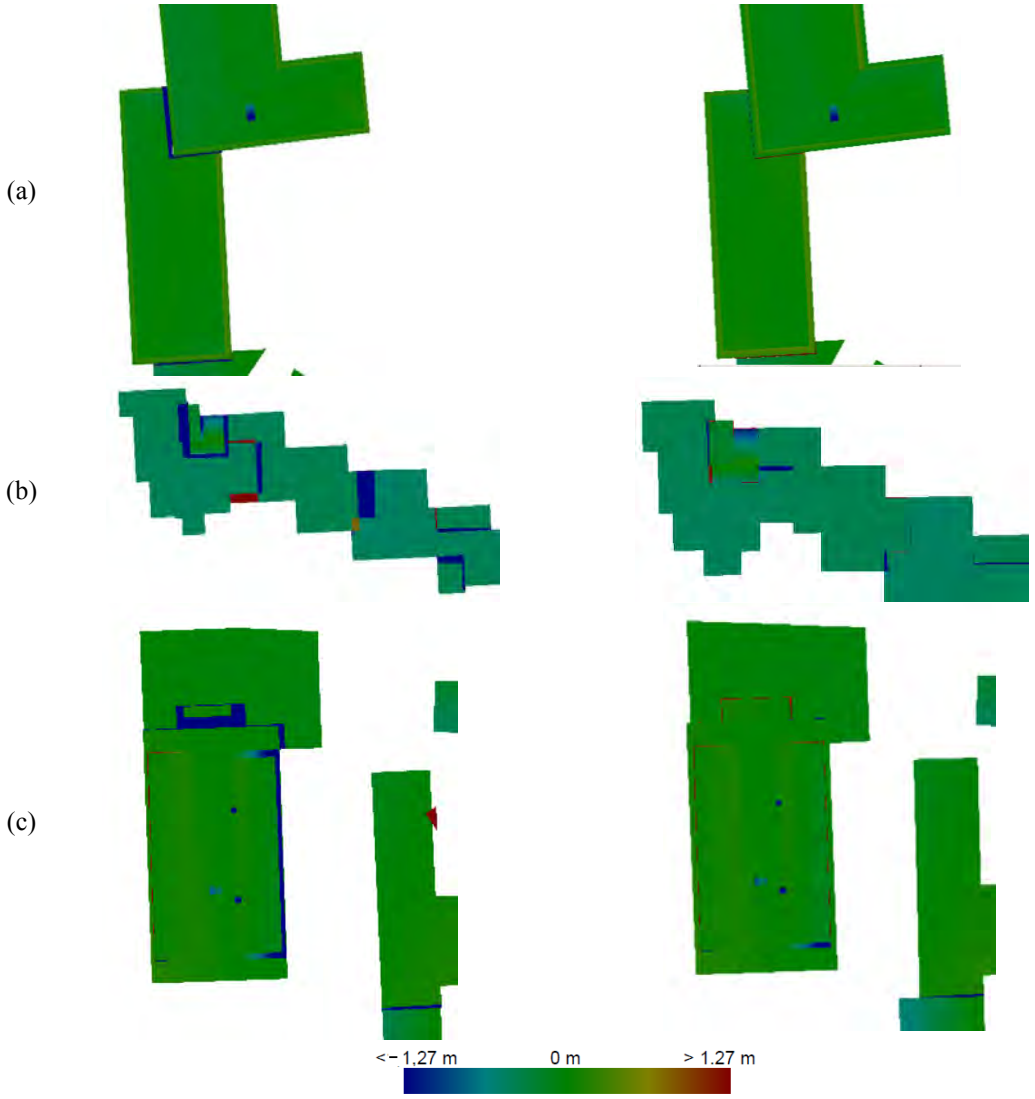

Figure 6.30: Comparison of vertical accuracy around step-edge locations between initial modes (left) and refined models (right): (a) sub set of scene1; (b) sub set of scene2; and (c) sub set of scene3.

Figure 6.31 compares the impact of the refinement process on gutter symmetry. The comparison says that the refinement further preserves the symmetries of roughly similar number of gutter pairs. Additionally, less symmetrical pairs, shown by blue arrows in Figure 6.31, are brought closer to symmetry. Also, a low number of occasions of rough symmetrical cases (e.g. $0.1m$-$0.2m$ range) are increased by the refinement process. However, due to the unavailability of reference data for the positions of gutter lines (not included in the ISPRS benchmark reference data), it is diffucult to further analyze which gutter pairs follow the symmetries and which do not. Since buildings in *scene2* don't follow symmetries (because they are flat and even available gable types building don't follow a symmetrical rule), it is left out from these analyses.

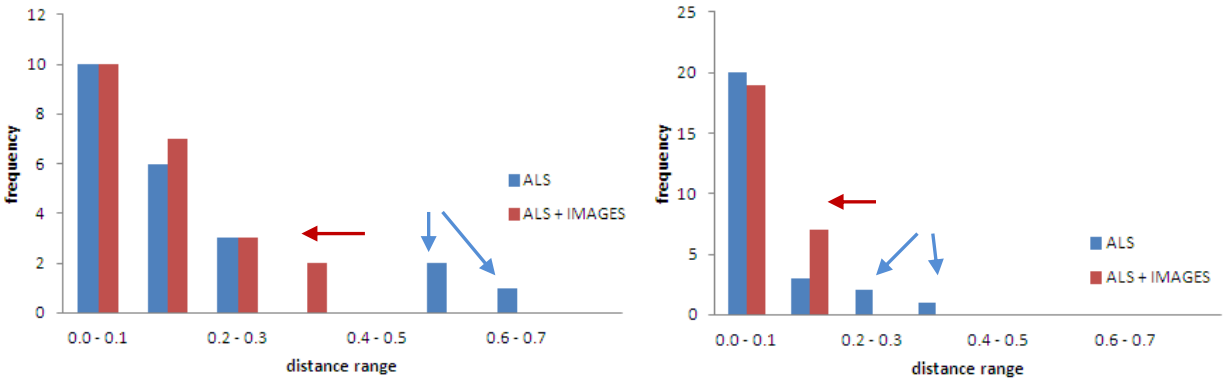

(a) (b)

Figure 6.31: Comparison of gutter symmetries of refined roof models with initial model data: (a) *scene1* and (b) *scene3* (blue arrows – gutter pairs which don't follow symmetries properly, dark red arrow - direction of movement).

Additionally, the special corner fixing strategy (see Section 5.7.3.2) properly maintains the correct geometry of roof models. Figure 6.32 demonstrates that none of the horizontal or vertical errors associated with the concave corner exists. As such, the maintaining of unequal gutters at two different height levels, while preserving the 90° concave corner, is correct than the normal procedure of snapping gutters into one convergence position on the corresponding ridge-line. Besides, these illustrations further reveal that when no single convergence is given by the intersection of three (or more) stable edges, the strategy of inserting the new node correctly retains the roof geometry and object complexity. Further discussion on the geometry of roof models is described under the per-pixel level evaluation in Section 6.2.3.5.

(a) (b) (c) (d)

Figure 6.32: Roof corner geometries at object complexities: (a) convergences of gutters having unequal heights; (b) intersecting while preserving the right angle corner; (c) planimetric errors; and (d) height errors at given corners (arrows indicate where the errors are).

6.2.3.3 Comparative evaluation on roof topology

Since the second objective of the model refinement is to rectify (some of) topological defects identified in initial roof models, it is of interest to assess how roof topology is enhanced by the refinement process. For the topological improvements, if any, the main contribution was given by the rectifications of defective step-edges or recovering of interlink connections which were hidden in the initial model.

As no intentional effort is made to solve segmentation issues in the refinement process, the overlap analysis doesn't exhibit substantial improvements from the topological point of view, which is an expectable fact. However, according to the Figure 6.33 which shows average instances of overlap

relations of *scene1*, *2* and *3* before and after refinement, the refinement process contributed towards increasing the 1:1 relations and under-segmentation instances slightly, while reducing over- and multiple-segmentation issues. The reason for the increase in under-segmentation would be the growth of some polygons owing to the refinement. Here, the growth would occur mainly along the roof outlines which exhibit some minor errors in the process of deriving object space boundary edges from image data. The shadow effect would probably have contributed to this.

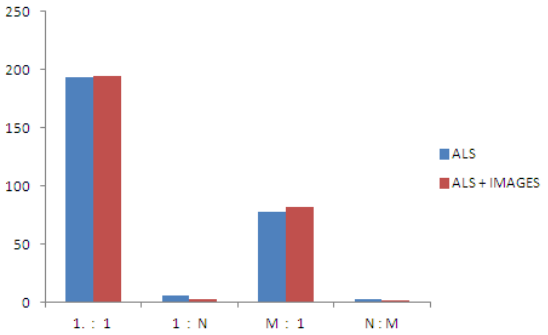

Figure 6.33: Total overlap relations for *scene1 – scene3* (X and Y axes indicate type of relations and their corresponding number of occurrences).

Interestingly, Table 6.9 illustrates that the absolute topological correctness of the refined models are almost 100%. However, due to the availability of three FP edges, correctness of *scene1* reached only up to 98%. Similarly, topological completeness is also substantially raised and reached nearly to, on average, the 90% limit. Although the refinement process didn't create new graph edges for some boundary updating, for instance Figure 6.34(a), for the purpose of this analysis, new graph edges were created after analyzing the buildings having *step-edge* relations. Indeed, when the updated *step-edge* goes beyond the boarder of its direct adjacent segment (segment 1), the refinement process doesn't create a new graph edge (blue line in Figure 6.34b). Because rather than doing a graph based analysis, new vertices of the segment 3 can simply be obtained by the intersection of new edges. To create a new graph edge, end-points of an updated step-edge (e.g. P, Q) are checked to identify whether they lie within the range of counter edges, for instance BC in this case, as shown in Figure 6.34(c).

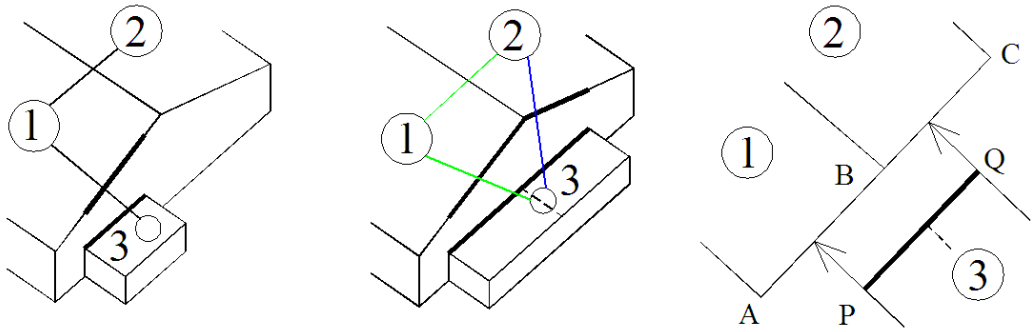

(a) (b) (c)

Figure 6.34: Creation of new graph edges relevant to step-edge updating (green lines – TP edges, blue line – FN edge).

The degree of increment, shown in Figure 6.35, further illustrates that the average topological improvements are considerable.

Table 6.9: Assessment of roof topology – refined roof models.

Site	Absolute values (based on CE)					
	Reference	Reconstructed			Completeness	Correctness
		TP	FN	FP		
scene1	187	15	30	3	84%	98%
scene2	48	47	1	0	98%	100%
scene3	85	75	10	0	88%	100%

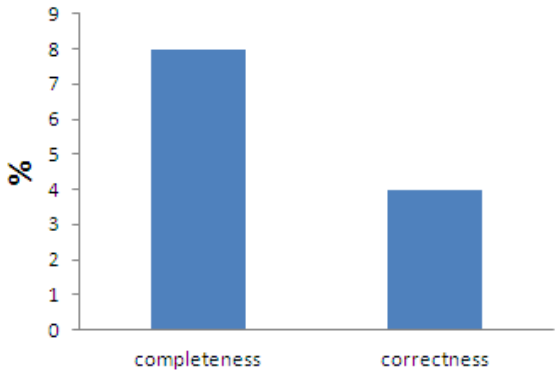

Figure 6.35: Degree of improvement in topological accuracy.

When considering the main contributions by the refinement process on to roof topology, they can be listed out as (i) combining of the split separate buildings into one connected building having step-edges in between roof planes (Figure 6.36a), (ii) altering of the erroneous step-edge relation in to ridge-line relation (Figure 6.36b), and (iii) establishing of defective hip-roof part (caused by data gaps) by inserting an equally elevated gutter line and replacing a ridge-line (Figure 6.36c).

Comparison of Figures 6.36(a – column i and iii) reveals that only one FN edge (blue line) exists in the refined model, which is impossible to rectify by the strategies used in the refinement process because the corresponding roof plane was missing in the initial model. Similarly, in other cases, it is clear that the accuracy of roof topology increased as the number of green edges is raised. Consequently, FN pixels decreased as the blue regions (refer to columns ii and iv in the Figure 6.36) declined comparatively after the refinement process.

However, as mentioned in Section 6.2.2.2, the erroneous corner fixing shown in Figure 6.14 (Q point) still remained as it is. This is because; (i) refinement process does not take into account the missing segments within this study, and (ii) extraction of new line segments which are connected to the projected model edges in image space was not attempted. The solutions for this type of issues will be given in the next chapter.

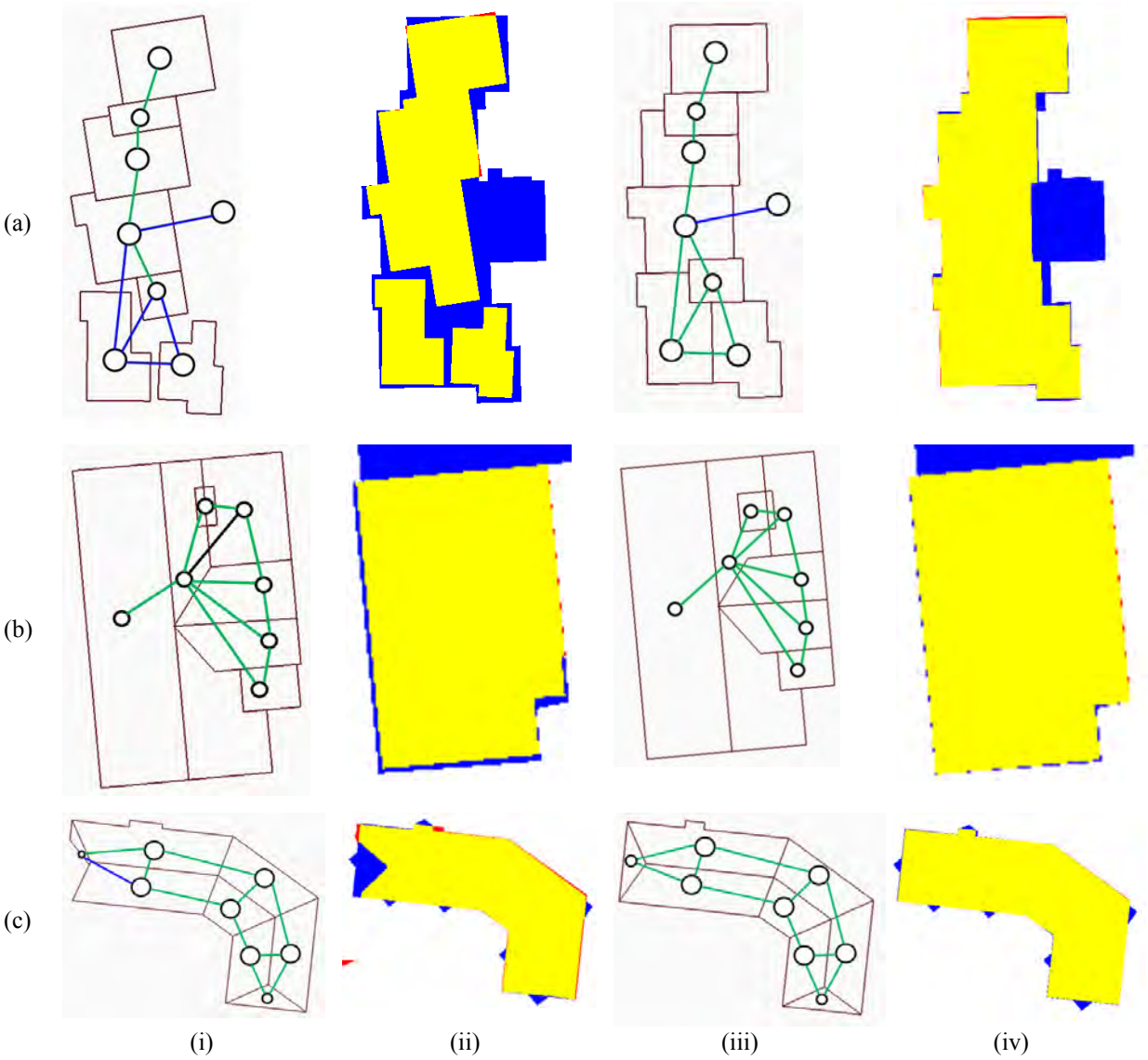

Figure 6.36: Contribution of refinement process towards the roof topology: (a) case of split separate buildings; (b) case of altering the feature lines; and (c) case of rectifying defective hip-roof part – in column: (i) initial model together with RTG; (ii) pixel-based evaluation result of 'i'; (iii) refined roof model together with rectified RTG; and (iv) pixel-based evaluation of 'iii'. (red, green and blue - edges in RTG indicating FP, TP, and FN edges respectively while yellow – TP, blue – FN and red – FP pixels).

6.2.3.4 Comparative evaluation on per-object level

Table 6.10 reveals that in all three test scenes, the overall correctness of the refined results reached the peak *i.e.* 100%. This indicates that there are no FP roof planes. Of course, some erroneous roof planes that existed in the initial result were discarded during the refinement process. If any line segment (3D boundary edge) relevant to a certain polygon is unable to be derived from image data, then assuming that such a polygon doesn't exist in reality and that it may belong to vegetation, those planes were removed. Results indicate that those are FP and belonging to vegetation. Although one small garage, which is fully covered by the vegetation (and didn't deliver a single line segment relevant to image data), was dropped out based on this rule, the statistics demonstrated the applicability of this assumption.

Table 6.10: Overall assessments of refined buildings - per object-level.

Site	overall		
	Completeness	Correctness	Quality
Scene1	73.3	100	73.3
Scene2	71.0	100	71.0
Scene3	73.6	100	73.6

Figure 6.37 is the average per-object evaluation results in terms of roof planes, and it illustrates that the correctness, completeness and quality of refined roof planes are also increased slightly by the refinement process. Since the refinement process considers only the available buildings in the initial modeling results, *i.e.* excluding the missed buildings (FN) caused in the feature extraction, it is impossible to expect significant improvements on the completeness and quality.

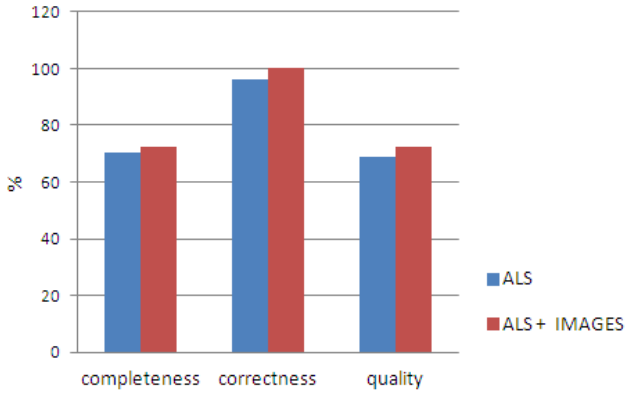

Figure 6.37: Average completeness, correctness and quality of model reconstruction before and after refinements (*scene* 1-3) – per-roof plane.

Figure 6.38 illustrates the per-object level overall completeness, correctness and quality of roof planes as a function of the area covered by a plane, which is very similar to the pattern given by the initial roof models (Figure 6.22). A better comparison is given in Figure 6.39, which shows the difference between two situations or how refinement has affected roof planes with respect to the area. As one can see in Figure 6.39, improvements in all three indices occurred mainly in roof planes whose area < $40m^2$. However, irrespective to the area, the planimentric positional accuracy has risen substantially in all buildings. Therefore, from these statistics, the improvements due to the refinement are not clearly visible. Therefore, the per-pixel evaluation has been done (Section 6.2.3.5).

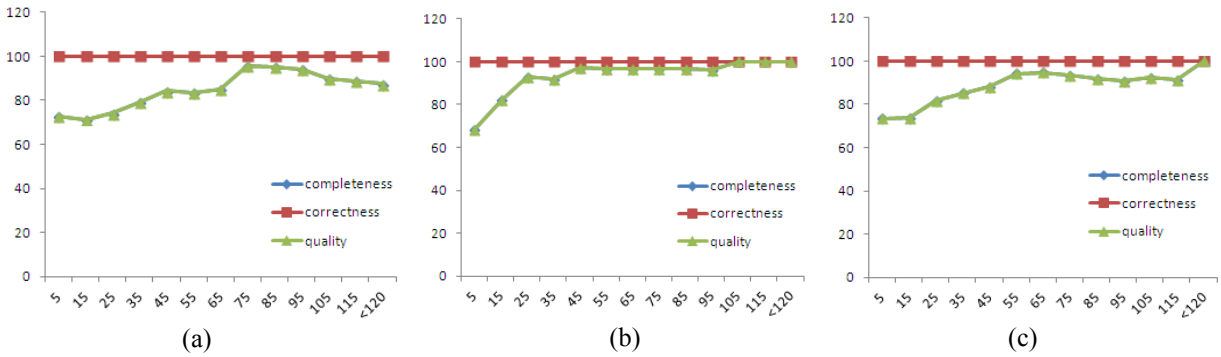

Figure 6.38: Overall completeness, correctness and quality of roof plane (cumulative): (a) *scene1*; (b) *scene2*; and (c) *scene3* – X and Y axes indicate areas (in square meters) and percentages.

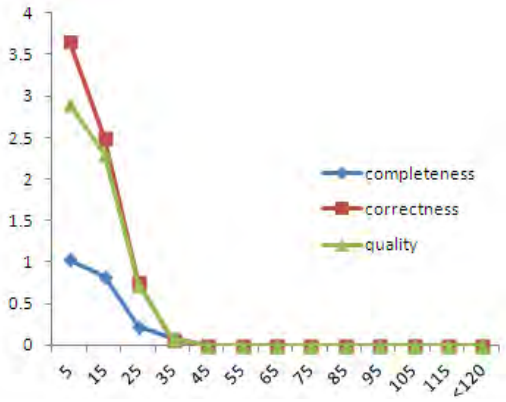

Figure 6.39: Average enhancements done by the refinement step towards completeness, correctness and quality indices (X and Y axes indicate degree of each measurer and their improvements).

6.2.3.5 Comparative evaluation on per-pixel level

Generally, the FP (red) and FN (blue) polygons, or parts of polygons, are reduced substantially while increasing the TP (yellow) due to the planimetric and topological enhancement obtained during the refinement process, which is evident by Figure 6.40. Large blue regions should be left out from the analysis as they are missed buildings in the course of feature extraction. Since no attempt is made to extract corresponding missed buildings from the image data, it is reasonable to do so. Comparison of per-pixel results relevant to initial models (shown in Figure 6.23) with the refined results clearly show that the red and blue regions appearing along the roof outlines are now substantially reduced. Of course, there still exist very narrow blue and red regions. These regions are probably due to errors in line extraction owing to the shadow effects, erroneous line matching which were fitted with given scene constraints, effect of rectifications, for instance erroneous alignment of defective eaves, and deviation of reality from their common regularities. Further experiments are needed for improving these situations.

(a) (b) (c)

Figure 6.40: Per-pixel level performance of roof reconstruction: (a) scene1; (b) scene2; and (c) scene3 (yellow-TP, blue-FN and red-FP).

In order to study the impact of the model refinement step towards building reconstruction in detail, some cases where problematic issues existed in the initial models were chosen. For recognizing their locations, please refer to arrows in Figure 6.40.

Figure 6.41(a) illustrates an effect due to the erroneous recognition of attached vegetation as the roof plane, leading to a FP error. This was successfully avoided based on the assumption "polygon which doesn't deliver any line segments from image data may represent an erroneously reconstructed roof". Similarly, Figure 6.41(b, c) shows some other examples that were able to be solved using the same criterion. Figure 6.41(d, e) illustrates erroneous overhangs caused by under-segmentation. In reality, these were effects due to the merging of close vegetation with the roof planes. All these effects were rectified during the refinement process. Combining the above used line discarding rule together with the structural arrangement of buildings, in particular by knowing the dominant horizontal gutter and whether it is a member of a gable roof, such deformations were solved while maintaining the roof outlines at their correct planimetric positions.

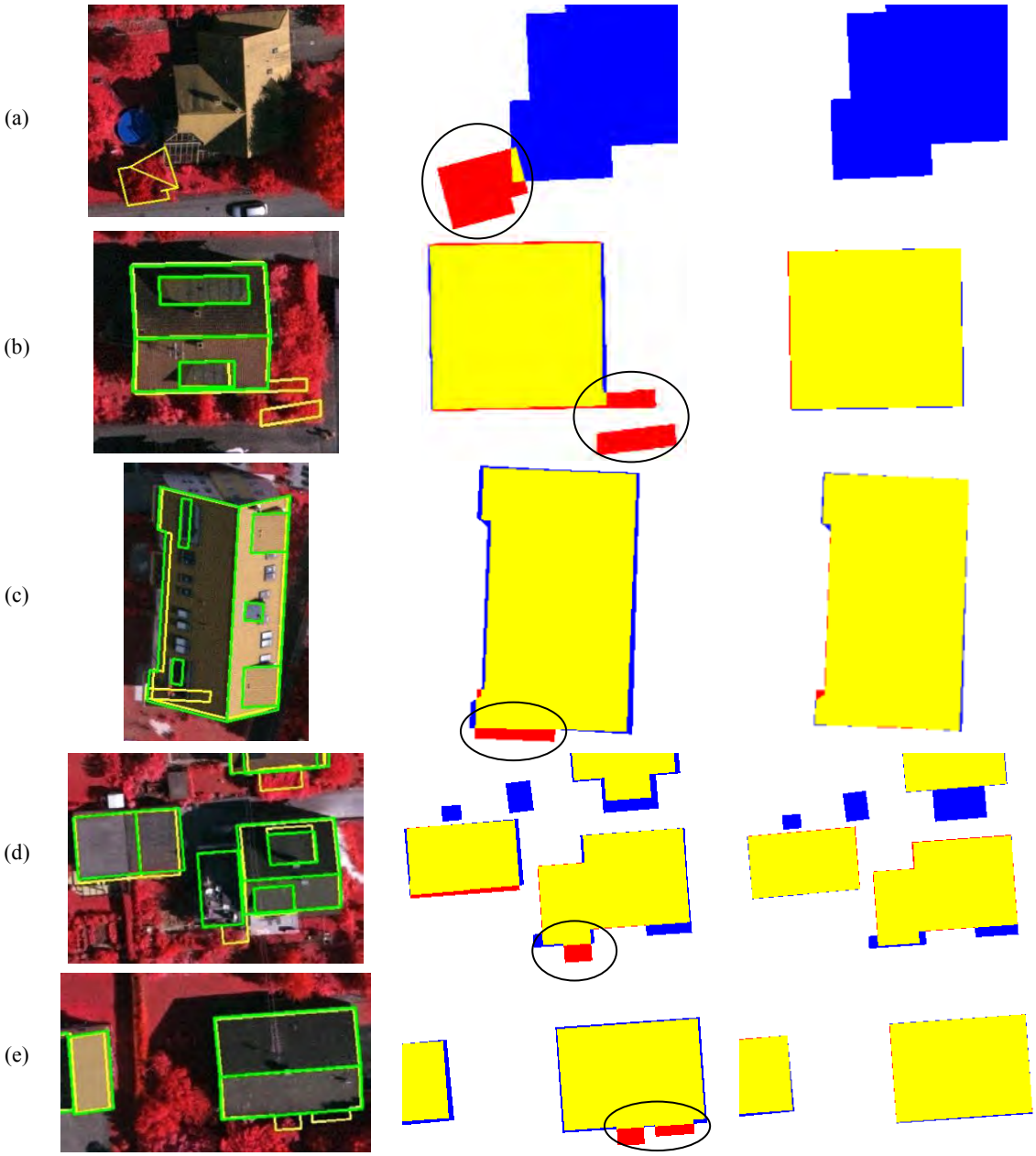

Figure 6.41: Rectification of errors caused by FP roof planes: (a); (b); and (c) erroneously detected vegetation polygon as roofs planes; (d) and (e) merging of attached vegetation leading to erroneous roof overhangs: (yellow lines – projected initial model lines, green lines – projected refined model lines, yellow – TP pixels, red – FP pixels, blue – FN pixels, and circle – erroneous locations).

Figure 6.42(a) shows an error caused by the orthogonality constraints imposed during the regularization of rectilinear lines fitted for representing the roof outlines. The effect is acceptably solved by the derived 3D line segments from image as described in Section 5.7.1. In this case, the azimuth deviation between the derived image based edge and the dominant ridge is higher than 3 degree, which permits the 3D line segments derived from image data to remain as the correct edge. Note that for maintaining some right angled corners, especially in flat roofs in *scene2*, and to compensate small directional deviations in-between opposite gutters in oblique roofs, the 3D line segments derived from image data which suffer from the above mentioned deviations, and whose deviations are less than 3°, were regularized with respect to the identified most probable direction. The threshold used here, which is experimentally determined, would be case sensitive and thus may not suite well for another data set.

Figure 6.42(b) shows an edge (i^{th}) which is established by joining near end-points of succeeding ($(i+1)^{th}$) and predecessing ($(i-1)^{th}$) boundary segments of the polygon. Due to slight deviation of their end-points, the newly installed line did not represent the exact roof edge which gives rise to the (FN roof parts) blue region of Figure 6.42(b-iii).

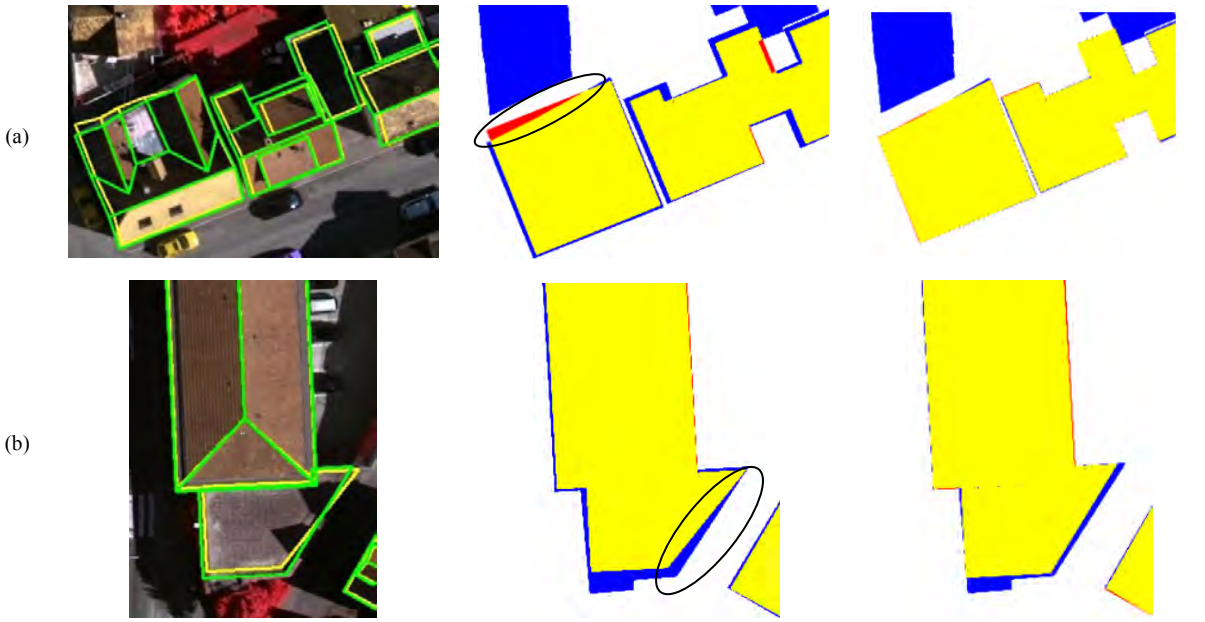

(a)

(b)

(i) Initial and refined roof models are projected on to image subsets

(ii) Per-pixel analysis on initial roof models

(iii) Per-pixel analysis on refined roof models

Figure 6.42: Refining the correct geometry of roof outlines: (a) error due to regularization of roof outlines; (b) filling gaps by connecting closer end-points of available line segments (yellow lines – projected initial model lines, green lines – projected refined model lines, yellow – TP pixels, red – FP pixels, blue – FN pixels, and circle – erroneous locations).

In addition to the above instances, there are many partly solved issues (e.g. Figure 6.43). These are mainly because the refinement step is unable to create new roof outlines or split an existing edge into a few more components without the proper evidences. For instance, Figure 6.44 illustrates the difficulty of deriving two parallel gutters based on only one guided gutter which yielded FN (or FP) roof polygon areas as shown in Figure 6.43(a, b). Similarly, from Figure 6.43(c), the difficulty of creating new roof components without having guidance is shown. As mentioned in Section 1.6, these are out of the scope of this thesis work; as such, these cases remain unsolved. The solutions for these issues, however, will be discussed in the next chapter under Section 7.2.

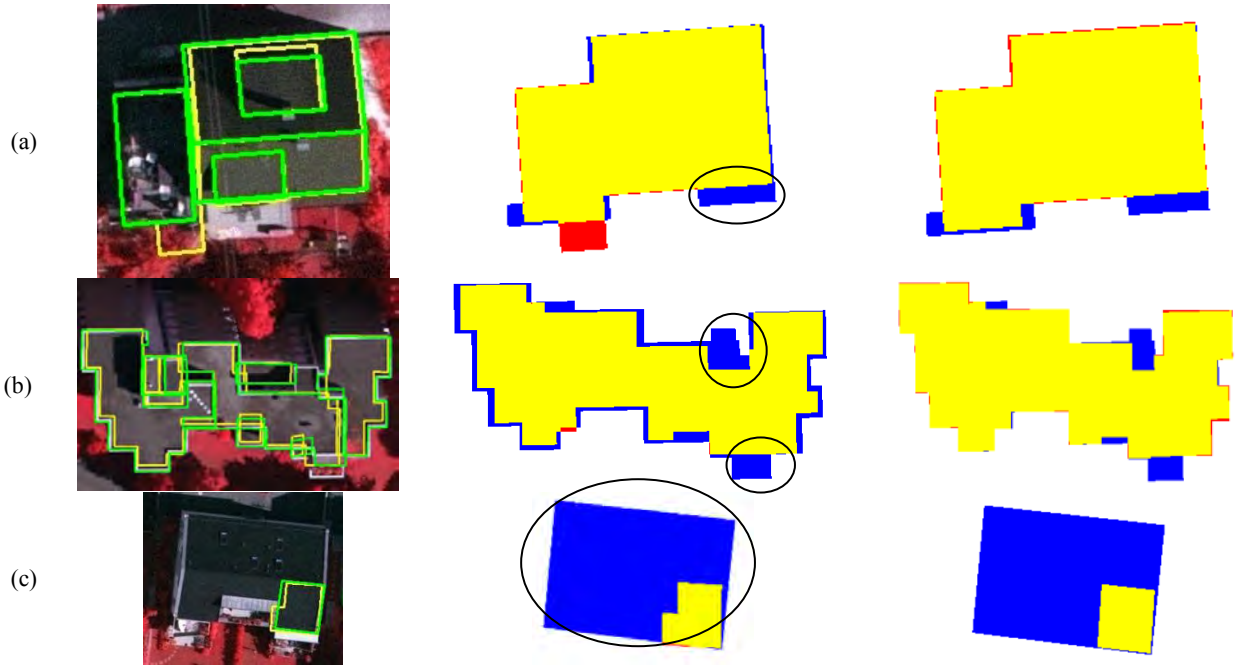

(i) Initial and refined roof models are projected on to image subsets

(ii) Per-pixel analysis on initial roof models

(iii) Per-pixel analysis on refined roof models

Figure 6.43: Partly solved issues by the refinement process: (a) and (b) difficulty of creating new roof outlines based on a single guided reference line; (c) difficulty of creating new roof polygons without having a guidance (yellow lines – projected initial model lines, green lines – projected refined model lines, yellow – TP pixels, red – FP pixels, blue – FN pixels, and circle – erroneous locations).

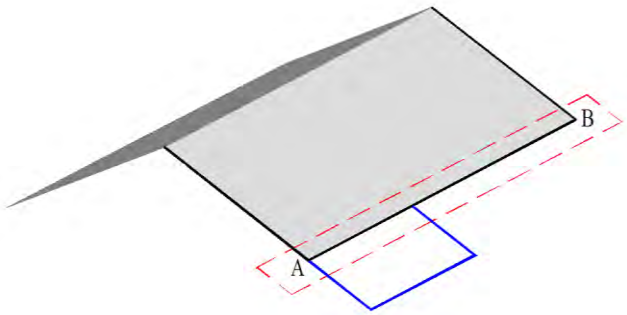

Figure 6.44: Limitation of guided searching and correspondence matching (AB – reference line segment, red dashed box – line searching buffer area based on AB, blue line – missed polygon part in initial roof models).

When comparing the refined results of flat roofs with oblique roofs having ridge-lines (in particular the flat roofs in scene2 with other roofs in *scene1, 2* and *3*), planimetric accuracy of flat roofs is better than that in oblique roofs (Figure 6.45). This could be due to high contrast differences around those building edges in images relevant to *scene2*. The top edge located along each flat roof would increase this contrast difference. Further, there would be some uncertainty in deriving object space line segments, especially because of the chosen global thresholds. This obviously led to weaken the positional accuracy of derived 3D line segments from the intersection of viewing planes and consequently the planimetric accuracy of roof outlines. Because of this, many situations could arise with some FP and FN narrow regions.

Based on the above situation, it could be concluded that it is necessary to have further experiments for increasing the positional accuracy of roof outlines.

(a) (b) (c) (d)

Figure 6.45: Comparison between flat and slanted roofs: (a) image subset – flat roof; (b) corresponding pixel analysis results; (c) image subset – slanted roof; (d) corresponding pixel-level analysis results (yellow – TP, red – FP, blue - FN).

6.2.3.6 Steering parameters

The fundamental parameters used in the experiments are shown in Table 6.11. As in the previous section, to set the parameters, user based knowledge is adopted. Few experimental routings were also carried out for selecting the acceptable parameters which fit a maximum number of object extractions. In general, for gathering potential boundary lines relevant to outer-boundaries and step-edges from the results of Burns line extractor, two diffident thresholds giving more flexibility for outer boundary line segments are set. This is mainly to compensate for errors caused by the underestimation of roof outlines, and to obtain many candidates for representing them. In general, for *scene1* and *3*, smaller thresholds are set when compared to *scene2*. Since the object complexities of these two sites are higher than the *scene2*, as a solution to avoid ambiguities, smaller constraints are used. To gather many candidate line segments, larger distance and angular thresholds set to the buffer are useful. The object space line segments of the flat roofs in *scene2* were constructed without imposing the symmetry constraints, as it is impossible to determine the symmetry in a flat roof.

Table 6.11: Explicitly defined parameters (O-B = Outer-boundary, S-E = step-edge).

Parameter	Scene1		Scene2		Scene3	
	O-B	S-E	O-B	S-E	O-B	S-E
Distance threshold for buffer width (# pixels)	6	6	12	12	8	8
Angle threshold (degree)	3	3	7	7	3	3
Coverage (meter)	0.1	0.1	0.1	0.1	0.1	0.1
Gradient threshold (degree)	5	5	5	5	5	5
Distance to plane (meter)	0.6	0.6	0.6	0.6	0.6	0.6
Pixel difference for symmetry threshold	2	2	-	-	2	2

6.3 Comparison with other peers

In this section, results of this study are compared with the peer results of those who took part in the ISPRS benchmark test project.

It is reported that fourteen participants have submitted the results of building roof models obtained by different methods for the evaluation with respect to the ISPRS benchmark reference data. Of these

approaches, ten methods use ALS point clouds while only one method (11th in the list) relies on raster DSM created from ALS data. Two methods utilize only images, while the other two methods, including the refined results submitted by this study, have used point clouds and image data. More description of the applied methodology of each submitted result are presented in Rottensteiner et al (2014) and (ISPRS Comm.3, 2011).

Table 6.12 summarizes the average quality indices of those fourteen submitted results relevant to scene 1, 2 and 3. Only four methods have been submitted on building model results with respect to the selected scenes. According to the reported results, it can be concluded that every method shows a high correctness rather than high completeness. This indicates that all the methods are concerned about preventing errors rather than the reconstruction of incomplete objects.

Table 6.12: Evaluation of the building reconstruction – average of scene 1-3: (PC – point clouds, DSM – digital surface model, IMG – images,) (Rottensteiner et al., 2014).

Data sources	Name	Completeness	Correctness	Quality	RMS_d (m) planimetry	RMS_Z (m) height
PC	MON	77.5	89.7	71.2	0.90	0.37
PC	VSK	74.2	98.6	73.5	0.83	0.27
PC	ITCE1	69.4	90.1	63.1	1.00	**0.17**
PC	ITCE2	69.8	98.3	68.7	1.03	**0.17**
PC	ITCX1	69.5	98.1	68.7	0.70	0.20
PC	ITCX2	82.0	92.9	76.8	0.70	0.27
PC	ITCX3	**82.8**	94.9	78.7	0.70	0.20
PC	CAS	68.5	**100.0**	68.5	0.75	0.25
PC	TUD1	70.0	95.8	67.8	0.70	0.20
PC	YOR	79.9	99.5	79.5	0.63	0.27
DSM	KNTU	80.4	96.7	78.3	0.90	0.40
IMG	FIE	82.6	83.1	70.7	1.10	0.40
IMG	CKU	82.1	96.8	**80.1**	0.73	0.63
PC+IMG	BNU	87.2	100.0	87.2	0.60	0.10
PC+IMG	TUD2	72.6	**100.0**	72.6	**0.55**	0.20

The highest correctness, *i.e.* 100%, is given by the methods which integrate point clouds and images, including the method proposed in this study. In general, correctness of each method delivers roughly more than a value of 90%. Yet it is hard to discriminate correctness of methods based on data such as point clouds and image data. As such, it difficult to state that point cloud based methods are better than the image based method, or vice versa, because all performed in a similar manner. When considering the level of completeness, the highest completeness level is given by ITCX3, who also used a graph based roof reconstruction approach. Conversely, one could argue that the completeness of image based methods is better than the point clouds methods because both methods that rely on images (FIE and CKU) provided over 80% completeness. However, another could argue that this may not be so and therefore it is hard to make a statement based on two submitted results.

When considering the planimeric accuracy, the refined roof models produced in this study provided the highest accuracy by giving the lowest RMS_d, equal to $0.55m$. Comparing to the other methods that integrate images and point clouds, *i.e.* $0.6m$ (BNU), and the one which gave the highest XY accuracy with respect to ALS, *i.e.* $0.63m$ (YOR), one could say that this is not a significant improvement. Yet, due to many closely located roof outlines in *scene1*, errors caused by missed outlines would be a

reason to receive a low positional accuracy for *scene1* which then reduces the average positional accuracy down to 0.55*m*. Besides, it could be stated that working only with image data doesn't always produce high planimetric accuracy as both methods which used only images show comparatively less planimetric accuracy, equal to 1.1*m* and 0.73*m* respectively. As the vertical accuracy of ALS point clouds is high, the maximum vertical accuracy 0.17*m* is given by ITCE1, and ITCE2, which is roughly equal to the accuracy that the point clouds delivers. Vertical accuracy of the roof models reconstructed in this study is given the second highest accuracy, reaching to 0.2*m*.

When compared with the other methods that were involved in this benchmark project, the method proposed in this study obtained the highest correctness (100%) and the highest planimetric accuracy (also a very high vertical) for the reconstructed roof models. Therefore, it is possible to state that the feasibility and robustness of the proposed strategies developed in this study are the highest. This further illustrates the importance of integrating both point clouds and image data for obtaining accurate geometries for the building models.

6.4 Discussion

In this section, the experimental results obtained using real data sets comprising of ALS point clouds and aerial images are analyzed to demonstrate the feasibility of the proposed methodology. This section intends to look at the results from a general point of view and in a summarized form.

Over 90% of the modeling performance indicates that the proposed cycle graph analysis method is robust and feasible to be applied in automatically reconstructing roof models even under complicated object scenarios. Roof topologies have been well preserved by the method, which is proved by the over 93% topological correctness. This emphasizes that the cycle graph analysis method is able to correctly discover available topologies which exist among the roof planes.

In contrast to this, per-object level completeness of the initial roof reconstruction dropped down considerably to the 70% range. This indicates that roughly 30% of roof planes were unable to be extracted by the initial processing steps. Further, few vegetation patches still remained as roof planes, and which slightly reduced the correctness of roof reconstruction by adding a few FP values. Considering this, the vegetation removal step should be improved further. Comparing the three test scenes, buildings in *scene1* is the most difficult and complicated to reconstruct. This is because it contains small roof planes, short feature lines and roof outlines. This phenomenon can be seen in most of *scene3* as well, but due to its gable shaped roofs, the complexity become moderate. As such, it is hard to obtain successful segmentation result, as well as to determine correct topological relations. These difficult issues were overcome, to some extent, by setting fine parameters as shown in Table 6.7. However, the obtained result can be enhanced further by following certain parameter tuning experiments or allowing the algorithm to choose parameters by analyzing the data in a statistical manner. The latter method, however, would be computationally expensive. Multi-layer flat roofs are dominant in *scene2*. Comparing to other test results provided by the ISPRS test participants who used ALS point clouds, step-edges reconstructed by the method proposed in this study represented the closest result to reality. Hence, one can say that the technique introduced in this study is suitable for both oblique and flat roof reconstruction. Considering the geometrical reconstruction from point clouds, segmentation issues, missing segments and the mismatch of parameters or assumptions are the main error sources which deform the geometry of reconstructed models, in particular roof topology. As it is, the vertical accuracy of the initial roof models is acceptable (0.2*m*) and confirms a similar accuracy roughly equal to the accuracy of point clouds. Conversely, the planimetric accuracy shows a comparatively low average value, *i.e.* 0.8*m*.

For enhancing the planimetric accuracy, Chapter 5 introduced a refinement step by integrating image data. The results exhibited that the accuracy of roof models is increased both planimetrically and topologically. Interestingly, the per-object level correctness increased to 100%. This indicates that no

error existed in the refined roof models. Further, the RMS_d decreased to $0.55m$, which is the highest figure when comparing with the other methods that took part in the benchmark project, including the approach (BNU, see Table 6.12) that integrated image and point clouds.

Image data integration certainly enhances the accuracy in many ways. One could say it allows for verification of existing roof outlines. This is correct because based on the image-based boundary segments, the study was able to obtain not only accurate roof outlines, but also to reduce FP errors caused by vegetation. Furthermore, the most interesting thing here is the recovery of topological relations which were hidden in the initial roof models due to occlusion and data gaps. The topological correctness of refined models has now become 100%. Indeed, the split separate buildings (see Figure 6.36a) were correctly connected by recognizing step-edge relations among the roof planes. In this regard, it is also possible to say this as a rectification of occlusion effect with the help of image data, or the rectification of graph error with additional data sources. All these are correct because once an edge is recognized as a step-edge, both facts can be realized. However, one erroneous roof corner which is associated with ridge-lines was not corrected by the refinement process. This is mainly because of the inability to create new line segments representing the new roof planes. Since the process follows some kind of guided line searching procedure, this barrier should be expected and should be avoided in future work.

Concerning the parameters used in the refinement process, thresholds for angle and width of the buffer are more important to be considered as these two thresholds restrict the number of candidates falling into the buffer area. It was sufficient to choose a distance of 6-8 pixels as the width of the buffer for *scene1* and *3*. For *scene2*, it was 12 pixels (mainly for flat roofs) because the flat roof boundaries in the initial model are highly underestimated. To obtain boundary lines which don't obey orthogonality and parallelism constraints with respect to the dominant direction, angular thresholds at roughly 5° are chosen. However, for the purpose of obtaining proper line segment candidates representing the actual boundaries of the split separated buildings in *scene2*, an angular threshold of 10° was set. Not to lose any potential extractions, a $0.1m$ distance threshold was set for the coverage which was common for all the scenes. Considering the scene constraints, the two most important constraints were the distance to the point and gradient. These two significantly accept the possible corresponding line derivations while rejecting erroneous ones. For the purpose of avoiding images having weak viewing geometries, a 20° angle threshold was used as the minimum angle between two viewing planes belonging to two different images.

When considering the small FP and FN pixels available along the refined results, it is difficult to identify the main reason for them to remain, as many factors contributed for this error propagation. It is reasonable to say that (i) errors in linear feature extraction - mainly due to the poor contrast and shadow effect, (ii) accumulated errors in object space line construction – mismatch of parameters and the reality, ambiguities (or complexities) of the actual scene, and (iii) incorrect line rectification – misalignment of defective edges, deviations from regularities, are caused for this. Further experiments are needed for improving these situations.

It should be mentioned that it is still difficult to compare the refined results produced by this study with other peers who were involved in similar research work. This is because the image based (or image integrated with point clouds) methods are still under development and only very few results have been submitted under this category to the benchmark test projects like ISPRS urban object modeling.

7. Conclusion and future work

This chapter summarizes the work presented in the thesis, and concludes with a discussion of the future work. In Section 7.1, the most important methodological insights and the major contributions of the research are highlighted. Furthermore, the research findings which were confirmed by the experimental results using three test scenes, as well as how they met the objectives of the research, are discussed. The conclusions are drawn based on the statistics for the obtained results. The ideas for future work are presented in Section 7.2.

7.1 Conclusion

As presented in Chapter 1, this research aimed at developing a new processing scheme for the automatic reconstruction of geometrically and topologically corrected 3D building models over complex scenes from ALS point clouds and digital aerial images. One of the most important objectives was to obtain a high level of accuracy, both planimetrically and vertically. The research was also expected to utilize RTG in an efficient way to reconstruct complex shape buildings without relying on external graphs. The following discussion demonstrates how these objectives were met, and what the benefits and the drawbacks of the research are.

In principle, the process was separated into two parts, namely (i) model reconstruction from point clouds, and (ii) refinement of the reconstructed models for enhancing the planimetric and topological accuracies. The most important aspect of the first part was to develop innovative solutions for the reconstruction of roof corner geometries with preserved topology without relying on external targets or library graphs. This aim was achieved by using a combination of data and RTG. For this, a novel cycle graph analysis concept was introduced for the first time. Of the cycles defined in this study, the shortest closed cycle correlates the convergence of feature lines, *i.e.* ridge-lines or step-edges leading to internal roof corners. The Dijkstra's algorithm was implemented as a way to extract the shortest cycles available in an RTG. Based on the shortest closed cycles, available internal corners were geometrically fixed. While the intersection of ridge-lines produced one corner point, the convergence of step-edges produced many intersection points at different height levels. Therefore, two different strategies were used for the fixing of these two types of corners. In fact, a weighted least square process was used for the first case, whereas a strategy of transferring the most reliable average position (XY) into different height levels was used for the latter case. In contrast to the shortest closed cycles, the outer roof corners were geometrically fixed by extracting the outermost cycle. For each RTG, a unique outermost cycle is available, which can be obtained by applying a few graph operations (see Section 3.2). With the forward traversing in the outermost cycle, the outer roof corners where the feature lines and the two outer-boundary line segments converge, were recognized and geometrically fixed. The strategy used to fix outer-boundaries was useful for maintaining the gutter symmetries and boundary alignments. However, the main prerequisite for fixing the corner based on the cycle analysis approach was the regularization of weakly defined boundary edges in advance. In this study, angular and placement regularization were applied to weakly defined boundary edges mainly in a piecewise manner. This enabled to rectify gutter lines having different directional orientations as in reality.

The main advantage of the cycle analysis process was its ability to reconstruct geometrically corrected detailed roof models without knowing their primitive shapes. Flat roofs having multi-layer height jumps were also correctly reconstructed, although some small planimetrical uncertainty existed along step-edges. The Modeling Performance (MP) > 90% demonstrated the robustness of the closed cycle graph concept for roof reconstruction. In spite of the low completeness of per-object level (71%), an

overall correctness (per-object) of 96% was reached. The main reason for the low completeness was the defects associated with the classification steps, in particular the merging step. In contrast, the high rate of correctness was maintained, over 93%, with the roof topology. When considering the polygon geometry, a high geometric accuracy (0.3m/0.7m for height and planimetry) was achieved in the process. Based on these statistics, it is reasonable to conclude that the cycle analysis process is robust, and can be successfully applied for complex scenarios.

It should also be stated that a few erroneous fixing of roof corners were generated by the cycle approach. These were mainly due to erroneous cycles caused by false positive and negative graph edges. These incorrect graph edges were the result of wrong topological relations caused by missing segments, occlusion effects, over-/under-segmentation, and mismatch of parameters. Although it was possible to recognize some of these errors using available cross edges (or borders) in the RTG, error correction was not performed as the completion of the second phase of the research was more important. However, future work will focus on this.

Considering the feature extraction, a rate of over 70% shows that the developed rule based roof plane extraction process is comparatively acceptable. Although the applied vegetation removal methods performed acceptably, it is concluded that it should be developed further due to a few false positive extractions.

When focusing on the second specific objective (second part of the thesis), the core aspect of it was to integrate image data for improving the planimetrical and topological accuracies of the reconstructed models. This objective was also achieved, while contributing several innovative aspects to the scientific community. It is already proved that the object space line segments can be derived by the matching of image-based line segments in projective geometry through the intersection of viewing ray planes. For this matching process, scene constraints were incorporated for minimizing the matching ambiguities within this study. Three well-defined evidences were determined with respect to the scene *i.e.* roof models reconstructed from point clouds. The gradient of a roof outline, distance of a point to the plane and symmetry between two gutters belonging to two opposite roof pairs were defined in this scenario. Fault correspondences representing edges on the footprint, or beneath the roof outline, or even somewhere on the wall, were avoided using the first two constraints. Having identified the rough symmetries, ambiguities especially relevant to oblique roofs, were further avoided. Similar to many other researchers, this experiment also had to deal with incompleteness issues such as gaps. In addition, some erroneous derivations, such as deviated edges for eave lines, were also found. The effects of these defects were avoided by predicting the most probable boundary edges that could be used to represent such cases. In this regard, known structural arrangements of roof models and especially defined convergence priors were applied. Although some false positive and negative narrow regions were given for some roof outlines, the process enabled to accomplish complete refined roof boundaries for each roof model. The evaluation results showed an increased planimetric accuracy (0.55m) for the refined building models. It is the highest planimetric accuracy when compared with the results of other methods submitted to the ISPRS project. As such, obviously this is a considerable achievement. In addition, correctness of per-object level accuracy and topological accuracy of refined models reached the peak *i.e.* 100%. These statistics prove that refinement strategies increased both the planimetric and topological accuracies considerably.

In contrast to improvements, there were still some narrow false positive and negative polygon areas along the roof outlines. As mentioned in Section 6.2.3, there could be many reasons for this, such as errors in line extraction owing to shadow effect, erroneous matching, errors caused by the prediction process, and so on. Therefore, further experiments are needed for further improvements.

Additionally, certain boundary segments relevant to some irregularities (mostly by short edges) which did not exist in the initial model were not refined. Similarly, buildings that were missed during the initial reconstruction remained unsolved. As mentioned in Section 1.5, rectification of those issues was not within the scope of this thesis, and as such, they were not focused upon. However, under future work, solutions for those issues are discussed.

7.2 Future work

In order to increase the completeness and correctness of results given by both methods, some aspects of processing strategies could be extended. Due to insufficient time, it was not possible to extend and test them fully. Therefore, for certain aspects, further attention is needed.

1. **Geometry and topology of initial models**

Rather than the intersection of line segments, intersection of planes supposing to converge would be more appropriate to fix inner corners relevant to ridge-lines. This is because more accurate weights can be assigned if one could rely on planes. The solution for this is also a weighted least square process.

In general, the difference of azimuth angles between two roof pairs should take a regular value. For instance, in a gable roof, it should be 180°. However, from the derived planes, this is given with some ($\pm\delta$) error. In this study, plane adjustments to be fitted with the azimuth regularities were not fully realized though ridge-line horizontality was maintained. In a connected roof cluster, starting from the plane which fits with the highest precision *i.e.* probably the plane that has the lowest height residual or *RMS error* with respect to segmented points, plane adjustment can be done. Besides, it is also possible to choose the size of the plane.

As mentioned in Section 6.2.2.2, once a cross edge (graph edge) is found from an RTG, then recalling the planar segmentation for point clouds or by integrating the results of image segmentation (described below) with the initial models, segmentation issues can be rectified. Taking guidance from one data source, new feature lines can be derived. Consequently, new graph edges can also be created.

2. **Geometry and topology of refined models**

The role of the structural arrangement of roof models and convergence priors can be developed further as a grammar based approach. If it is possible to extract roof primitive features, such as roof planes and boundary features, as disconnected line segments, the feature composition tree can be developed with these derived elements. This then leads to develop the grammars.

This study assumes that the ridge-lines relevant to intersection of planes derived from point clouds are precise. Of course it is correct, but ridge-lines can be further refined by incorporating planes derived from image data. Here, by having four or more planes, the least square adjustment process can be applied to derive parameters of new ridge-lines. Weights could be assigned to each plane, giving a higher contribution to the ALS derived planes. Then if one wants to regularize the image-based eave or even gutter lines, it could be realized more accurately.

It is hard to find global parameters that suit every situation. Currently, the study relies on global thresholds for many aspects such as line searching, line matching and refinement. It obviously causes some ideal line segments to drop out and to accumulate erroneous ones. If the process can be extend in a way to iteratively change the parameters, it would be more advantageous to reduce gaps or missed lines.

When considering the best line predictions, at the moment the prediction depends only on evidences. In addition to evidences, if the procedure can be extended to be linked with the accuracy of the derived line segments from image data, then more stable predictions can be defined. For instance, the decreasing accuracy is given in the sequence of (i) intersecting multiple viewing planes, (ii) stereo

planes, and (iii) one plane with the roof. Therefore, a weight can be assigned to represent the method (among 1 - 3) by which a certain boundary edge is derived. Then at the time of rectifying the lines, a higher contribution can be obtained from the line segments those that have higher weights. This could probably reduce the false positive and negative errors further.

In the viewing geometry, it is always beneficial if higher weights can be given to nadir view images.

Considering the irregularities which are not represented in the roof outlines of the initial model, if new image-based line segment(s) representing the roof outlines can be found (from image space) in between two existing edges in the initial model, then irregularities can be reconstructed accurately. To find new line segments, a moving search window can be applied at the end of each already used line segment in each image. Once a 2D line segment is found, this can be projected on to the next image to find the corresponding candidates for that search line. Having suitable candidates for all four images, by intersecting their viewing ray planes, the relevant new line segments can be derived. In a similar way, the boundaries of the missed buildings can also be found. However, in order to get guidance for the margins for such polygons, image segmentation could first be followed. Then by integrating the recognized homogeneous segments which represent those missed polygons with the extracted line segments, line segments that represent the polygons' boundary can be easily recognized. By intersecting their viewing ray planes, relevant object space boundary edges can be derived, which enables to recover the missed buildings in the point clouds.

Integration of the results of image segmentation together with the initial models, missed segments can be found. As such, new feature lines can be demarcated roughly, and refined later, using a similar procedure to that has been proposed in this study. Also, RANSAC based outlier removal process would be more useful when intersecting multiple planes.

Bibliography

Ameri, B., 2000. Feature based model verification (FBMV): a new concept for validation in building reconstruction. International Archives of Photogrammetry and Remote Sensing 33 (Part B3/1), 24-35.

Ameri, B., Fritsch, D., 2000. Automatic 3D building reconstruction using plane-roof structures. In: ASPRS Congress, Washington, DC, pp. 12.

Arefi, H., Hahn, M., 2005. A hierarchical procedure for segmentation and classification of airborne LIDAR images. In: International Geoscience and Remote Sensing Symposium, vol. 7, p. 4950.

Baillard, C., Zisserman, A., 2000. A plane-sweep strategy for the 3D reconstruction of buildings from multiple images. International Archives of Photogrammetry and Remote Sensing 33 (Part B2), 56 - 62.

Baillard, C., Schmid, C., Zisserman, A., Fitzgibbon, A., 1999. Automatic line matching and 3D reconstruction of buildings from multiple views. In: ISPRS Conference on Automatic Extraction of GIS Objects from Digital Imagery, Vol. 32, pp. 69-80.

Beder, C., 2004. A unified framework for the automatic matching of points and lines in multiple oriented images. The International Archives of Photogrammetry, Remote Sensing, and Spatial Information Sciences 35 (Part B3), 1109-1113.

Brenner, C., 2005. Building reconstruction from images and laser scanning. International Journal of Applied Earth Observation and Geoinformation 6 (3), 187–198.

Brenner, C., Haala N., Fritsch D., 2001. Towards fully automated 3D city model generation. In: Workshop on Automatic Extraction of Man-Made Objects from Aerial and Space Images III, Ascona.

Brenner, C., 2000. Towards fully automatic generation of city models. International Archives of Photogrammetry, Remote Sensing and Spatial Information Sciences 33 (Part 3B), 85–92.

Burns, J. B., Hanson, R., Riseman, E.M., 1986. Extracting straight lines. IEEE Transactions on Pattern Recognition and Machine Intelligence 8(4), 425–455.

Canny, J., 1986. A computational approach to edge detection. IEEE Transactions on Pattern Analysis and Machine Intelligence 8(6), 679–698.

Cheng, L., Tong, L., Chen, Y., Zhang, W., Shan, J., Liu, Y., Li, M., 2013. Integration of LiDAR data and optical multi-view images for 3D reconstruction of building roofs. Optics and Lasers in Engineering, 51(4), 493-502.

Cheng, L., Gong, J., Li, M., Liu, Y., 2011. 3D building model reconstruction from multi-view aerial imagery and LiDAR data. Photogrammetric Engineering and Remote Sensing, 77(2), 125-139.

Collins, R. T., Jaynes, C. O., Cheng, Y. Q., Wang, X., Stolle, F., Riseman, E. M., Hanson, A. R., 1998. The Ascender System: Automated Site Modeling from Multiple Aerial Images. Computer Vision and Image Understanding, 72(2), 143-162.

Cramer, M., 2010. The DGPF-Test on Digital Airborne camera evaluation overview and test design. Photogrammetrie-Fernerkundung Geoinformation, 2(2010), 73 – 82.

Dal Poz, A., de Souza Correia, L., Fazan, A., Marcato, V., Simonsen, R., 2009. 3D lidar building roof refinement using photogrammetric data. In: International Cartography conference 24, Santiago.

Diestel, R., 2010. Graph Theory, fourth ed. Springer-Verlag., Heidelberg.

Dorninger, P., Pfeifer, N., 2008. A comprehensive automated 3D approach for building extraction, reconstruction, and regularization from airborne laser scanning point clouds. Sensors 8 (11), 7323-7343.

Elaksher, A. F., 2008. Multi Image Matching of Straight Lines with Geometric Constraints. In : Proceeding of ISPRS Geographic Object Based Image Analysis.

Förstner, W., 1999. 3D-city models: automatic and semiautomatic acquisition methods. Proceedings of Photogrammetric week 1999.

Förstner, W., Gülch, E., 1987. A fast operator for detection and precise location of distinct points, corners and centres of circular features. In: Proceedings of ISPRS Conference on Fast Processing of Photogrammetric Data. Interlaken, Switzerland, pp. 281–305.

Gröger, G., Kolbe, T. H., Czerwinski, A., Nagel, C. 2008. OpenGIS city geography markup language (CityGML) encoding standard, Version 1.0.0, OGC Doc. No. 08-007r1
http://www.opengeospatial.org/standards/citygml (Accessed: 29th March 2013).

Haala, N., Kada, M., 2010. An update on automatic 3D building reconstruction. ISPRS Journal of Photogrammetry and Remote Sensing 65, 570-580.

Haala, N., Hastedt, H., Wolf, K., Ressl, C., Baltrusch, S., 2010. Digital photogrammeric camera evaluation generation of digital elevation models. Photogrammetrie-Fernerkundung Geoinformation 2(2010), 99 – 115.

Haala, N., Brenner, C., 1998. Interpretation of urban surface models using 2D building information. Computer Vision and Image Understanding 72 (2), 204–214.

Habib, A.F., Zhai, R., Kim, C. 2010. Generation of complex polyhedral building models by integrating stereo-aerial imagery and LiDAR data. Photogrammetric Engineering and Remote Sensing 76 (5), 609–623.

Habib, A., Ghanma, M., Mitishita, E., 2004. Co-registration of Photogrammetric and LiDAR data: Methodology and Case study. Brazilian Journal of Cartography (RBC) 56/01, pp.1-13.

Habib, A., Kelley, D., 2001. Single-photo resection using the modified Hough transform. Photogrammetric engineering and remote sensing 67(8), 909-914.

Henricsson, O., 1998. The Role of Color Attributes and Similarity Grouping in 3-D Building Reconstruction. Computer Vision and ImageUnderstanding 72(2), 163-184.

Heuel, S., 2004. Uncertain projective geometry: statistical reasoning for polyhedral object reconstruction. Vol. 3008, Springer, 2004.

Heuel, S. Forstner W., 2001. Matching, reconstructing and grouping 3D lines from multiple views using uncertain projective geometry. In: Proceedings of the IEEE Computer Society Conference on Computer Vision and Pattern Recognition, Vol. 2, pp. 511-517, Kauai Marriott, Hawaii.

Hofmann, A. D., 2004. Analysis of TIN-structure parameter spaces in airborne laser scanner data for 3-D building model generation. International Archives of Photogrammetry, Remote Sensing and Spatial Information Sciences, 35(B3), 302-307.

Hough, P. V., 1962. Method and means for recognizing complex patterns. United States Patent 3069654, Washington, DC: U.S. Patent and Trademark Office.

Huang, H., Brenner, C., Sester, M., 2013. A generative statistical approach to automatic 3D building roof reconstruction from laser scanning data. ISPRS Journal of Photogrammetry and Remote Sensing 79, 29-43.

Huang, H., Brenner, C., 2011. Rule-based roof plane detection and segmentation from laser point clouds. In: Joint Urban Remote Sensing Event (JURSE), 11-13 April. IEEE, Munich, Germany, pp. 293–296.

ISPRS Comm.3, 2011. ISPRS test project on urban classification and 3D building reconstruction. http://www.isprs.org/news/announcements/110314_ISPRS_Intercomparision-Flyer.pdf (Accessed: 29th January 2012).

Jaw, J. J., Perny, N. H., 2008. Line feature correspondence between object space and image space. Photogrammetric Engineering & Remote Sensing 74(12), 1521-1528.

Kada, M., McKinley, L., 2009. 3D building reconstruction from LiDAR based on a cell decomposition approach. International Archives of Photogrammetry, Remote Sensing and Spatial Information Sciences 38, Part (W4).

Kada, M., 2009. The 3D Berlin project. In: Fritsch, D. (Ed.), Photogrammetric Week 2009. Wichmann Verlag, Heidelberg, pp. 331–340.

Karantzalos, K., Paragios, N., 2010. Large-scale building reconstruction through information fusion and 3D priors Geoscience and Remote Sensing, IEEE Transactions 48, 2283-2296.

Kim, K., Shan, J., 2011. Building roof modeling from airborne laser scanning data based on level set approach. ISPRS Journal of Photogrammetry and Remote Sensing, 66(4), 484 - 497.

Kim, C., Ghanma, M., Habib, A., 2006. Integration of Photogrammetric and LIDAR data for realistic 3D model generation. Department of Geomatics Engineering, University of Calgary, Canada.

Kim, Z., Nevatia, R., 2004. Automatic Description of Complex Buildings from Multiple Images. Computer Vision and Image Understanding 96(1), 60-95.

Khoshelham, K., 2005. Region refinement and parametric reconstruction of building roofs by integration of image and height data. In: International Archives of Photogrammetry and Remote Sensing and Spatial Information Sciences, 36, Part (3/W24), 693-698.

Kraus, K., Pfeifer, N., 1998. Determination of terrain models in wooded areas with airborne laser scanner data. ISPRS Journal of Photogrammetry and remote Sensing, 53(4), 193-203.

Kwak, E., 2013. Automatic 3D building model generation by integrating LiDAR and aerial images using a hybrid approach. PhD Thesis, The University of Calgary.

Lafarge, F., Mallet, C., 2012. Creating large-scale city models from 3D-point clouds: a robust approach with hybrid representation. International Journal of Computer Vision 99 (1), 69–85.

Lafarge, F., Descombes, X., Zerubia, J., Pierrot-Deseilligny, M., 2010. Structural approach for building reconstruction from a single DSM. IEEE Transactions on Pattern Analysis and Machine Intelligence 32 (1), 135–147.

Lafarge, F., Descombes, X., Zerubia, J., Pierrot-Deseilligny, M., 2008. Automatic building extraction from DEMs using an object approach and application to the 3D-city modeling. ISPRS Journal of Photogrammetry and Remote Sensing 63 (3), 365–381.

Lee, D. H., Lee, K. M., Lee, S. U., 2008. Fusion of lidar and imagery for reliable building extraction. Photogrammetric Engineering & Remote Sensing 74(2), 215-225.

Lin, H., Gao, J., Zhou, Y., Lu, G., Ye, M., Zhang, C., Liu, L., Yang, R., 2013. Semantic decomposition and reconstruction of residential scenes from lidar data. ACM Transactions on Graphics 32 (4), 66:1-66:10.

Li, Y., Wu, H., An, R., Xu, H., He, Q., Xu, J., 2013. An improved building boundary extraction algorithm based on fusion of optical imagery and LIDAR data. Optik-International Journal for Light and Electron Optics, 124(22), 5357-5362.

Maas, H.G., Vosselman. G., 1999. Two algorithms for extracting building models from raw laser altimetry data. ISPRS Journal of Photogrammetry and Remote Sensing 54 (2-3), 153-163.

Maas, H. G., 1999. Fast determination of parametric house models from dense airborne laser scanner data. In: International Workshop on Mobile Mapping Technology, Vol. 32, No. 2W1, pp. 1-6.

Ma, R., 2005. DEM generation and building detection from lidar data. Photogrammetric Engineering and Remote Sensing, 71(7), 847-854.

Ma, R., 2004. Building model reconstruction from LiDAR data and aerial photographs. Ph.D. dissertation. Columbus, Ohio, The Ohio State University, 166 p.

Mcintosh, K., Krupnik, A., 2002. Integration of laser-derived DSMs and matched image edges for generating an accurate surface model, ISPRS Journal of photogrammetry and Remote Sensing, 56(3), 167–176.

Medioni, G., Nevatia, R., 1985. Segment-based stereo matching. Computer Vision, Graphics, and Image Processing 31(1), 2-18.

Meer, P., Georgescu, B., 2001. Edge detection with embedded confidence. Pattern Analysis and Machine Intelligence, IEEE Transactions on 23(12), 1351-1365.

Meng, X., Wang, L., Currit, N., 2009. Morphology-based building detection from airborne LiDAR data. Photogrammetric Engineering and Remote Sensing 75 (4), 437-442.

Milde, J., Zhang, Y., Brenner, C., Pluemer, L. Sester, M., 2008. Building reconstruction using a structural description based on a formal grammar. International Archives of Photogrammetry, Remote Sensing and Spatial Information Sciences 37 (Part 3B), 227-232.

Musialski, P., Wonka, P., Aliaga, D. G., Wimmer, M., Van Gool, L., Purgathofer, W., 2012. A survey of urban reconstruction. In. Eurographics State of the Art Reports, Eurographics Association, 1-28.

Nalani, H. A., 2013. Automatic tree stem detection – A geometric feature based approach for MLS point clouds. In: ISPRS workshop on Laser Scanning, 11-12 November, Antalya, Turkey.

Noronha, S., Nevatia, R., 2001. Detection and Modeling of Buildings from Multiple Aerial Images. IEEE Transactions on Pattern Analysis and Machine Intelligence, 23(5), 501-518.

Nyaruhuma, A. P., Gerke, M., Vosselman, G., 2012. Verification of 3D building models using mutual information in airborne oblique images. ISPRS Annals of Photogrammetry, Remote Sensing and Spatial Information Sciences 1, 275-280.

Ohta, Y., Kanade, T., 1985. Stereo by intra-and inter-scanline search using dynamic programming. Pattern Analysis and Machine Intelligence, IEEE Transactions on 2, 139-154.

Ok, A. O., Wegner, J., D., Heipke, C., Rottensteiner, F., Soergel, U., Toprak, V., 2011. Accurate matching and reconstruction of line features from ultra high resolution stereo aerial images. In: Proceedings of ISPRS Hannover Workshop, High Resolution Earth Imaging for Geospatial Information, Hannover, Germany.

Ok, A. O., Wegner, J. D., Heipke, C., Rottensteiner, F., Soergel, U., Toprak, V., 2010a. A stereo line matching technique for aerial images based on a pair-wise relation approach. International Archives of Photogrammetry and Remote Sensing, 38(1/W17).

Ok, A. O., Wegner, J. D., Heipke, C., Rottensteiner, F., Soergel, U., Toprak, V., 2010b. A new straight line reconstruction methodology from multi-spectral stereo aerial images. International Archives of Photogrammetry and Remote Sensing 38(3A), 25-30.

Oude Elberink, S., Vosselman, G., 2011. Quality analysis on 3D building models reconstructed from airborne laser scanning data. ISPRS Journal of Photogrammetry and Remote Sensing 66 (2), 157–165.

Oude Elberink, S., 2010. Acquisition of 3D topography: Automated 3D road and building reconstruction using airborne laser scanner data and topographic maps. Ph.D. dissertation, University of Twente, Enschede, The Netherlands.

Oude Elberink, S., 2009. Target graph matching for building reconstruction. International Archives of Photogrammetry, Remote Sensing and Spatial Information Sciences 38 (Part 3/W8), 49-54.

Oude Elberink, S., Vosselman, G., 2009. Building reconstruction by target based graph matching on incomplete laser data: Analysis and limitations. Sensors 9 (8), 6101- 6118.

Oude Elberink, S., 2008. Problems in automated building reconstruction based on dense airborne laser scanning data. In: Proceedings of the XXI congress: Silk road for information from imagery, 3-11 July, Beijing, China. Comm. III, WG III/3 Beijing, pp. 93-98.

Oude Elberink, S., Maas, H.G., 2000. The use of anisotropic height texture measures for the segmentation of airborne laser scanner data. International Archives of Photogrammetry, Remote Sensing and Spatial Information Sciences 33 (Part 3B), 678–684.

Park, S., Lee, K., Lee, S., 2000. A Line Feature Matching Technique Based on an Eigenvector Approach. Computer Vision and Image Understanding 77, 263-283.

Perera, G. S. N., Maas, H. G., 2014. Cycle graph analysis for 3D roof structure modeling: Concepts and performance. ISPRS Journal of Photogrammetry and Remote Sensing. 281-286.

Perera, G.S.N., Nalani, H.A., Maas, H.-G., 2012. An automated method for 3D roof outline generation and regularization in airborne laser scanner data. ISPRS Annals of the Photogrammetry, Remote Sensing and Spatial Information Sciences 1 (3/W4), 281-286.

Perera, G.S.N., Maas, H.-G., 2012. A topology based approach for the generation and regularization of roof outlines in airborne laser scanner data. In: DGPF Tagungsband, Potsdam, Germany, on CD_ROM.

Perera, G.S.N., 2007. Segment based filtering of LASER scanner data, Master thesis, ITC, The Netherlands.

Pu, P., Rutzinger, M., Vosselman, G., Oude Elberink, S., 2011. Recognizing basic structures from mobile laser scanning data for road inventory studies. ISPRS Journal of Photogrammetry and Remote Sensing 66 (6), 28-39.

Rau, J. Y., Lin, B. C., 2011. Automatic roof model reconstruction from ALS data and 2D ground plans based on side projection and the TMR algorithm. ISPRS Journal of Photogrammetry and Remote Sensing, 66(6), S13-S27.

Rottensteiner, F., Sohn, G., Gerke, M., Wegner, J. D., Breitkopf, U., Jung, J., 2014. Results of the ISPRS benchmark on urban object detection and 3D building reconstruction. ISPRS Journal of Photogrammetry and Remote Sensing 93, 256 – 271.

Rottensteiner, F., Sohn, G., Jung, J., Gerke, M., Baillard, C., Benitez, S., Breitkopf, U., 2012. The ISPRS benchmark on urban object classification and 3D building reconstruction. ISPRS Annals of the Photogrammetry, Remote Sensing and Spatial Information Sciences 1 (3/W4), 293-298.

Rottensteiner, F., 2010. Roof plane segmentation by combining multiple images and point clouds. International Archives of Photogrammetry Remote Sensing and Spatial Information Sciences 38 (Part 3A), 245-250.

Rottensteiner, F., 2006. Consistent estimation of building parameters considering geometric regularities by soft constraints. The International Archives of the Photogrammetry, Remote Sensing and Spatial Information Sciences 36 (Part 3), 13–18.

Rottensteiner, F., Summer, G., Trinder, J., Clode, S., Kubik, K., 2005. Evaluation of a method for fusing lidar data and multispectral images for building detection. In: Stilla U, Rottensteiner F, Hinz S (Eds) CMRT05. IAPRS, Vol. XXXVI, Part 3/W24, Vienna, Austria, August 29-30, 2005.

Rottensteiner, F., Trinder, J., Clode, S., Kubik, K., 2005. Automated delineation of roof planes from lidar data. International Archives of Photogrammetry, Remote Sensing and Spatial Information Sciences 36 (Part 3/W4), 221-226.

Rottensteiner, F., Briese, C., 2003. Automatic generation of building models from lidar data and the integration of aerial images. International Archives of Photogrammetry, Remote Sensing and Spatial Information Sciences 34 (Part 3/W13), 174-180.

Rottensteiner, F., Briese, C., 2002. A new method for building extraction in urban areas from high-resolution lidar data. International Archives of Photogrammetry, Remote Sensing and Spatial Information Sciences 34 (Part 3A), 295–301.

Rutzinger, M., Rottensteiner, F., Pfeifer, N., 2009. A comparison of evaluation techniques for building extraction from airborne laser scanning. IEEE Journal of Selected Topics in Applied Earth Observations & Remote Sensing 2(1), 11-20.

Sampath. A., Shan, J., 2010. Segmentation and reconstruction of polyhedral building roofs from aerial lidar point clouds. IEEE Transactions on Geoscience and Remote Sensing 48 (3), 1554-1567.

Sampath, A. Shan, J., 2008. Building roof segmentation and reconstruction from LiDAR point clouds using clustering techniques. International Archives of Photogrammetry, Remote Sensing and Spatial Information Sciences 37(Part B3a), 279-284.

Sampath. A., Shan, J., 2007. Building boundary tracing and regularization from airborne lidar point clouds. Photogrammetric Engineering & Remote Sensing 73 (7), 805-812.

Schenk, T., Csatho, B., 2002. Fusion of LIDAR data and aerial imagery for a more complete surface description. International Archives of Photogrammetry Remote Sensing and Spatial Information Sciences, 34(3/A), 310-317.

Schmid, C. Zisserman, A., 1997. Automatic Line Matching Across Views. In: Proceedings of CVPR, pp. 666–671.

Scholze, S., Moons, T., Ade, F., Van Gool, L., 2000. Exploiting Color for Edge Extraction and Line Segment Stereo Matching. International Archives of Photogrammetry and Remote Sensing, 815–822.

Schwalbe, E., Maas, H.-G., Seidel, F., 2005. 3D building model generation from airborne laser scanner data using 2D GIS data and orthogonal point cloud projections. International Archives of Photogrammetry, Remote Sensing and Spatial Information Sciences 36 (Part 3/W19), 209-213.

Sithole, G., Vosselman, G., 2004. Experimental comparison of filter algorithms for bare earth extraction from airborne laser scanning point clouds. ISPRS Journal of Photogrammetry and Remote Sensing 59 (1-2), 85-101.

Sohn, G., Huang, X., Tao, V., 2008. Using a binary space partitioning tree for reconstructing polyhedral building models from airborne lidar data. Photogrammetric Engineering & Remote Sensing 74 (11), 1425-1438.

Suveg, I., Vosselman, G., 2004. Reconstruction of 3D building models from aerial images and maps. ISPRS Journal of Photogrammetry and remote sensing, 58(3), 202-224.

Taillandier, F., 2005. Automatic building reconstruction from cadastral maps and aerial images. The International Archives of the Photogrammetry, Remote Sensing and Spatial Information Sciences 36 (Part 3/W24), 105–110.

Tarsha-Kurdi, F., Landes, T., Grussenmeyer, P., 2008. Extended RANSAC algorithm for automatic detection of building roof planes from lidar data. The Photogrammetric Journal of Finland 21 (1), 97-109.

Tian, Y., 2011. Building reconstruction from terrestrial video image sequences. Ph.D. dissertation, University of Twente, Enschede, The Netherlands.

Tóvári, D., Pfeifer, P., 2005. Segmentation based robust interpolation – a new approach to laser data filtering. International Archives of Photogrammetry, Remote Sensing and Spatial Information Sciences 36 (Part 3/W19), 79-84.

UN-Habitat, 2012. State of the world's cities 2012/2013: Prosperity of Cities. Earthscan/James & James.

Verma, V., Kumar, R. Hsu, S., 2006. 3D building detection and modeling from aerial lidar data. In: The IEEE Computer Society Conference on Computer Vision and Pattern Recognition, 17-22 June, IEEE Computer Society, Washington, DC, USA, pp. 2213-2220.

Vosselman, G., 2012. Automated planimetric quality control in high accuracy airborne laser scanning surveys. ISPRS Journal of Photogrammetry and Remote Sensing 74, 90-100.

Vosselman, G., Maas, H.-G., 2010. Airborne and terrestrial laser scanning. Whittles, CRC Press, 336p.

Vosselman, G., Gorte, B., Sithole, G., Rabbani, T., 2004. Recognising structure in laser scanner point clouds. International Archives of Photogrammetry, Remote Sensing and Spatial Information Sciences 36 (Part 8/W2), 33-38.

Vosselman, G., Suveg, I., 2001. Map based building reconstruction from laser data and images. Automatic Extraction of Man-Made Objects from Aerial and Space Images (3), 231-239.

Vosselman, G., Dijkman, S., 2001. 3D building model reconstruction from point clouds and ground plans. International Archives of Photogrammetry Remote Sensing and Spatial Information Sciences, 34(3/W4), 37- 44.

Vosselman, G., 2000. Slope based filtering of laser altimetry data. International Archives of Photogrammetry and Remote Sensing, 33(Part 3: B3/2), 935-942.

Vosselman, G., 1999. Building reconstruction using planar faces in very high density height data. International Archives of Photogrammetry, Remote Sensing and Spatial Information Sciences 32 (Part 3/2W5), 87-92.

Wang, S., Tseng, Y., 2002. Image orientation by fitting line segments to edge pixels. In: Asian conference on Remote Sensing (ACRS), Vol. 2002.

Zhang, C., Baltsavias, E. P., 2000. Edge matching and 3D road reconstruction using knowledge-based methods. In: Schriftenreihe der Fachrichtung Geodaesie, Darmstadt, Germany, 10, pp. 251-265.

Zhang, L., 2005. Automatic Digital Surface Model (DSM) Generation from Linear Array Images. PhD Thesis, Swiss Institute of Technology Zurich.

Zhongliang, F., Zhiqun, S., 2008. An algorithm of straight line features matching on aerial imagery. International Archives of Photogrammetry, Remote Sensing and Spatial Information Sciences 37, 97-102.

Zhou,Q.-Y., Neumann,U., 2012. 2.5D building modeling by discovering global regularities. In: The IEEE Computer Society Conference on Computer Vision and Pattern Recognition, 16-21 June. IEEE Computer Society, Providence, RI, USA, pp. 326–333.